UNIVERSITÀ DEGLI STUDI DI MILANO

Dottorato di Ricerca in Scienze della Terra
Ciclo **XXVIII**

Experimental and statistical methods to improve the reliability of spectral induced polarization to infer litho-textural properties of alluvial sediments

Ph.D. Thesis

Silvia Inzoli
R10112

Tutor
Prof. Mauro Giudici

Academic Year
2014-2015

Coordinator
Prof. ssa Elisabetta Erba

a Massimo,

per un’avventura che finisce e un futuro che inizia

Index

List of symbols and abbreviations

a	tortuosity factor of Archie's law [-]
AC	alternate current
ADC	analog-to-digital converter card
AEC	anion exchange capacity [cmol/Kg]
B	equivalent conductance of sodium cations [S]
c	phenomenological frequency exponent of Cole-type models [-]
c	coarse (sand)
C	cophenetic correlation coefficient [-]
C_v	input capacitance of the amplifier [F]
CA	cluster analysis
CEC	cation exchange capacity [cmol/Kg]
d	grain diameter [mm, μm]
dt	time sampling rate of a chirp signal [s]
D	time duration of a chirp signal [s]
DC	direct current
e	$1.6022 \cdot 10^{-19}$ C, elementary (proton or electron) charge
e_a	data error on the electrical resistivity amplitude [Ωm]
e_I	data error on the imaginary part of electrical resistivity [Ωm]
e_p	data error on the electrical resistivity phase [rad]
e_R	data error on the real part of electrical resistivity [Ωm]
E	electric field [V/m]
EDL	electrical double layer
EIT	electrical impedance tomography
ERGI	electrical resistivity ground imaging
EQ_v	electrical conductivity at zero water-conductivity [μS/cm]
EU(s)	electrostratigraphic unit(s)
f	frequency [Hz]
f_i	initial frequency of a chirp signal [Hz]
f_f	final frequency of a chirp signal [Hz]
f	fine (sand)
F	formation factor [-]
F_a	apparent formation factor [-]
F_s	formation factor for a system of spherical grains [-]
F_0	equivalent formation factor [-]
G, g	gravel, gravelly
G(τ)	relaxation time distribution function
GPR	ground penetrating radar
GSM	gravel-sand-mud ternary diagram

GU	geological unit
HU(s)	hydrostratigraphic unit(s)
I_n	Fourier transformed current at electrode n [As]
I_s	Fourier transformed current at the shunt resistor [As]
I_x	Fourier transformed current between potential electrodes [As]
IHP	inner Helmoltz plane
IP	induced polarization
IQR	interquartile range
j	current density [A/m^2]
k	phenomenological frequency exponent of Cole-type models [-]
k_B	$1.3806 \cdot 10^{-23}$ m^2 kg/s^2 K, Boltzmann constant
l	resistor’s length [m]
LFP	*Livello Fondamentale della Pianura* (formation)
LGM	Last Glacial Maximum
m	cementation exponent of Archie’s law [-]
m	chargeability [-]
m_a	apparent chargeability in time domain [ms, mV/V]
m_n	normalized chargeability [µS/cm]
m	medium (sand)
M, m	mud, muddy
M_t	total chargeability [-]
MF	metal factor [-]
MSAF	*Marne di S. Agata Fossili* (formation)
n	saturation exponent of Archie’s law [-]
OHP	outer Helmoltz plane
Q_v	charge concentration per unit volume [C/m^3]
p	volume fraction of clay [-]
PCA	principal component analysis
PCB	printed circuit board
(P)FE	(percentage) frequency effect [(%) -]
Q1	first quartile
Q3	third quartile
r	particle or pore radius [µm]
R	ohmic resistance [Ω]
R_s	shunt resistance [Ω]
REV	representative elementary volume
RMSE,RMSE*	root-mean-square error [-]
RMSEam	root-mean-square error on the amplitude [-]
RMSEph	root-mean-square error on the phase [-]
$\bar{s}$	mean silhouette value [-]
S, s	sand, sandy
S	cross-sectional area [m^2]

S_p	surface-area-to-pore-volume ratio [μm^{-1}]
S_w	saturation relative to the water phase [-]
SCF	*S. Colombano Formation*
SIP	spectral induced polarization
t	time [s]
T	temperature [°C, K]
TDEM	time-domain electromagnetic
TDS	total dissolved solids [mg/L]
v_{cw}	volume of adsorbed water on clay particles [μm^3]
vc	very coarse (sand)
vf	very fine (sand)
U_c	curvature coefficient [-]
U_n	Fourier transformed electrical potential at electrode n [Vs]
U_x	Fourier transformed potential between potential electrodes [Vs]
$U_{\tau 60}$, $U_{\tau 90}$	non-uniformity coefficients of the cumulative chargeability curve [-]
$U_{\tau c}$	curvature coefficient of the cumulative chargeability curve [-]
U_{60}, U_{90}	non-uniformity coefficient [-]
V_{DC}	electrical potential during stationary transmitting period [V]
V_{ip}	transient electrical potential response [mV]
V_{pp}	peak-to-peak potential of a chirp signal [V]
V_S	electrical potential at the moment current is switched off [mV]
VES	vertical electrical sounding
X	reactance [Ω]
z	ion valence [-]
Z	electrical impedance [Ω]
Z_x	electrical impedance between potential electrodes [Ω]
Z_{en}	electrode impedance at electrode n [Ω]
Z_v	input impedance of the amplifier [Ω]
α	termic coefficient [$°C^{-1}$]
Γ_d	coarse-to-fine ratio [kg/kg] with threshold diameter d [mm]
ΔA	relative amplitude difference [-]
$\Delta \phi$	relative phase difference [-]
$\varepsilon^{(*)}$	(complex) permittivity or dielectric constant [F/m]
ε_r	relative permittivity or relative dielectric constant [-]
ε_s	low frequency limit of permittivity [F/m]
ε_∞	high frequency limit of permittivity [F/m]
ε_0	$8.8542 \cdot 10^{-12}$ F/m, permittivity of vacuum
ζ	zeta potential [mV]
θ	porosity [m^3/m^3]
λ_d	Debye length [nm]
$\rho^{(*)}$	(complex) electrical resistivity [Ωm]

$\lvert\rho^*\rvert$	electrical resistivity amplitude [Ωm]
ρ'	real part of electrical resistivity [Ωm]
ρ''	imaginary part of electrical resistivity [Ωm]
ρ_a	electrical resistivity at low frequency [Ωm]
ρ_w	electrical resistivity of water [Ωm]
ρ_0	DC electrical resistivity [Ωm]
ρ_∞	high frequency limit of electrical resistivity [Ωm]
$\sigma^{(*)}$	(complex) electrical conductivity [μS/cm]
σ'	real part of electrical conductivity [μS/cm]
σ''	imaginary part of electrical conductivity [μS/cm]
σ_c	electrical conductivity of clay particles [μS/cm]
σ_{cw}	electrical conductivity of adsorbed water on clay particles [μS/cm]
σ_{el}	electrolytic conductivity [μS/cm]
σ_{int}	interface conductivity [μS/cm]
σ_s	surface conductivity [μS/cm]
σ_w	electrical conductivity of water [μS/cm]
σ_0	DC electrical conductivity [μS/cm]
σ_∞	high frequency limit of electrical conductivity [μS/cm]
$\bar{\tau}$	mean relaxation time [s]
τ_0	characteristic relaxation time [s]
τ_n	relaxation time at n% of the total chargeability cumulative curve [s]
φ	phi-unit [-]
ϕ	electrical resistivity phase lag [rad]
ω	angular frequency [Hz]

Chapter 1

Introduction

1.1 Background

The characterization of the shallow subsurface and the knowledge about the processes that here occur constitute challenging issues in several applications of science and engineering. On one side, the shallow subsurface supports natural ecosystems and human activities, such as agriculture or exploitation of mineral, industrial, and water resources; on the other side, it is strongly impacted from waste disposal and dispersion of contaminants. The need of investigation tools suitable for a non-invasive but effective characterization of the subsurface has been largely addressed in the literature, focusing on different aspects and considering different length scales. Among the other disciplines, hydrogeophysics deals with the use of geophysical methods for the exploration, management, and monitoring of soil and groundwater (*Binley et al.*, 2010; *Binley et al.*, 2015). Geophysical parameters, and in particular electrical properties, are related to sediment's properties such as water content, porosity, specific surface area, grain-size-distribution, which are key factors also in the determination of hydrodynamic quantities. Thus, a main subject of hydrogeophysics is the study of the petrophysical relationships between electrical properties and hydraulic conductivity, mainly through the dependence of such physical parameters on other properties (*Hubbard and Rubin*, 2000; *Slater*, 2007). Even if hydrogeophysics was born from the enormous experience of geophysics applied to hydrocarbon and ore exploration, the strong differences in the physico-chemical environmental conditions, in the available technical and financial resources, and in the goals of the investigations prevent from a straightforward application of the acquisition and elaboration techniques and the use of the same empirical relationships. As a paradigmatic example, the fundamental Archie's law (*Archie*, 1942) was derived for reservoir rocks saturated with connate saline waters and can be directly applied in other cases only with care not to deviate from clean conditions of the porous material and high salinity of the saturation fluid.

In a basic review about estimation of hydraulic parameters from geoelectrical measurements, *Slater* (2007) identified three groups of electrical prospecting methods characterized by an increasing amount of achievable information, but also by an increasing uncertainty due to the superposition of effects related to multiple factors (Fig. 1.1). The bulk of the pertinent scientific literature refers to direct current (DC) surveys, which provide the real part of the complex electrical conductivity (σ'). This component is controlled by the electrolytic conductivity (σ_{el}), dependent on pore-volume properties (e.g., porosity), and the surface and interface conductivity (σ_{int}), dependent on pore-surface properties (e.g., surface area). Such a double dependence constitutes a limitation in the power of DC techniques to distinguish between lithological and pore-water heterogeneities. Therefore, increasing attention has been devoted to the imaginary component of conductivity (σ''), which can be measured with induced polarization (IP) methods and mostly depends on pore-surface characteristics. However, both porosity and specific surface area are bulk properties and do not provide a detailed and comprehensive characterization of the textural composition. Thus, multi-frequency analysis of conduction and polarization properties (spectral induced polarization methods; SIP) has been introduced. Additional electrical parameters can be obtained from the shape of the spectra of complex conductivity (i.e., conductivity amplitude and phase lag as a function of frequency). In particular, the spectral shape is expected to be related to the characteristic lengths of the investigated system, which are essential parameters controlling the fluid flow. Thus, IP and SIP methods are expected to overcome the limitations of DC surveys. In fact, at the frequency commonly used for IP and SIP methods (<10 kHz), polarization processes are associated to local redistribution of charges at the mineral-fluid interface and are strictly related to the presence of clay and silt.

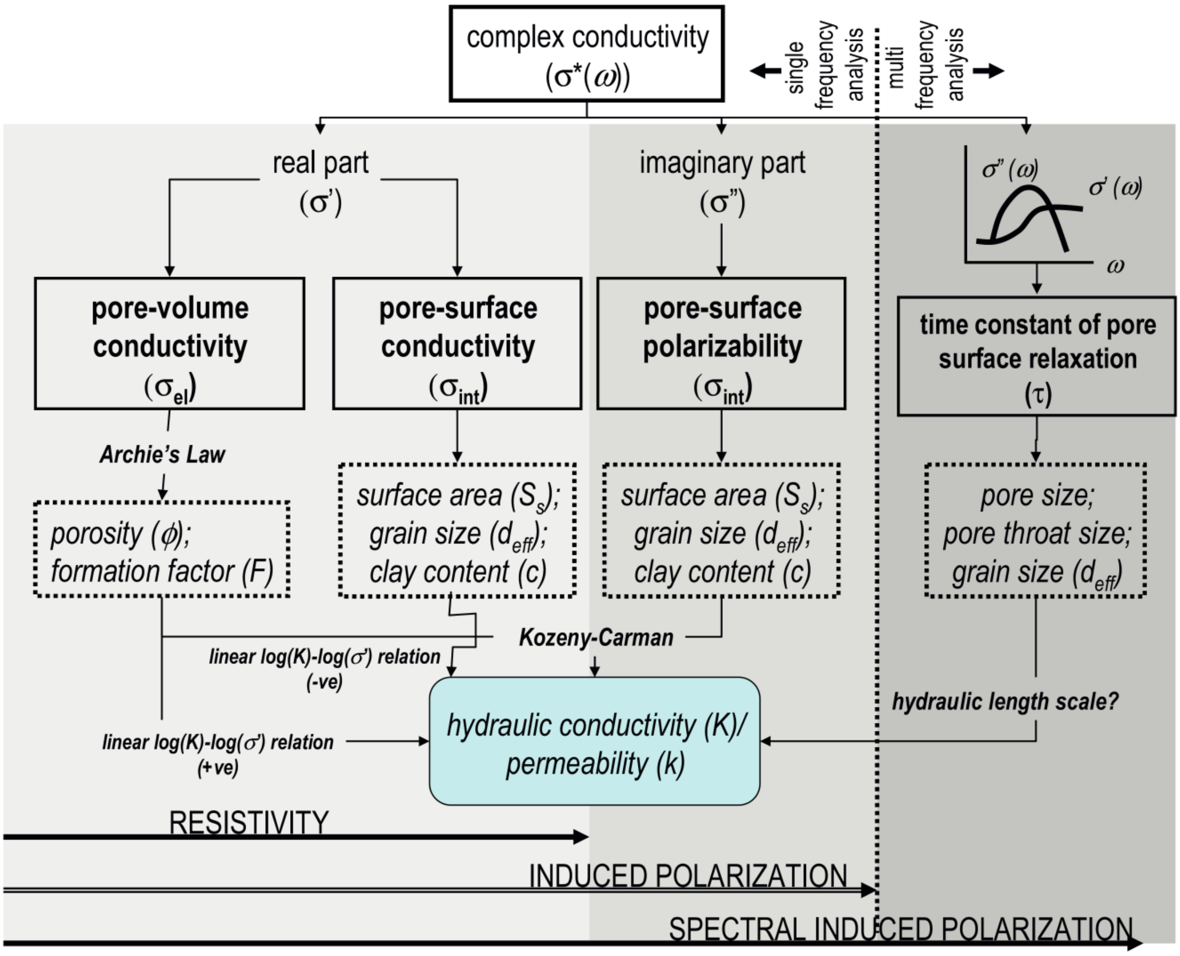

Fig. 1.1 - Schematic representation of the three groups of electrical prospecting techniques used in hydrogeophysics (DC, IP, and SIP), with the corresponding electrical properties and the established or expected relationships with textural parameters (*Slater*, 2007).

1.2 Motivation and aims

Within this general framework, one of the key problems is to interpret the electrical response of saturated sediments in terms of hydrostratigraphic units (HUs). In particular, this work is focused on alluvial sediments of the Po plain (northern Italy), which is an example of a sedimentary basin hosting multi-layered alluvial aquifers, whose geometry and heterogeneity are controlled by sedimentary and tectonic evolution. Such a system is considered among the most rich and precious freshwater resources in Europe and worldwide. More specifically, a quasi-3D hydrostratigraphic structure of the Quaternary alluvial succession located south-east of Milan has been obtained from geoelectrical data (vertical electrical sounding and electrical resistivity ground imaging), calibrated with well-log stratigraphic data and geological surveys on outcrops and shallow drillings. The integration between geological, hydrogeological and geophysical data was based on the definition of electrostratigraphic units (EUs) characterized by specific range of electrical resistivity and lateral persistence of the vertical resistivity association (*Bersezio et al.*, 2007; *Mele*, 2008; *Mele et al.*, 2010; *Mele et al.*, 2012; *Mele et al.*, 2013; *Giudici et al.*, 2015). The interpretation of the EUs in terms of HUs was in turn based on the mutual dependence of electrical resistivity and hydraulic conductivity on a textural parameter, namely the coarse-to-fine ratio (i.e., the weight ratio between the coarse-grained and the fine-grained fractions of the sediment determined with a specific grain diameter threshold). This parameter is useful to discriminate subsurface units on the basis of the proportion between coarse sediment fraction and fine fraction, which correspond to electrolytic-dominated and shale-dominated conduction intervals. The recognized EUs and HUs correspond to levels with increasing hierarchical order with depth (from individual beds to facies associations), but the coarse-to-fine ratio can always be used to gain information on the relative amount of coarse-grained and fine-grained portions and to infer the dominant hydrological behaviour at that length scale (*Mele et al.*, 2015). In addition, DC laboratory investigations were conducted on materials collected from the same alluvial successions outcropping along the rivers' terraces (*Mele et al.*, 2014). This scale length reduction from the field to the laboratory allowed to formulate an empirical model including an electrolytic conduction component, dependent on porosity and water conductivity, a surface conduction component, dependent on the intrinsic surface conductivity of clay and silt particles, and an interface conduction component, dependent on both the intrinsic conductivity of particles and on the conductivity of the water in the electrical double layer (EDL). All these mechanisms were still weighted on the coarse-to-fine ratio and the model could thus be applied on electrical data to indirectly estimate the hydrodynamic properties. Nevertheless, in absence of independent information on the surface or EDL conductivity, the use of DC surveys does not allow to distinguish the components of electrical conduction related to the movement of free ions within the interconnected pores (i.e., electrolytic conduction) and to the presence of particles such as clay responsible for the formation of an EDL (i.e., shale conduction, including surface and interface conduction). This limitation prevents from a full distinction between two end-member materials represented by coarse-grained sediments saturated with brine and fine-grained sediments saturated with freshwater. Such a distinction is particularly important in environments characterized by the simultaneous presence of both end-members. The Po plain (Italy) constitutes an example of such a complex environment. In fact, a succession of different aquifer groups is recognized in the subsurface (*Regione Emilia-Romagna and Eni-Agip*, 1998; *Regione Lombardia and Eni-Agip*, 2001). A salt-freshwater interface intersects this succession and it is locally uplifted due to the thrust-folding of the outer Apennine arcs, which often do not have a morphological correspondence at surface. The distinction between a dominant electrolytic conduction associated to freshwater or saline aquifers and a dominant shale conduction associated to aquitards is of paramount importance for a correct management, exploitation, and protection of these groundwater resources.

The general aim of this work consists in an investigation of porous materials typical of alluvial environments, at the representative elementary volume (REV) scale, with alternate current (AC) methods (i.e., SIP method). The driving question of the research is the feasibility of the use of SIP data to characterize both the textural assemblage of the sediments and the fluid properties. The basic idea is to acquire complex resistivity data on a set of unconsolidated porous materials typical of alluvial environment, characterized by different grain-size distributions and electrical resistivity of the saturation water. The achievement of this objective is conditional to the design and realization of a proper experimental system suitable for the acquisition of complex resistivity data with sufficient accuracy, especially on the phase (1 mrad). The goal of the SIP analysis is the compilation of a local reference database for alluvial sediments and the identification of empirical relationships between the electrical parameters and the sedimentological properties. In the literature, several works have addressed this topic but with a main focus on consolidated or specifically prepared materials, such as highly-sorted sands or sand-clay mixtures. Here, the laboratory investigation is aimed at understanding the degree of resolution, with which the effects of different factors can be separately identified from the bulk complex electrical behaviour of samples directly collected in the field. Particular attention is placed on the effects related to the textural assemblage and to the water resistivity, in presence of disturbing and interacting effects related to particles' mineralogy, organic matter, sediments' fabric, etc. The results constitute a step forward towards the interpretation of future SIP acquisition in the field.

1.3 Workflow

The research aims were achieved in four successive work phases. The first phase concerns the study of the theoretical basis of conduction and polarization in porous media and the methods and systems currently available for the measurement of complex electrical resistivity with their limitations (see chapter 2). The second phase consists in the collection of a set of samples representative of the alluvial successions of the Lodi sector of the Po plain and in their litho-textural characterization (see chapter 3). The third part of the work focuses on design and construction of the experimental system for the measurement of complex electrical resistivity on unconsolidated and saturated repacked sediments (see chapter 4), and its validation by comparison with theoretical data and with a reference instrument. Finally, the fourth phase addresses the analysis of the electrical data, their processing and modelling, and the identification of the relevant petrophysical relationships (see chapters 5, 6, and 7).

The conceptual scheme at the basis of the research is provided in the following as a general overview of the work. The sampled sedimentary layers are characterized by a sedimentary structure and texture, colour, thickness, compaction degree, and position within the outcropping succession (Fig. 1.2a). The corresponding samples are representative of the layers in terms of texture, whereas structure and porosity are lost due to the sampling process and the repacking within the holder. The water content is also modified since samples are fully saturated with NaCl-solutions with prescribed initial electrical resistivity. Thus, the samples can be considered as porous media, homogeneous at the scale of investigation (i.e., about 10 cm), and composed of two phases (Fig. 1.2b).

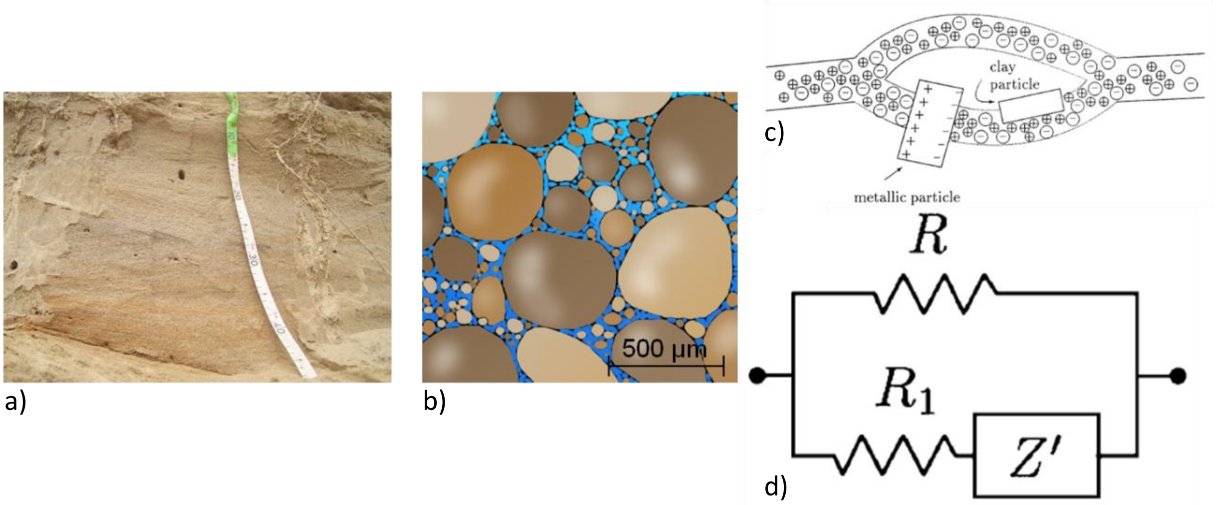

Fig. 1.2 - Layer of a sedimentary succession outcropping in a selected sampling site of the Po plain (a); representation of the sample as a two-phase system with solid particles and water (b); scheme of a unit cell with a free pore channel supporting the movement of ions, and a blocked channel supporting the occurrence of charge storage processes (c, from *Dias*, 2000); equivalent electrical circuit analog of the unit cell according to the Cole-Cole model (d, from *Dias*, 2000).

The solid phase is characterized by the same grain-size-distribution curve of the sedimentary layer, and is eventually provided with a series of additional information regarding the organic matter content and the mineralogy of the mud fraction. The fluid phase is characterized through its electrical resistivity, measured before and after the SIP test, and sometimes complemented with the chemical analysis of the major cations. The conduction and polarization processes occurring in the porous medium are analyzed as the analogous of a unit cell constituted by a free pore channel and a pore channel blocked or covered by clay and/or metal particles (Fig. 1.2c). The complex electrical resistivity of the unit cell is modelled through a combination of ideal resistors and capacitors, whose configuration varies according to the selected models (Fig. 1.2d). The model parameters (i.e., the circuital elements) are first correlated with solid or fluid properties by simple one-to-one relationships, and then analyzed with multivariate statistical tools in order to avoid misinterpretations in presence of competing factors responsible for similar electrical responses. In particular, a combination of principal component analysis and cluster analysis is adopted to classify the samples on the basis of their complex electrical behaviour and to determine the most relevant parameters that should be selected to explain the variability of the current SIP database.

Finally, a further step of the work was devoted to preliminary field SIP measurements. This part was addressed in order to provide some key points for a future planning of research aimed at adapting the empirical relationships studied at the REV scale to field case studies.

Chapter 2

Basic principles

2.1 Fundamental objects

The shallow subsurface is a complex environment, where the elements of lithosphere, hydrosphere, cryosphere, atmosphere, and biosphere come into contact and interact through biogeochemical cycles. Even if the distinction among these compartments is not always definite, this classification helps to contextualise the fundamental objects of the investigation into a schematic reference panorama. This allows to simplify the system but also to bear in mind the additional components that can affect it at different levels of detail or at different length scales. In this research, the fundamental objects are sediment and water, which are analysed in the following sections to introduce some definitions or notations adopted throughout the text.

2.1.1 Solid phase: the sediment

The word sediment refers to a solid fragment of inorganic or organic material that is transported by water, wind, or ice, and deposited on a solid substrate. Several classifications have been proposed for sediments according to the agent responsible for their transport and deposition (fluvial, glacial, eolian, volcanic, etc.), to the depositional environment (fan, delta, beach, reef, etc.), to the dominant mineralogical composition (terrigenous, carbonatic, hydrated oxides, etc.), or to the particle-size. For the aim of the work, the last classification is adopted, in the form of the ternary diagram of *Blott and Pye* (2012), based on the proportions of gravel, sand, and mud (GSM; Fig. 2.1).

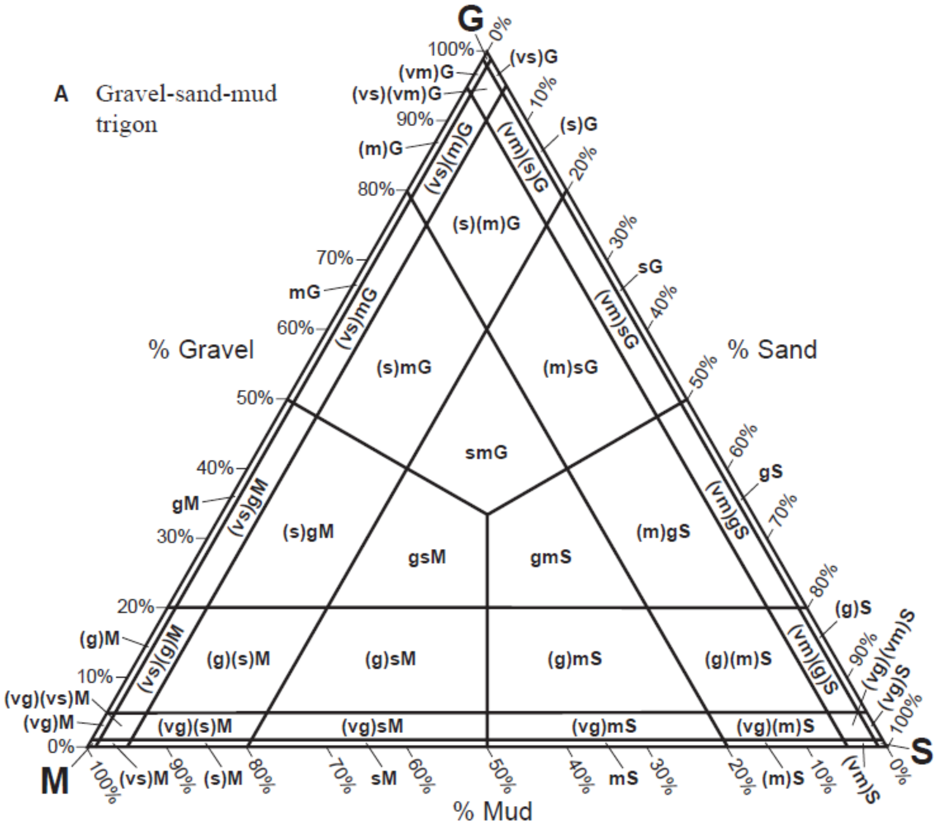

Fig. 2.1 - GSM ternary diagram for textural classification of sediments (*Blott and Pye*, 2012). Acronyms for the 48 fields are explained in the text.

This ternary scheme accounts for 48 textural classes; each class is identified by a first-order noun for the most abundant component, forerun by second-order descriptive terms for each other component more abundant than 1%. The qualifiers “slightly” and “very slightly” are added for content between 5% and 20% and between 1% and 5%, respectively. In the corresponding acronyms, the major component is written in upper case (G for gravel, S for sand, and M for mud) and the adjectives in lower case (g for gravelly, s for sandy, and m for muddy). The additional qualifications are represented by brackets and by brackets and a letter v. The size limits among the granulometric classes are chosen according to the classification of *Wentworth* (1922; Tab. 2.1). Gravel includes particles with diameter larger than 2 mm. The sandy fraction (grain diameter between 63 μm and 2 mm) is further distinguished into five sub-classes, i.e., very coarse (*vc*), coarse (*c*), medium (*m*), fine (*f*) and very fine (*vf*) sand. Silt refers to particles with a diameter between 4 μm and 63 μm, and clay to particles smaller than 4 μm. The term mud is used to indicate the sum of silt and clay, regardless their relative proportion. Besides the dimensional scale, an adimensional logarithmic scale (φ-scale) is also commonly adopted (*Krumbein*, 1936; Tab. 2.1). Phi-unit (φ) is defined as

$$\varphi = -\log_2 \frac{\mathrm{d}}{\mathrm{d}_0}, \tag{2.1}$$

where d is the particle diameter and $\mathrm{d}_0 = 1$ mm is a reference grain diameter.

Particle-size		**Size class**	**Ternary diagram**
φ	**d**		
-11	2048 mm	cobbles	Gravel (G)
-10	1024 mm		
-9	512 mm		
-8	256 mm		
-7	128 mm		
-6	64 mm		
-5	32 mm	pebbles	
-4	16 mm		
-3	8 mm		
-2	4 mm		
-1	2 mm	granules	
0	1 mm	very coarse sand (*vc*S)	Sand (S)
1	500 μm	coarse sand (*c*S)	
2	250 μm	medium sand (*m*S)	
3	125 μm	fine sand (*f*S)	
4	63 μm	very fine sand (*vf*S)	
5	31 μm	silt	Mud (M)
6	16 μm		
7	8 μm		
8	4 μm		
9	2 μm	clay	

Tab. 2.1 - Dimensional and logarithmic particle-size scales, according to the classifications of *Wentworth* (1922) and *Krumbein* (1936), respectively. The correspondence with the GSM ternary diagram is highlighted in the last column.

For the sake of precision, the term clay needs some further discussion because it can be used with different meanings. As already seen above, clay can indicate only a specific range of particle-size. In general, the term clay is used throughout the text with this textural meaning. Other definitions relate the term clay to natural unconsolidated fine-grained materials that are plastic at appropriate water content (i.e., can be permanently deformed to any shape without rupturing), and harden by drying or firing. They are mainly composed of phyllosilicates, but secondary associated minerals that do not impart plasticity can also be present, such as quartz, calcite, dolomite, feldspars, oxides, hydroxides, organic phases, and also non-crystalline phases as colloidal silica, iron hydroxide gels, and organic gels (*Guggenheim and Martin*, 1995). A third meaning of the term clay refers to hydrous phyllosilicate minerals that are usually classified according to the stacking of tetrahedral silicate sheets and octahedral sheets in the mineral unit cell, to the cationic valence in the octahedral sheet (Al^{3+} or Mg^{2+}), and to the intra-layer species. However, these mineralogical classification efforts are not fully successful because clay minerals exhibit a great compositional range, due to the formation of solid solutions and poly-phased crystals by interstratification (mixed-layer minerals). Furthermore, crystals can form aggregates through weak bonds or deposition of hydroxides and/or organic matter (*Meunier*, 2005).

Mineralogical clays are an important fraction of sediments, because of their peculiar characters. In fact, tetrahedral and octahedral substitutions are responsible for the presence of an excess of negative electric charge on the surfaces of the sheets forming the stratified structure of the minerals. The number of negative charges able to fix cations with low-energy bonds (i.e., reversibly) defines the cation exchange capacity (CEC), measured in cmol/kg or meq/100 g. Typical CEC values for the main clay mineral species vary between 5 cmol/kg and 150 cmol/kg (Tab. 2.2).

Mineral	**CEC [cmol/kg]**	
	from *Meunier* (2005)	**from *Carrol* (1959)**
Kaolinite	5-15	3-15
Illite	25-40	20-40
Vermiculite	100-150	100-150
Montmorillonite	80-120	80-100
Chlorite	5-15	10-40
Phyrophyllite		4
Talc		0.2
Zeolites		230-620
Quartz (d<63 μm)		0.6-5.3

Tab. 2.2 - Typical cation exchange capacity values for the main clay mineral species and other silicates, according to *Meunier* (2005) and *Carrol* (1959). Values are reported at pH=7.

Actually, the CEC is directly related to the interlayer electric charge up to an excess of charge equal to 0.75, whereas for higher interlayer charges cations are fixed irreversibly (Fig. 2.2). Furthermore, exchangeable cations can retain also their hydration shell, thus building from one to three layers of polar molecules (typically water) within the interlayer space. This results in a progressive expansion of the unit cell dimension (swelling) that can be identified with X-ray diffraction analysis. Water molecules can be released by heating between 80°C and 120°C.

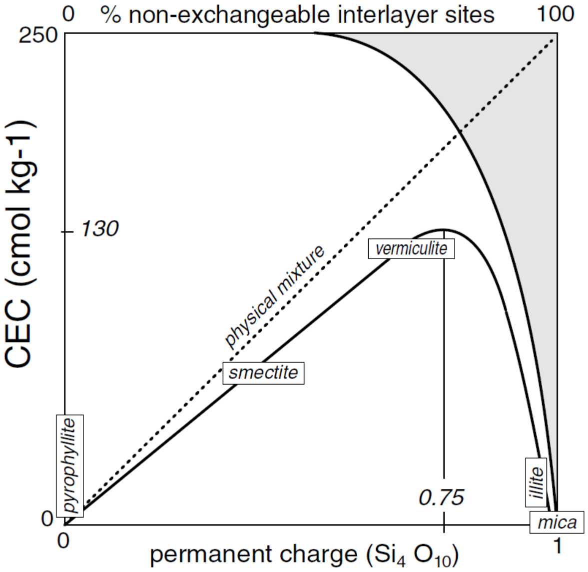

Fig. 2.2 - Cation exchange capacity of clay minerals as a function of the interlayer electric charge per unit cell (*Meunier*, 2005).

Even if at a lower extent, also other silicate minerals show a CEC that depends on the interrupted bonding along the crystal surfaces or on the presence of crystal defects. *Carroll* (1959) reports, for example, values between 0.6 cmol/kg and 5.3 cmol/kg for quartz particles ranging in dimension from silt to clay (Tab. 2.2). The cation exchange rate is controlled by the selectivity coefficient, i.e., the equilibrium constant of the exchange reaction. A cation with the same valence and a smaller diameter is more likely to be adsorbed, but selectivity is also affected by ion concentration. In natural soils, the replacement order of the exchangeable ions is $Li^+ < Na^+ < (H^+_{\text{low pH}}) < K^+ < Rb^+ < Cs^+$ for monovalent ions, and $Mg^{2+} < Ca^{2+} < Sr^{2+} < Ba^{2+}$ for bivalent cations. Trivalent cations are unlikely adsorbed on clay surfaces because they form insoluble hydroxides, such as $Al(OH)_3$ and $Fe(OH)_3$. At low pH values, H^+ ions are available both as exchangeable ions and to bond with OH^- groups of tetrahedral and octahedral sheets forming water molecules that are displaced from the structure by other anions (anion exchange capacity, AEC). The point of zero charge corresponds to the pH value for which AEC equals CEC.

2.1.2 Fluid phase: the water

For the aim of this work, water represents the fluid phase that occupies pore spaces in different conditions and forms. The *adsorbed water* (or hygroscopic water, or film water) is constituted by water molecules bonded to the solid surfaces by electrochemical forces. This water is not mobile and available for tree roots and its properties differ from those of the free water (higher density and viscosity). The *capillary water* is the fraction that occupies narrow pores and is separated from air by concave menisci. This is due to the high surface tension of water (72.8 mN/m at 20°C) that results from the strong cohesion among molecules, which in turn derives from their polarity. A portion of the capillary water can be extracted from the soil by roots. Finally, the *gravitational water*, or free water, is mobile under gravity forces and fill those pores with a size large enough to make the surface tension negligible.

The water content of a porous medium is the ratio between the mass or the volume of water and the total mass or volume. It depends on the method used to dry the sample; in this work, the contribution of adsorbed water is neglected for the computation of the water content since only air drying is used. In an analogous way, porosity is the ratio between the volume of the pores and the total volume, while effective (or drainage) porosity refers only to the volume occupied by mobile water.

2.1.3 Solid-fluid interface: the electrical double layer

The presence of ions in solution, combined with the occurrence of a charged solid surface, permits the formation of an electrical double layer (EDL). This concept was firstly introduced by Helmholtz in 1879 to describe the result of the electrostatic forces acting between localized charges on the solid surface and ions or polar molecules in solution. The model is equivalent to a plane electrical capacitor with a potential that decreases linearly with distance. The Gouy-Chapman model (1910-1913) considers a larger region perturbed by the charged surface, by introducing the effect of thermal motion in addition to the effects of Coulomb's forces. In fact, it includes a region where the counter-ions (i.e., the ions with the opposite charge with respect to the surface) are not electrostatically bonded to the surface and tend to diffuse back. The electrical potential decreases exponentially in this region. Conditions of equilibrium correspond to a null net flux of charges in the interface region and derive from the compensation of the migration of ions towards the charged surface with the back-diffusion of ions supported by the concentration gradient. In 1924, Stern took into account also the finite dimension of the ions and of their hydration shell composed of solvent molecules, and introduced a distance of maximum approach to the surface (Stern layer). According to this model, the potential has a linear drop near the surface and follows an exponential decay beyond the Stern layer. In other words, the Stern model is a combination of the Helmholtz and Gouy-Chapman theories. In 1947, Grahame modified the Stern model introducing also a localized chemisorption of ions (Fig. 2.3; triple electrical layer). This kind of interaction does not depend on electrostatic forces but on short range bonds between specific chemical species. Thus, it is independent from the sign of the charged particles. In presence of chemisorption, ions or charged complexes partially lose their solvation shells and approach the solid surface up to the inner Helmholtz plane (IHP). Instead, solvated ions remain at a greater distance from the solid surface, in correspondence of the so-called outer Helmholtz plane (OHP). The diffuse layer composed of dispersed solvated ions is still present outside the two Helmholtz planes. In the absence of chemisorption, the OHP only is present and it coincides with the Stern layer of the previous model.

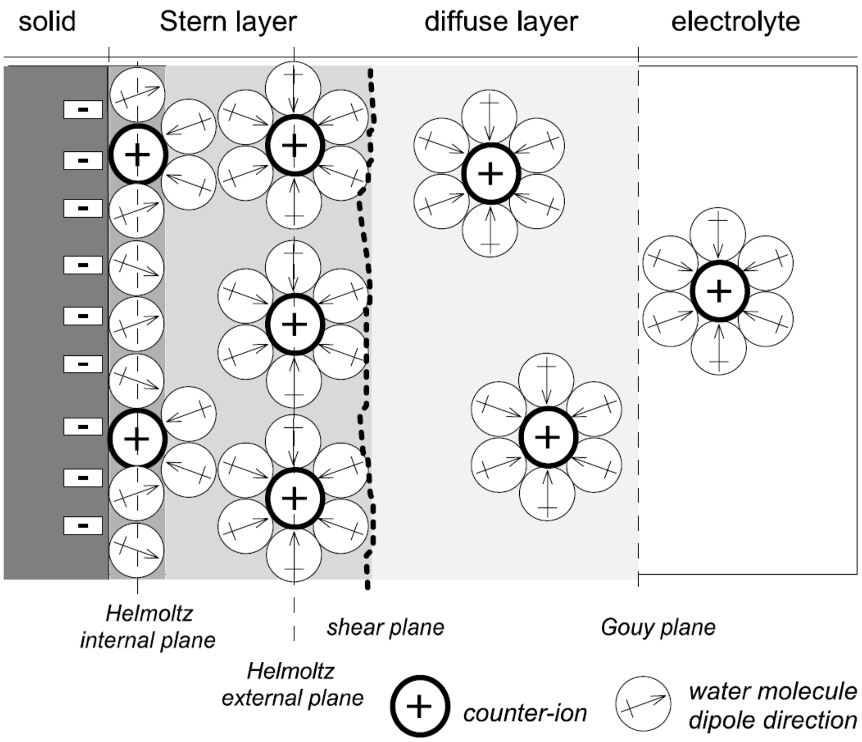

Fig. 2.3 - Schematic representation of the grain-electrolyte interface, according to the double subdivision on the upper side and to the triple subdivision on the lower side of the picture (*Meunier*, 2005).

In Fig. 2.3, the plane of separation between the Stern layer and the diffuse layer is called shear plane. In fact, the inner part of the EDL is rigidly coupled with the solid, whereas the outer portion can migrate under the effect of an external electrical field. The potential difference between the mobile and immobile parts of the EDL is called zeta potential (ζ) and affects the stability of colloidal systems. For high ζ, repulsive forces among particles are dominant and prevent from flocculation, while $\zeta < 30$ mV is indicative of an incipient instability. The condition for which $\zeta = 0$ is called isoelectric point.

The thickness of the whole perturbed electrical layer (double or triple) increases with temperature, as a result of thermal disorder, and with relative dielectric constant. It also increases with a decrease of the bulk concentration or the ions valence, because a lower number of charges are available in solution, for a constant volume, to compensate the surface charge. The thickness of the perturbed region is known as Debye length and is expressed as

$$\lambda_d = \left(\frac{\varepsilon k_B T}{4\pi e^2 \sum_i (z_i^2 Q_{vi})}\right)^{1/2}, \tag{2.2}$$

where ε is the dielectric constant, k_B is the Boltzmann constant, T is the absolute temperature, e is the elementary charge, z_i and Q_{vi} are the valence and the bulk concentration expressed in number of charges per unit volume of the i-th ionic species.

2.2 Electrical conduction

The electrical conduction in the matter is defined as the average motion of charged species (atomic elementary particles, ions, polar molecules, etc.). This motion can be activated by an electric field, a concentration gradient, or a movement of the medium that host the charges (e.g., a fluid convection), and occurs according to different mechanisms that are explained in the next section. In any case, by historical convention, the direction of motion of positively charged particles is defined as a positive current. The ability of a material to conduct an electric current is expressed through a physical quantity called electrical conductivity. It is denoted with the Greek letter σ and its units in the international system are S/m. It is the inverse of the electrical resistivity, denoted with ρ and measured in Ωm, that quantifies how strongly the material opposes to the current flow. According to the definition

$$\rho = R\frac{S}{l}, \tag{2.3}$$

where R is the ohmic resistance, i.e., the ratio of the potential difference across a resistor with cylindrical shape and the current flowing through it, S is the cross-sectional area, and l is the length of the resistor, the electrical resistivity is an intensive property. Alternatively, resistivity is defined as

$$\rho = \frac{E}{j}, \tag{2.4}$$

where E is the electric field, and j the corresponding current density, namely the electric current per unit area. In an anisotropic materials, ρ is a rank-2 tensor, but for the aim of the work is considered as a scalar quantity associated to the REV composed of sediment and water arranged in a specific geometry.

2.2.1 Conduction mechanisms

Electronic conduction is typical of metals, since it is supported by electrons that are not specifically bonded to any atom but constitute a shared cloud within the metal lattice (electron sea). Under stationary conditions these free electrons have a random motion and no net movement of electric charge is observable. A net movement results instead as a consequence of the application of an electric field. An increase in temperature limits the movement of the electrons by increasing the kinetic energy of the particles and intensifying the inelastic collisions among them. Similarly, impurities in the metal lattice disrupt the electron sea and limit their flow. At a reference temperature of 20°C, the order of magnitude of the electrical resistivity for metals is about 10^{-8} Ωm.

Most crystalline solids, amorphous systems, and some pure elements are semi-conductors, characterized by valence electrons involved in covalent bonding. Under these conditions, the electrical conduction is possible if energy is provided to the electrons in order to break the bond and leave a “hole”. The free electrons are negative charge carriers, while the holes are considered as positive charge carriers, because the region is characterized by a lack of negative charge. The electrical resistivity of semiconductors decreases with temperature. At 20°C, the order of magnitude of the resistivity for semiconductors typically ranges between 10^{-6} Ωm and 10^4 Ωm. Materials with electrical resistivity greater than 10^4 Ωm are considered insulators. Except for metallic particles, mineral grains are insulators and contribute to a negligible extent to the overall conductivity of soils and sediments. An exception is constituted by particles with an unbalanced excess of charges on the exposed surfaces (e.g., mineralogical clays). These particles allow the formation of a fluid layer at the solid-liquid interface with different characteristics with respect to the bulk liquid phase (see section 2.1.3). The excess charges of this layer can move under the application of an electrical field. This phenomenon is sometimes addressed as a further conduction mechanism called *surface conduction*.

The *electrolytic conduction* refers to the movement of ions, usually in a fluid phase. It is the most common conduction mechanism in soils and rocks with connected and saturated pores or fractures. The electrical resistivity of the fluid is strictly related to the concentration of total dissolved solids (TDS). Distilled water, for example, has a resistivity of about 10^4 Ωm, while drinkable water ranges between 20 Ωm and 2000 Ωm, and sea water has a typical resistivity of about 0.2 Ωm. An approximation of the linear relationship between TDS and water electrical conductivity (σ_w) is provided, for example, by *Atekwana et al.* (2004) through the following equation

$$\mathrm{TDS} = \mathrm{k_e}\sigma_\mathrm{w}, \tag{2.5}$$

where $\mathrm{k_e}$ is a correlation factor ranging from 0.55 to 0.80 when TDS is given in mg/L and σ_w in μS/cm. As TDS increases, the average distance between ions decreases and the interactions between positive and negative ions increase, up to the formation of ion-pairs with a shared solvation shell. In these conditions, the conductivity tends to reach an upper limit (Fig. 2.4).

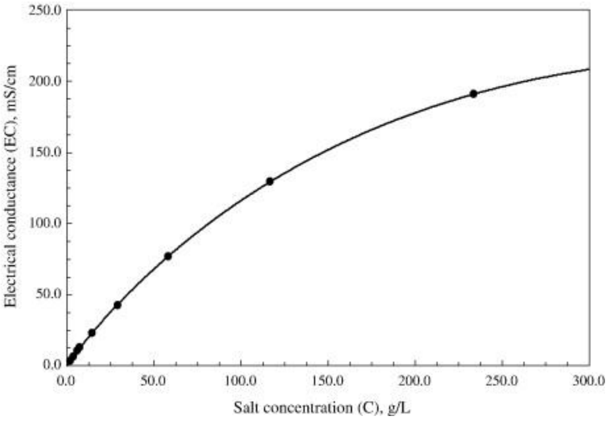

Fig. 2.4 - Electrical conductivity of a NaCl-solution at 25°C as a function of the salt concentration (*Rao and Thyagaraj*, 2007).

An increase in temperature favours the ions mobility and thus reduces the electrical resistivity. The relationship between resistivity and temperature can be expressed as

$$\rho(\mathrm{T}) = \frac{\rho_0}{1 + \alpha(\mathrm{T} - \mathrm{T}_0)}, \tag{2.6}$$

where ρ_0 is the resistivity at a temperature T_0, usually equal to 20°C, and α is an empirical termic coefficient. In the literature, α varies between 0.019°C^{-1} and 0.025°C^{-1} for geological materials (*Hadzick et al.*, 2011).

2.2.2 Empirical models

The importance of electrical resistivity for geologists and geophysicists derives from the relationships that have been found to relate it to other properties of the porous medium. The principal relationships and models proposed in the scientific literature are presented in the following.

Archie, 1942

Doubtless, the most famous of these petrophysical relations is Archie's law (*Archie*, 1942), an empirical model relating the resistivity measured with log tool for the exploration of hydrocarbon reservoirs to the electrical resistivity of the saturation fluid (ρ_w), the porosity of the formation (θ), and the saturation degree relative to the water phase (S_w)

$$\rho = \rho_w \theta^{-m} {S_w}^{n}. \tag{2.7}$$

When S_w=1, the ratio between ρ and ρ_w is the intrinsic formation factor F. In equation (2.7), m is called the cementation exponent because it describes the variation of resistivity due to pore-network changes. According to *Archie* (1942), the phenomenological parameter m ranges between 1.8 and 2.0 for consolidated sandstones and is expected to be between 1.3 and 2.0 for loosely or partly consolidated sands. The n exponent, or saturation exponent, is about 2. A third phenomenological parameter (a) is sometimes added to the Archie's law in the form of a multiplicative factor. Different terminology has been used for it, but it is commonly known as tortuosity factor, because it is expected to be related to the path length of the current flow. Different ranges for m and a have been obtained for different datasets and are summarized in Tab. 2.3. The hypotheses for such a great range of variability address shape, sorting and packing of grains, type of porosity and pore geometry, pressure, wettability of rock surface, clay type and content. This last item is particularly important because it constitutes a deviation from the conditions to validate Archie's law (i.e., clean sands saturated with brines).

Lithology	a [-]	m [-]	references
sands		2.7	*Williams* (1950)
		2 - 2.3	*Salem and Chilingarian* (1999)
sandstones		2.15	*Winsauer* (1952)
	0.47 - 1.8	1.64 - 2.23	*Hill and Milburn* (1956)
	0.62 - 1.65	1.3 - 2.15	*Carothers* (1968)
	1.0 - 4.0	0.57 - 1.85	*Porter and Carothers* (1970)
	0.48 - 4.31	1.2 - 2.21	*Timur et al.* (1972)
	0.004 - 17.7	0.02 - 5.67	*Gomez-Rivero* (1976)
		<1.3	*Maute et al.* (1992)
		2	*Hamada* (2001)
shaly sandstones		1.79 - 1.81	*Hartmann et al.* (1999)
carbonates		>1.3	*Maute et al.* (1952)
	0.73 - 2.3	1.64 - 2.10	*Hill and Milburn* (1956)
	0.45 - 1.25	1.78 - 2.38	*Carothers* (1968)
	0.33 - 78.0	0.39 - 2.63	*Gomez-Rivero* (1976)
	0.35 - 0.8	1.7 - 2.3	*Schon* (1983)

Tab. 2.3 - Variability ranges of the tortuosity coefficient and the cementation exponent for different sediments and rocks (modified after *Worthington*, 1993; *Salem and Chilingarian*, 1999; *Kadhim et al.*, 2013).

Waxman and Smits, 1968

The first conductivity model for shaly sands was developed by *Waxman and Smits* (1968), who considered two separated conductivity terms related to the free electrolyte contained in the pores and to the concentration of exchangeable counter-ions per unit volume associated to the clay component. The equation can be written in terms of electrical conductivity as

$$\sigma = \frac{1}{F_a}(BQ_v + \sigma_w), \tag{2.8}$$

where BQ_v is the product of the equivalent conductance of exchange sodium cations (B), that is a function of water resistivity, and the concentration of charge per unit pore volume (Q_v). F_a is the ratio between ρ and ρ_w (or between σ_w and σ) outside Archie's conditions and is thus called apparent formation factor (*Worthington*, 1993). The ratio F/F_a varies with ρ_w and with Q_v; in particular, as Q_v increases, shale effects become more significant even at low water resistivity. For practical purposes, *Worthington* (1993) suggested $F/F_a \geq 0.9$ as the requirement to satisfy Archie's conditions.

Clavier et al., 1984

The model of *Clavier et al.* (1984) assumed the presence of water in two different conditions: adsorbed water surrounding clay particles, with an electrical conductivity σ_{cw} independent of the type and the amount of clay and dependent exclusively on the counter-ion species, and gravitational water, with a conductivity σ_w depending on the salinity of the bulk water[1]. The equation has the form

$$\sigma = \frac{1}{F_0}[v_{cw}Q_v(\sigma_{cw} - \sigma_w) + \sigma_w], \tag{2.9}$$

where v_{cw} is the volume of adsorbed water associated with 1 meq of counter-ions and F_0 is the formation factor of a rock with a pore network identical to that of the investigated material, but in which clay is substituted by a non-conducting mineral phase.

Sen et al., 1988

In 1988, *Sen et al.* considered a further additive term EQ_v to quantify the conductivity contribution related to a continuous path constituted by counter-ions even in a condition of $\sigma_w = 0$. The bulk electrical conductivity is equal to:

$$\sigma = \frac{1}{F_a}\left(\frac{AQ_v}{1 + \frac{CQ_v}{\sigma_w}} + \sigma_w\right) + EQ_v, \tag{2.10}$$

where $A = \mu_{EDL}m_s$, μ_{EDL} is the mobility of the ions in the EDL, m_s is a surface tortuosity factor, and C is an empirical factor. Equation (2.10) identifies two portions with different slopes in the σ vs. σ_w curve. For high water conductivity, $CQ_v/\sigma_w \ll 1$ and equation (2.10) simplifies to a form similar to equation (2.8), where the slope is $1/F_a$. For low water conductivity, $CQ_v/\sigma_w \gg 1$ and the slope is greater than $1/F_a$. The slope variation is explained as a variation in the distribution of the electrical field, that is more concentrated in the pore space at high salinity and in the EDL at low salinity.

de Lima and Sharma, 1990

A further step forward was provided by *de Lima and Sharma* (1990) with the formulation of two expressions accounting for the distribution of clay. The former applies to non-conducting spherical silicate grains coated with a shell of conducting clay with fixed thickness, and the latter to the case of clay particles occurring within the pores of the sandy matrix. In this case, a three-component mixture is considered, where θ is the water fraction when $S_w = 1$ and p is the volume fraction of clay in the solid phase. The conductivity equation for this system is

$$\sigma = \frac{1}{F_s}\left(-\frac{3p}{2}(F_s - 1)\sigma_c + \sigma_w\right), \tag{2.11}$$

where F_s is the formation factor of a system of spheres ($F_s = \theta^{-3/2}$), and σ_c is the clay conductivity. This model differs from Waxman's, Clavier's, and Sen's models because it is based only on macroscopic parameters derivable, for example, from conventional

---

[1] In the original paper the two waters are referred to as clay water and "far" water, respectively. Here, the names used in section 2.1.2 are adopted.

geophysical logs. The usage of microscopic parameters related to the electrochemical principles of the EDL is substituted by a volumetric averaged approach. The basic theory of this kind of approach is the effective medium theory, or Maxwell-Wagner-Bruggeman-Hanai theory.

Mele et al., 2014

Within the volumetric averaged approach, *Mele et al.* (2014) adopted the coarse-to-fine textural ratio (Γ_d) to quantify the electrolytic and the shale conduction in a saturated porous medium as

$$\sigma = \theta \frac{\Gamma_d}{\Gamma_d + \gamma} \sigma_w + \left(\frac{\gamma}{\Gamma_d + \gamma} \sigma_c + \beta \frac{\Gamma_d}{\Gamma_d + \gamma} \sigma_w \right). \tag{2.12}$$

Γ_d is defined as the weight ratio between the sediment fractions with particle-size larger and smaller than d. The electrolytic component, i.e., the first term of the right hand side of equation (2.12), is directly related to the porosity θ and the water conductivity σ_w and is weighted on the volume of the coarser sediment fraction, determined on the base of Γ_d with a threshold diameter $d = 0.063$ mm. The shale component, i.e., the second term of equation (2.12), can be considered as the sum of two contributions: the pure surface conduction, dependent on the intrinsic conductivity σ_c and weighted on the volume of the fine sediment fraction, and the interaction component between the pore water and mud particles, dependent on σ_w and the dimensionless parameter β. This phenomenological parameter follows an exponential decay with Γ_d and accounts for the volumetric water fraction of the EDL. In equation (2.12), γ is a fitting parameter. At high water conductivity and in absence of a fine-grained component, equation (2.12) reduces to Archie's law (equation 2.7), while at low water conductivity the shale conduction term becomes dominant and σ is no more dependent on σ_w. This behaviour has been observed in numerous samples, from shaly sandstones to unconsolidated muddy sands (Fig. 2.5).

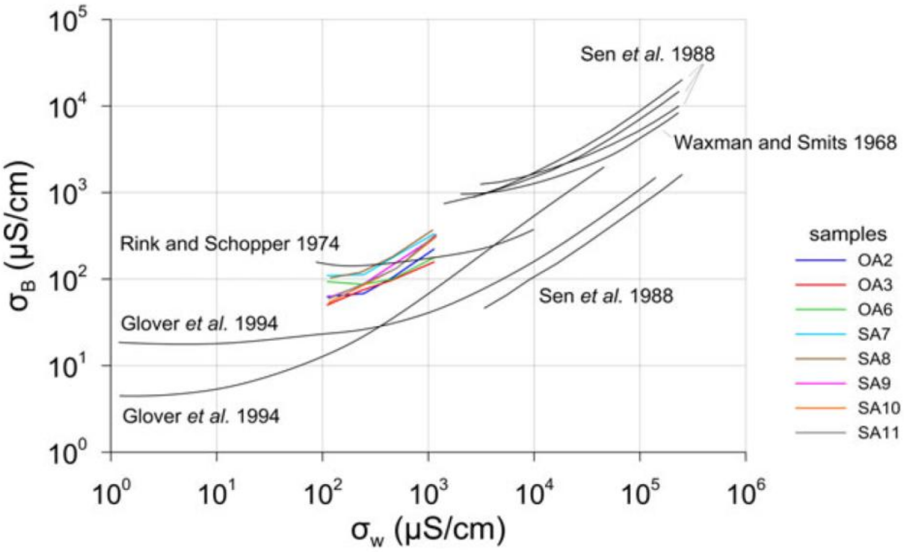

Fig. 2.5 – Bulk conductivity as a function of water conductivity for different rocks and sediments (*Mele et al.*, 2014).

2.3 Electrical polarization

In the previous section, a definition of electric resistance was provided as the ratio between voltage and direct current. Analogously, it is possible to define electrical impedance Z as the same ratio considering alternating current. The impedance is still measured in Ω and corresponds to the sum of a real resistance term R and an imaginary reactance term X:

$$\mathrm{Z} = \mathrm{R} + i\mathrm{X}, \tag{2.13}$$

where i is the imaginary unit. The reactance includes both a capacitive reactance and an inductive reactance, which describe the opposition against the change of voltage and current, respectively. By convention, the capacitive reactance contributes negatively to the total reactance and thus, if $\mathrm{X} > 0$ the total reactance is called inductive, and if $\mathrm{X} < 0$ is called capacitive. The impedance is purely resistive when $\mathrm{X} = 0$. The reciprocal of the electrical impedance is the admittance, i.e., the complex sum of conductance and susceptance, both measured in siemens.

Analogously, also the electrical resistivity can be analysed as a complex quantity

$$\rho^* = \rho' - i\rho'', \tag{2.14}$$

with an in-phase or real component ρ', related to the transport of charge through ohmic conduction currents, and an out-of-phase or imaginary component ρ'', related to the storage of charges through polarization processes. ρ^* can also be expressed in polar form through its magnitude and phase

$$\rho^* = |\rho^*|e^{-i\phi}, \tag{2.15}$$

where $|\rho^*| = \sqrt{(\rho')^2 + (\rho'')^2}$ and $\phi = \tan^{-1}(\rho''/\rho')$.

Complex resistivity is, in general, affected by a dispersive behaviour, i.e., it is frequency dependent, and is expressed as $\rho^*(\omega)$, where $\omega = 2\pi f$ is the angular frequency and f the ordinary frequency.

Polarization phenomena refer to the distortion of a charge distribution as a consequence of the application of an electric field. An ideal dielectric does not conduct current by the movement of its electrons, but these electrons are displaced from their equilibrium positions under the effect of an external field. Therefore, even in the absence of a flux of charges, a net displacement of positive charges in the direction of the field and of negative charges in the opposite direction is present and constitutes an induced dipole moment. Polarizability is defined as the ratio between the induced dipole moment and the corresponding electric field. The average dipole moment per unit volume of a dielectric material is called polarization density and the constant of proportionality between the polarization density and the electric field is the electric susceptibility. On the opposite, the measure of the ability of a material to oppose to the electric field is called absolute permittivity. It is usually denoted with ε and expressed by the product $\varepsilon = \varepsilon_0 \varepsilon_r$, where ε_0 is the vacuum permittivity and ε_r the relative permittivity. Polarization is causal to the application of an external electric field and non-instantaneous. Thus it is often treated as a complex and frequency-dependent quantity $\varepsilon^*(\omega)$. Complex conductivity, complex resistivity, and complex permittivity are related by the expression

$$\sigma^*(\omega) = \frac{1}{\rho^*(\omega)} = i\omega\varepsilon^*(\omega), \tag{2.16}$$

where each term contains an energy loss contribution (conduction) and an energy storage one (polarization). A comprehensive model for the complex electrical conductivity of a porous medium usually includes two additive conduction mechanisms, i.e., the electrolytic contribution supported by the movement of ions in the interconnected pores, and the surface contribution supported by the EDL at the mineral-fluid interface. At $f < 10^9$ Hz, the electrolyte can be considered non-polarisable and the electrolytic conduction term is purely real (σ_{el}). On the other hand, the surface conductivity shows both an in-phase and an out-of-phase component ($\sigma_s^* = \sigma_s' + i\sigma_s''$), so that

$$\sigma^* = \sigma_{\mathrm{el}} + \sigma_s^* = (\sigma_{\mathrm{el}} + \sigma_s') + i\sigma_s'' \tag{2.17}$$

The empirical models already described in section 2.2.2 refer to the real part of this equation, whereas the models of the section 2.3.2 are descriptive for the whole complex electrical behaviour as a function of frequency.

2.3.1 Polarization mechanisms

According to the charged element affected by the excitation field and to the characteristic response time, different types of polarization can be identified: electronic, atomic and ionic, orientational, and interfacial.

The *electronic polarization* involves the displacement of the centre of the electron cloud with respect to the atomic nucleus (Fig. 2.6). It consists in a resonant behaviour, because electrons respond as harmonic oscillators around their undisturbed positions. It is typical of optical and ultraviolet frequencies (from 10^{15} Hz to 10^{16} Hz).

In *atomic polarisation*, the displacement involves atoms or groups of atoms within a molecule, while *ionic polarisation* refers to the displacement of atoms bonded by ionic bonds (Fig. 2.6). They are typical at infra-red and optical frequencies (from 10^{12} Hz to 10^{15} Hz).

The *orientational* or dipolar *polarization* affects polar molecules characterized by a permanent dipole moment, such as water. In fact, they tend to orient their dipole according to the external electric field, even if thermal motion acts to preserve the random status (Fig. 2.6). Orientational polarizability is thus inversely proportional to temperature. Furthermore, interactions between neighbouring molecules are another limiting factor for the dipole orientation. This polarization typically occurs between 10^9 Hz and 10^{12} Hz.

The *interfacial polarization*, or space charge polarization, or Maxwell-Garnett(-Sillars) polarization, is related to the presence of an interface between conducting and non-conducting phases, or between phases with a different main mechanism of conduction (Fig. 2.6). Two examples of these conditions are the interface between an insulating silicate grain and an electrolytic solution, and the interface between the electrode and the porous medium, respectively. This type of polarization consists in the accumulation of charges at the interface, due to the displacement of free charges over distances greater than the molecular size. For this reason, the polarizability at an interface can assume greater values than the polarizability of the individual involved materials. Interfacial polarization is typically observed below 10^6 Hz.

In the same frequency range, *membrane polarization*, or electrolytic polarization, is associated to the formation of a net charge dipole at a constriction within a pore channel that blocks the flow of ions (Fig. 2.7a), or around negatively charged clay particles or filaments of fibrous minerals (Fig. 2.7b). It thus involves a variation in the mobility of ions. The total polarization of a material is the sum of the effects of all the polarization processes. However, interfacial and membrane polarization mechanisms are those of maximum interest for this work, due to their characteristic time.

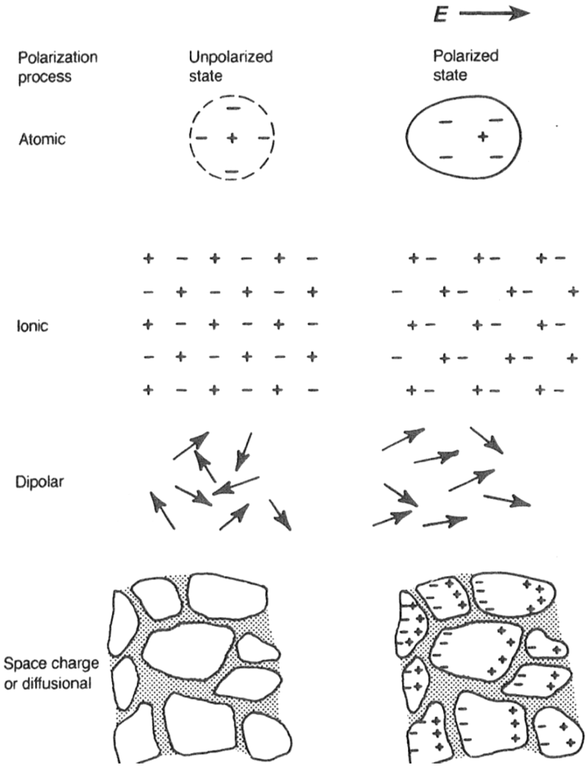

Fig. 2.6 - Schematic representation of the main polarization mechanisms from high to low frequency.

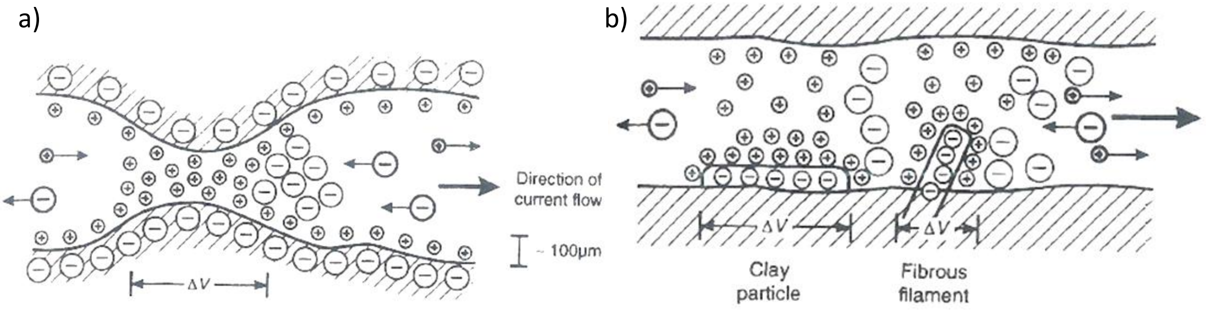

Fig. 2.7 - Schematic representation of membrane polarization associated to pore channel constriction (a), and negatively charged particles (b; *Reynolds*, 2011).

The occurrence of an external electric field is not the only cause of polarization phenomena. Piezoelectricity, for example, refers to the formation of an electric field in asymmetrical crystals due to mechanical compression in specific directions, while pyroelectricity is the development of polarization effects after heating. Ferroelectricity is the spontaneous alignment of dipoles by mutual interactions related to the concentration of magnetic moments (see, for example, *Shivola*, 1999). However, these effects are usually smaller in magnitude than polarization processes associated with electric fields and are not considered in the following.

2.3.2 Relaxation models

The term relaxation refers to the return of a perturbed system to an equilibrium condition after the removal of the exciting field. The characteristic time required by each relaxation process is called relaxation time. This is a fundamental parameter in every phenomenological model that has been proposed to describe the complex electrical behaviour of a material as a function of time or frequency. According to equation (2.16), relaxation models can be expressed in terms of complex resistivity, complex conductivity, or complex permittivity through proper conversions. Typically, permittivity is used in colloidal sciences, where models were originally developed mostly for absorption studies on liquids, whereas resistivity or conductivity are commonly used in geophysics. The models of interest for this work are synthesized under the generalized Cole-Cole model, whose expression in terms of permittivity in the frequency domain is

$$\varepsilon^*(\omega) = \varepsilon_\infty + \frac{\varepsilon_s - \varepsilon_\infty}{(1 + (i\omega\tau_0)^c)^k}, \tag{2.18}$$

where i is the imaginary unit, ω is the angular frequency, τ_0 is the characteristic relaxation time, ε_s and ε_∞ are the low and high frequency limits of permittivity, and c and k are two phenomenological exponents. The same model is expressed in terms of complex resistivity as

$$\rho^*(\omega) = \rho_0 \left[1 - m\left(1 - \frac{1}{(1 + (i\omega\tau_0)^c)^k}\right)\right] \tag{2.19}$$

where ρ_0 is the DC electrical resistivity, m is the chargeability, and c and k are the exponents that describe the broadness and the skewness of the relaxation, respectively, and vary between zero and one. The model assumes different names, according to the values of c and k, as summarized in Tab. 2.4.

Model (acronym)	**c**	**k**
Generalized Cole-Cole (GCC)	$0 < c < 1$	$0 < k < 1$
Cole-Cole (CC)	$0 \leq c < 1$	1
Warburg (W)	0.5	1
Cole-Davidson (CD)	1	$0 \leq k < 1$
Debye (D)	1	1

Tab. 2.4 - Names and acronyms of major resistivity relaxation models, according to the values of the exponents c and k in equation (2.19).

The models are often compared in terms of relaxation time distribution function $G(\tau)$, which represents the fraction of the total dispersion that is contributed by polarization processes per unit relaxation time, so that

$$\int_0^\infty G(\tau)\,d\tau = 1. \tag{2.20}$$

For the models described above, $G(\tau)$ is represented in Fig. 2.8 and calculated according to the following equations

$$G(\tau) = \frac{\sin(k\Theta)}{\pi\left(\left(\frac{\tau}{\tau_0}\right)^{-2c} + 2\left(\frac{\tau}{\tau_0}\right)^{-c}\cos(\pi c) + 1\right)^{\frac{k}{2}}}, \tag{2.21}$$

$$\Theta = \frac{\pi}{2} - \tan^{-1}\left(\frac{\left(\frac{\tau}{\tau_0}\right)^{c} + \cos(\pi c)}{\sin(\pi c)}\right). \tag{2.22}$$

Strictly speaking, equations (2.18) and (2.19) are not equivalent. The first is the original formulation of *Cole and Cole* (1941), while the second is the formulation of *Pelton et al.* (1978), who substituted permittivity terms with resistivity terms considering Seigel's definition of chargeability (*Seigel*, 1959)

$$m = \frac{\rho_0 - \rho_\infty}{\rho_0} = \frac{\sigma_\infty - \sigma_0}{\sigma_\infty}, \tag{2.23}$$

where ρ_0 and σ_0 are the zero-frequency limits of resistivity and conductivity, and ρ_∞ and σ_∞ are the corresponding high-frequency limits. According to the relations among the complex quantities ε^*, σ^*, and ρ^* expressed in equation (2.16), this modification has a poor physical meaning at high frequency.

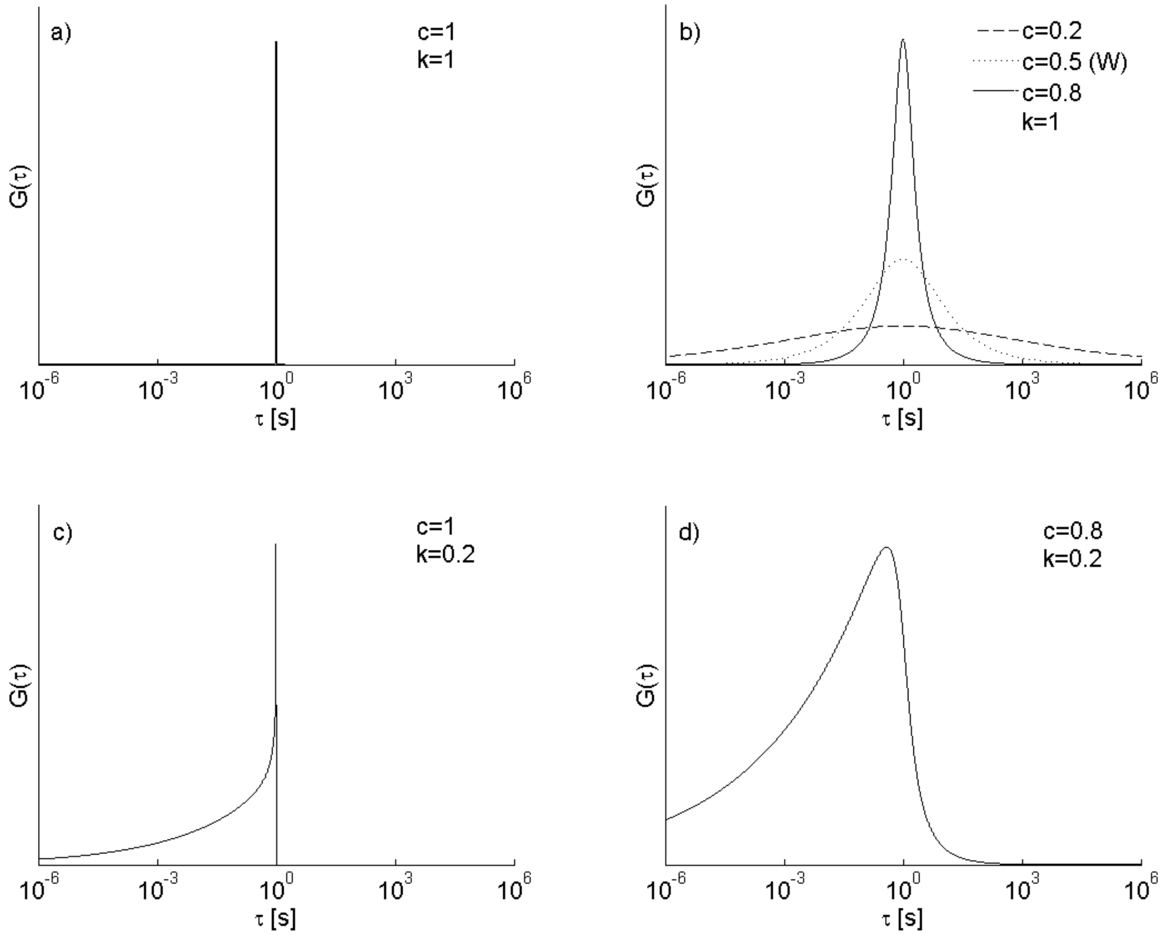

Fig. 2.8 - Relaxation time distribution functions for Debye model (a), Cole-Cole model and Warburg model (b), Cole-Davidson model (c), and Generalized Cole-Cole model (d), calculated according to equations (2.21) and (2.22). Characteristic relaxation time is equal to 1 s in each case.

In addition, a high frequency dielectric response is sometimes included in the model to improve the data fitting above 1 kHz (e.g., *Florsch et al.*, 2014) and this is not trivial in the resistivity formulation. However, the traditional choice of using the model derived from the resistivity formalism is often adopted because of its effectiveness as an approximating function of measured data and in analogy with many other works (*Nordsiek and Weller*, 2008; *Zisser et al.*, 2010; *Breede et al.*, 2012; *Keery et al.*, 2012; *Ustra et al.*, 2012; *Bairlein et al.*, 2014). As explained in details by *Tarasov and Titov* (2013), equation (2.18) corresponds to a circuit with two capacitors and one resistor, while equation (2.19) corresponds to a circuit with two resistors and one capacitor. Thus, the selected formalism needs to be carefully considered in any relationship between model parameters and sediment properties, and in any comparison with previously published results. For example, the characteristic relaxation time differs between the two formulations according to

$$\tau_{\varepsilon} = \tau_{\rho}(1 - m)^{1/c}, \tag{2.24}$$

where τ_{ε} and τ_{ρ} are the characteristic relaxation times in the permittivity formulation and in the resistivity formulation, respectively (the subscript 0 is omitted for simplicity).

A convergence to a unique value of τ is obtained for low chargeability and for a frequency exponent c close to 1 (*Florsch et al.*, 2012; *Tarasov and Titov*, 2013). In the following, the resistivity formulation is used, and a review of the equivalent circuits of the above mentioned models for this case is reported by *Dias* (2000). At the basis of the models is the assumption that the electrical circuit represents the fundamental unit of the bulk electrical behaviour of the porous medium (Fig. 1.2c), and the medium is composed of many units whose total behaviour do not differ from the unit one unless for a scale factor. Each circuit is composed of two basic components combined in parallel, where the first is a simple resistor that describes the pure ohmic conduction and dominates the asymptotic behaviour at low frequency, and the second is a combination of resistors and capacitors that describes the polarization processes (Fig. 1.2d). This element accounts for the non-linear frequency-dependent behaviour. In the comparison with a unit volume cell of the porous medium, the first path represents the electrolytic conduction in a free channel and the second path the charge storage and back-diffusion along a channel with walls covered by clay particles or characterized by throats (*Dias*, 2000; *Boadu and Seabrook*, 2006).

Alternatively, it is also possible to describe the total pore-network as a superposition of unit cells with different characteristic relaxation times, related to different charge storage phenomena (e.g., grain surface, pore throat, EDL, etc.). According to this approach, the complex electrical resistivity can be modelled as

$$\rho^*(\omega) = \rho_0 \left[1 - \sum_{k=1}^{N} m_k \left(1 - \frac{1}{1 + i\omega\tau_k}\right)\right], \tag{2.25}$$

where m_k and τ_k are the individual chargeability and relaxation time of N Debye relaxation processes (*Nordsiek and Weller*, 2008). This approach is called Debye decomposition (DD) and the discrete approximation of its relaxation time distribution function is

$$G(\tau_k) = \frac{m_k}{M_t}, \tag{2.26}$$

where M_t is the total chargeability, i.e., the sum of all the chargeability terms m_k. In other words, m_k quantifies the relative change of conductivity for each individual relaxation term in a narrow frequency interval, whereas M_t corresponds to the magnitude along the whole frequency range. Finally, a Warburg decomposition (WD) was also proposed by adding a c exponent equal to 0.5 to the $i\omega\tau_k$ member of equation (2.25) (*Florsch et al.*, 2014; *Revil et al.*, 2014).

The representation of $\rho^*(\omega)$ is commonly done in the form of dispersion diagrams with the real and the imaginary parts as a function of frequency, or the amplitude and the phase lag as a function of frequency (Bode plot; Figs. 2.9a, 2.9b, and 2.9c). Alternatively, the Argand plane with the real part on the x-axis and the opposite of the imaginary part on the y-axis is used (Fig. 2.9d, 2.9e, and 2.9f). These plots are also called Cole-Cole plots or Nyquist plots. The models with a single relaxation time (D, CC, CD, and GCC) appear as an arc of a circle that intercepts the x-axis at ρ_∞ and ρ_0. For a simple Debye material, the phase spectrum shows a symmetric peak (Fig. 2.9a), and the Argand plot is a semi-circle (Fig. 2.9d). The tangents to the arc in correspondence of the intercepts with the x-axis make an angle of 90°. Both the phase peak and the highest absolute value of the imaginary component are reached at an angular frequency corresponding to the inverse of the characteristic relaxation time. In the CC model, the phase spectrum is still symmetric with respect to the phase peak but this occurs at $\omega = 1/(\tau_0(1-\mathrm{m})^{1/2c})$ (Fig. 2.9b). Both the tangents to the circle on the Argand plot make an acute angle with the x-axis equal to $c\pi/2$ (Fig. 2.9e). On the other hand, CD and GCC models are asymmetric (Fig. 2.9c): in the former, the low-frequency side of the phase peak has a constant slope of 45° and the high-frequency side a slope dependent on k, whereas in the latter the low-frequency and the high-frequency side slopes are dependent on c and on kc, respectively (Fig. 2.9f). In these cases, the maximum imaginary component does not occur in correspondence of $\omega = 1/\tau_0$.

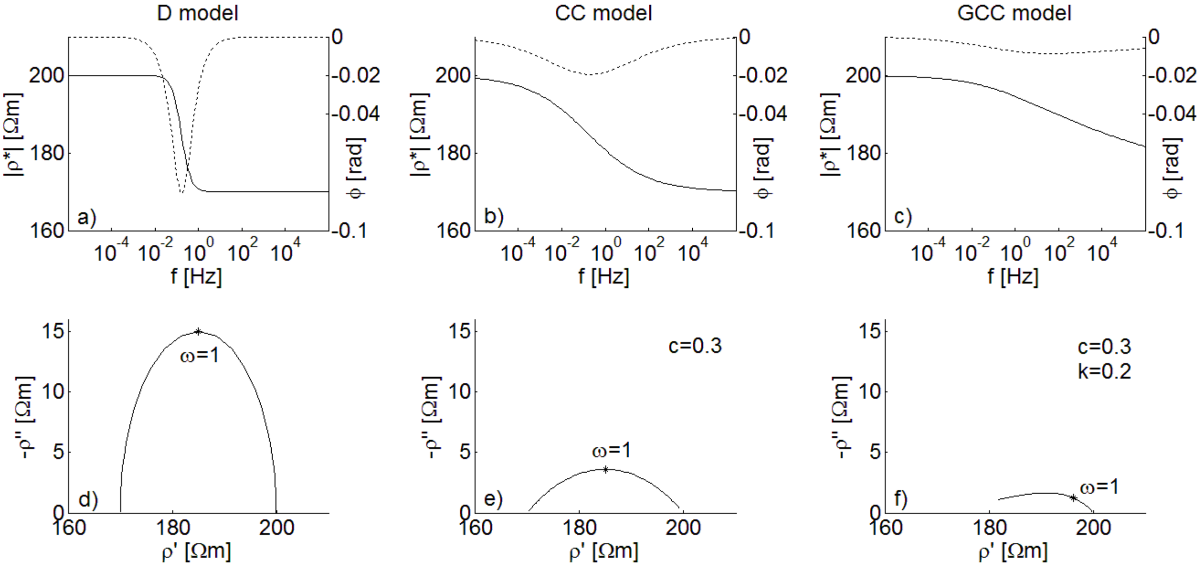

Fig. 2.9 - Amplitude (solid line on left axis) and phase (dotted line on right axis) spectra of a Debye material (a), a Cole-Cole material (b) and a Generalized Cole-Cole material (c), with the corresponding Argand plots (d, e, and f). Direct current resistivity is equal to 200 Ωm, characteristic relaxation time to 1 s, and chargeability to 0.15 in each case.

2.4 Measure of complex electrical properties

Determination of complex electrical properties can be performed both in the time domain and in the frequency domain (e.g., *Reynolds*, 2011). In the time domain, induced polarization (IP) methods are based on the injection of current pulses and the measure of the decay rate of the potential discharge after the current has been turned off. Chargeability is the representative measure of polarizability. It is usually expressed in mV/V since it is defined as the ratio between the potential V_S after a sudden removal of the energizing field (i.e., the potential at the moment the current is switched off) and the potential in stationary condition V_{DC} (i.e., prior to the moment the current is switched off)

$$m = \frac{V_S}{V_{DC}}. \tag{2.27}$$

Practically, the potential is measured at discrete intervals of time t_i after the cut-off along the transient response V_{ip} and the values are integrated with respect to time (Fig. 2.10). Apparent chargeability (or integral chargeability, or partial chargeability) is defined as

$$m_a = \frac{1}{V_{DC}} \int_{t_i}^{t_{i+1}} V_{ip}(t) dt, \tag{2.28}$$

when measured in ms, or

$$m_a = \frac{1}{V_{DC}(t_{i+1} - t_i)} \int_{t_i}^{t_{i+1}} V_{ip}(t) dt. \tag{2.29}$$

when expressed in mV/V. Assuming that the current is injected over a period of time long enough to let the system reach a steady state condition, V_{ip} can be modelled with an exponential decay

$$V_{ip} = V_S e^{-\frac{t}{\tau_0}} = V_{DC} m e^{-\frac{t}{\tau_0}}, \tag{2.30}$$

where τ_0 and m are the same relaxation time and chargeability parameter of equation (2.19) in the Debye formulation.

According to equations (2.28) and (2.29), apparent chargeability is affected by t_i and t_{i+1}, and thus particular care should be exercised in selecting the appropriate time window to maximize the signal-to-noise ratio and to compare different datasets. Usually, a series of successive time windows (gates) are used to sample the decay curve, and a delay after the cut-off is applied to reduce the effects of electromagnetic coupling (*Dahlin and*

Leroux, 2012). Recent studies tend to focus on the extraction of spectral information from IP decay and on the use of the full decay curve for the inversion processes instead of the integral chargeability and direct current resistivity only (e.g., *Hördt et al.*, 2006; *Honig and Tezkan*, 2007; *Tarasov and Titov*, 2007; *Fiandaca et al.*, 2012). In this way, comparison between frequency domain and time domain can be done in terms of relaxation time distribution.

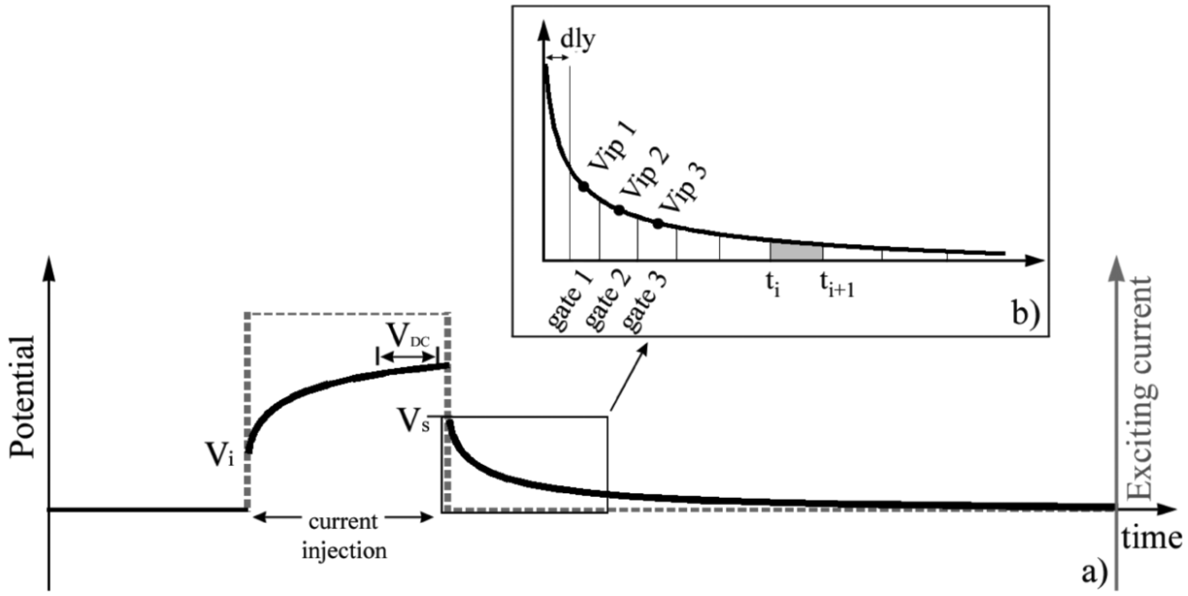

Fig. 2.10 - Schematic representation of the potential response to the injection of a square current wave (a); detail of the potential discharge curve and the series of gates used for time domain IP measurements (b; *Gazoty et al.*, 2012).

Electrode configuration for time domain IP can in principle be the same as for DC resistivity, i.e., at least two current electrodes and two potential electrodes arranged in different geometric configurations. However, signal-to-noise ratio, electromagnetic effects, and electrode polarization effects should be carefully considered in the choice of the electrode array. These issues lead to a preferential use of dipole-dipole configuration with non-polarisable electrodes, and no multi-core cables, for good imaging results in the field (*Dahlin et al.*, 2002).

In the frequency domain, electrical resistivity is calculated from the ratio between the current and the potential difference, using at least two different frequencies of current injection. In IP methods, the frequencies are usually smaller than 10 Hz, and used to calculate the frequency effect (FE, or percentage frequency effect PFE)

$$\mathrm{FE} = \frac{\rho_1 - \rho_2}{\rho_1}, \tag{2.31}$$

and the metal factor (MF)

$$\mathrm{MF} = \mathrm{A}\,\frac{\rho_1 - \rho_2}{\rho_1 \rho_2} = \mathrm{A}(\sigma_2 - \sigma_1), \tag{2.32}$$

where ρ_1 and ρ_2 are the two resistivity values with $\rho_1 > \rho_2$, σ_1 and σ_2 the corresponding conductivity values, and $A = 2\pi \cdot 10^5$. More recently, IP has been replaced by spectral induced polarization (SIP) methods, in which a wide range of frequency of applied current is used, resulting in a resistivity spectrum that typically covers the range from 1 mHz to a few kHz. A revision of the experimental details for SIP measurements is provided in section 4.1.

Chapter 3

Study sites and samples characterization

3.1 Sampling sites

The samples collected for this study mainly derived from the Po plain (northern Italy). This sedimentary basin developed as a Plio-Quaternary foreland basin controlled by competing effects of continental sediment supply, mostly from the alpine side, dynamics of regional and local base-levels, glacial cycles, and syn-depositional tectonics. More specifically, the sampling was made in the southernmost Lodi plain (Lombardy), the region bounded by the present-day Po river to the south and by the Lambro and Adda river valleys to the west and east, respectively. The Quaternary evolution of the Po plain in Lombardy is controlled by the northwards propagation of the northern Apennine thrusts of the Emilia Arc (*Pieri and Groppi*, 1981), the flexural rebound of the forebulge on the alpine side (*Bresciani and Perotti*, 2014), the isostatic response to glacial cycles (*Arca and Beretta*, 1985; *Carminati et al.*, 2003; *Scardia et al.*, 2006, 2012), and the onset of the major Plio-Quaternary glaciations on the southern side of the Alps (*Penk and Bruckner*, 1909; *Bini*, 1987, 1997; *Muttoni et al.*, 2003).

The widest morphological unit of the area is the *Livello Fondamentale della Pianura* (LFP; *Castiglioni and Pellegrini*, 2001) that corresponds to the current interfluves plain, but is a patchwork of non-coeval continental deposits, mainly sandy, with silty lenses and thin gravelly layers (green unit in Fig. 3.1a). Post-glacial to recent river valleys are entrenched into the LFP with a series of lowered terraces (pale blue in Fig. 3.1a), whereas isolated reliefs (e.g., San Colombano, Casalpusterlengo, Zorlesco, brown in Fig. 3.1a) are present in correspondence of some structural culminations (purple plus symbols in Fig. 3.1b) of the Apennine thrust-related folds (*Desio*, 1965; *Anfossi et al.*, 1967; *Cremaschi*, 1987; *Pellegrini et al.*, 2003; *Baio et al.* 2009; *Livio et al.*, 2009; *Bersezio et al.*, 2010; *Bresciani and Perotti*, 2014).

Outcropping and subsurface continental deposits are divided by *Fantoni et al.* (2004), Baio *et al.* (2009), and *Bersezio et al.* (2010) in the *pre-Besnate Unit* (Early p.p.-Middle Pleistocene), composed of fluvio-glacial gravels and sands with a deeply weathered profile attributed to the distal equivalents of the glacio-fluvial sediments of the *Binago*, *Specola*, and *Bozzente* glaciations (*Bini*, 1987, 1997; *Bini et al.*, 2004), the *Besnate Allogroup* (Late Pleistocene) with trough cross-bedded sands with minor gravel bars and silty-clay flood plain lenses with local thin weathering profile, and the *Cantù Alloformation* (Late Pleistocene, Last Glacial Maximum or LGM) made of fluvial and glacio-fluvial alluvial sandy deposits with silty lenses and thin gravelly intercalations.

The Post-Glacial to recent units correspond to the alluvial valley terraces of the meandering Lambro, Adda, and Po rivers, and to the abandoned Sillaro riverbed. They are constituted by sands and gravels deposited after the reworking of *Besnate* sediments, and silty flood deposits. Coarse-grained portions of these units are widely exploited for construction materials.

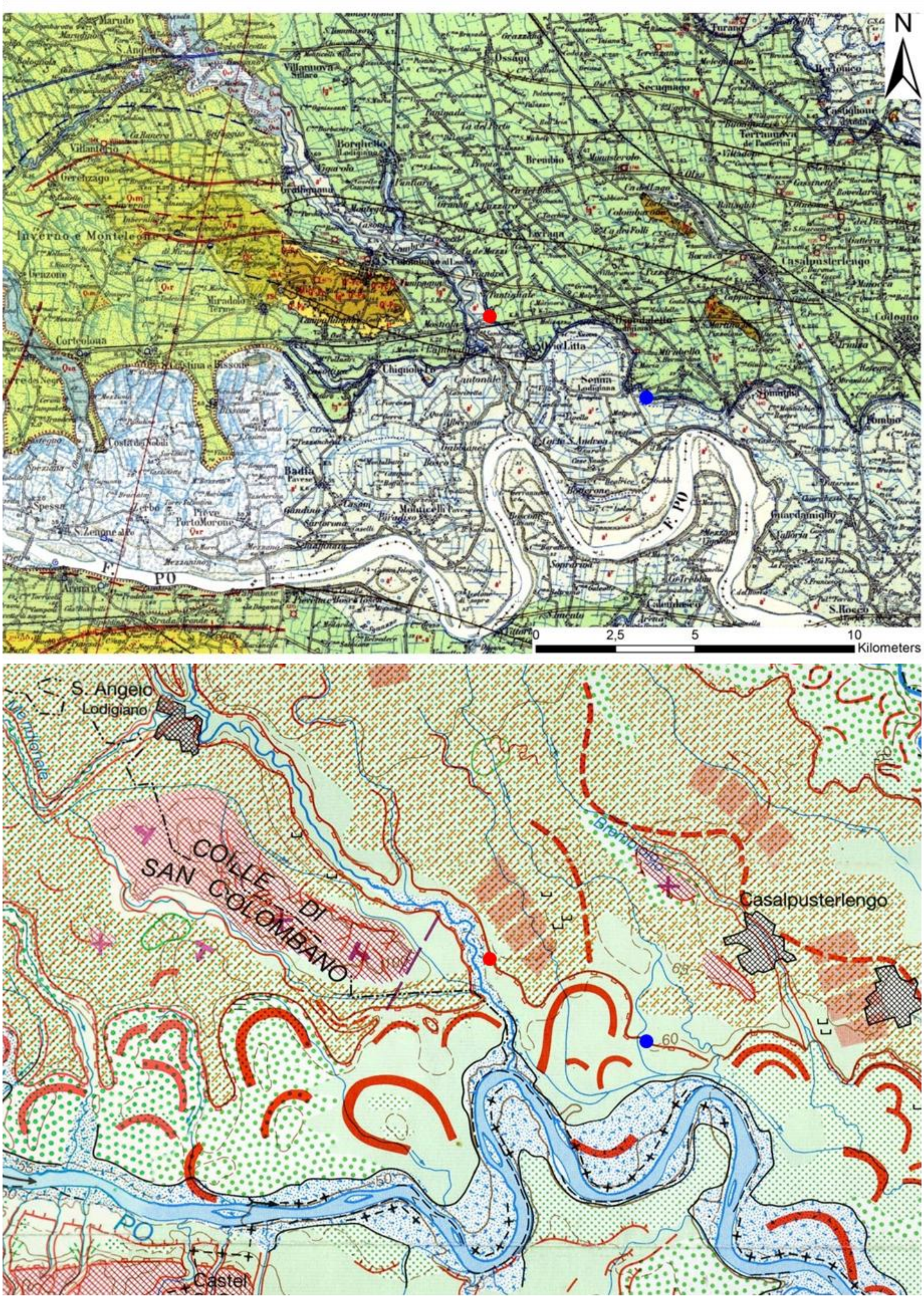

Fig. 3.1 - Geological map of the southernmost Lodi plain (a; extracted from the 1:100.000 map, *Anfossi et al.*, 1967; *Boni*, 1967); geomorphological map of the southernmost Lodi plain (b; extracted from the 1:250.000 map, *Castiglioni et al.*, 1997). The red and blue dots locate the sampling sites of Orio Litta and Senna Lodigiana, respectively.

On the San Colombano al Lambro anticlinal relief, the most ancient geological units outcrop, with the name of *Marne di S. Agata Fossili* (MSAF) and *San Colombano Formation* (SCF; *Anfossi et al.*, 1967; *Bersezio et al.*, 2010). They are Miocene and Lower Pleistocene marine units, composed of marlstones with rare sandy layers the former, and clays rich in micro- and macro-fauna, with sandy and gravelly intercalations and local calcareous lenses, the latter. At the hill top, an uplifted, deeply weathered and truncated unit of Lower(?)-Middle Pleistocene alluvial sands is exposed (*Mindel*, *Anfossi et al.*, 1967; *Cascina Parina Unit*, *Pellegrini et al.*, 2003). It might correspond to the very similar weathered sands which have been exposed at the quarry sites of the Casalpusterlengo and Zorlesco isolated reliefs (*Desio*, 1965; *Bersezio et al.*, 2010).

The subsurface geological architecture of the Lodi plain has also been investigated with an integrated multi-scale approach including geologic and geomorphologic surveys, correlations of borehole and well-log data, geophysical data of vertical electrical sounding (VES), electrical resistivity ground imaging (ERGI), ground penetrating radar (GPR), and time-domain electromagnetic surveys (TDEM), and geostatistical simulations of facies distribution (*Bersezio et al.*, 2007; *Mele et al.*, 2010; *dell'Arciprete et al.*, 2011; *Mele et al.*, 2012; *Mele et al.*, 2013).

Four stratigraphic units of highest rank are named from GU0 to GU3 in ascending order (*Bersezio et al.*, 2010):

- the geological unit 0 (GU0; Early Pleistocene) constitutes the marine substratum of blue, cyan, and grey clays with intercalated sandy and gravelly layers. It is gently folded into two separated WNW-ESE anticlines (Casalpusterlengo and Maleo-Chiesiolo) related to the Apennine active thrusting;

- GU1 (Middle Pleistocene) lays over GU0 in an onlap geometry marked by an erosional surface. It is composed by four fining-upwards sequences from gravelly sands to sands and sandy silty clays. The uplifting deformation decreases according to the stratigraphic polarity up to the sealing of the buried structures;

- GU2 (Middle-Upper Pleistocene) fills an erosional depression with fining-upwards sequences from gravel and sand to silty-clay with peat and terminates against the terraced flanks of the anticlines. It is not involved in active folding, but in a differential subsidence after the phase of tectonic deformation;

- GU3 (Upper Pleistocene) is formed by at least two fining upwards sequences from sandy-gravel to sandy-silt that carve some terraced valleys;

- a further unit (GU4 for analogy; Post glacial-Holocene) is described by *Cantone* (2008) as sandy and gravelly stationary sequences and gravelly-sand to silty-clay positive sequences, located only in the Adda and Po river valleys and locally outcropping in the interfluve Adda-Lambro.

The interpretation of these units in terms of paleogeographic evolution suggests the transition from a marine environment to a transitional one, with small bays and delta systems (GU0), followed by a continental deposition associated both to the tectonic uplifting and to the lowering of the sea-level due to Pleistocene glaciations. Deposition of GU1 is associated to estuary and distal flood plain environments, whereas GU2 to a proper meandering system with mixed-load transport. Deposition of GU3 and GU4 occurred in confined fluvial valleys produced by incision after the LGM.

At the regional scale, the hydrostratigraphy of the area is outlined by *Regione Lombardia and Eni-Agip* (2001) as built up by four aquifer groups, named D to A in ascending order (Fig. 3.2). Groups D and C are hosted in the Lower-Middle Pleistocene succession, whereas group B and A are located in the Middle-Upper Pleistocene succession and correspond to the traditional phreatic and semi-confined aquifers. A salt/freshwater interface generally intersect the deepest group D and rarely also the lower part of group C. Uplifts of saline waters are present in correspondence of the tectonically uplifted successions and were clearly recognized by geoelectrical surveys and resistivity logs (*Agip*, 1994; *Alfano and Mancuso*, 1996; *Mele et al.*, 2012; *Mele et al.*, 2013).

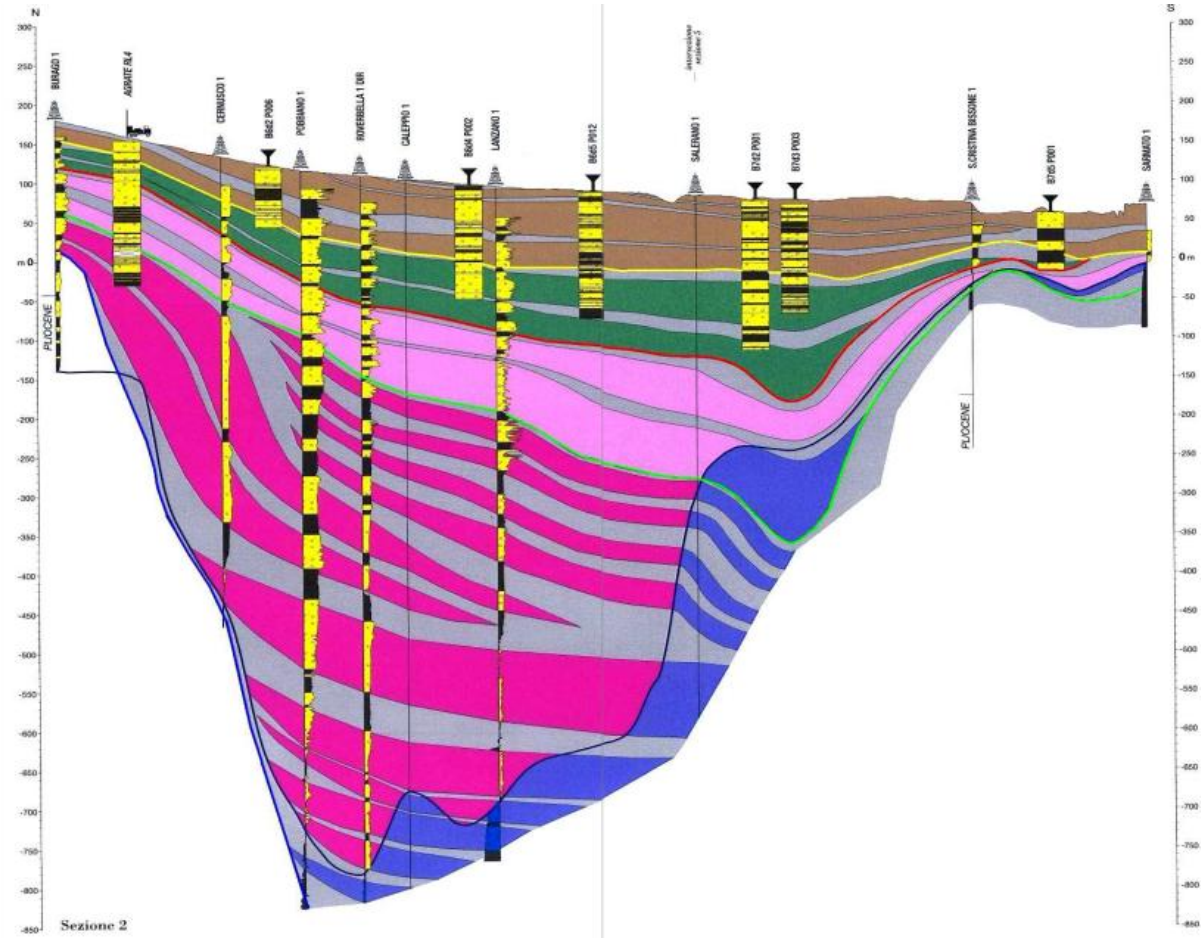

Fig. 3.2 - Illustrative hydrostratigraphic section (N-S) of the Po plain (vertical exaggeration 50x). In the stratigraphic logs yellow represents aquifer units and black aquitard units; in the hydrostratigraphic section aquifer A is represented in brown, aquifer B in green, aquifer C in pink, aquifer D in purple, and saltwater aquifer in blue (*Regione Lombardia and Eni-Agip*, 2001).

Besides this regional description, the characterization of the sampling sites is provided at the outcrop scale in the following sections. In particular, most of the samples come from the outcrops of Orio Litta and Senna Lodigiana that are located in the Lodi plain along the Po terrace (Fig. 3.1). These sites were selected on the basis of the occurrence of sedimentary layers that could be easily sampled. The collected materials are considered representative of the textural variability of the alluvial deposits described at the regional scale. The textural composition is in fact one of the key factors analyzed for the estimation of empirical correlations with electrical parameters. Two other sites (Lozzolo and Landriano) were also selected to obtain materials with a finer granulometric distribution, in order to enrich the investigated dataset; a short regional geological description is provided for them within the corresponding sections. Furthermore, in the sites of Senna Lodigiana, Landriano, and Lozzolo, field acquisitions of SIP data were executed. The selection of these sites was mainly based on the evaluation of the expected results with an electrode array of about 30 m and an estimated investigation depth of about 5 m. In particular, the presence of contrasting coarse-grained and fine-grained layers and a degree of saturation as close as possible to the full saturation were considered as positive factors in order to compare field and laboratory data. The accessibility to the site in order to carry and handle instruments under safe conditions and the space available for the cables layout and the acquisition system were also considered as essential requirements. A short summary of previous geophysical surveys performed in these sites is also included as a reference background in the appropriate sections.

3.1.1 Orio Litta

The sampling site of Orio Litta (LO, Italy, coordinates 45°9'59.09"N 9°32'20.01"E; Fig. 3.3) was a quarry wall 3.6 m high, 1 m width in the basal portion, and 3 m width in the upper portion, located on the north side of the provincial road 234 (SP234), approximately 1 km east from the Lambro river and along the principal terrace of the Po river, with W-exposition. The site is located within the *Cantù Alloformation*, and in the morphological unit LFP. The first sampling was executed in September 2011 and seven beds were recognized on the outcrop, which are described in the following in descending order:

- landfill, with thickness variable from 10 cm to 60 cm;
- gS with erosional lower boundary, 50 cm thick, interested by illuviation yellowish clay – sample O6;
- massive *fm*S, 40 cm thick, with aggregation degree increasing upward, and brown-reddish marks interpreted as effects of water table oscillations – sample O5;

- gS with erosional lower boundary, massive structure in the basal portion and rounded and sub-rounded pebbles of about 3-4 cm in diameter (30 cm thick – sample O3) and trough cross lamination in the upper portion (80 cm thick – sample O4);
- graded bed from *c*S with pebbles to *m*S, with erosional lower boundary, 25 cm thick;
- *mc*S with planar cross-beds, 50 cm thick – sample O2;
- *mf*S with massive structure, 35 cm thick (lower boundary non-visible) – sample O1;

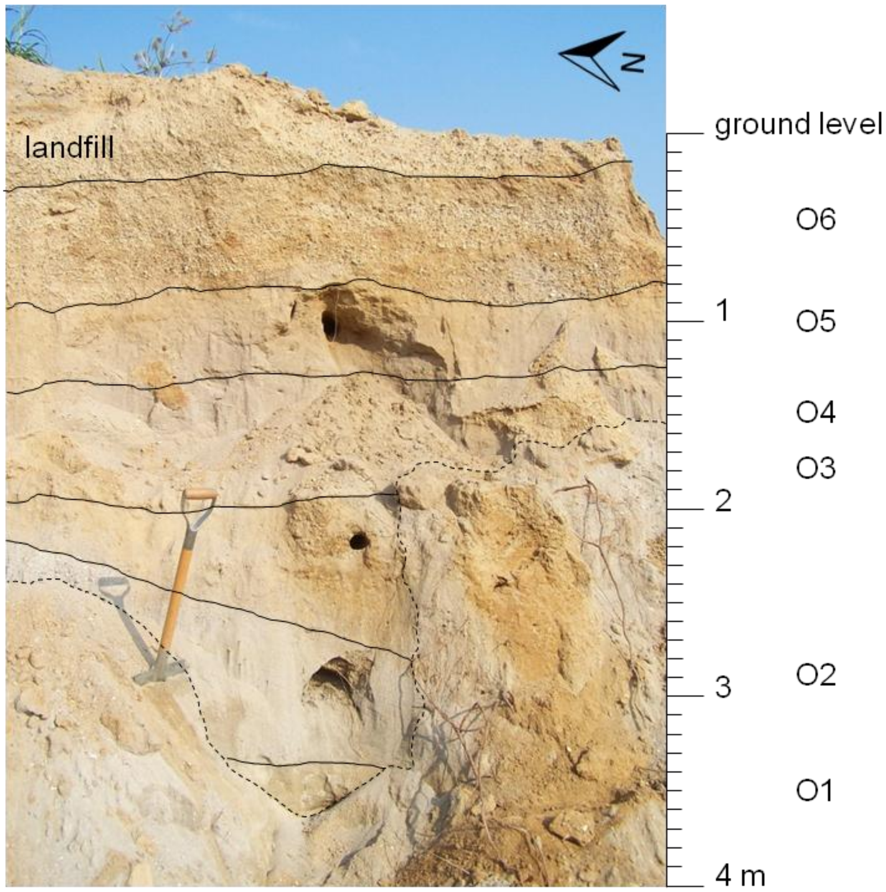

Fig. 3.3 - Outcrop of Orio Litta. The observed stratification is marked by solid lines and the position of sampling is reported on the right side of the picture.

A secondary sampling was executed in September 2014 on an adjacent small outcrop (2 m high and 2 m width). Sample Ob18 and Ob19 corresponded to a bed of *mc*S with massive structure, and to the overlaying bed of *mf*S with massive structure. A correlation between the two sites was not feasible, due to the strong modifications of the quarry morphology that was still active during the first campaign.

3.1.2 Senna Lodigiana

The site of Senna Lodigiana (LO, Italy, coordinates 45°8'43.60"N 9°36'1.66"E; Fig. 3.4a) offered a wide outcrop (3 m high on the average and about 30 m width) that remained almost unchanged during the two sampling activities of September 2011 (samples named S) and September 2014 (samples named Sb). For this reason, if the exact sampling position was identified, the number of the sample was kept equal, with the addition of a letter b to indicate the secondary sampling. The outcrop corresponded to the wall of an abandoned quarry on the principal terrace of the Po river, with direction N167E and E-exposition. It was located on the provincial road 206 (SP206) on the opposite side of the municipal graveyard, at a distance of about 5.5 km from Orio Litta. The site is located within the Post-Glacial and Holocene Units. Five beds were recognized in the outcrop, whose spatial distribution is apparent from Fig. 3.4a and Fig. 3.4b. From top to bottom, they are:

- landfill, with variable thickness from 20 cm to 1 m;
- sG with concave erosional lower boundary, located between x = 28 m and x = 37 m in Fig. 3.4a, maximum thickness of about 1 m;
- *mf*S with trough cross lamination (samples S9 and Sb9), with erosional lower boundary that deepens with a concave-up shape in the southern portion of the outcrop. Here, the unit is trough cross-laminated at the top (Fig. 3.4c), with trough cross-beds in the middle portion, and massive in the basal portion. The erosional surface is delimited by sub-rounded pebbles and sub-angular mud clasts, and in the southern portion is characterized by a diffused reddish colour that interests both the sand and the mud clasts;
- *mc*S sand with erosional lower boundary lined by rounded pebbles and sub-angular mud clasts up to 15 cm in diameter, non-continuous unit located between x = 22 m and x = 29 m in Fig. 3.4a, maximum thickness 70 cm, with planar cross bedding, (Fig. 3.4d) – samples S10 and Sb10;
- clayey silt with transitional lower boundary characterized by the presence of centimetric sandy lenses, 60 cm thick on the average, the upper portion is affected by hydroplastic deformation marked by colour variations (Fig. 3.4e) – sample Sb8;
- alternation of clayey silt and *f*S, total thickness variable between 1.50 m and 3 m (lower boundary non-visible), with horizontal or small scale, concave, oblique lamination, in millimetric to pluri-centimetric (25 cm) levels with lenticular shape, passing to slightly-silty *fm*S, with massive structure and local horizontal lamination (more marked towards the north side of the outcrop – samples S11 and Sb17). The unit is interested by the presence of diffuse pedogenetic structures (Fig. 3.4f) in the upper portion.

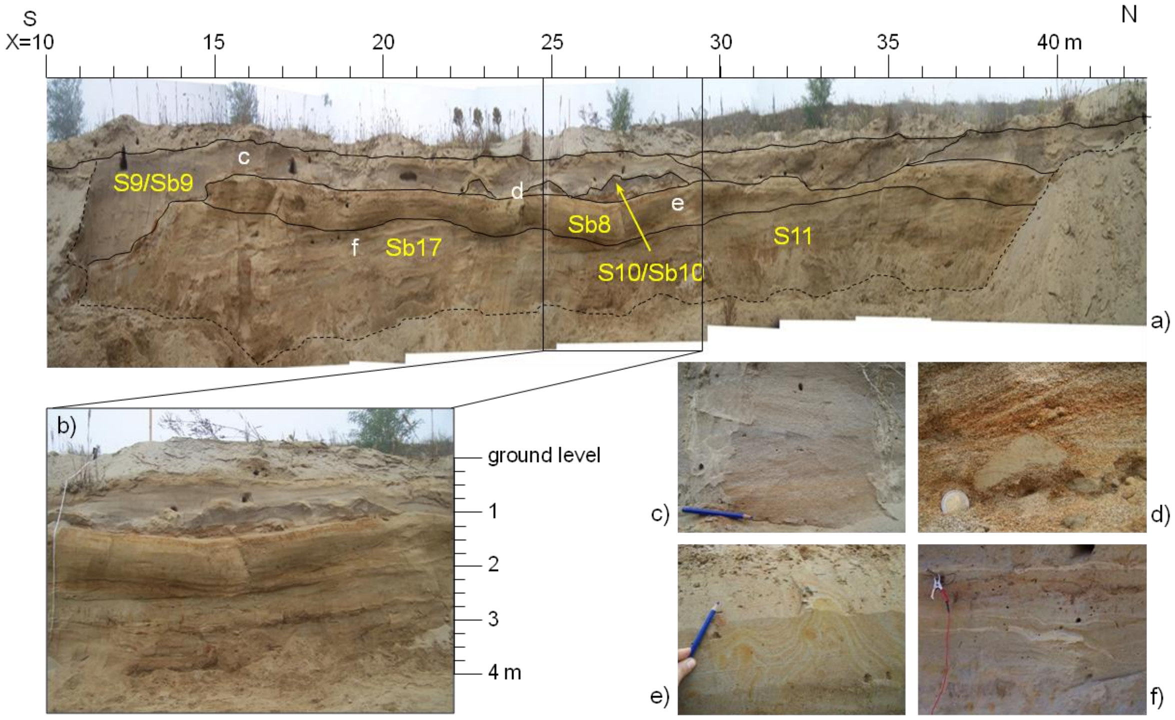

Fig. 3.4 - Outcrop of Senna Lodigiana. The observed stratification and the position of sampling is reported on subplot a (vertical exaggeration 2x). Subplot b is the 1:1 representation of the central portion of the outcrop. Subplots c to f are detailed pictures of cross-lamination of level S9, mud clasts of level S10, hydroplastic deformation in level S8, and pedogenetic structures in level S11.

Two further samples (S7 and Sb7) were collected on the opposite quarry wall in a reddish sandy soil layer with clay, developed on a substrate equivalent to the grey sandy layer of sample S9.

In this site, a geophysical survey was conducted in October 2011 with a combination of ERGI, VES, GPR, and refraction seismic. A summary of the results is reported in Fig. 3.5.

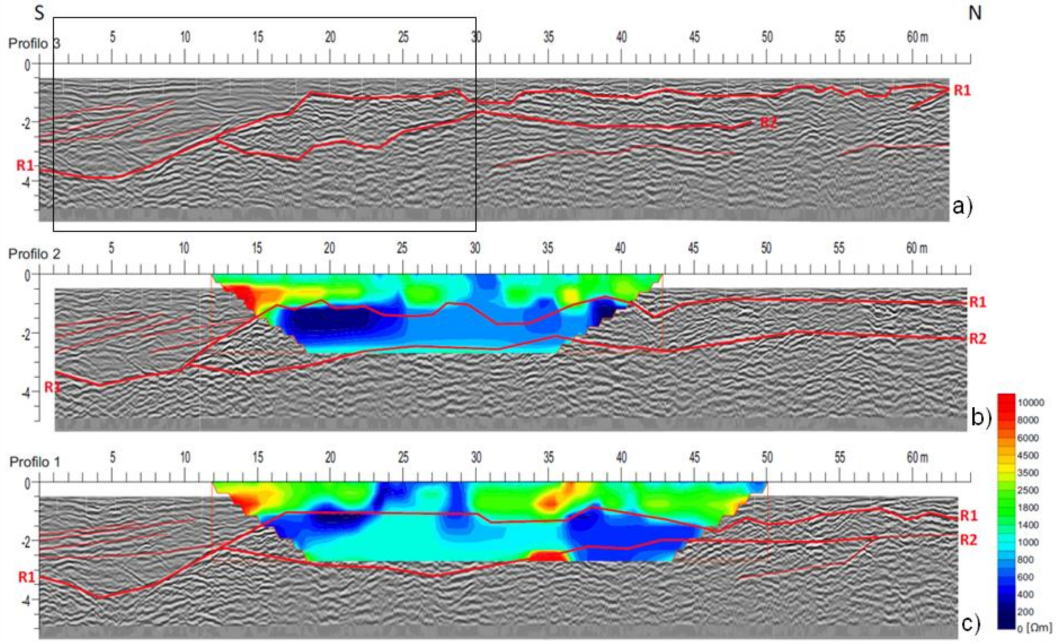

Fig. 3.5 - GPR and DC resistivity surveys performed along parallel profiles at a distance of 7 m (a), 5 m (b) and 3 m (c) from the sampling wall (*Inzoli*, 2012). Red lines highlight the main GPR reflectors, whereas the black box in subplot a corresponds to the investigation area of the field EIT survey (see section 7.4.2).

A continuous reflector (R1) appears on the southern side of all profiles at a depth of about 4 m and decreases its depth to about 1 m in correspondence of x = 16 m. A second reflector (R2) runs parallel to the former at a depth between 2 m and 3 m and ends against R1 around x = 12 m. The layer above R1 is mostly characterized by electrical resistivity higher than 1000 Ωm, whereas the layer between R1 and R2 is characterized by resistivity lower than 1000 Ωm. By direct comparison with the outcropping front, R1 is interpreted as the base of level S9 (Fig. 3.4a), whereas the low resistivity layer could be the association of level Sb8 and S11/Sb17.

3.1.3 Landriano

The site of Landriano (PV, Italy, coordinates 45°19'19.99"N 9°16'8.16"E; Fig. 3.6a) did not present any outcrop. It is a crop field within the Menozzi farm, about 1.3 km ENE from the Lambro Meridionale river, in the LFP unit. A shallow trench approximately 1 m depth was excavated in November 2012 within the agricultural soil layer (Fig. 3.6b) and showed from the ground level:

- 25 cm of silty sand with clay;
- 70 cm of slightly sandy silty clay – sample LA12.

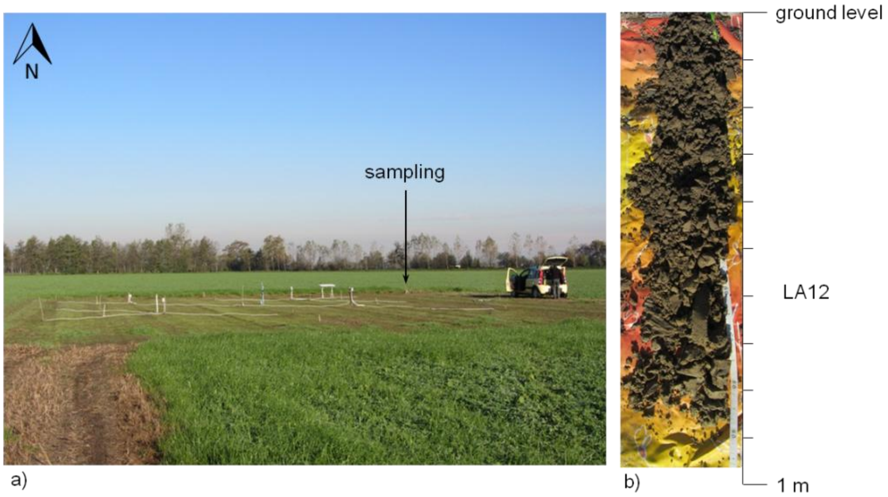

Fig. 3.6 - Sampling site of Landriano (a) and core sample of the shallow trench with the approximated sample position (b).

At this depth the water table was observed (ρ_w = 7 Ωm at 20°C) and confirmed at the scale of the field through geoelectrical imaging. It was interpreted as a suspended aquifer fed by the irrigation waters, oscillating between 0.5 m depth during summer and 3 m during winter (*Ortuani et al.*, 2013). A further geophysical survey was conducted by *Ortuani et al.* (2015) in the northern adjacent crop field (coordinates 45°19'31.68"N - 9°15'47.36"E) with electro-magnetic (EM) sensors and DC resistivity. Here the water table was again easily recognized at a depth of about 2.5 m (Fig. 3.7). In addition, a lateral decrease of resistivity was observed from NE to SW in the unsaturated zone (Fig. 3.7a). This transition was observed in the whole crop by EM maps of surface resistivity distribution.

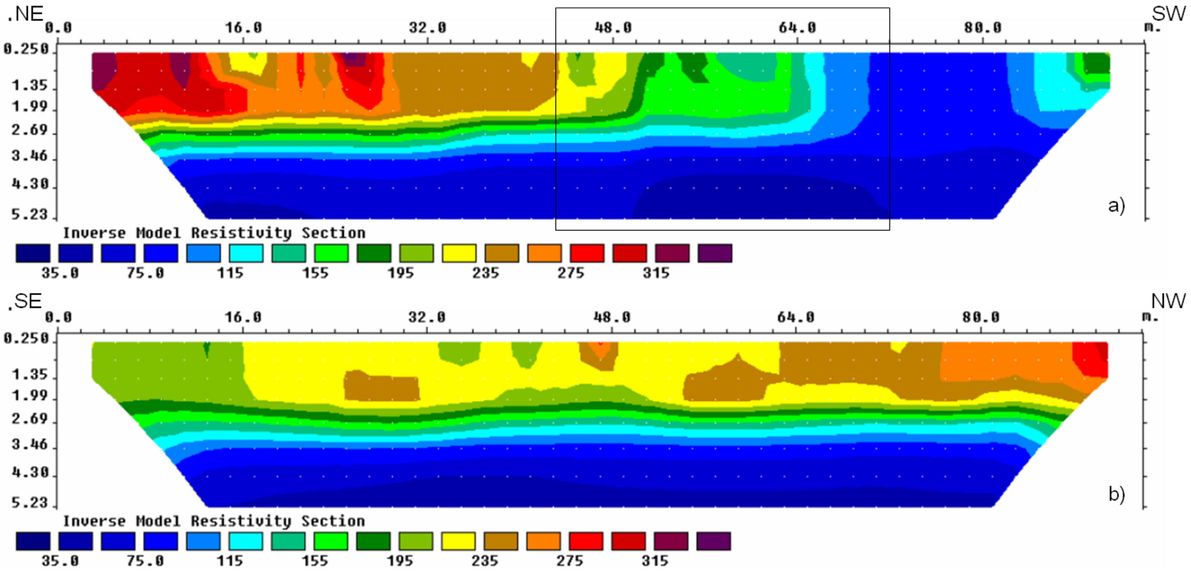

Fig. 3.7 - DC resistivity surveys performed along two perpendicular profiles (*Ortuani et al.*, 2015). The black box on subplot a corresponds to the projection of the investigation area of the field EIT survey (see section 7.4.1).

3.1.4 Lozzolo

The site of Lozzolo (VC, Italy, coordinates 45°37'12.79"N 8°18'51.06"E; Fig. 3.8) was chosen in order to extend the database with fine-grained sediments. It is a kaolinitic mine with a very complex geo-structural and stratigraphic setting, which is briefly outlined in the following (see, e.g., *Carraro et al.* 1967; *Bottino*, 1973). The mining area Fornaccio is located in a Plio-Pleistocene sedimentary sequence constituted by transitional and continental fluvio-lacustrine lenticular bodies (*Successione Villafranchiana*) deposited above Permian volcanites. Lenses vary in grain-size from clay and clayey sands to conglomerates and mostly represent the erosion and alteration products of the volcanites, the granitic plutons of the *Serie dei Laghi* and their metamorphic embedding rocks (pelitic-arenitic protolites, equilibrated in amphibolitic facies). The *Successione Villafranchiana* is subdivided into three formations, named in ascending order with the typical jargon of the extraction activity (*Casati*, 2012):

- *Complesso Basale*, constituted by reddish-brownish-yellowish sands and silty sands, in lenses (*Volpina* – sample LZ13), greenish silty and clayey sands with sparse volcanic pebbles, 3 m thick on the average but discontinuous (*Balmino Verde*), and white silty and clayey sands with sparse volcanic pebbles, present only in the NE area of the mining claim with a thickness varying from 1 to 4 m (*Balmino Bianco*);

- *Complesso Inferiore* or *Caolino*, constituted by light grey and grey kaolinitic clayey sands with sandy lenses and a basal thin layer of monogenic conglomerate (sub-angular pebbles of altered volcanites) – sample LZ14;

- *Complesso Superiore* or *Ghiaione*, constituted by gravels and sands in lenticular shape, with highly clayey portions – samples LZ15 and LZ16.

The sedimentary complexes are separated by erosional surfaces and limited at the top by Quaternary glacio-fluvial sediments (14-10 ka). Sub-vertical faults affect the area. Samples were provided by RM Ricerche Minerarie from borehole drillings of June 2013 and Januar 2014.

Fig. 3.8 - Panoramic view of the Fornaccio mining area in the site of Lozzolo. The spatial location of the sampled units is not straightforward due to the complex geological setting and the anthropic morphological modifications.

3.2 Analytical techniques

This section is devoted to the description of the analytical techniques adopted for the characterization of the investigated samples. It is worthwhile noting that the characterization includes only the analysis of interest for the aim of the work, i.e., the evaluation of empirical correlations with electrical parameters. For this reason, the granulometric analysis and the X-ray powder diffraction analysis on the mud fraction are selected for the solid phase since grain-size-distribution and mineralogy of the fine-grained fraction are key factors in determining SIP properties. A chemical analysis of the major elements is also performed on the fluid phase of some samples as an additional check of the interactions between solid and fluid. For each analytical technique, the main parameters of the acquisition are provided in the appropriate section with a short description of the operating principle.

3.2.1 Grain-size analysis

Determination of particle-size-distribution can be obtained with different methods based on several physical principles: sieve, sedimentation, photoanalysis, optical counting, electroresistance counting, laser diffraction, etc. Due to the ease of execution and interpretation, the cheapness, and the available facilities at the Sediments and Soils Laboratory of the Department of Earth Science (Università degli Studi di Milano), the traditional sieve analysis was chosen to obtain the grain-size-distribution of the investigated samples. The protocol consisted of the following phases:

- determination of the total mass of the sample, after air drying (Fig. 3.9a);
- separation of the solid fraction with $d > 2$ mm (Fig. 3.9b);
- quartering of the remaining fraction to obtain a representative sub-sample with a mass between 90 g and 150 g (Fig. 3.9c);
- oxidation of the organic matter with 130-volume hydrogen peroxide (H_2O_2) for at least 24 hours and as long as liberation of vapour was visible (Fig. 3.9d). The organic matter content was also determined for some selected samples by measuring the concentration of $K_2Cr_2O_7$ through titration with a solution of $(NH_4)_2Fe(SO_4)_2 \cdot 6H_2O$ after the reduction of the $K_2Cr_2O_7$ by the organic matter (*Walkley and Black*, 1934);
- humid sieving with a non-reacting liquid (tap water) through a series of ten sieves (1400-1000-710-500-355-250-180-125-90-63 μm) and preservation of the mud fraction into settling boxes (Fig. 3.9e);

- dry sieving through the same set of sieves on a vibrating column[2] (Fig. 3.9f);
- repetition of the humid and dry sieving for the gravel fraction (42.25-31.5-22.6-16-11.2-8-5.66-4-2.8-2 mm series);
- determination of the mass retained at each sieve;
- calculation of the percentage of retained and passing material with respect to the total mass of the sample.

In addition, the protocol included a densimeter test, when the mud fraction constituted at least 10% on the total weight, in order to define the grain-size-distribution curve for $d < 63\ \mu m$. The method consists in the preparation of a mud suspension with a fixed volume of water and the addition of an anti-flocculant (Fig. 3.9g). The relative density of the suspension is measured at successive time intervals with the densimeter, together with temperature. A conversion table allows to determine the amount of the deposited fraction at each time step and to relate it to the diameter of the particles.

Fig. 3.9 - Phases of particle-size-distribution analysis: weighting (a), separation of the gravel fraction (b), quartering (c), oxidation of organic matter (d); humid sieving (e), dry sieving (f), and densimeter test (g).

From the grain-size data, other textural parameters were calculated:

- the characteristic diameters d_x, corresponding to the grain diameter at a percentage threshold x of material passing at the sieve;
- the coefficients of uniformity U_{60} and U_{90}, calculated as the ratio between d_{60} and d_{10} or d_{90} and d_{10}, where the smaller the number the larger the sorting;

---

[2] For samples Ob18, Ob19, Sb7, Sb8, and Sb17, only a reduced series of sieves was available (2000-1000-710-500-250-125-50 μm) and the dry sieving was done manually without the vibrating column.

- the coefficient of curvature U_c, calculated as

$$U_c = \frac{d_{30}^2}{d_{10} d_{60}}; \tag{3.1}$$

- the coarse-to-fine ratios Γ_d, with threshold grain diameter d equal to 0.063 mm, 0.125 mm, and 0.250 mm (*Mele et al.*, 2012; *Mele et al.*, 2014).

3.2.2 X-ray powder diffraction

The X-ray powder diffraction technique is based on the diffraction principle, i.e., the deviation of the propagation trajectory of an electromagnetic wave due to the interaction with matter. The Panalytical X'Pert Pro diffractometer of the X-ray Powder Diffraction Laboratory of the Department of Earth Science (Università degli Studi di Milano) was used to analyze some selected samples (Fig. 3.10).

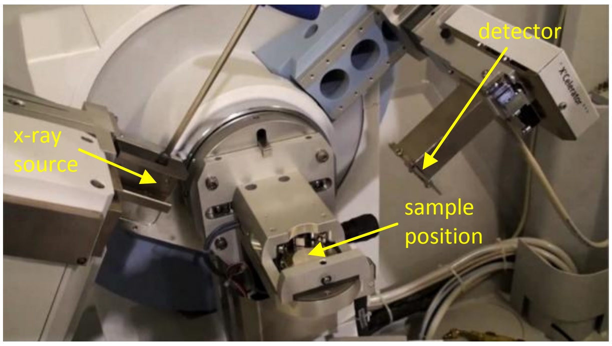

Fig. 3.10 - Panalytical X'Pert Pro diffractometer, with the position of the main elements.

The crystalline powder is inserted in a small disc, placed at the centre of a goniometer and progressively tilted of an angle θ starting from the direction parallel to the rays direction. Simultaneously, the detector rotates of an angle 2θ and collects the reflections of those particles oriented with a crystallographic plane parallel to the sample holder face. The product of the measurement is a diffractogram with the number of counts as a function of the angle 2θ. In the acquisitions, the angle 2θ was varied between 4° and 80°, with a step of 0.016° and time per step of 450 s. The beam of X-rays used as source radiation is produced by the bombarding of a metallic target with electrons derived from a current flowing through a white-hot tungsten filament and directed by a high potential difference of the order of tens of kV against the target. Actually, the radiation obtained with this bombarding is constituted by a deceleration radiation, produced by the deceleration of a charged particle deflected by another charged particle (e.g., an electron and an atomic nucleus), and by characteristic X-rays with specific wavelengths and intensity that depend on the target material (copper, molybdenum, cobalt, iron, or chromium). Commonly, $K_{\alpha1}$, $K_{\alpha2}$ and K_{β} are recognized among the characteristic wavelengths. Practically, $K_{\alpha1}$ and $K_{\alpha2}$ are sufficiently close in wavelength so that both of them can be used as incidence source. The Panalytical X'Pert Pro diffractometer is equipped with a monochromator that allows high resolution measurements with the $K_{\alpha1}$ only.

Two diffractograms were produced for each sample, one on the mud fraction (d < 0.063 mm; Fig. 3.11a) and one on the clay fraction (d < 0.002 mm). For the preparation of the latter a suspension was obtained by stirring the mud fraction in distilled water and by pipetting the upper solution after about 15 minutes. According to Stoke's law, it was expected that this solution contained only clay particles. The solution was then placed on a glass slide for the drying at room temperature and then analysed in the diffractometer.

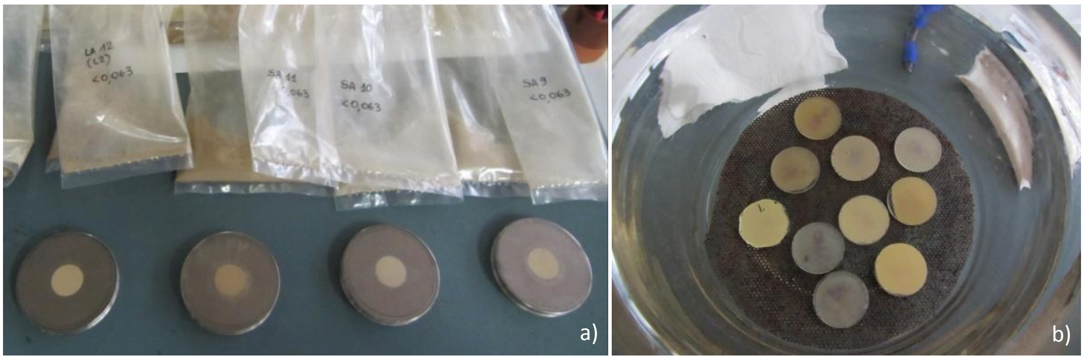

Fig. 3.11 - Samples ready to be analyzed with the X-ray powder diffractometer (a); samples exposed to ethylene glycol vapour (b).

Furthermore, a glycol treatment was applied on these samples after the first set of measurements, in order to identify the presence of smectites (e.g., montmorillonite and beidellite). The treatment consisted in the exposition of the slides to the vapour of ethylene glycol (Fig. 3.11b), in order to make the swelling clay minerals expanding and producing a shift of the 001 reflections from the range between 12 Å and 15 Å to about 17 Å.

In each diffractogram, the position of the peaks is characteristic of the mineralogical phases and their identification is obtained for comparison with standard diffractograms. The intensity of the reflections depends on the amount of the phase in the powder, but also on the quality of the statistical orientation of the crystallographic directions, which can be worse in presence of easily orientable plate minerals.

3.2.3 Emission spectrometer

A microwave plasma-atomic emission spectrometer (Agilent 4100 MP-AES) was available at the X-Ray Fluorescence Spectroscopy Laboratory of the Department of Earth Science (Università degli Studi di Milano) for quantitative chemical analysis of major, minor and traces elements in fluids, rocks, soils, and plants. For the aim of the work, the instrument was used for the analysis of some selected solutions used to saturate the samples or extracted from the samples after the SIP tests. The MP-AES operates with a magnetically-excited nitrogen plasma (quartz torch) generated using microwave technology (Fig. 3.12). The gas for the plasma is obtained from an Agilent 4107 Nitrogen Generator, which uses pressure swing absorption technology to produce 25 L/min nitrogen (>99.5% purity) from compressed air (input flow 115 L/min at 620 kPa). This high energy (approximately 5000 K) produces the dissociation of the sample in atoms and their excitation. The relaxation from the excited state to the ground state is accompanied by an emission, with a wavelength characteristic of the element and an intensity proportional to its amount, that is detected by a monochromator (wavelength range from 178 nm to 780 nm). Detection limits in a water sample are between 0.05 ppb and 0.65 ppb for the major elements. The investigated elements were Na, K, Ca, Mg, Mn, and Fe.

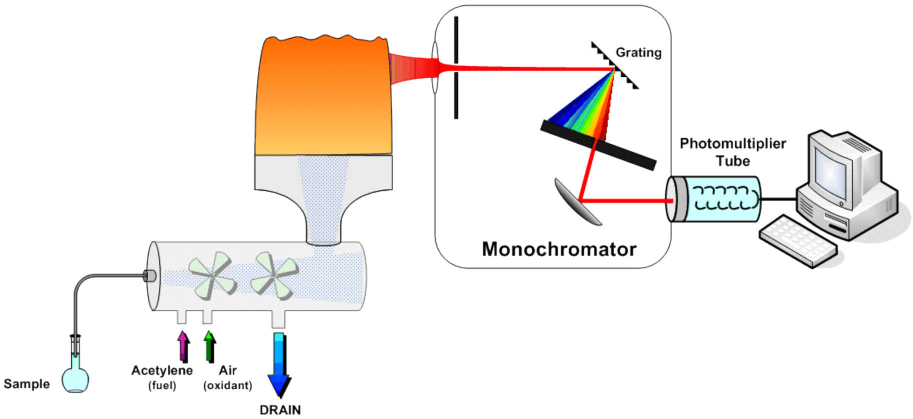

Fig. 3.12 - Schematic representation of an atomic emission spectrometer (from http://faculty.sdmiramar.edu/ fgarces/labmatters/ instruments/aa/aa.htm).

3.3 Samples characterization

The results of the characterization of the investigated samples are summarized in this section. The investigated materials are classified into two categories: the first includes the materials directly collected in the field (section 3.3.1), whereas the second consists of materials specifically prepared and mixed for the work starting from pure components (section 3.3.2). In the following the two categories are denoted as “natural samples” and “artificial samples”, even if both classes of samples are actually made of non-synthetic constituents. Finally, section 3.3.3 is devoted to the description of the water solutions used to saturate the samples.

3.3.1 Natural samples

Natural samples show a textural variability ranging from gravelly sands to slightly-sandy muds. The upper limit is constrained by the dimension of the sample holder for SIP measurement, the lower limit by the occurrence of such fine-grained sediments in the investigated sites. The ternary diagram of Fig. 3.13 summarizes the textural composition of these samples.

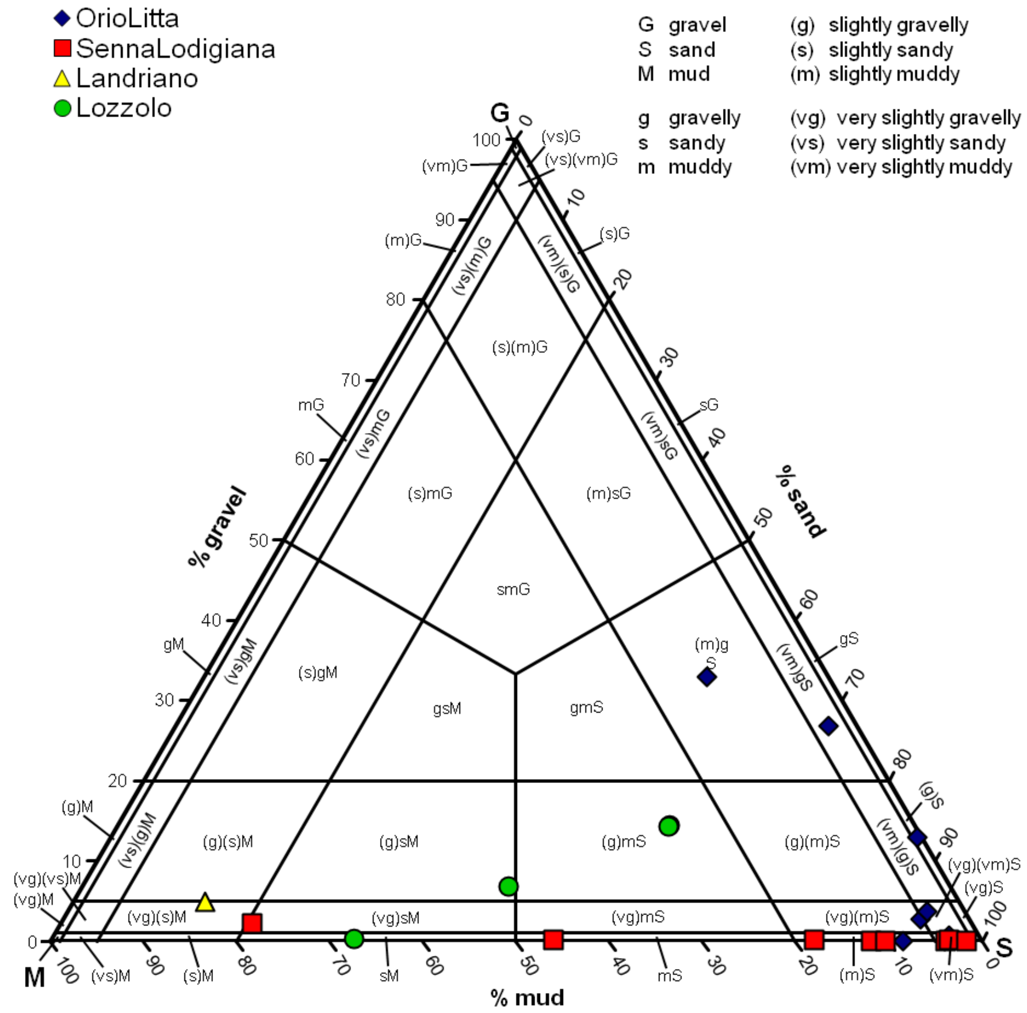

Fig. 3.13 - GSM triangle for the textural classification of samples according to *Blott and Pye* (2012).

The organic matter content of the samples varied between 0% and 0.4%. Similar values were expected also for non-analysed samples, due to their comparable colour and similar response observed during the oxidation phase prior to the grain-size analysis (see section 3.2.1).

All the samples analysed with the X-ray powder diffraction technique showed the presence of quartz and plagioclase, sometimes associated to calcite and dolomite. Within the phillosilicates, different associations of kaolinite, chlorite, muscovite, serpentine, vermiculite, and mixed layer minerals were identified. Amphiboles were also recognized in a few samples. Variations between the two textural classes of the same sample concerned most the relative amount of mineralogical phases, rather than their occurrence.

The cumulative grain-size-distribution of each sample and the diffractograms of the mud and clay fraction with the list of the identified mineralogical phases are provided in Appendix A. The value of G, S, and M percentage, characteristic diameters, uniformity coefficients, coarse-to-fine ratios, and organic matter content are provided in Appendix C.

3.3.2 Well-sorted sands and sand-clay mixtures

Artificial samples were prepared to perform some preliminary SIP tests on reference materials and check the consistency of data. They were produced by sorting sands into limited grain-size classes (well-sorted sands, named TR1 to TR4) and by mixing these sands with clay (sand-clay mixtures, named M50, M5, and M05). The sandy material derived from fluvial silicate sands for concrete production (Gras Calce S.p.a.), washed through the 0.063 mm sieve. Clay fraction consisted mostly of clay and silt particles with a mineralogical composition obtained by mixing 50% of Remblend PL10 Kaolin, 40% of Ukrainian clays (UA50 and DBM2 in equal quantities), and 10% of illite (Fig. 3.14a). X-ray powder diffraction analysis confirmed that the mixture was composed of kaolinite, illite and quartz (Fig. 3.14b and Tab. 3.1).

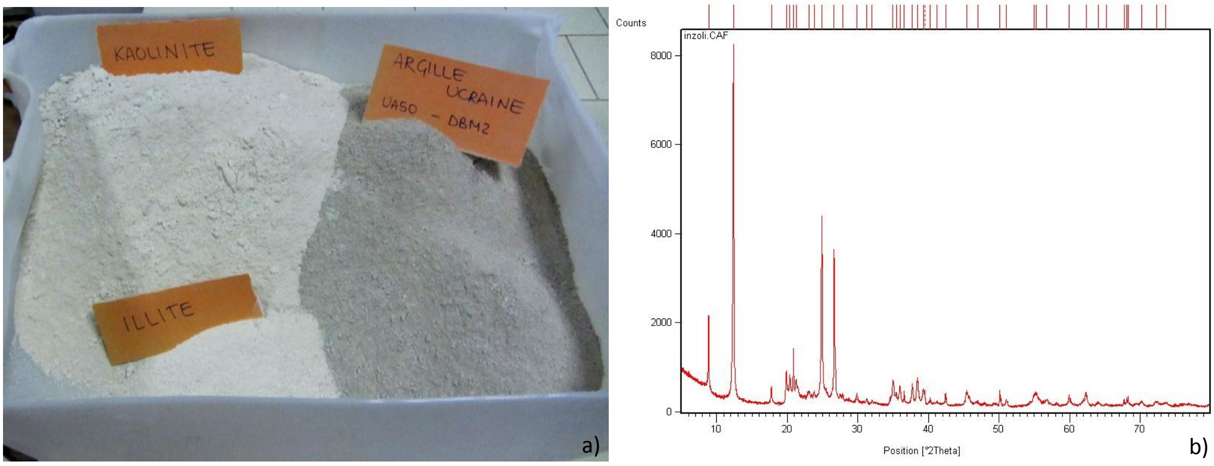

Fig. 3.14 - Clay mixtures used for the composition of artificial sand-clay samples (a) and corresponding diffractogram (b).

	Remblend PL10 Kaolin [%]	Ukrainian clays UA50 [%]	DBM2	Illite A [%]
SiO_2	48.80	57.50	56.10	54.50
Al_2O_3	37.00	28.50	28.90	27.60
Fe_2O_3	0.80	1.01	1.45	0.45
TiO_2	0.05	1.47	1.47	0.07
CaO	0.06	0.38	0.31	0.14
MgO	0.30	0.55	0.62	2.46
Na_2O	0.10	0.34	0.47	0.01
K_2O	1.90	2.25	2.91	7.42
loss on ignition	11.90	8.03	7.59	7.25
	100.11	100.03	99.81	99.90

Tab. 3.1 - Oxides weight percentage for the clays used in the sample preparation. Data of Remblend PL10 Kaolin are available on the technical sheets of the material, whereas data of Ukrainian clays and Illite A were provided by RM Ricerche Minerarie.

Finally, in addition to the mixtures, also three other pairs of samples were prepared, with about 2% of clay or hematite in a centimetric layer arranged in two configurations: in a single layer located in the middle of the sample holder between silicate medium sand, and dispersed within the silicate sand between the potential electrodes. These samples were referred to as KL_L and KL_D for kaolinite in a single layer and dispersed, respectively; analogously IL_L and IL_D for illite, and HE_L and HE_D for hematite.

3.3.3 Water solutions

The saturation solutions for the samples were obtained mainly through dissolution of NaCl into deionised water. Actually, the parameter to distinguish the different concentration of salt was the electrical resistivity due to the ease of measurement as compared to the salt concentration. The nine solutions were named from w1 to w9 in descending order of electrical resistivity (Tab. 3.2). These values are not indicative of the actual resistivity value of the water at the equilibrium condition between the solid and the fluid phases during SIP tests, but allow to compare the electrical behaviour of samples under the same initial conditions. Some initial tests on sand-clay mixtures were performed also with $CaCl_2$ solutions. In this case, initials of Tab. 3.2 were used with the addition of a letter C.

code	w1 (C)	w2	w3 (C)	w4 (C)	w5 (C)	w6	w7	w8	w9
$\rho_{w(i)}$ [Ωm]	446±39	291±24	202±2	96±13	43±2	21±2	9±2	2	0.9
N	9	29	6	19	19	9	8	3	2

Tab. 3.2 - Electrical resistivity of the water solutions used to saturate the samples and corresponding identification codes. N stands for the number of samples analysed with the corresponding water. Underlined codes refer to the waters used with natural samples.

Single-salt solutions are not strictly representative of natural freshwaters, especially for the evaluation of cation dissolution, adsorption, exchange and thus length of the EDL for a specific salt type and concentration (see equation 2.3). However, for the aim of this work, microscopic investigations of the electrochemical processes in the pores and at the grain-water interfaces were avoided in favours of a volumetric averaged approach at the scale of the sample's REV. Thus, simple cations (Na^+ or Ca^{2+}) were chosen and only bulk electrical resistivity was considered to relate the bulk electrical behaviour to the electrical properties of the solution. A comparison of the electrical measurements of samples saturated with both type of solutions is addressed in section 6.1. The chemical composition of the solutions from w1 to w5 was proved to be monocationic with the emission spectrometry analysis described in section 3.2.3. On the other hand, the analysis performed on the water extracted from the samples at the end of the electrical tests revealed a general decrease of electrical resistivity due to the presence of other major cations in different proportions (Appendix B).

Under the hypothesis of full saturation, the water content was adopted as an estimate of the porosity of the samples after the packing into the sample holder. The water content was calculated as the ratio between the volume of water and the total volume of the sample holder, where the volume of water was the difference between the weight of the saturated sample and the weight of the solid phase, considering water density equal to one. On the average, the porosity of the natural samples was 0.40±0.06, within a variation range from 0.26 to 0.63. Values between 0.26 and 0.48 are coherent with the theoretical porosity of a material made of equigranular spherical particles arranged in a structure changing from rhombohedral to cubic. Higher values are indicative of the lacking of a complete grain-sustained structure and the occurrence of a suspension, and are effectively associated to samples with a significant amount of mud, whereas lower values can be associated to non-sorted material with pores filled with smaller and smaller particles. Porosity values related to each sample prepared for SIP measurements are reported in Appendix B, together with the electrical resistivity values of the saturation solution before ($\rho_{w(i)}$) and after ($\rho_{w(f)}$) the interaction with the solid phase.

Chapter 4

Experimental system

4.1 Reference instruments

SIP measurements can be executed both in the laboratory and in the field (surface or borehole techniques). In the following sections, a reference experimental system is described for each category, together with a description of the main issues that have to be considered for accurate results at the corresponding length scale.

4.1.1 Laboratory measurements

Kemna et al. (2012) recommend the adoption of established and standardized procedures for sample preparation, and a detailed tabulation of the physical and chemical characteristics of the sample and of the technical specifications of the experimental apparatus, to support researchers' efforts at comparing results or repeating measurements, improving understanding of the factors that control conductive and polarization behaviour, and validating models. The main considerations regard:

- number and type of electrodes;
- dimension of the sample holder;
- input signal;
- cables and electronic components;
- validation and correction procedures;
- sample packing and saturation.

A sample holder equipped with four electrodes is required for $f < 1$ kHz. In fact, the separation of current and potential electrodes allows avoiding large electrode polarization effects that are unavoidable in measurements with two electrodes (*Dahlin*, 2000). On the opposite, two electrodes are preferable at higher frequency in order to reduce electromagnetic coupling between different parts of the system (*Volkmann and Klitzsch*, 2015). The impedance between current electrodes is almost independent from electrode material above 10 Hz, whereas a phase shift is measured below 10 Hz. The shift is higher passing from porous bronze to copper and to stainless steel plate electrodes (*Zimmermann et al.*, 2008b). More important is the polarization at potential electrodes. The removal of metal electrodes from the current path inside the sample avoids spurious phase effects of about 10 mrad. Porous ceramic electrodes can further reduce polarization effects but produce a high frequency error due to the high contact impedance (*Zimmermann et al.*, 2008b). Other authors used non-polarisable electrodes, such as Cu-$CuSO_4$ (*Gomaa and Alikaj*, 2010) or Pb-PbCl (*Dahlin et al.*, 2002). Point electrodes can record a bias in the potential difference in case of heterogeneous samples, due to a non-uniform electrical field. On the other hand, extended electrodes, such as rings, can be affected by a potential gradient that constitutes a source of noise (*Kemna et al.*, 2012).

The greater the distance between current and potential electrodes, the lower the phase error, especially if an inhomogeneous contact between current electrode and sample creates a potential difference along the electrode surface. *Zimmermann et al.* (2008b) suggest a distance at least twice the sample width in order to achieve a phase accuracy of 0.1 mrad.

For the input signal, high voltage should be preferred to improve the signal-to-noise ratio. However, current density should be low enough to avoid non-linear effects (*Zimmermann et al.*, 2008 did not report them up to 2 A/m^2). Finally, an oscillation frequency equal to the domestic distribution of the alternate current (50 Hz or 60 Hz, according to the country) has to be avoided due to the high noise.

Short coaxial or triaxial cables with the outer shield connected to ground potential are favoured to reduce cross-talk and parasitic leakage currents. Furthermore all channels should be constructed in an identical way to minimize gain differences (*Zimmermann et al.*, 2008b). The resolution of the analog-to-digital converter card affects the resolution of the measured potential, when considered together with the amplitude of the input signal.

Test measurements on simple circuits with known elements and reference material with known electrical parameters (e.g., solutions with different electrical resistivity or permittivity) are essential to validate the experimental apparatus and to estimate the accuracy, especially for the phase (*Zimmermann et al.*, 2008b; *Ustra et al.*, 2012).

Finally, particular care should be taken for the analysis of repacked unconsolidated materials. *Kemna et al.* (2012) and *Bairlein et al.* (2014) showed that the packing method has a strong influence on the measured phase spectrum. In particular, *Bairlein et al.* (2014), compared the response of a sand and two muds prepared according to four different procedures of filling. They recognized a large data reproducibility for the sand, with only minor effects related to the packing, whereas major changes affected the muddy samples considering both different filling methods and also the measurement reproducibility using the same packing method. As a consequence, the packing has to be precisely described among the properties of the experimental setup, because it affects the pore space geometry and structure, which cannot be easily controlled.

Among the recommendations provided by *Kemna et al.* (2012), several derive from the validation of the impedance spectrometer ZEL-SIP04-V02 of *Zimmermann et al.* (2008b) that is therefore presented here as the reference instrumental apparatus for complex electrical resistivity measurements in laboratory (Fig. 4.1). In addition, this system was used for a set of SIP measurements performed at the SIP Laboratory of the Agrosphäre Institut of Forschungszentrum Jülich GmbH. The system includes a function generator Agilent 33120A, an amplifier unit with four operational amplifiers JFET OP AD825 with input resistance of 500 GΩ and input capacitance of 6 pF, a shunt resistor (10 Ω, 100 Ω or 1kΩ), a cylindrical (or parallelepiped) sample holder 36 cm high and 6 cm in diameter, and an analog-to-digital converter card NI4472 with four channels, 24-bit resolution, and digital anti-aliasing filters (Fig. 4.1a).

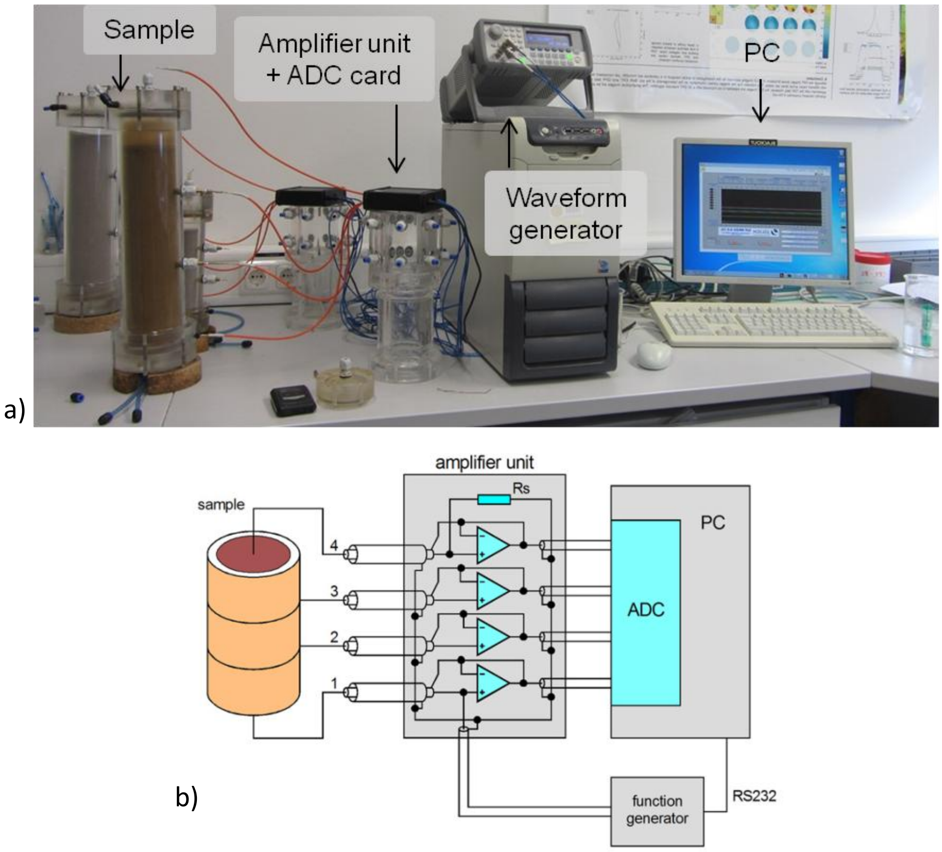

Fig. 4.1 – Picture (a) and schematic representation (b) of the measurement system ZEL-SIP04-V02 (*Zimmermann et al.*, 2008b). Electrodes 1 and 4 are for current injection and electrodes 2 and 3 for potential measurement. $\mathrm{R_s}$ is the shunt resistor and ADC the analog-to-digital converter card.

Generator and ADC card are controlled by LabVIEW (National Instruments, Austin, TX, USA). The acquisition protocol consists in current injection through sinusoidal excitation voltage with peak-to-peak amplitude of 10 V and a set of stable frequency in the range from 1 mHz to 45 kHz. For each input signal three cycles are used for the calculation of the mean and standard deviation. Voltage-time series are imported in MATLAB® (Mathworks, Natick, MA, USA), where the time drift is removed and the Fourier transform is computed. According to the electrical model of Fig. 4.1b, the Fourier transformed current flowing in the sample region between the two potential electrodes (i.e., electrodes 2 and 3) is calculated as

$$\mathrm{I_x = I_s + I_3 + I_4 = \frac{U_4}{R_s} + \frac{U_3}{Z_v} + \frac{U_4}{Z_v}}, \tag{4.1}$$

where $\mathrm{I_s}$ is the Fourier transformed current flowing through the shunt resistor, $\mathrm{I_3}$ and $\mathrm{I_4}$ are the Fourier transformed leakage currents at electrodes 3 and 4, $\mathrm{U_3}$ and $\mathrm{U_4}$ the

Fourier transformed voltage at electrodes 3 and 4, and Z_v the input impedance of the amplifiers. The Fourier transformed potential difference between the two potential electrodes is calculated as

$$U_x = U_2\left(1 + \frac{Z_{e2}}{Z_v}\right) - U_3\left(1 + \frac{Z_{e3}}{Z_v}\right), \tag{4.2}$$

where U_2 and U_3 are the Fourier transformed potentials measured at the potential electrodes, and Z_{e2} and Z_{e3} the contact impedances at the corresponding electrodes. If $Z_v \gg Z_e$, U_x can be effectively approximated by the difference $U_2 - U_3$. However, at high frequency this condition is often not fulfilled. Thus, for the estimation of the contact impedances, a so-called reciprocal measurement was proposed by *Huisman et al.* (2015).

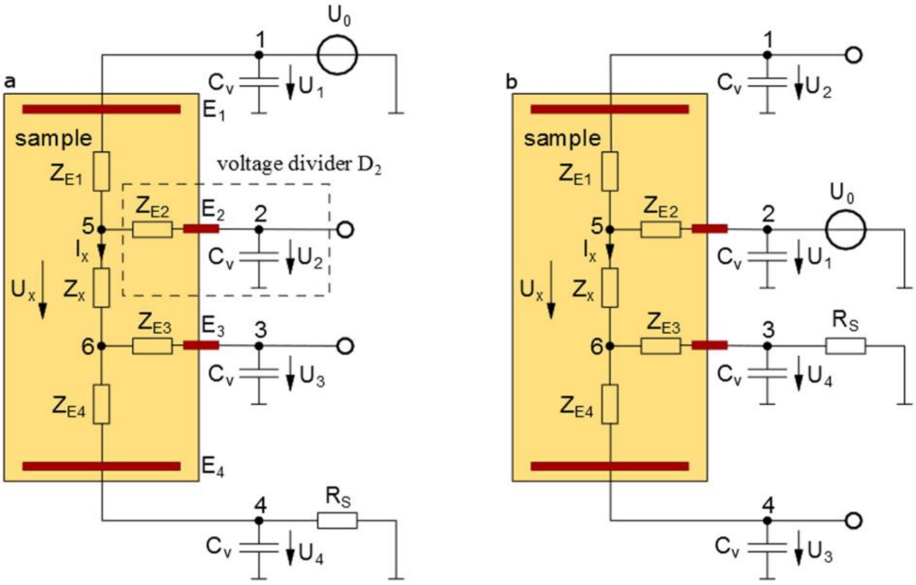

Fig. 4.2 - Simplified representation of the sample and the measurement system in the normal configuration (a) and in the reciprocal configuration (b). C_v is the capacitance of the amplifier (*Huisman et al.*, 2015).

In the reciprocal measurements the current and the potential electrodes are switched (Fig. 4.2) and a current injection with low intensity is used to avoid non-linear effects. Z_{e2} is determined as the ratio between the difference of potential at node 2 and potential at node 5, and the current. Potential at node 5 is assumed to be equal to the potential at node 1, due to relatively low electrode impedance as compared to the high input impedance of the amplifiers. Z_{e3} is calculated in an analogous manner from potential at nodes 6 and 4. The dependence of electrode impedance on frequency is neglected and the mean value between 1 kHz and 2 kHz is used for the correction in the whole range. This correction produces a considerable improvement at frequencies above 100 Hz, with a decrease of the phase error to less than 0.1 mrad that is comparable with the error at lower frequency. Finally, the impedance of the sample is calculated as the ratio

$$Z_x = \frac{U_x}{I_x}, \tag{4.3}$$

and the complex resistivity is derived in accordance to equation (2.3) where the ohmic resistance is substituted by the electrical impedance.

A similar measurement system has been implemented to determine complex resistivity distribution in soils and sediments (*Zimmermann et al.*, 2008a). This imaging technique is usually called electrical impedance tomography (EIT) and joins spectral induced polarization and electrical resistivity ground imaging techniques. The system proposed by *Zimmermann et al.* (2008a) is similar to the one described above, equipped with 32 channels for current injection and up to 96 channels for potential measurement that can be arranged on a variety of sample holders (Fig. 4.3). Amplifiers are mounted near the electrodes (1 cm) in order to minimize the capacitive load. A successive instrument was equipped with 40 electrodes modules with integrated amplifiers for electric potential measurements and switches for current injection, in order to make them suitable for reciprocal measurements (*Zimmermann et al.*, 2010). Voltages are measured with respect to the ground potential of the system and are collected simultaneously at all electrodes excluding those used for the current injection. In this way, the potential differences can be numerically calculated between any pair of electrodes without *a priori* specification. Similarly to the SIP instrument, current errors are corrected on the base of a simplified electric circuit model of the sample and the measurement system. The accuracy on the phase estimation is about 1 mrad in the frequency range from 1 mHz to 1 kHz.

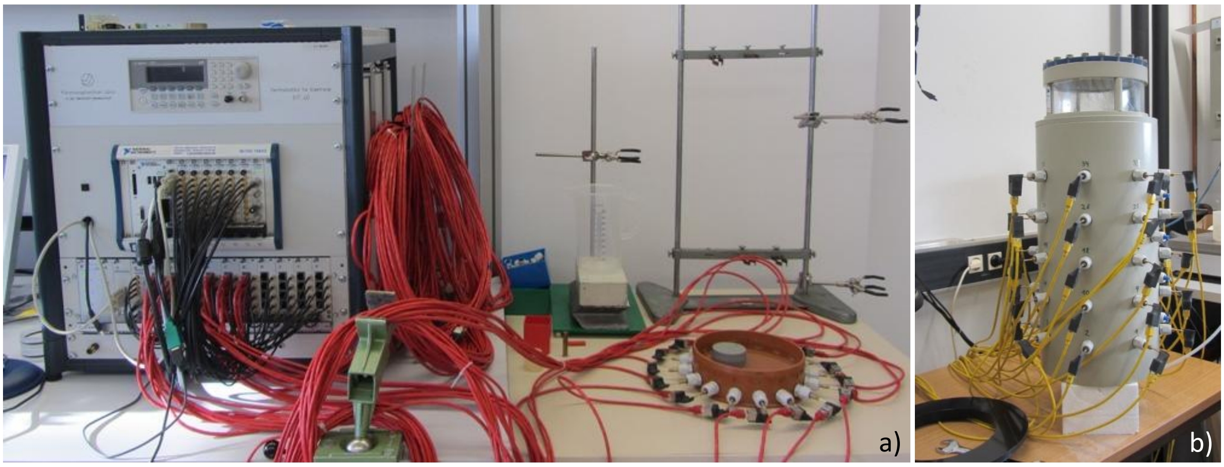

Fig. 4.3 - Pictures of laboratory EIT systems, with electrodes located all around a cylindrical sample holder at a single height (a) and at different heights (b).

Besides systematic errors that are related to electromagnetic coupling, especially for frequency above 10 Hz, random data error due to environmental noises and fluctuations in the contact between the electrodes and the investigated materials or in the current pathway, is especially critical for the phase angle both in SIP and EIT surveys. A first approach to estimate data error consists in using the deviation of the experimental data from theoretical data as representative of the instrumental accuracy and of the random errors (*Zimmermann et al.*, 2008b; *Ustra et al.*, 2012). This kind of calibration is possible on water solutions, whose theoretical phase response can be calculated as

$$\tan \phi = -\frac{2\pi f \varepsilon}{\sigma_w}, \tag{4.4}$$

where ε is calculated with a relative permittivity equal to 80.1, and the minus sign follows the convention that capacitive effects are negative and inductive effects are positive. Alternatively, an estimation of data error can be done through the standard deviation calculated on at least three repeated measurements in a short time interval or through reciprocal measurements, as suggested by *Slater and Binley* (2003). Finally, another approach is based on the formulation of a phase error model. *Flores Orozco et al.* (2012) proposed, for example, an inverse power-law relationship between the phase error and the corresponding resistance and a methodology to compute the parameters of the error model. This technique is referred to as bin analysis since it consists in the partitioning of normal-reciprocal phase discrepancy into several bins with respect to the resistance values. The assumed error model is then fitted to the standard deviation calculated for each bin.

4.1.2 Field measurements

Field SIP measurements can be subdivided into two categories: surface and borehole measurements. The first are the up-scaled version of laboratory EIT methods and most of the observation reported in the previous section directly apply also for this case, whereas borehole techniques require the consideration of some additional issues. *Kemna et al.* (2012) identified the most critical aspects of an appropriate acquisition protocol of field EIT in the execution of normal-reciprocal measurements for data error estimation, the minimization of electrode polarization effects by means of avoiding current injection prior the potential reading at one electrode or using non-polarisable electrodes, and the definition of standardized elaboration procedures such as the identification of outliers to be removed prior the inversion and the implementation of an error model.

In surface EIT measurements (Fig. 4.4) care should also be placed in the layout of cables. A radial symmetric distribution of straight cables from the measurement system to the electrodes helps in the calculation of electromagnetic inductive coupling and in the following correction. Furthermore, a similar degree of contact between each cable and the ground ensures a similar effect of capacitive coupling for all measurement configurations and reduce its effect on phase determination.

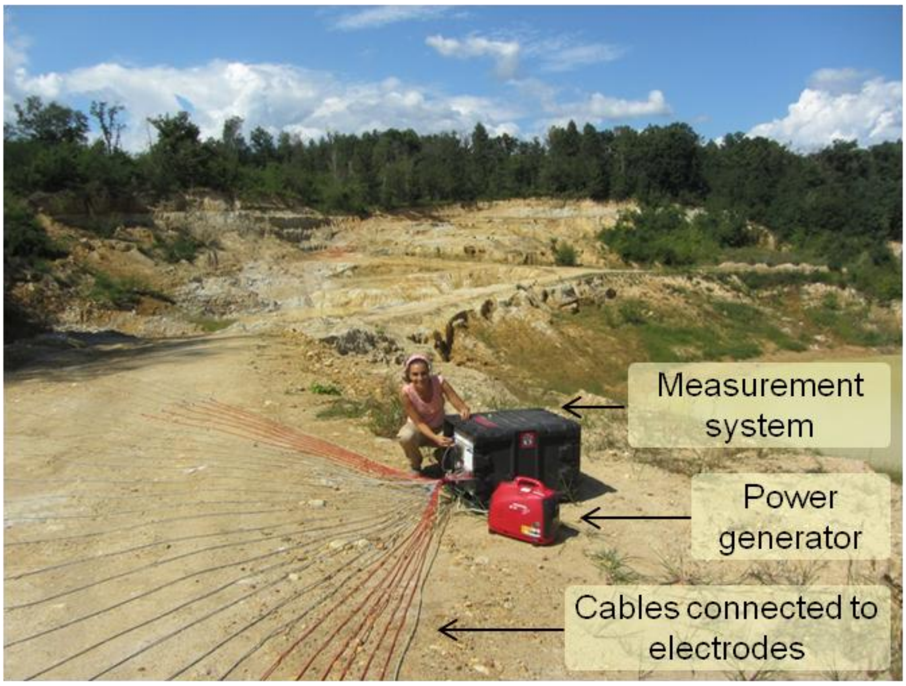

Fig. 4.4 - Example of measurement system and cable layout for field EIT acquisition.

Zhao et al. (2013) extended the acquisition system of *Zimmermann et al.* (2008a) with logging tools and electrode chains for near-surface borehole measurements. The borehole logging tool is equipped with four electrodes at a distance of about 16 cm, located at the end of a cable 25 m long (Fig. 4.5a), whereas the electrode chain is equipped with eight electrodes at a distance of 100 cm and a maximum length of the cable of 25 m (Fig. 4.5b). In both cases the brass electrodes are ring-shaped, with a diameter of 42 mm and a height of 10 mm. The electrode modules include also amplifiers for the potential measurement and switches for current injection. As in the surface EIT system, potential is measured against the ground reference potential of the cable shield.

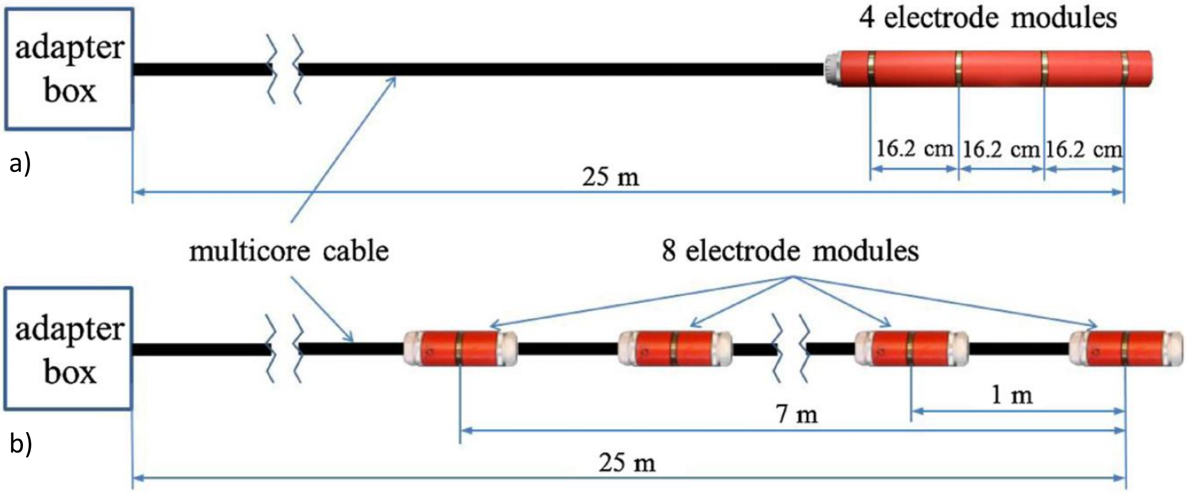

Fig. 4.5 – Schematic representation of the borehole logging tool (a) and of the borehole electrode chain (b) (*Zhao et al.*, 2013).

The additional problem associated with the borehole configuration is related to the multicore cable. In fact, the length and the proximity of current wires lead to a non-negligible inductive coupling. In addition, the length of the shielded cable make the outer and inner surfaces of the insulating material acting like a capacitor. Inductive coupling can be modelled and corrected if an accurate knowledge of the geometry of the wires is available and stable. This correction is under study also for cross-borehole acquisitions. Capacitive coupling depends on the conductivity distribution, which cannot be known a priori; however, *Zhao et al.* (2013) proposed an approximated correction based on a numerical integration. In controlled conditions a phase accuracy of 0.8 mrad was achieved at 10 kHz. However, environmental noises are less controlled than in laboratory conditions and can thus affect different portions of the spectral response. Similar inductive and capacitive correction can be applied also on surface EIT data, by considering the geometry of the cables lay-out.

Finally, the correct use of the borehole tools is subject to the presence of a water table to ensure a good contact between electrodes and drilling walls and the absence of metallic casing that badly affect SIP measurements.

4.2 Design and construction

In order to perform measurements of complex electrical resistivity at the Laboratory of Hydrogeophysics of the Department of Earth Sciences (Università degli Studi di Milano), an experimental system, called ST.sip13, was planned and assembled for saturated samples of unconsolidated sediments. On the basis of the impedance spectrometer of *Zimmermann et al.* (2008b) described in the previous section, the experimental apparatus ST.sip13 is composed of five main parts (Fig. 4.6):

- a waveform generator Agilent 33220A, substituted by a waveform generator Agilent 33511B from 16.06.2014[3];
- an USB oscilloscope PicoScope 4424 with four channels[4];
- a laptop computer, where two utility software are installed: the PicoScope 6 Software version 6.4.28.0 and the executable file PICO_GEOFIS developed by dr. T. Sanvito (Department of Physics, Università degli Studi di Milano);
- an amplifier unit;
- a sample holder.

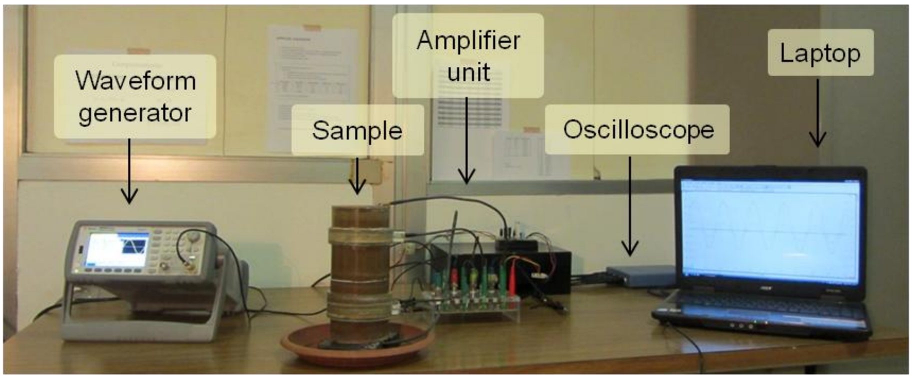

Fig. 4.6 - Components of the experimental system ST.sip13 for SIP measurements.

The electrical circuit of the amplifier unit was firstly designed and printed on a tracing paper and then transferred on a printed circuit board (PCB) through a photoengraving process. This consisted in the superposition of the circuit mask to a photosensitive PCB to shield those areas that have to remain conductive, the exposition to ultraviolet light, the washing of the PCB in a universal developer to remove the photoresist from unshielded areas, and the application of an acid solvent prepared with ferric chloride hexahydrate ($FeCl_3 \cdot 6H_2O$) and water to wash away the copper from the upper side of

---

[3] The technical specifications can be found at http://literature.cdn.keysight.com/litweb/pdf/5988-8544EN.pdf?id=187648 and http://literature.cdn.keysight.com/litweb/pdf/5991-0692EN.pdf?id=2202606, respectively (last access 06.2015).

[4] The technical specifications can be found at https://www.picotech.com/download/datasheets/PicoScope4000Series.pdf (last access 06.2015).

the board. Afterwards, the PCB was drilled to allow the welding of the electronic components, i.e., the female connectors pins for the function generator, the electrodes' cables from the sample holder to the operational amplifiers and from the amplifiers to the ADC, and the amplifiers with their associated capacitors. The amplifiers, as suggested by *Zimmermann et al.* (2008b) were the JFET OP AD825, characterized by high input resistance, with a supply voltage of ±12 V and a set of four capacitors to limit uncontrolled oscillations[5]. The input impedance of each amplifier was modelled as a parallel circuit with a resistor and a capacitor, whose values were obtained by the technical sheets. The shunt resistor of the amplifier unit was equal to 1 kΩ.

Seven sample holders were assembled as polycarbonate cylinders with an internal diameter of 8.6 cm, closed by two copper plates that work as current electrodes (Fig. 4.7). They were modified after the sample holder designed by *Mele et al.* (2014) for DC resistivity measurements. The distance between potential electrodes was 11.2 cm on the average, with maximum variations of 0.6 cm among different sample holders. The correct dimension was used for the resistivity calculation in each complex resistivity calculation.

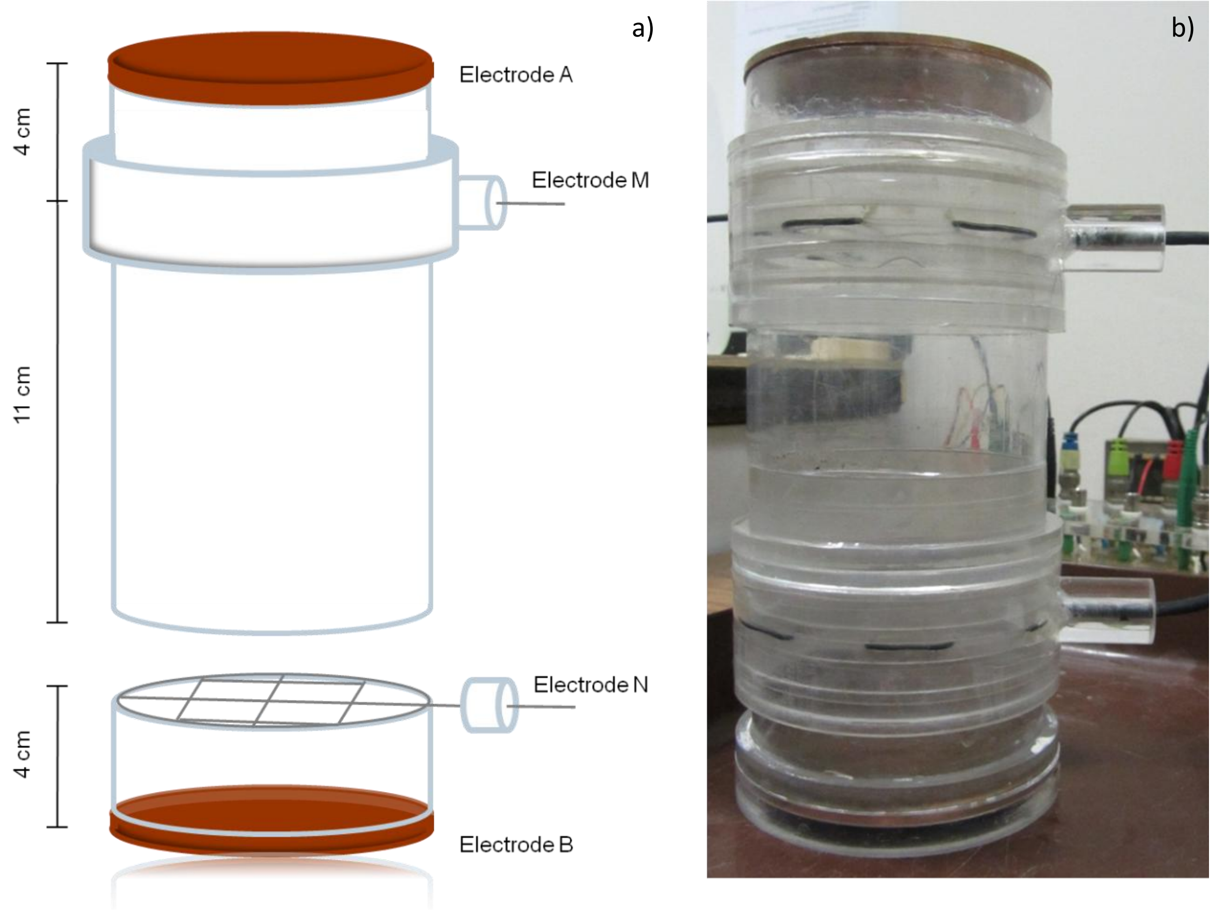

Fig. 4.7 – Schematic representation (a) and photograph (b) of a sample holder of the ST.sip13 system.

Potential electrodes were non polarisable. They were prepared by deposition of a solid thin layer of silver chloride (AgCl) on a grid-shaped silver wire with a red-ox reaction

---

[5] The complete technical specifications can be found at http://www.analog.com/media/en/technical-documentation/data-sheets/AD825.pdf (last access 06.2015).

supported by electrolysis. The two grids were simultaneously immersed in a tank containing a solution of HCl 0.1 M and connected to the positive pole of a battery, whereas a thin foil of Pt with a comparable surface area was connected to the negative pole (Fig. 4.8). The reactions involved were $H^+_{(aq)}+e^-_{(aq)}\leftrightarrow H_{2(g)}$ and $Ag^+_{(aq)}+Cl^-_{(aq)}\leftrightarrow AgCl_{(s)}+e^-_{(aq)}$. In order to produce a homogeneous layer, a density current of about 0.5 mA/cm^2 was required. For this reason a voltmeter measured the potential drop on a high precision resistor to calculate the current, and a variable resistor was used to keep constant the current density. The process lasted a few hours for each side of the grids and was executed in a dark environment since illumination quickly degrades AgCl. Ag-AgCl electrodes are commonly used as reference electrodes, since they are inexpensive, stable, non toxic, and AgCl has a low solubility. Their intrinsic potential only depends on the concentration of Cl^-, which can be considered constant in the whole sample.

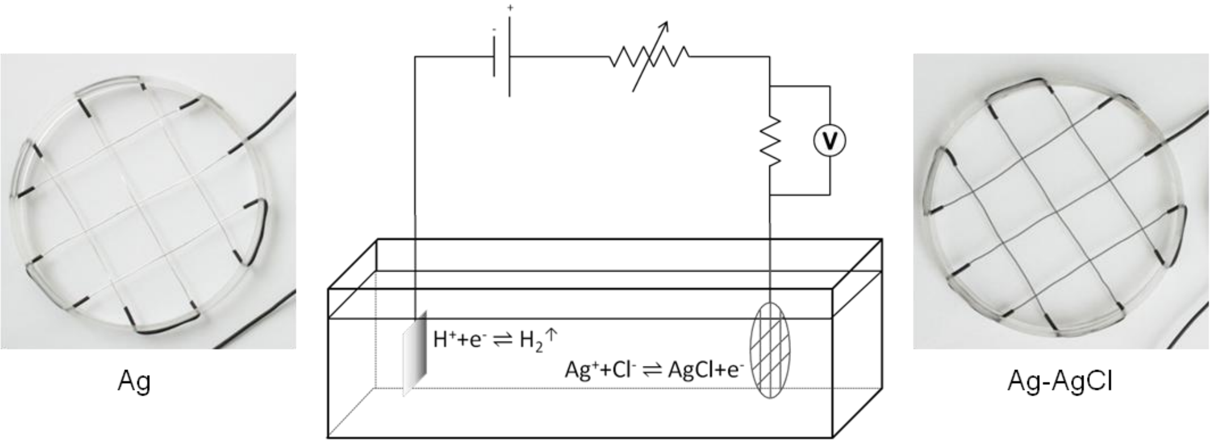

Fig. 4.8 - Schematic representation of the set-up for the chlorination of silver grids (for simplicity only one grid is drawn, whereas the real process is optimized for the chlorination of two grids symmetrically located on both sides of the platinum foil). On the left and right sides a grid is shown before and after the chlorination, respectively.

The grid favours large contact area between the electrode and the sample and thus a low contact impedance. This guarantees the fulfilment of the approximation $Z_e \gg Z_v$ also at high frequency, and the possibility to avoid the contact impedance correction in equation (4.2), as it was proven also by a set of reciprocal measurements. In addition, it provides an averaged response from the investigated volume without bias due to small-scale heterogeneities. The objection about the location of the potential electrodes inside the electric field (*Kemna et al.*, 2012) is not consistent in this case, because no metal surface is in direct contact with the electrolyte and electrode polarization does not take place. In addition, even a possible polarization is expected to be small if the sample is homogeneous and the electric field is plane and perpendicular to the grids. In this case, in fact, no potential gradient occurs across the grid. This results in no current flux in the grid and no polarization.

In order to evaluate the order of magnitude of the spurious phase signal in the case of non-homogeneous samples and/or non-homogeneous contact between current electrodes and sample, a test was conducted on a sample designed to increase the distortion of the electric field and to induce a potential gradient with a component parallel to the grid. This sample was constituted by quartz sand saturated with distilled water (σ_w=10 μS/cm) and contained a highly porous sponge in half of the upper third of the cylinder (Fig. 4.9). The comparison of the phase spectrum of the inhomogeneous sample with the corresponding homogeneous one, composed by sand only, showed differences of the order of 0.5 mrad between 10^{-1} Hz and 10^2 Hz.

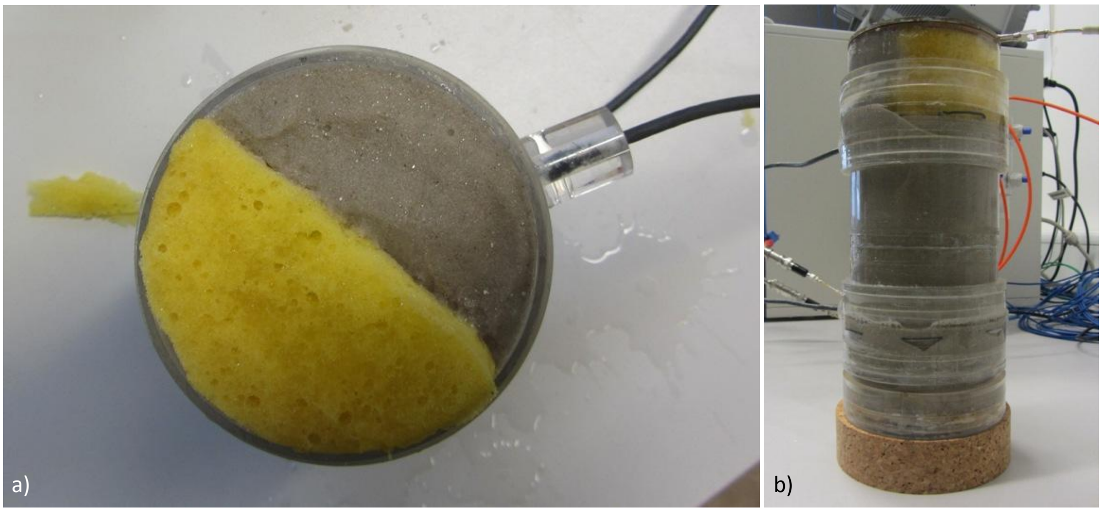

Fig. 4.9 - Inhomogeneous sample composed of sand and sponge, from top view (a) and lateral view (b).

The potential electrodes were endowed with insulated portions along borders to avoid the measurement of the perturbation produced by the sample holder wall on the electrical field. Other researchers proposed systems with guard electrodes to control similar problems (*Pettinelli et al.*, 2005).

Short triaxial cables connected the electrodes to the amplifier unit and coaxial cables connected the amplifier unit to the ADC. The outer shield was connected to the ground potential in both cases.

The above described technical specifications of the sample holder were defined after a series of tests aiming at analyzing the effects of different planning choices (e.g., the material and the distance between potential electrodes) on the phase accuracy, while amplitude is affected by these factors only to a negligible extent. Tests were performed on water solutions with known electrical resistivity and theoretical phase spectrum. Fig. 4.10 shows the main results obtained by changing the material of potential electrodes and their distance. Both metallic electrodes (copper and silver) and non-polarisable electrodes (Ag-AgCl) were tested. The formers greatly affected the phase signal introducing strong polarization effects along the whole frequency range in the case of copper and a limited electrode polarization signal of about 1 mrad at 0.1 Hz in the case of silver. Instead, non-polarisable electrodes satisfactorily matched the theoretical phase spectrum up to 1 kHz (Fig 4.10a). Above this frequency, a deviation towards positive phase values was observed independently from the kind of potential electrodes.

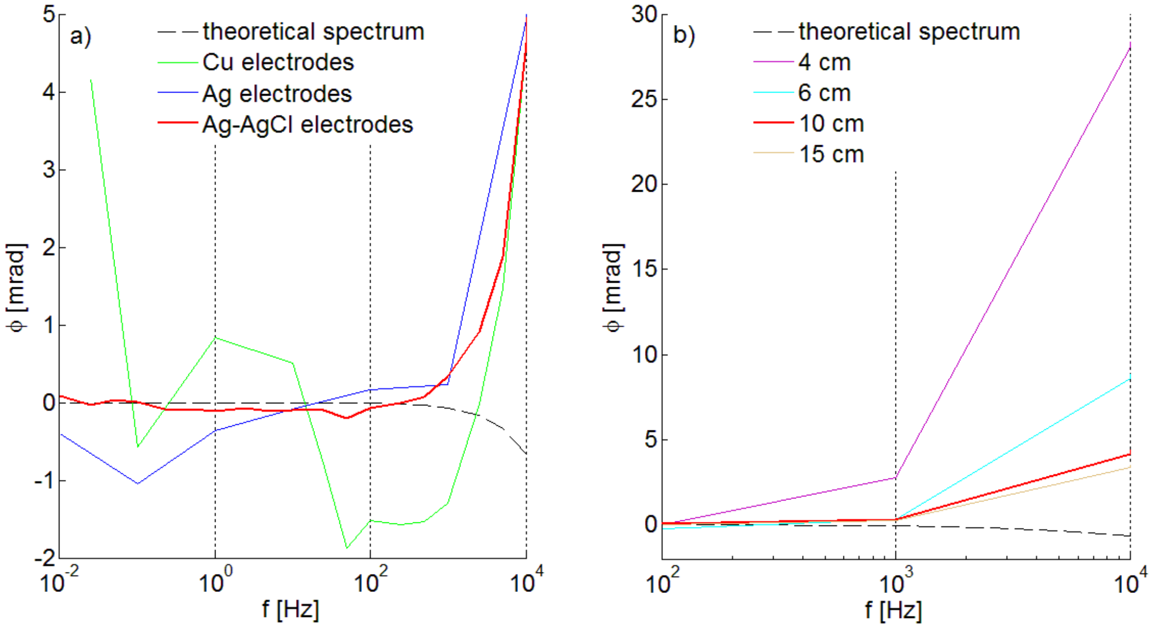

Fig. 4.10 - Experimental resistivity phase spectra of tap-water ($\rho_w = 15$ Ωm), obtained with different kinds of potential electrodes (a) and with different distances between potential electrodes for Ag-AgCl type (b).

An improvement on the phase accuracy at high-frequency was obtained by increasing the distance between potential electrodes (Fig 4.10b). However, a compromise between phase accuracy improvement and increase in sample volume was considered and supported the choice of an effective distance between potential electrodes of about 10 cm. In fact, moving from 10 cm to 15 cm implied an increase of about 290 cm^3 in the investigated sample's volume (i.e., 770 g considering quartz density) with a phase improvement of less than 1 mrad. Instead, a more effective capacitance correction was applied to reduce the high-frequency error and it is discussed later in section 4.4.

4.3 Acquisition protocol

Data acquisition was programmed through the code PICO_GEOFIS that provided a simple interface for the choice of input parameters, outdoing the PicoScope 6 software that is less flexible and less appropriate for the aim of the work. However, PicoScope 6 was used when a simultaneous visualisation of the voltage-time series at the electrodes was necessary to check the presence of the signal and the absence of weird noises. Input parameters included the voltage range, the rate of sampling, and the time interval between two successive acquisitions. The number of samples in each acquisition was fixed to 2000001. Data were saved in a specified output folder in binary format and consisted in the time sequence and the four voltage series corresponding to the four electrodes, together with date and absolute time of acquisition, and input parameters. Conversion from binary to text file could be done with the same code. Shape, frequency, and amplitude of the input signal were instead set up on the function generator. The input signal was constituted for each measurement by three separated chirp signals, whose characteristics are listed in Tab. 4.1.

chirp	**f_i [Hz]**	**f_f [Hz]**	**trend**	**D [s]**	**dt [s]**	**V_{pp} [V]**
1	10^5	10^2	linear	5	$2.5 \cdot 10^{-6}$	1
2	10^2	10^0	linear	50	$2.5 \cdot 10^{-5}$	1
3	10^0	10^{-2}	linear	500	$2.5 \cdot 10^{-4}$	1

Tab. 4.1 - Characteristics of the input signals: chirp number, initial and final frequency of the chirp (f_i and f_f), type of frequency modification, total duration of the signal (D), sampling rate (dt), and peak-to-peak voltage amplitude (V_{pp}).

The duration of the acquisition corresponded to the duration of the chirp, whereas the voltage range was doubled to allow correct registration of offsets. With a total range of 2 V and a 12-bit ADC, the voltage resolution was about 0.5 mV. A potential offset was measured especially at current electrodes. This is expected to be due to the Volta effect, i.e., the establishment of a small potential difference between two metallic conductors in contact at the same temperature (in this case electrodes, wires and connectors pins).

MATLAB® codes were developed for data processing and can be found in Appendix E. The first step consisted in a constant offset removal for each channel to have a zero average signal prior to the Fourier transformation and the calculation of the electrical impedance through the expression

$$Z = \frac{U_2 - U_3}{\frac{U_4}{R_s} + \frac{U_3}{Z_v} + \frac{U_4}{Z_v}}, \tag{4.5}$$

that corresponds to the ratio between equations (4.2) and (4.1) under the approximation $Z_v \gg Z_e$, multiplied by the geometric factor. Furthermore, a temperature correction was applied to refer all measurements to 20°C according to equation (2.6), and using a termic coefficient α equal to 0.025°C^{-1} (*Keller and Frischknecht*, 1966). The temperature of the sample was measured after each test inserting into the sample a digital thermometer Sunartis, with a resolution of 0.1°C, an accuracy of 1°C in the temperature range of interest, and a time response between 4 s and 10 s.

The subsequent processing step consisted in the filtering of anomalous points based on a manual insertion of a threshold value. This was defined on the basis of the graphical representation of the difference between resistivity phase at two successive frequencies, reported at zero average. Typical threshold values were 0.04 rad, 0.003 rad, and 0.004 rad, for the three chirps respectively. Anomalous points were substituted by the mean value of the two non-anomalous adjacent points. After this filtering the impedance vectors were joined and interpolated on a new frequency vector with logarithmically spaced points. The whole dataset was then smoothed with a mobile average with windows of 500 samples. Finally, impedance was converted into complex resistivity introducing the geometric dimension of the sample (see equation 2.3) and a sequence of points were selected to proceed with the data elaboration. The frequency series was chosen as comparable as possible with the acquisition sequence of the experimental system ZEL-SIP04-V02 (Appendix D).

Impedance measurements were performed repeatedly on the same sample at 24-hours intervals until an equilibrium resistivity amplitude spectrum was achieved, with a tolerance of about 5%. Resistivity variations with time were partly due to the compaction of the sample and the decrease in porosity but above all to the dissolution of ions in water. Usually, 48 hours were sufficient to reach the equilibrium condition for the analyzed samples. At the end of the SIP tests, electrical conductivity of the saturating water (for coarse sediments) and of the supernatant water (for fine sediments) was measured with an handheld conductivity meter Cond 330i (WTW GmbH) that is characterized by an accuracy of ±0.5% on electrical conductivity and ±0.1°C on temperature.

The packing of the material within the sample holder was executed through an alternate filling with water and solid phase and tapping on the side to favour the settling and the release of possible trapped air bubbles. This method corresponds approximately to the method 2 of *Bairlein et al.* (2014), partly modified with the simultaneous filling and tapping to limit the formation of macroscopic layers. The water level was always kept higher than the level of the solid material in the sample holder, but the presence of trapped air bubbles cannot be completely excluded. Nonetheless, saturation was considered complete in every measurement. The method 4 of *Bairlein et al.* (2014) was instead used for the set of measurements performed at Forschungszentrum Jülich GmbH. This method consisted in the pre-wetting of the solid phase with the solution used for the saturation and the subsequent pouring into the sample holder, already partly filled with fluid, while stirring with a spoon.

4.4 Validation and data error

Samples of tap water and deionised water with the addition of NaCl in variable concentrations were used to test the experimental apparatus and to estimate the accuracy in resistivity amplitude and phase at different investigation frequencies. This choice is due to the possibility of measuring the electrical conductivity and the temperature of liquid samples with a commercial handheld conductivity meter and to calculate the theoretical phase spectrum according to equation (4.4). In particular, eight waters were used, with electrical conductivity ranging between 11 µS/cm and 1570 µS/cm. An additional sample with $\sigma_w = 3780$ µS/cm was soon excluded from the dataset due to signal instability and huge errors in the whole frequency range. The comparison between measured and theoretical phase value is represented in Fig. 4.11b, whereas the amplitude is compared with the values measured with the conductivity meter (Fig. 4.11a) under DC conditions.

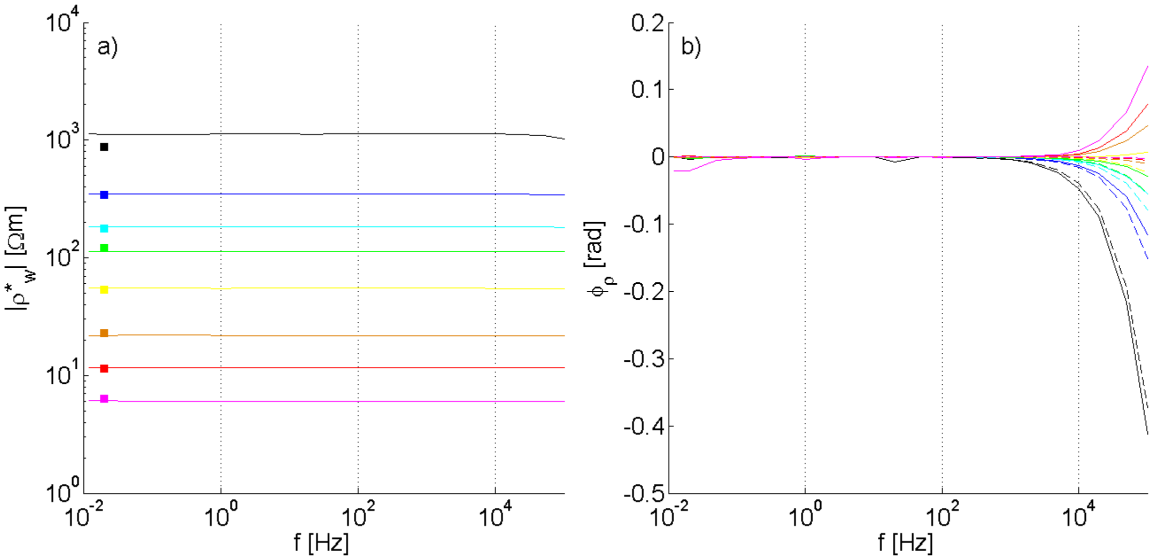

Fig. 4.11 - Resistivity amplitude (a) and phase (b) spectra of eight water samples. Squares are DC resistivity values measured with the handheld conductivity meter, solid lines are the experimental data obtained with the ST.sip13 system and dashed lines are the theoretical phase curves calculated with equation (4.4) on the basis of the DC resistivity values.

The average deviation of resistivity amplitude at low frequency from DC measurements was 4%, and the discrepancy increased up to 22% only for the most resistive water. The accuracy of the conductivity meter is declared as ±0.5%. Measured phase spectra exhibited a peculiar *fan-effect* for frequency higher than 1 kHz, whereas theoretical spectra tend to get closer to the x-axis for an increase in the water conductivity. Conductive waters showed even positive phase values that are not consistent neither with the physical process of orientational polarization of water molecules nor with electrode polarization. In order to determine if this effect was due to the sample holder or to the electrical circuit a simple test with the amplifier unit connected to a pure resistive element of 1 kΩ was performed (Fig. 4.12). Results of this test are represented in Fig. 4.13. It is apparent that the error on the amplitude is only 1%, but an extra phase is added to the signal especially for frequency beyond 1 kHz.

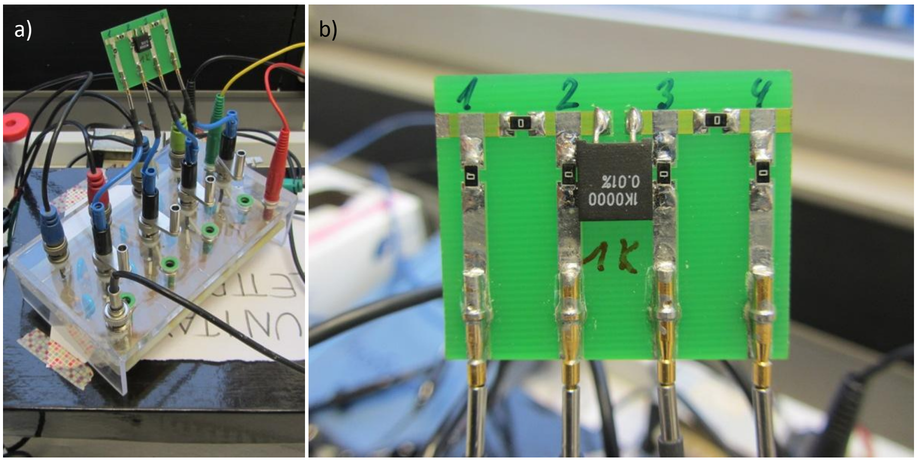

Fig. 4.12 - Amplifier unit of the ST.sip13 system connected to the calibration circuit (a) and detail of the latter (b).

This phenomenon can be corrected by considering an additional capacitance to the input capacitance provided by the technical specification of the amplifiers, which accounts for the cable and the connector pins' capacitances. In particular, a value of 20 pF instead of 6 pF allowed reducing the phase error to less than 1 mrad up to 10 kHz (Fig. 4.13b). This correction did not generate any significant change in the amplitude spectrum (Fig. 4.13a).

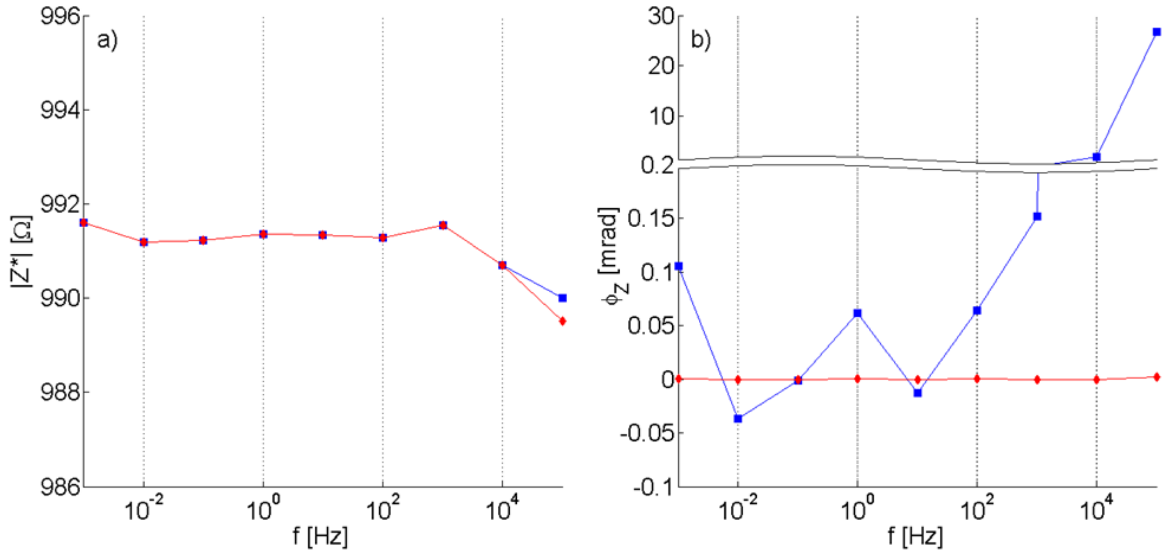

Fig. 4.13 - Impedance amplitude (a) and phase (b) spectra of the simple circuit made of a pure resistor ($R = 1$ kΩ). Blue lines are the experimental data obtained by modelling the amplifier unit capacitance only with the input capacitance of the amplifiers (6 pF), whereas red lines are the curves obtained with a total capacitance of 20 pF.

According to this correction also spectral data of water samples were improved. The *fan-effect* was still observable in the phase spectra, but its extension was reduced and so did the deviation of the experimental curves with respect to the theoretical ones (Fig. 4.14).

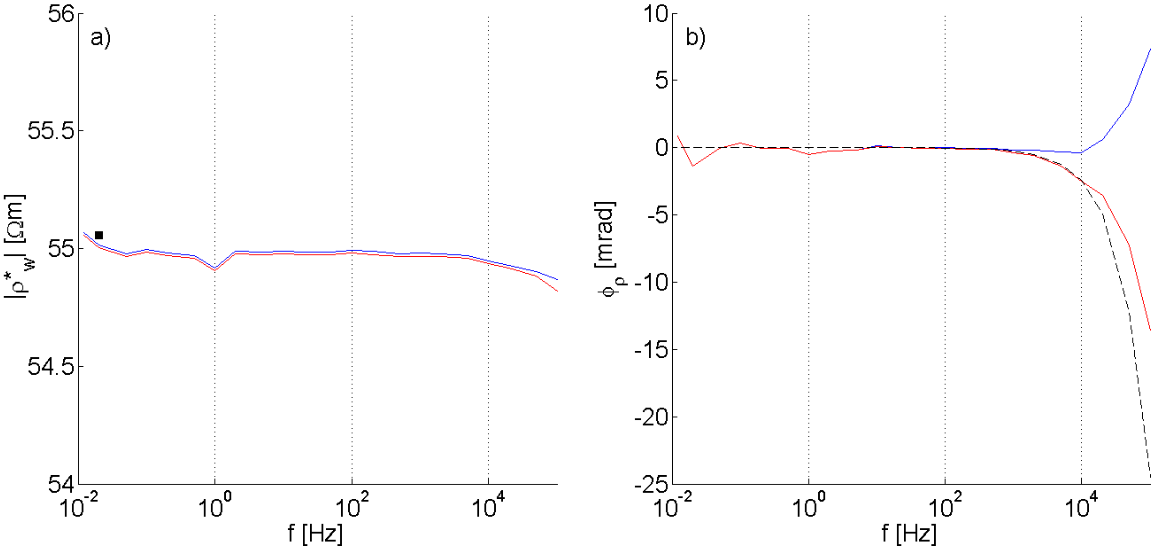

Fig. 4.14 - Resistivity amplitude (a) and phase (b) spectra of a water sample (yellow curve of Fig. 4.11). Black square and black dashed line are the conductivity meter DC reference value and theoretical phase spectrum, respectively. Blue lines are the experimental data obtained by modelling the amplifier unit capacitance only with the input capacitance of the amplifiers (6 pF), whereas red lines are the curves obtained with a total capacitance of 20 pF.

In Fig. 4.15, the root-mean-square error (RMSE) of the phase after the capacitance correction is represented as a function of the water resistivity, separated for frequency decade. As a general observation, RMSE tends to increase toward extreme water conductivity (pink and black data) and toward extreme frequency decade (Fig. 4.10a and 4.15g).

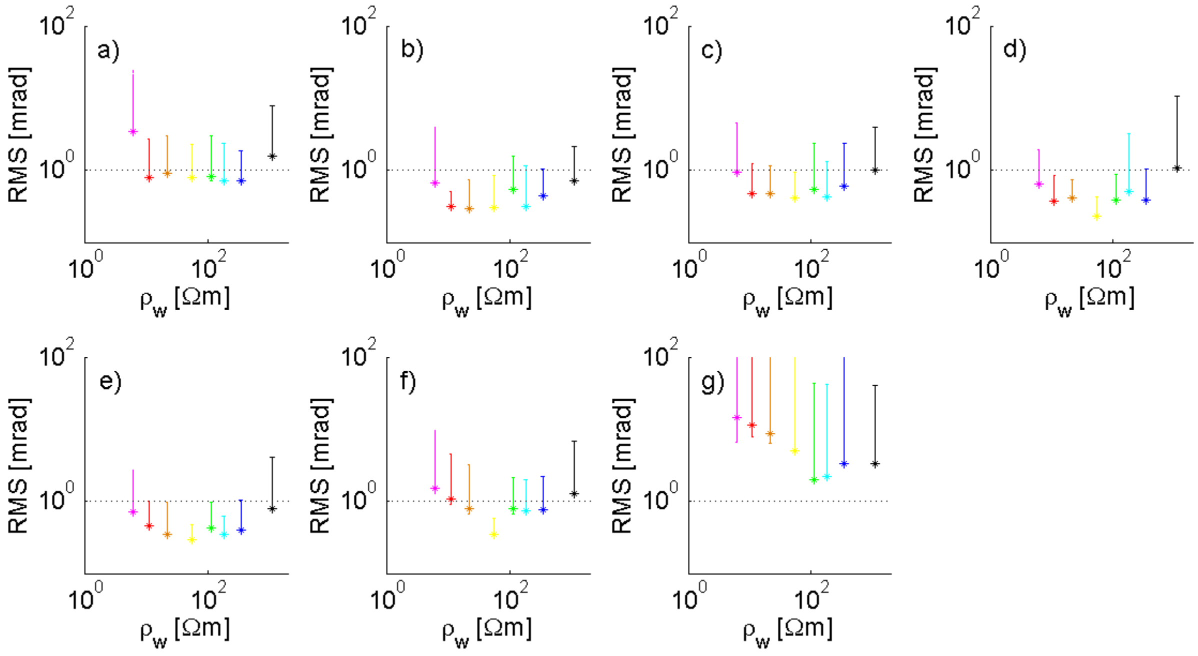

Fig. 4.15 - Root-mean-square error of the phase as a function of the water resistivity, for the frequency decades 10^{-2} Hz-10^{-1} Hz (a), 10^{-1} Hz-10^0 Hz (b), 10^0 Hz-10^1 Hz (c), 10^1 Hz-10^2 Hz (d), 10^2 Hz-10^3 Hz (e), 10^3 Hz-10^4 Hz (f), and 10^4 Hz-10^5 Hz (g). Star symbols represent the mean RMSE, whereas error bars the minimum and maximum values. Dotted lines highlight a threshold of 1 mrad.

On the basis of these considerations, the analysis of SIP data was conducted between 10 mHz and 10 kHz. Excluding the last frequency decade (f > 10 kHz; Fig. 4.9g), which has a mean RMSE of 6.3 mrad with peaks of more than 700 mrad due to the *fan-effect*, the global mean RMSE for all the other tests is 0.7 mrad. It is also worthwhile noting that for each water sample the RMSE is located close to the minimum error, thus suggesting the presence of few anomalies in a globally satisfactory spectrum.

In summary, data errors were considered equal to 1 mrad for the phase and to 1% for the amplitude, in the frequency range from 10 mHz to 10 kHz. Furthermore, data errors on the real (e_R) and on the imaginary (e_I) components of resistivity were calculated through the error propagation law as

$$e_R = e_a \cos\phi - |\rho^*| e_p \sin\phi, \tag{4.6}$$

$$e_I = e_a \sin\phi - |\rho^*| e_p \cos\phi, \tag{4.7}$$

respectively. Here, e_a is the data error on amplitude in Ωm, and e_p the data error on phase in rad.

4.5 Measurement repeatability

A sample of muddy sand (S7 and Sb7) was chosen to evaluate the reproducibility of measurements with the ST.sip13 system and the corresponding filling procedure by lateral tapping. Fig. 4.16 shows that some variations are observable both in the amplitude and in the phase among measurements performed on the same material but after independent filling of the sample holders. Amplitude differences are expected to be related mainly to variations in final water resistivity (46±5 Ωm) and porosity (0.40±0.03). The differences in the effective particle-size-distribution of the investigated volume and the arrangement of the fine- and coarse-grained components seem to play key roles in determining the variance encountered in the phase spectra, which regards both the absolute values at different frequencies (maximum deviation of about 10 mrad) and the position of the local peak (between 0.8 Hz and 20 Hz). In any case, the general phase trend differs from that obtained by changing the packing method, thus suggesting that the stirring operation disrupt the characteristic arrangement of the sample to a deeper extent than the preparation of the sample without a tight control on the effective distribution of different granulometric fractions and pores but with the same less-invasive method. On the other hand, the stirring procedure generally improves the repeatability (*Bairlein et al.*, 2014).

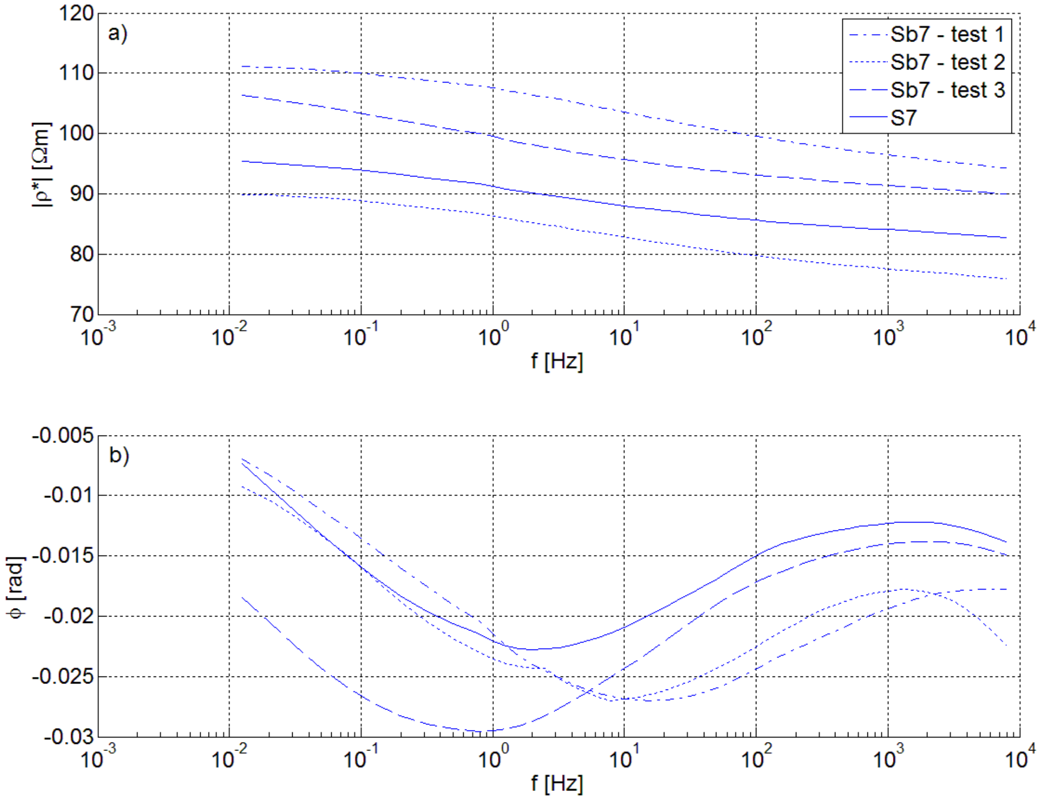

Fig. 4.16 - Comparison of the resistivity amplitude (a) and phase (b) spectra of sample S7 and samples Sb7, saturated with water w4, and measured with the ST.sip13 system.

4.6 Systems comparison

The experimental system ST.sip13 and the corresponding measurement protocol used to collect laboratory SIP data was also compared to the ZEL-SIP04-V02 system described in section 4.1.1. This was necessary not only for a further validation of the home-made system, but also because the dataset discussed in the following sections includes data collected with the two instruments. The comparison was based on phase lag spectra, which depend on sample holder characteristics, such as geometry and materials, and filling procedures, more than amplitude spectra. The data acquired with the two experimental approaches were very similar for sandy samples S9 and S10 (Fig. 4.17), whereas some differences were observed for samples with a significant amount of silt and clay, such as S7 and LZ15 (Fig. 4.18).

A difference in the phase accuracy for the two systems (i.e., about 0.1 mrad at 1 kHz for ZEL-SIP04-V02 and 1 mrad for ST.sip13) was already established with validation tests on reference electrical circuits and it is mainly due to the lower resolution of the of ST.sip13. However, the differences between measured spectra exceeded this discrepancy up to about 20 mrad for samples S7 and LZ15. An effect related to some characteristics of the sample holder would have been expected for both sandy and muddy-sandy samples, and should have been arisen also in the phase spectra of the water tests described in section 4.4. Thus, the discrepancy of Fig 4.18 was associated to differences in the packing procedures that largely affect the distribution of the fine sediment fraction with respect to the coarse-grained framework.

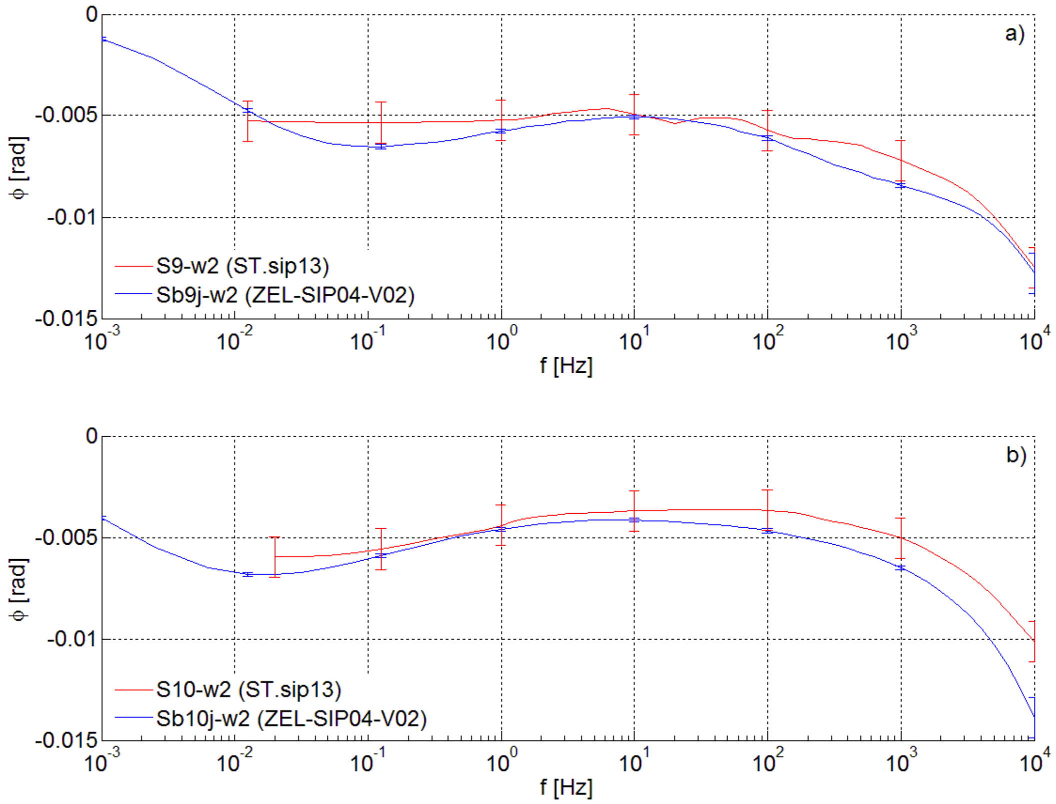

Fig. 4.17 - Comparison of the phase spectra of samples S9 (a) and S10 (b), measured with ST.sip13 and ZEL-SIP04-V02 systems.

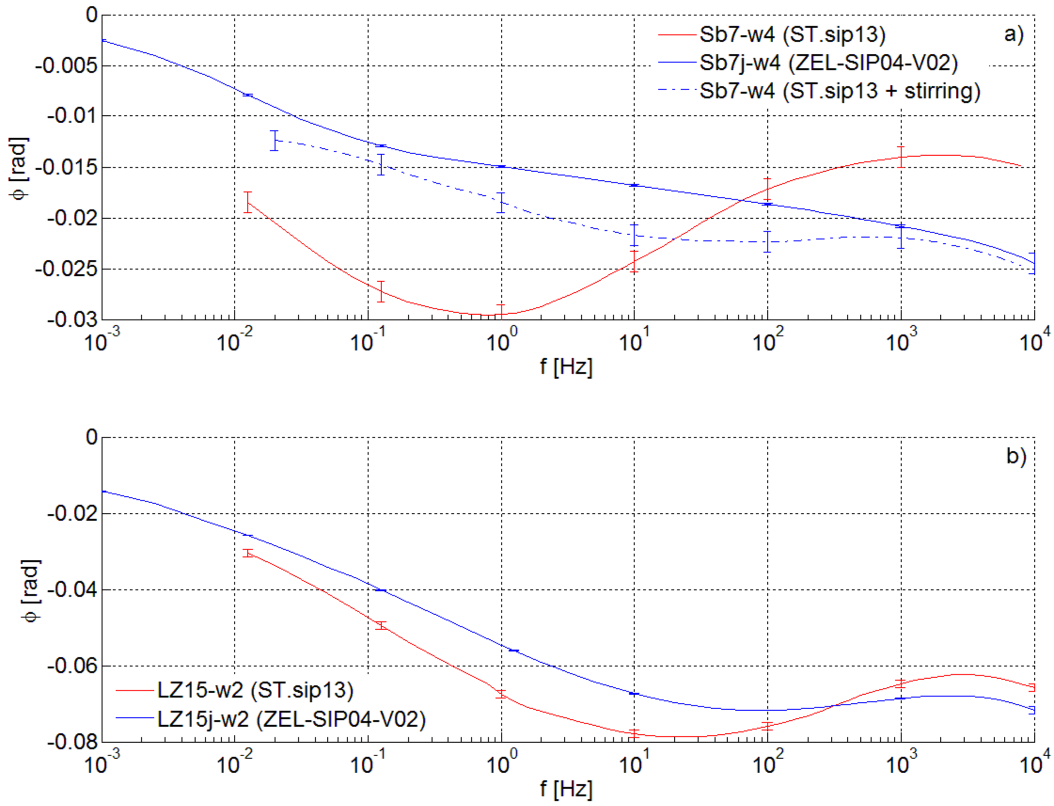

Fig. 4.18 - Comparison of the phase spectra of samples S7 (a) and LZ15 (b), measured with ST.sip13 and ZEL-SIP04-V02 systems, respectively. In subplot a, the dashed line represents the phase spectrum obtained with the ST.sip13 system but using the packing method typical of the other system.

The filling of the sample holder of the system ZEL-SIP04-V02 was accompanied by a repeated stirring, which was responsible for a high mobilisation of the finest fraction that tended to migrate in the liquid phase and stay in suspension until the sedimentation at the top of the sample, i.e., outside the investigated volume between potential electrodes. On the other hand, the internal grids of ST.sip13 prevented from the use of this method, which was substituted by the tapping on the lateral side of the holder. This method was less effective in the mobilisation of fine particles.

The comparison of *Bairlein et al.* (2014) of methods 2 (tapping) and 4 (stirring) for a slightly-sandy mud (sample C) reflected to a certain extent the spectral shape differences of sample LZ15 (Fig. 4.19). Furthermore, the usage of ST.sip13 system associated with a stirring method as similar as possible to the filling procedure used with the ZEL-SIP04-V02 system, increased the similarity with the latter measurement (Fig. 4.18a). This confirms that discrepancies in the measured responses are not related to the sample holder characteristics.

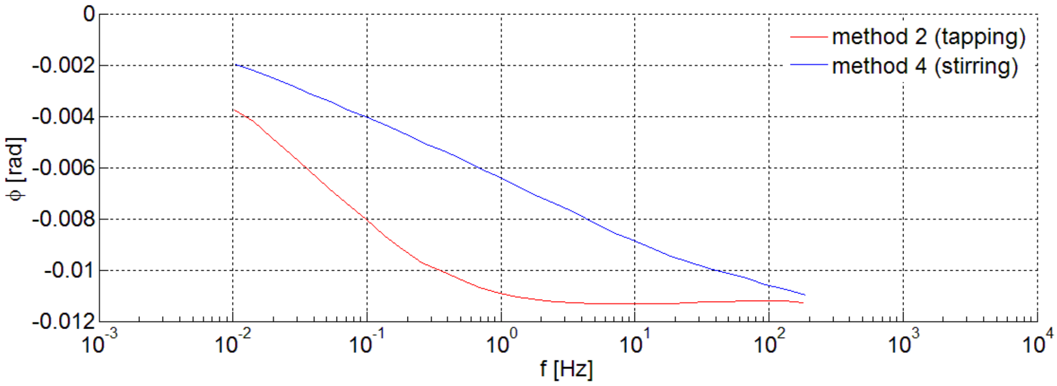

Fig. 4.19 - Comparison of the phase spectra of samples C (*Bairlein et al.,* 2014), prepared with two different packing procedures comparable to those used in this study in association with the two experimental systems.

Chapter 5

Data processing procedures

5.1 Modelling

A great variety of deterministic models have been proposed to fit SIP data (see section 2.3.2). These models are both empirical functions that are fully explained by a few model parameters (single-relaxation model), and multiple-relaxation formulations where a lot of parameters are necessary. The determination of the best-fitting model is conditional upon the assessment of the fitting error. Typically, the minimization of the root-mean-square error (RMSE) is the chosen criterion. RMSE is defined as

$$\mathrm{RMSE} = \sqrt{\frac{1}{\mathrm{N}}\sum_{\mathrm{k}=1}^{\mathrm{N}}\left|\frac{\mathrm{d_k} - \mathrm{g_k(mp)}}{\mathrm{e_k}}\right|^2}, \tag{5.1}$$

where **d** is the vector of experimental data (ρ^* or Z), **g** is the corresponding vector of predicted values obtained with the model and the set of model parameters (mp), **e** is the data error, and N is the total number of data points (measured frequencies). In the field of SIP, the application of equation (5.1) often leads to the achievement of a low RMSE and thus to the stopping of the inversion process even if the phase fitting is still far from acceptable. This is due to the huge difference between the real and the imaginary parts of ρ (or similarly between amplitude and phase): ρ'' can be lower than ρ' by up to three orders of magnitude. For this reason, *Boadu and Seabrook* (2006) considered a combination of the real and imaginary parts to define the objective function as

$$\chi^2 = \sum_{\mathrm{k}=1}^{\mathrm{N}}\left(\left|\frac{\rho'_{\mathrm{k,obs}} - \rho'_{\mathrm{k,pre}}}{\rho'_{\mathrm{k,obs}}}\right| + \left|\frac{\rho''_{\mathrm{k,obs}} - \rho''_{\mathrm{k,pre}}}{\rho''_{\mathrm{k,obs}}}\right|\right), \tag{5.2}$$

where the subscripts obs and pre represent the observed and predicted values, respectively. Alternatively, *Kemna* (2000) defined RMSE using log-transformed impedance amplitude, and also proposed the estimation of an RMSE obtained by substituting the quantities in equation (5.1) with the corresponding imaginary parts

$$\mathrm{RMSEim} = \sqrt{\frac{1}{\mathrm{N}}\sum_{\mathrm{k}=1}^{\mathrm{N}}\left(\frac{\rho''_{\mathrm{k,obs}} - \rho''_{\mathrm{k,pre}}}{\mathrm{Im(e_k)}}\right)^2}, \tag{5.3}$$

where the imaginary part of the complex data error correspond to the standard deviation of the phase. In fact, $\mathrm{e_k}$ is defined as

$$\mathrm{e_k} = \mathrm{s}(\ln|\rho^*_{\mathrm{k}}|) + i\mathrm{s}(\phi_{\mathrm{k}}), \tag{5.4}$$

where s(·) represents the standard deviation of the argument. RMSEim was used to run additional inversion iterations, once the complex inversion of tomographic datasets was finished and the distribution of resistivity magnitude was fixed (final phase improvement). The efficiency of this routine was firstly demonstrated through synthetic examples and then applied to measured data by *Flores Orozco et al.* (2012). Later, *De Donno* (2013) modified equation (5.4) to define RMSE associated to the absolute phase values

$$\mathrm{RMSEpha} = \sqrt{\frac{1}{N}\sum_{k=1}^{N}\left(\phi_{k,obs} - \phi_{k,pre}\right)^2}, \tag{5.5}$$

and to the relative amplitude values

$$\mathrm{RMSEamp} = \sqrt{\frac{1}{N}\sum_{k=1}^{N}\left(\frac{\left|\rho^*_{k,obs}\right| - \left|\rho^*_{k,pre}\right|}{\left|\rho^*_{k,obs}\right|}\right)^2}. \tag{5.6}$$

In presence of non-constant data error, equations (5.5) and (5.6) are weighted on the observed standard deviations for the phase and amplitude dataset, expressed in mrad and % respectively (*De Donno and Cardarelli*, 2014).

In the following sections, references to the computing method and the fitting error estimation are provided for some single-relaxation model (section 5.1.1), and a multiple-relaxation model (section 5.1.2). The aim is to supply the information for a reproduction of the data processing procedures applied to the measured data, whereas the corresponding theoretical basis have already been addressed in sections 2.3.2. MATLAB® codes used to perform the data modelling can be found in Appendix E. Data collected with the systems ST.sip13, after the preliminary operations described in section 4.3, and data collected with the ZEL-SIP04-V02 had a very similar structure that allowed to perform the elaboration steps in a quite similar way, with only a few differences in the codes in order to account, for example, for the frequency decade from 10^{-3} Hz to 10^{-2} Hz that is not present in the first dataset.

5.1.1 Cole-type models

Among the phenomenological models listed in section 2.3.2, the Cole-Cole model (CC) and the Generalized Cole-Cole model (GCC) were selected to fit the spectral data in terms of complex resistivity.

A simple comparison of the shape of the theoretical Argand plots of Cole-type models (Fig. 2.9) with the experimental ones, showed that in most cases these models could be suited only for a small portion of the measured spectra. For this reason, a first data analysis was conducted to determine the appropriate frequency range for the application of these models. As a rough distinction, the diagrams of the imaginary part as a function of the real part of complex resistivity were subdivided into three categories (Fig. 5.1):

- curve with negative curvature in the investigated frequency interval up to very high frequency (type I);
- curve with negative curvature at low frequency followed by a segment with increasing imaginary component (type II);
- almost flat or irregular curve (type III).

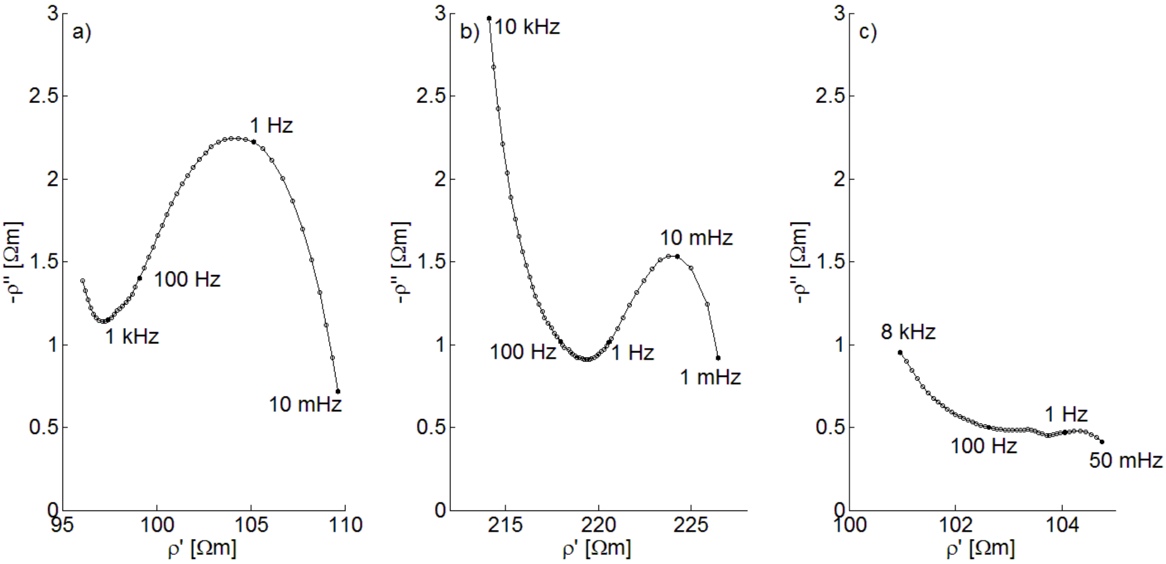

Fig. 5.1 - Paradigmatic Argand plots for type I (a), type II (b), and type III (c) samples.

This distinction, even if only qualitative, was used to avoid an intrinsic incompatibility between models and data. In particular, samples associated to the first and second types were fitted until the frequency corresponding to the end of the line with negative curvature. For the last type both a fitting along the whole frequency interval and a fitting only in the low frequency range were tried, but the results were of low quality for both of them.

In order to assess the discrepancy between measured and modelled data, a modification of equation (5.2) was used

$$\mathrm{RMSE}^* = \sqrt{\frac{1}{\mathrm{N}}\sum_{\mathrm{k}=1}^{\mathrm{Np}}\left[\left(\frac{\rho'_{\mathrm{k,obs}}-\rho'_{\mathrm{k,pre}}}{\mathrm{e}_{\mathrm{R}\mathrm{k}}}\right)^2+\left(\frac{\rho''_{\mathrm{k,obs}}-\rho''_{\mathrm{k,pre}}}{\mathrm{e}_{\mathrm{I}\mathrm{k}}}\right)^2\right]}, \tag{5.7}$$

where the contribution of the real and the imaginary parts to the squared error was weighted with the corresponding measurement error (see section 4.4). Besides this approach, a multi-objective optimization was also adopted to verify the separated effects of the resistivity amplitude and phase in the determination of the best fitting parameters and to check the reliability of the weighting of the real and the imaginary components of the complex resistivity introduced in equation (5.7). Two indicators of the goodness of fit were defined similarly to equations (5.5) and (5.6), respectively as

$$\mathrm{RMSEph} = \sqrt{\frac{1}{\mathrm{N}}\sum_{\mathrm{k}=1}^{\mathrm{N}}\left(\frac{\phi_{\mathrm{k,obs}} - \phi_{\mathrm{k,pred}}}{\mathrm{e}_{\mathrm{p}_\mathrm{k}}}\right)^2}, \tag{5.8}$$

$$\mathrm{RMSEam} = \sqrt{\frac{1}{\mathrm{N}}\sum_{\mathrm{k}=1}^{\mathrm{N}}\left(\frac{\left|\rho^*_{\mathrm{k,obs}}\right| - \left|\rho^*_{\mathrm{k,pred}}\right|}{\mathrm{e}_{\mathrm{a}_\mathrm{k}}}\right)^2}, \tag{5.9}$$

where the data error on the amplitude and on the phase are defined in section 4.4.

In an ideal case a unique optimal parameter set would minimize simultaneously both RMSEam and RMSEph. However, since the fitting was often referred to a limited frequency range and non-systematic errors on amplitude and phase data were assumed to be uncorrelated (*Barsoukov and Macdonald*, 2005), a Pareto analysis was conducted in order to determine Pareto-optimal solutions (also called non-dominated or efficient solutions), i.e., the arrays of model parameter for which one of the two misfit objective functions could not be reduced unless an increase of the other function occurred. The set of Pareto-optimal solutions is called the Pareto set or Pareto frontier (*Marler and Arora*, 2004). The concept of Pareto optimality was introduced by the economist Vilfredo Pareto at the end of the 19th century to identify the most efficient state of resources allocation when considering conflicting or independent objectives. Then, it has been diffusely used as a decision-making tool in a large variety of subjects, e.g., engineering, game theory, artificial intelligence (*Hwang and Masud*, 1979; *Steuer*, 1986), hydrological modelling (*Gupta et al.*, 1998; *Yapo et al.*, 1998; *Boyle et al.*, 2000; *Boyle et al.*, 2001; *Madsen*, 2003; *Vrugt et al.*, 2003; *Blasone et al.*, 2007; *Baratelli et al.*, 2011; *Nassar and Ginn*, 2014), and also geophysical applications (*Dal Moro and Pipan*, 2007; *Dal Moro*, 2010). In this work, Pareto analysis allowed to determine a plausible variability range for each model parameter, rather than a single solution to the inverse problem as in the single-objective optimization.

Within the Pareto set, it is usually required to identify a single solution in order to make decision or simply represent the results of the inverse problem. This solution is called best-compromise (*Efstratiadis and Koutsoyiannis*, 2010) and can be selected through a variety of criteria, from the simple intuition to the use of external criteria. In this work, the point of the Pareto set nearest to the origin of the Cartesian plane of the two misfit functions (corner point) was chosen as the representative solution. All other solutions of the set were used to define the maximum interval of variability of each model parameter.

Two further constraints were applied for the identification of the Pareto frontier, i.e., thresholds on both the objective functions to avoid the inclusion into the Pareto set of solutions with an amplitude or phase fitting error greater than 1. This means that the Pareto frontiers is reduced to those solutions that have a fitting error equal or lower than the data error, considering separately amplitude and phase. Sometimes, these constraints produced an empty Pareto set and only the best fitting solution of the single-objective optimization was considered. The lacking of solutions with a fitting error comparable with the data error can be due to an incorrect selection of the frequency points to be fitted with the Cole-type models, especially for type III samples.

The method used to search both the best-fitting solution according to equation (5.7) and the set of Pareto-optimal solutions with the two objective functions (5.8) and (5.9) was the grid-search method (*Menke*, 2012). The model parameters were 4 for the CC model and 5 for the GCC model. Their *a priori* distributions were chosen as locally uniform, varying between 0 and 1 for the frequency exponents, between -4 and 3 for the 10-based logarithm of the relaxation time (in seconds), between 0 and $1.05\mathrm{M}_t$ for the chargeability, and between ρ_a and ρ_0 (only integer numbers) for the direct current resistivity, where ρ_a is the resistivity at low frequency and ρ_0 a corrected value (see next section for more details). Variations steps were fixed to 0.1 for $\log_{10}\tau_0$, 0.02 for m, c, and k, and 1 for ρ_0.

5.1.2 Debye decomposition

The modelling of complex electrical resistivity as a function of frequency was performed also following the decomposition approach introduced by *Nordsiek and Weller* (2008) and later modified by *Zisser et al.* (2010). This method always allowed to consider the whole frequency range, without *a priori* selection of the fitting interval. In the formulation of *Nordsiek and Weller* (2008), the reference equation (2.26) was reformulated by normalizing the complex electrical resistivity as

$$\rho^*_{\mathrm{norm}}(\omega) = \frac{\rho_0 - \rho^*(\omega)}{\rho_0}, \tag{5.10}$$

where ρ_0 is the direct current resistivity, and separating the real and the imaginary parts in order to obtain a system of linear equations with 2N equations (i.e., the number of measured frequencies for the two components) and P values of chargeability m_k to be determined

$$\begin{bmatrix} \frac{(\omega_1\tau_1)^2}{1+(\omega_1\tau_1)^2} & \cdots & \frac{(\omega_1\tau_P)^2}{1+(\omega_1\tau_P)^2} \\ \vdots & \ddots & \vdots \\ \frac{(\omega_N\tau_1)^2}{1+(\omega_N\tau_1)^2} & \cdots & \frac{(\omega_N\tau_P)^2}{1+(\omega_N\tau_P)^2} \\ \frac{\omega_1\tau_1}{1+(\omega_1\tau_1)^2} & \cdots & \frac{\omega_1\tau_P}{1+(\omega_1\tau_P)^2} \\ \vdots & \ddots & \vdots \\ \frac{\omega_N\tau_1}{1+(\omega_N\tau_1)^2} & \cdots & \frac{\omega_N\tau_P}{1+(\omega_N\tau_P)^2} \end{bmatrix} \cdot \begin{bmatrix} m_1 \\ \vdots \\ m_P \end{bmatrix} = \begin{bmatrix} \rho'_{norm}(\omega_1) \\ \vdots \\ \rho'_{norm}(\omega_N) \\ \rho''_{norm}(\omega_1) \\ \vdots \\ \rho''_{norm}(\omega_N) \end{bmatrix}. \tag{5.11}$$

A solution to equation (5.11) was searched with a least squares algorithm with a predetermined set of P values of relaxation time and non-negative constraints on m_k. This algorithm is already implemented in MATLAB® under the function *lsqnonneg*. In the code developed to apply it to the collected data (Appendix E), 1000 values of relaxation time logarithmically distributed between 10^{-6} s and 10^{4} s were used. This range corresponded to the maximum investigated frequency range, i.e., from 10^{-3} Hz to 10^{5} Hz, with an extra decade on both sides.

For the direct current resistivity, a correction procedure was applied on the approximated value ρ_a, i.e., the resistivity value at low frequency (*Zisser et al.*, 2010). This correction consisted in solving separately the system of linear equations for the real and the imaginary parts, in order to obtain two values of apparent total chargeability ($M_t^{a,R}$ and $M_t^{a,I}$) that are functions of M_t, ρ_a, and ρ_0. From them, the correct value of DC resistivity was calculated as

$$\rho_0 = \rho_a\left(1 + M_t^{a,I} - M_t^{a,R}\right). \tag{5.12}$$

The non-negative least squares algorithm provided a non-continuous relaxation time distribution function that is physically not very likely. In order to overcome this limit, a least squares algorithm with Tikhonov regularization was considered in an overview of the algorithms to solve equations' system (5.11) (*Zisser*, SERfit. A MATLAB package and GUI for quantification of spectral electrical response, *Unpublished*). The optimization problem changed from

$$\min_{x_k \geq 0}\{\|\mathbf{Am} - \boldsymbol{\rho}_{\mathbf{norm}}\|^2\} \tag{5.13}$$

of the non-negative least squares algorithm to

$$\min_{x_k \geq 0}\{\|\mathbf{Am} - \boldsymbol{\rho}_{\mathbf{norm}}\|^2 + \lambda^2\|\mathbf{Lm}\|^2\} \tag{5.14}$$

of the Tikhonov regularization, where $\|\cdot\|$ denotes the Euclidean norm, $\mathbf{Am} = \boldsymbol{\rho}_{\mathbf{norm}}$ is the compact form of equations' system (5.11), λ is the regularization parameter, and $\mathbf{L}$ is a suitably chosen matrix that is often a multiple of the identity matrix. The routine to implement this algorithm was provided within the SERfit package in MATLAB® language. The same ρ_0 and variability range for the relaxation times of the previous algorithm were used, with 100 values of non-predetermined relaxation time. The option for the removal of relaxation times with negative chargeability was activated. The estimation of λ was done by progressively increasing the value of the regularization parameter from 0.1 to 15 and stopping when a satisfying balance between the goodness of data fitting, quantified by the fitting root-mean-square error of the phase component, and the smoothing of the relaxation time distribution was achieved. **L** matrix was kept equal to the identity matrix. The main difference of the Tikhonov algorithm from the non-negative least squares method was visible in the relaxation time distribution (Fig. 5.2), which was continuous and thus closer to the theoretical G(τ) relative to a synthetic model for the former algorithm.

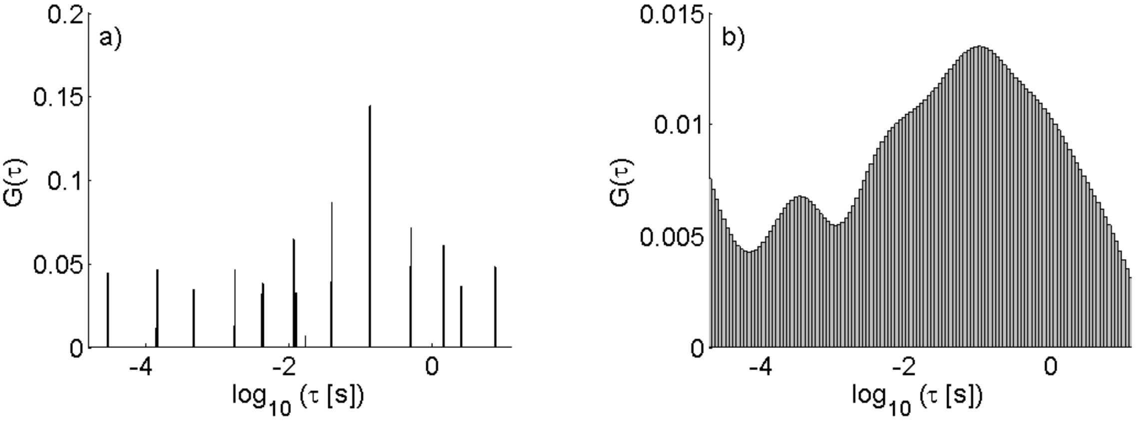

Fig. 5.2 - Relaxation time distribution function obtained for the same sample using the *lsqnonneg* algorithm (a) and the Tikhonov regularization algorithm (b).

In the application of both algorithms, a weighting factor for the imaginary part was added into equation (5.11). According to *Zisser et al.* (2010), it can be calculated as

$$w = h\frac{\sum_{k=1}^{p} \rho'_{\mathrm{norm}}(\omega_k)}{\sum_{k=1}^{p} \rho''_{\mathrm{norm}}(\omega_k)}, \tag{5.15}$$

with an optimal h varying between 0.3 and 0.9. In this study, a fixed value of 0.6 was chosen as the most appropriate for the whole dataset. An additional weighting factor on the frequencies was used to remove occasional anomalous data points from both the amplitude and phase spectra.

In order to improve the effectiveness in the comparison of the integrating parameters of spectral data acquired with the two different experimental systems and protocols, the overlapping frequency range from 10^{-2} Hz and 10^{4} Hz was chosen. The use of the DD produces a huge amount of model parameters that must necessary be compressed into a smaller set of parameters in order to compare the measured spectral responses. Similarly to *Nordsiek and Weller* (2008), some integrating parameters were calculated:

- the direct current resistivity ρ_0;
- the total chargeability

$$\mathrm{M_t} = \sum_{\mathrm{k}=1}^{\mathrm{P}} \mathrm{m_k}\,; \tag{5.16}$$

- the normalized chargeability (*Weller et al.*, 2010)

$$\mathrm{m_n} = \frac{\mathrm{M_t}}{\rho_0}, \tag{5.17}$$

- the mean relaxation time

$$\bar{\tau} = \mathrm{e}^{\frac{\sum_{\mathrm{k}=1}^{\mathrm{P}} \mathrm{m_k} \cdot \ln \tau_{\mathrm{k}}}{\mathrm{M_t}}}; \tag{5.18}$$

- the series of the characteristic relaxation times τ_{m}, with m varying from 10 to 90 with a ten-step and corresponding to a percentage threshold on the cumulative chargeability curve[6];
- the non-uniformity parameters, analogous to the non-uniformity coefficients used to describe the granulometric distribution (see section 3.3)

$$\mathrm{U}_{\tau 60} = \frac{\tau_{60}}{\tau_{10}} \tag{5.19}$$

$$\mathrm{U}_{\tau 90} = \frac{\tau_{90}}{\tau_{10}} \tag{5.20}$$

$$\mathrm{U}_{\tau \mathrm{c}} = \frac{(\tau_{30})^2}{\tau_{10}\tau_{60}}. \tag{5.21}$$

The numerical values of these parameters for all the natural samples are summarized in Appendix C. The goodness of fitting of the DD was evaluated similarly to the Cole-type phenomenological models through RMSE* (equation 5.7), RMSEph (equation 5.8), and RMSEam (equation 5.9).

---

[6] The cumulative curve is built up in the direction of increasing relaxation times. This corresponds to the sum of chargeability contributions from high to low frequencies.

5.2 Multivariate analysis

Data processing included statistical tools to identify significant relationships between model parameters and textural, compositional, physico-chemical properties of the investigated sediment-water systems. These relations are commonly referred to as petrophysical relationships and usually consist in site-specific empirical relationships between individual geophysical variables and a parameter of interest. This approach have been applied to IP and SIP parameters by several authors for the correlation with:

- textural properties, such as a representative grain or pore size, the grain or pore size distribution (*Lesmes and Morgan*, 2001; *Robinson and Friedman*, 2001; *Scott and Barker*, 2003; *Slater and Glaser*, 2003; *Tong et al.*, 2006; *Kruschwitz et al.*, 2010; *Revil and Florsch*, 2010; *Volkmann and Klitzsch*, 2010; *Koch et al.*, 2011; *Koch et al.*, 2012; *Revil et al.*, 2012; *Revil et al.*, 2013; *Revil et al.*, 2014; *Slater et al.*, 2014), and the grain shape (*Jones and Friedman*, 2000);
- surface properties of the fine-grained particles, such as the amount or type of clay (*Boadu and Seabrook*, 2006; *Slater et al.*, 2006; *Oh et al.*, 2007; *Leroy and Revil*, 2009; *Breede et al.*, 2012;), the cation exchange capacity (*Revil et al.*, 2013), and the specific surface area (*Kruschwitz et al.*, 2010; *Weller et al.*, 2010);
- fluid properties, such as the solute concentration or the electrical conductivity (*Lesmes and Frye*, 2001; *Ponziani et al.*, 2011; *Revil and Skold*, 2011; *Skold et al.*, 2011; *Weller et al.*, 2011; *Hördt and Milde*, 2012; *Kavian et al.*, 2012a; *Weller and Slater*, 2012;), the type of solutes (*Slater et al.*, 2005; *Vaudelet et al.*, 2011a, b; *Weller et al.*, 2011; *Chen et al.*, 2012), and the saturation degree (*Ulrich and Slater*, 2004; *Oh et al.*, 2007; *Ghorbani et al.*, 2009; *Gomaa*, 2009; *Jougnot et al.*, 2010; *Ponziani et al.*, 2011; *Breede et al.*, 2012; *Kavian et al.*, 2012a, b; *Grunat et al.*, 2013);
- organic fraction properties (*Ponziani et al.*, 2012), including also the presence of bacteria (*Abdel Aal et al.*, 2010) or contaminants (*Vanhala*, 1997; *Martinho et al.*, 2006; *Saltas et al.*, 2007; *Cassiani et al.*, 2009; *Magill*, 2010; *Schwartz et al.*, 2012; *Ustra et al.*, 2012);
- the metal content (*Slater et al.*, 2006; *Oh et al.*, 2007; *Werkema Jr et al.*, 2010; *Joyce et al.*, 2012).

However, most of the cited studies refer to specific subsets of samples (especially consolidated materials, and well-sorted or bimodal unconsolidated samples). Thus the results are completely effective in limited and controlled conditions, whenever only a few parameters change, whereas the remaining ones are constant and do not affect the empirical correlations. On the other hand, the effectiveness of these empirical relationships has not yet been completely established for alluvial sediments with wide grain-size-distributions, different and often unknown spatial arrangements of grains, and indeterminate types and content of clay and organic matter. For these reasons, simple correlations of individual electrical and sedimentological parameters were not considered to be satisfactory for the goals of this work and a multivariate analysis was conducted. In particular, a principal component analysis (PCA) and a cluster analysis (CA) were adopted. This joint approach was addressed to evaluate the kind and amount of information extractable from SIP data collected with standardized acquisition procedure on saturated sediments with wide particle-size-distribution, possible presence of clays with different mineralogical compositions, different salinity of the saturation water and so on. This analysis was performed only on the subset of natural samples (O-, Ob-, S-, Sb-, LA-, and LZ-samples). The following sections are devoted to provide the technical details of the adopted statistical tools. The corresponding MATLAB® code can be found in Appendix F.

5.2.1 Principal Component Analysis

PCA is a statistical tool for dimensionality reduction, i.e., re-expression of a big dataset in a more meaningful coordinate system that reduces the redundancy of information and maximizes the variance in the projected space (for a simple and comprehensive treatment on PCA refer to *Shlens*, 2014). Basically, PCA is an orthogonal linear transformation of possibly correlated variables into a set of uncorrelated variables called principal components (PC). The transformation is usually applied to the correlation matrix or to the covariance matrix, which are symmetric and can thus be diagonalized, and acts in such a way that the first PC has the largest possible variance and each succeeding component has the highest possible variance under the constraint that it is orthogonal to the preceding components. The elements of the main diagonal are the eigenvalues of the matrix and their values weigh the relative importance of the different PCs. Each PC is a linear combination of the original variables. However, even if the number of PCs is in principle equal to the number of original variables, the transformation should provide a limited set of new variables that explain most of the total variance of the system. Typically, some heuristic criteria are used to determine the proper number of PCs that are useful to describe the system under investigation:

- eigenvalues larger than 1;
- eigenvalues larger that the mean of the eigenvalues;
- cumulative explained variance higher than a specific threshold (80% or 90%);
- point of slope change in the so-called screen plot (eigenvalues of PCs in descending order).

The interpretation of the meaning of the new variables identified with PCA can be developed on the basis of the Pearson correlation coefficient between individual PCs and the original variables. Pearson coefficient is a measure of the linear correlation between two variables X and Y, defined as

$$R = \frac{\mathrm{cov}\,(X, Y)}{\sigma_X \sigma_Y}, \tag{5.22}$$

where cov is the covariance and σ the standard deviation. R varies between -1 and 1, with the extreme values indicating a perfect inverse and direct linearity, whereas a value of 0 indicates no linear correlation.

In this work, the chosen input variables were 12: the direct current resistivity ρ_0, the total chargeability M_t, the characteristic relaxation times τ_{10}, τ_{50}, and τ_{90} in 10-based logarithmic form, and the curvature coefficient $U_{\tau c}$ in 10-based logarithmic form, all deriving from the DD. In addition, the relative phase differences between six fixed, logarithmically-spaced frequencies from 10^{-1} Hz to 10^4 Hz were considered. These were indicated as $\Delta\phi_x$, where $x = \mathrm{Log}\, \nu$ and ν the starting frequency (in Hz) for the relative phase difference estimation[7]. The selection considered only the variables that were not strongly correlated (R^2>0.8) with other variables already included in the input matrix, in order to avoid an overrepresentation of some characteristics (*Davis*, 1973; *Sarstedt and Mooi*, 2014). For example, the relative amplitude variations (ΔA) between successive fixed frequencies were directly correlated to ρ_0 and were thus excluded from the input dataset. All the selected variables were standardized before the calculation of the correlation matrix, i.e., transformed into distributions with zero mean and unit variance, in order to assign the same weight to all the variables. This method is referred to as the R-mode (e.g., *Davis*, 1973).

5.2.2 Cluster Analysis

Contrary to PCA, CA is not a specific, single algorithm. It refers, instead, to the task of grouping objects in such a way that the elements in each group are more similar to each other than to elements belonging to other groups. In other words, clustering is a classification procedure that can be implemented with different algorithms according to the aim of the work and the type of data. As a rough distinction, clustering algorithms can be subdivided in partitioning methods (each object belongs to a cluster), overlapping methods (an object may belong to more than one cluster), and hierarchical methods (an object belonging to a child cluster also belongs to its parent clusters). *Tronicke et al.* (2004) used a partitioning method on velocity and attenuation data derived from GPR acquisitions to delineate a lithological and hydrogeological zonation of the investigated region. Instead, for the aim of this work, a hierarchical method was considered. In fact, a continuous range of spectral variability among investigated samples was expected, with samples that could partly share similar

---

[7] For example, $\Delta\phi_0 = (\phi_{1\mathrm{Hz}} - \phi_{0.1\mathrm{Hz}})/\phi_{1\mathrm{Hz}}$.

characters only in limited frequency ranges, only in the shape of the spectra, or only in the absolute values. In such a situation, a hierarchical approach had the advantage to keep the relations between samples classified in different groups easily visible. The usage of a hierarchical clustering permitted also to work simultaneously with different levels of aggregation, without any prior assumption on the number of clusters.

The clustering was performed on the same set of variables adopted for the PCA, using the average linkage method (*Sokal and Michener*, 1958). At each stage of aggregation, it merges the two clusters for which the average distance between all pairs of objects, made of one object from each group, is the minimum. This average distance is defined as

$$d_{rs} = \frac{1}{n_r \cdot n_s} \sum_{i \in r} \sum_{j \in s} d_{ij}, \tag{5.23}$$

where n_r and n_s are the number of objects contained in clusters r and s, respectively, and d_{ij} is the Euclidean distance between the observations i and j

$$d_{ij} = \sqrt{\frac{\sum_{k=1}^{N} \left(X_{ik} - X_{jk}\right)^2}{N}}. \tag{5.24}$$

In equation (5.24), X_{ik} and X_{jk} denote respectively the k^{th} variable measured on samples i and j, and N the total number of measured variables.

In addition, the Ward's minimum variance algorithm (*Ward Jr*, 1963) was also considered. It combines pairs of objects in binary clusters and then combines clusters with other clusters or other objects until all the observations are gathered in a hierarchical tree. The objective function minimized to iteratively couple the observations or the clusters is the total within-cluster variance, defined as

$$f = \frac{n_r n_s}{(n_r + n_s)} {d_{rs}}^2, \tag{5.25}$$

where d_{rs} is the distance between clusters r and s and the initial distance between observations is again the Euclidean distance.

The quality of the clustering was evaluated using the cophenetic correlation coefficient C and the mean silhouette value $\bar{s}$. The former statistic reflects the distortion of the pairwise distance between the observations after clustering (D'_{ij}) with respect to the original distance (D_{ij}), according to

$$C = \frac{\sum_{i<j} \left(D_{ij} - \overline{D}\right) \cdot \left(D'_{ij} - \overline{D'}\right)}{\sqrt{\sum_{i<j} \left(D_{ij} - \overline{D}\right)^2 \cdot \sum_{i<j} \left(D'_{ij} - \overline{D'}\right)^2}}, \tag{5.26}$$

where $\overline{\mathrm{D}}$ and $\overline{\mathrm{D}}'$ are the mean distances before and after clustering. The second statistic is an indicator of how well the objects lie within their cluster (*Rousseeuw*, 1987). It is calculated as the mean value of the silhouette of each observation ($\mathrm{s_i}$)

$$\mathrm{s_i} = \frac{\mathrm{b_i} - \mathrm{a_i}}{\max\{\mathrm{a_i}, \mathrm{b_i}\}}, \tag{5.27}$$

where $\mathrm{a_i}$ is the average dissimilarity of the observation i with respect to all other data within the same cluster, $\mathrm{b_i}$ is the lowest average dissimilarity of i with respect to any other cluster, and dissimilarity is quantified by the squared Euclidean distance. $\mathrm{s_i}$ varies between -1 and 1, and the highest value is attained when the object is perfectly matched to its cluster and badly matched to the neighbouring one (vice versa for the least value). For $\mathrm{s_i} = 0$, the object is located on the exact border of two neighbouring clusters. The mean silhouette value refers instead to the whole dataset and is a comprehensive indicator of how well the objects lie within their cluster (*Rousseeuw*, 1987). A reasonable structure with objects well-matched to their own cluster and poorly-matched to the others is associated with $\bar{\mathrm{s}} > 0.5$, according to the classification of *Kaufman and Rousseeuw* (2005) reported in Tab. 5.1.

$\bar{\mathrm{s}}$	**type of structure**
> 0.70	strong structure
0.51 - 0.70	reasonable structure
0.26 - 0.50	weak structure, could be artificial
< 0.26	no structure

Tab. 5.1 - Thresholds of mean silhouette values for the evaluation of the structure produced by the clustering (*Kaufman and Rousseeuw*, 2005).

Chapter 6

Results

The results presented in this chapter are organized into five sections that follow the conceptual workflow and gradually add elements of complexity in the data elaboration.

Section 6.1 is devoted to the presentation of the spectral variability due to the modification of single variables (e.g., water resistivity, dominant granulometric class, clay content, etc.) in the subsets of well-sorted sands and sand-clay mixtures; these effects are discussed only in terms of raw data, without referring to equivalent circuital models.

In section 6.2, a similar approach is applied to the main dataset made of natural samples. In particular, after a brief introduction about the notation used for the samples' coding, some observations are proposed about the global variability of the resistivity amplitude at low frequency (i.e., a first approximation of the direct current resistivity), the relative reduction of resistivity with frequency, and the typologies of phase spectra recognized in the data.

In section 6.3, the fitting with single-relaxation models is introduced, with some remarks about the global errors and the errors considered separately for the amplitude and the phase components (according to the methods described in section 5.1.1). Furthermore, section 6.3 takes into consideration the comparison of model parameters between CC and GCC models.

In section 6.4, the fitting with the Debye decomposition approach (or multiple-relaxation model; see section 5.1.2) is analysed, both with the *lsqnonneg* and the Tikhonov regularization algorithms.

Finally, section 6.5 is devoted to the additional use of the principal component analysis and the cluster analysis on the model parameters derived from the Debye decomposition, following the approaches described in sections 5.2.1 and 5.2.2.

The discussion in chapter 7 retraces this path, focusing on the relationships between the electrical parameters and the sedimentological properties of the investigated samples.

6.1 Effects produced by single variables

The bulk complex electrical response of the investigated samples is determined by a large number of factors, whose characteristic signals are possibly of comparable order of magnitude and affect the amplitude and/or phase spectra in the same frequency range. For this reason, some preliminary tests were performed on the well-sorted sands and the sand-clay mixtures to identify the spectral characters produced by individual properties, when the variability of the others is kept to a minimum.

Water resistivity

In the subset of well-sorted materials (TR-samples; Fig. 6.1), a decrease in water resistivity from 449 Ωm to 9 Ωm (i.e., from water w1 to w7) causes a strong reduction in bulk resistivity (Fig. 6.2a), almost independently from grain-size. Indeed, the porosity of these samples is almost constant (0.40±0.02). In the phase spectra, water effect is also visible: passing from high to low water resistivity, phase spectra flatten at about -1 mrad (Fig. 6.2b). A polarization signal is observable only for TR1 (*vf*S), which is the finest-grained sample of this group. An occurrence of a residual fraction of mud cannot be excluded, but also a polarization due to the very fine sand particles is plausible.

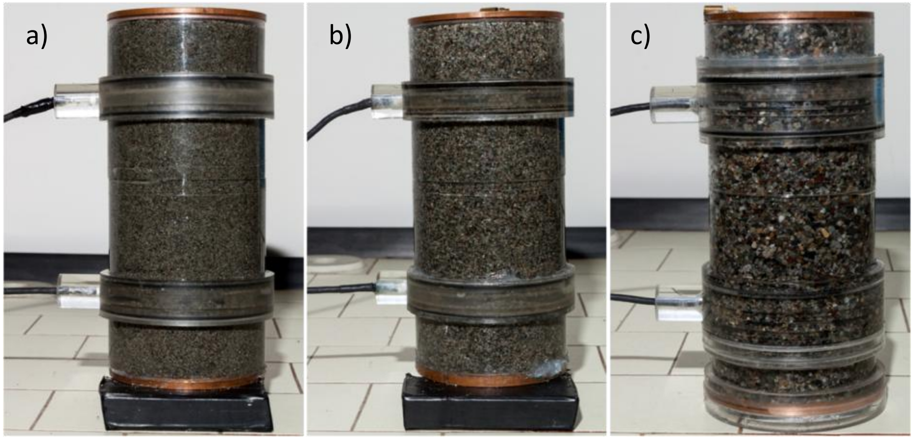

Fig. 6.1 - Samples TR2-w1 (a), TR3-w1 (b), and TR4-w2 (c) in the sample holders for SIP measurements (ST.sip13 system).

In the subset of sand-clay mixtures (M-samples), a decrease in water resistivity of one order of magnitude (from 446 Ωm to 43 Ωm on the average, i.e., from w1 to w5) causes a sharp decrease in the resistivity amplitude only for sample M50 (Fig. 6.3a), whereas variations for samples M5 and M05 are restricted to narrow intervals (Figs. 6.4a and 6.5a). Irrespective of the water resistivity, all M50 samples show a bulk resistivity higher than that of the water, whereas samples M05 always show a bulk resistivity lower than the water resistivity. This means that the conductivity of the sample is higher than the water conductivity, indicating the presence of an additional contribution to the electrolytic conduction, associated to the mud component.

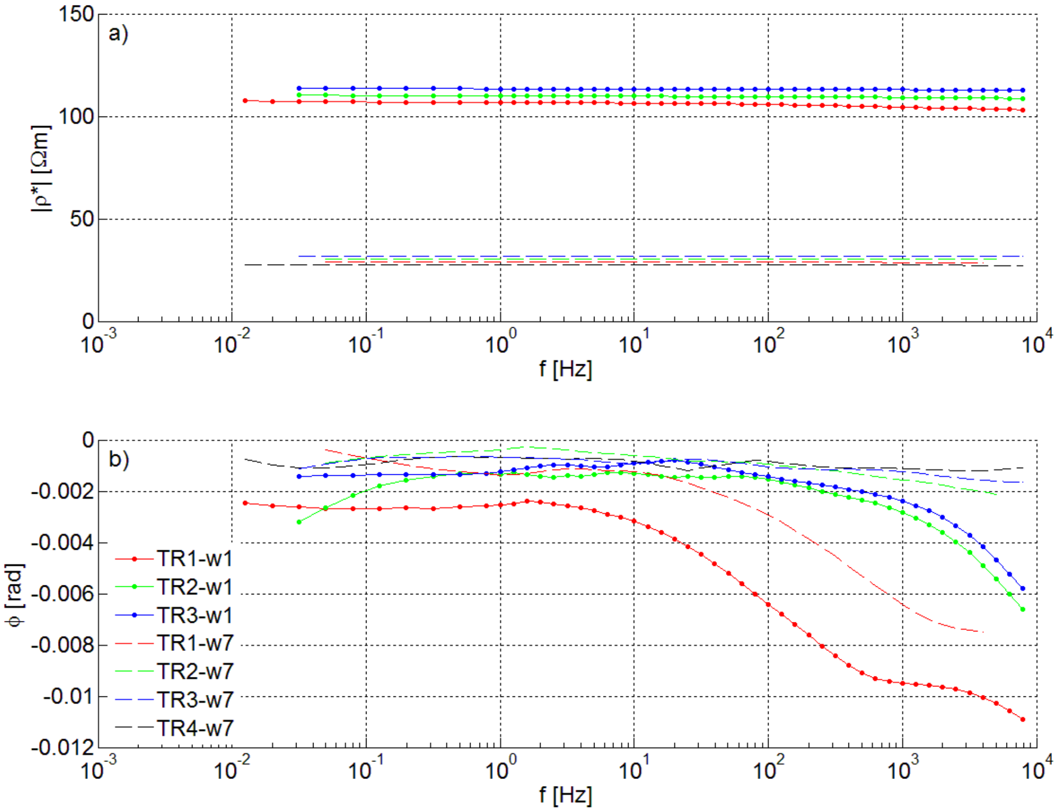

Fig. 6.2 - Resistivity amplitude (a) and phase (b) spectra of TR-samples, saturated with high- and low-resistivity waters.

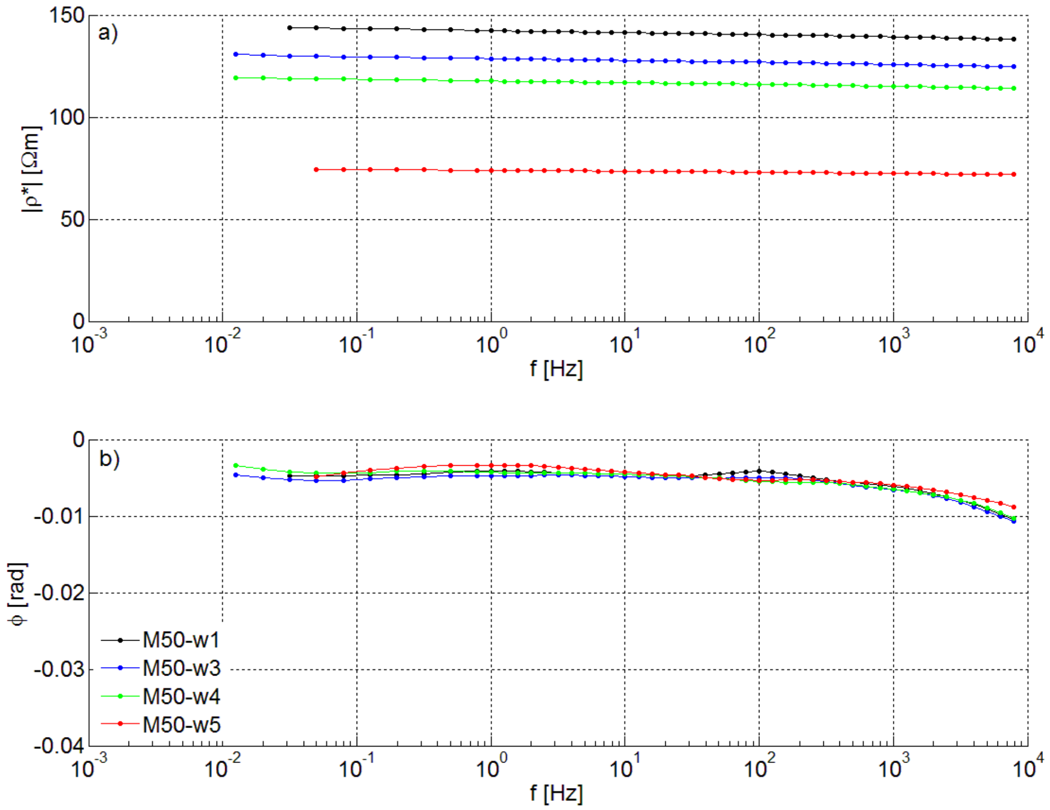

Fig. 6.3 - Resistivity amplitude (a) and phase (b) spectra of M50-samples, saturated with waters from w1 to w5.

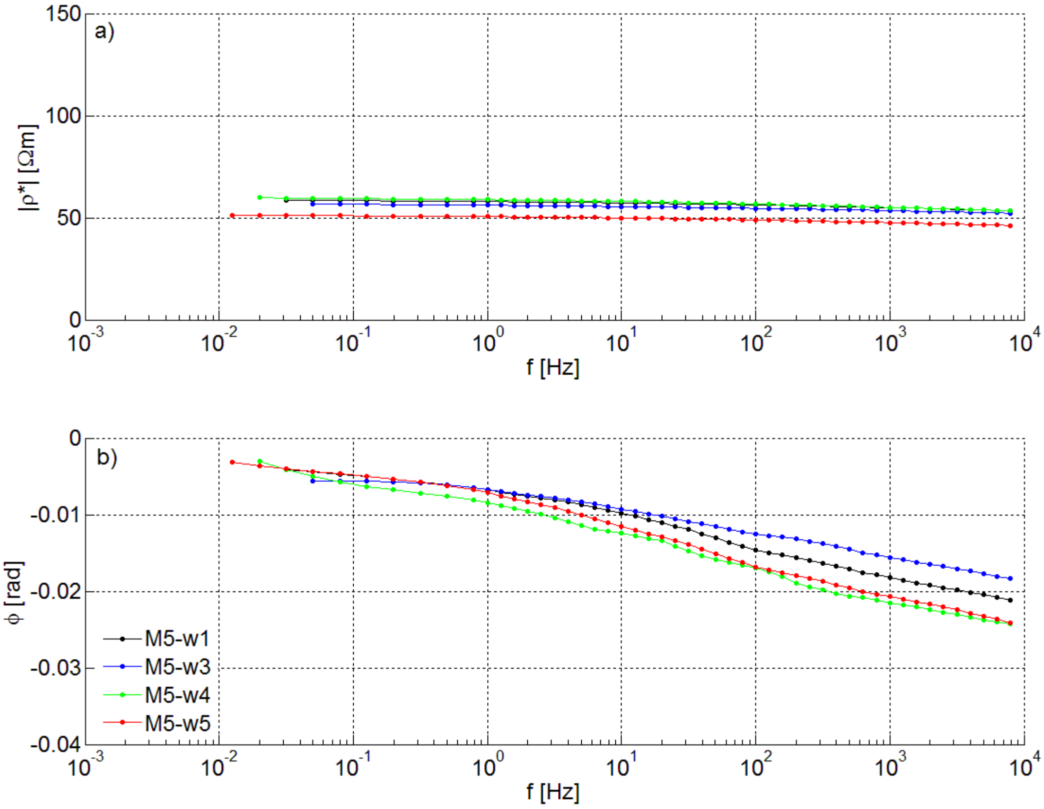

Fig. 6.4 - Resistivity amplitude (a) and phase (b) spectra of M5-samples, saturated with waters from w1 to w5.

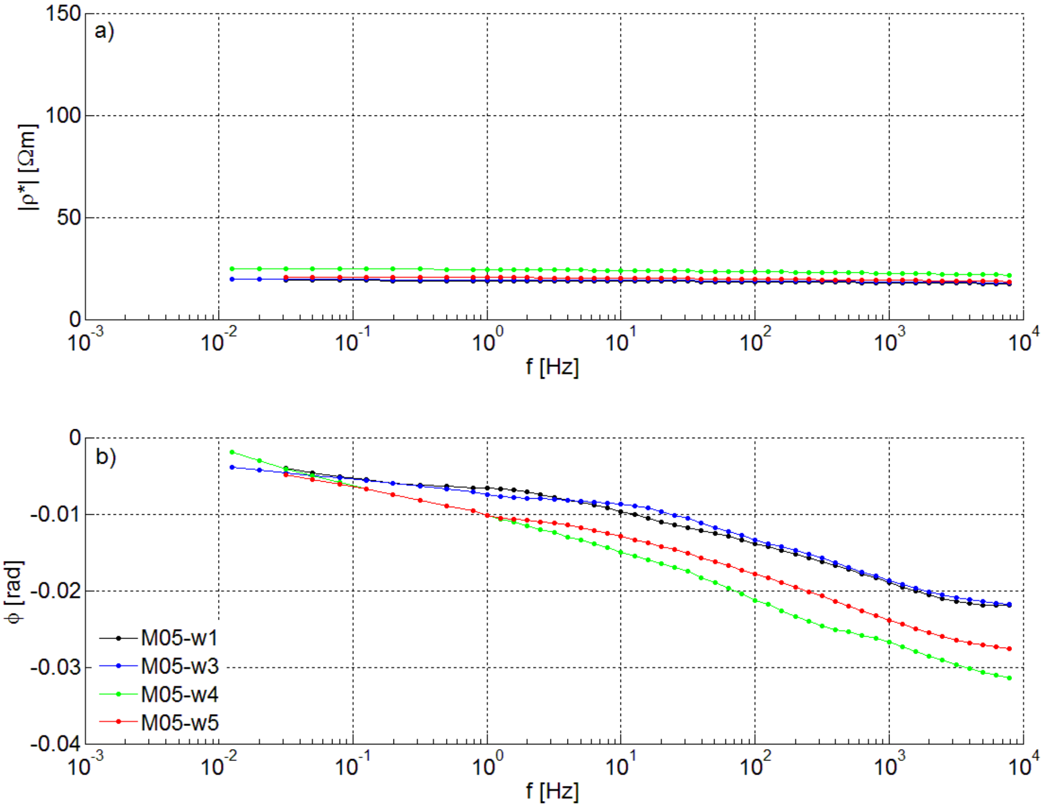

Fig. 6.5 - Resistivity amplitude (a) and phase (b) spectra of M05-samples, saturated with waters from w1 to w5.

Variations in the phase spectrum are limited in 1 mrad interval for sample M50 (Fig. 6.3b), and in 10 mrad interval for samples M5 and M05 (Figs. 6.4b and 6.5b), without a regular trend associated with water resistivity. Since a decrease in the absolute phase values is expected with a decrease of water resistivity, the variability of other factors such as the distribution of clay and the porosity probably prevent from a clear identification of this trend. Similar considerations apply also for the salt type. In fact, both amplitude and phase response do not strongly depend on the type of salt in solution, rather by its concentration and thus electrical resistivity. However, the concentration being equal, the presence of a divalent cation (Ca^{2+}) determines a shortening of the EDL thickness (see equation 2.2) with respect to monovalent cation (Na^{+}), and a decrease of polarizability is expected.

Coarse-to-fine ratio

An increase in $\Gamma_{0.063}$ (from 0.56 of M05 to 4.82 of M5 and to 56.19 of M50; Fig. 6.6) is associated with a sharp increase in resistivity amplitude, for both sodium and calcium solutions and for all tested ρ_w (Figs. 6.7a, 6.8a, 6.9a, and 6.10a). On the phase spectra, a decrease in the absolute phase values is instead observed. This is particularly evident for M50-samples (Figs. 6.7b, 6.8b, 6.9b, and 6.10), whereas differences between samples M5 and M05 are less pronounced and the trend is even inverted in some cases (Figs. 6.7b and 6.8b), especially below 100 Hz.

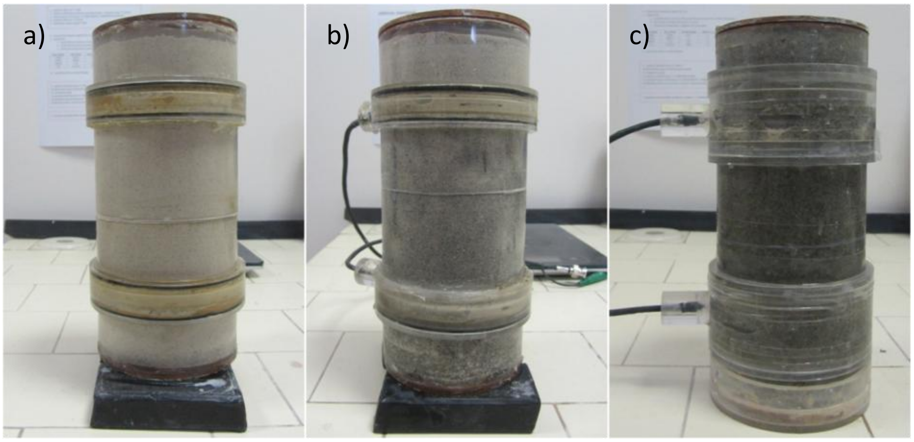

Fig. 6.6 - Samples M05-w1 (a), M5-w1 (b), and M50-w1 (c) in the sample holders for SIP measurements (ST.sip13 system).

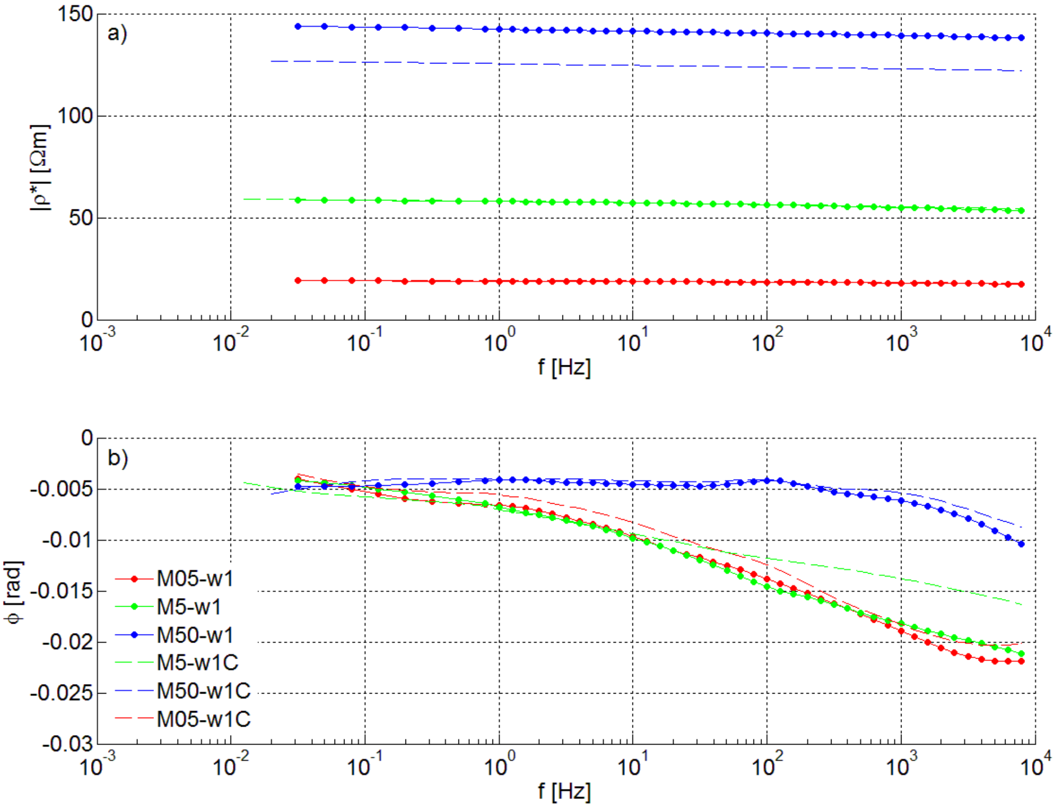

Fig. 6.7 - Resistivity amplitude (a) and phase (b) spectra of M05-, M5-, and M50-samples, saturated with water w1.

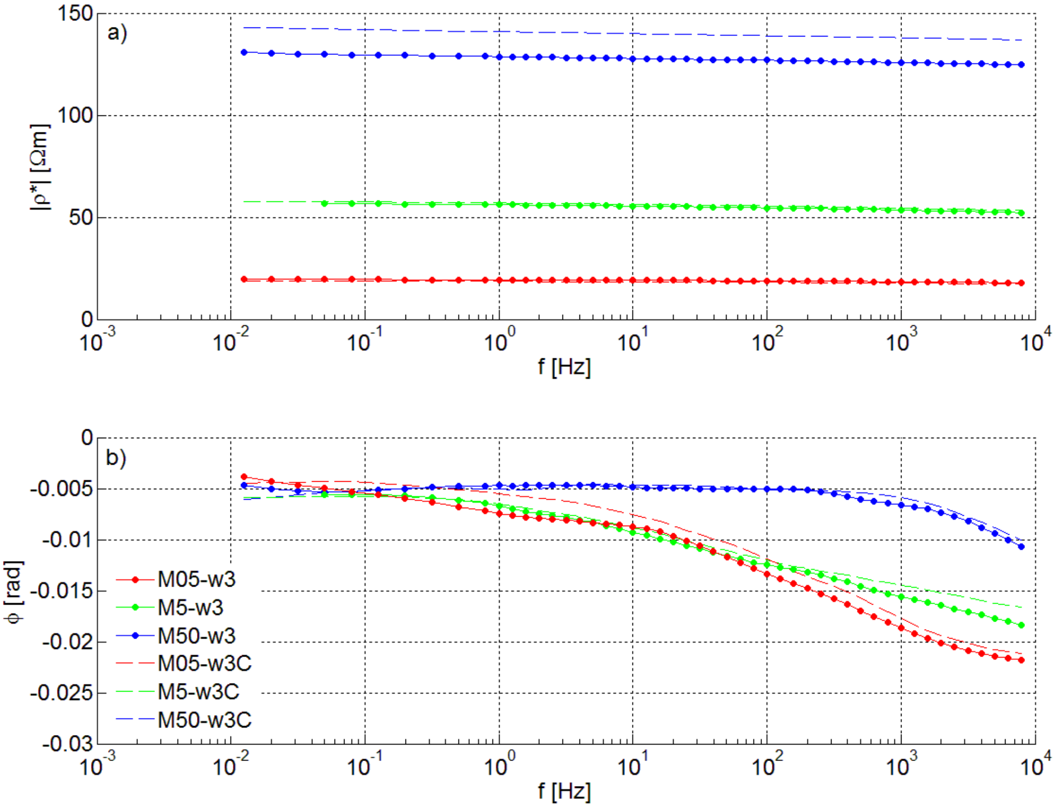

Fig. 6.8 - Resistivity amplitude (a) and phase (b) spectra of M05-, M5-, and M50-samples, saturated with water w3.

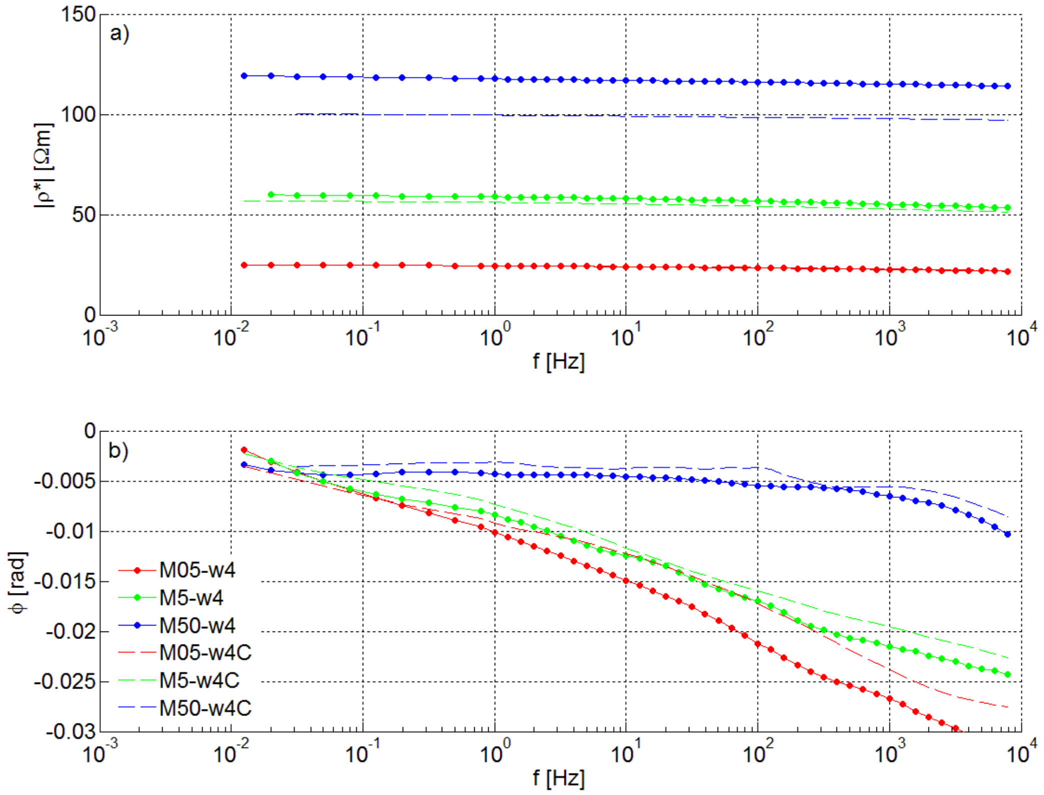

Fig. 6.9 - Resistivity amplitude (a) and phase (b) spectra of M05-, M5-, and M50-samples, saturated with water w4.

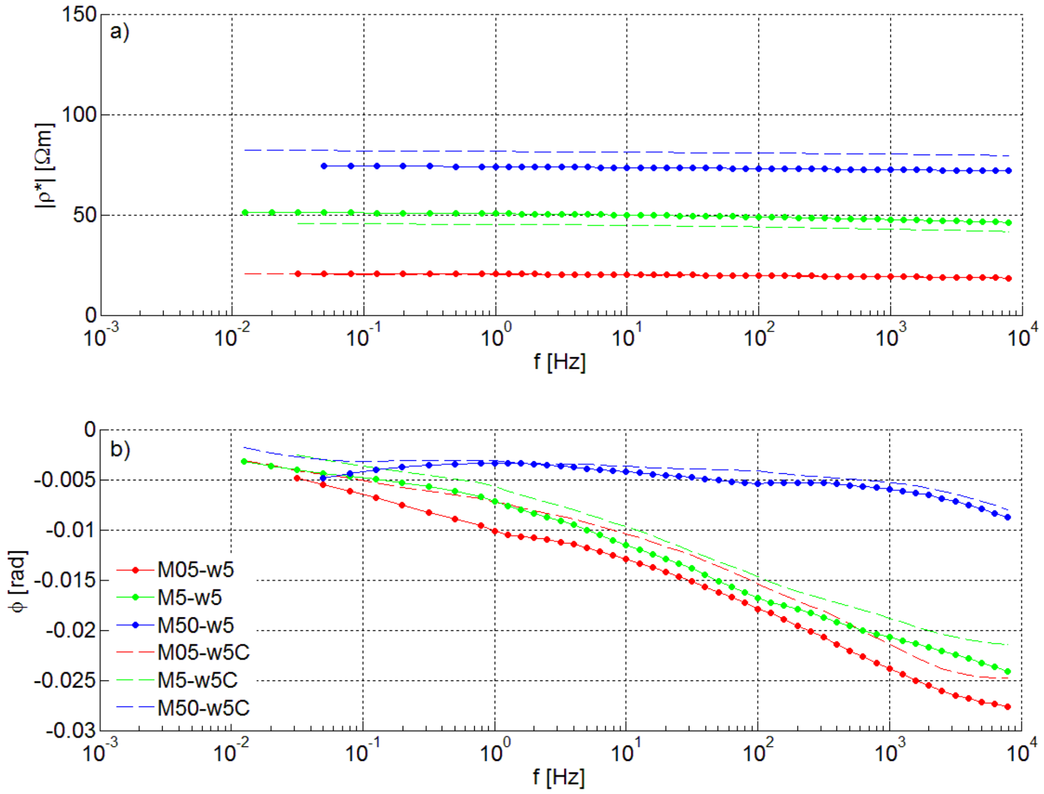

Fig. 6.10 - Resistivity amplitude (a) and phase (b) spectra of M05-, M5-, and M50-samples, saturated with water w5.

This anomaly can somehow be related to the packing, i.e., the assemblage of the different granulometric classes. In fact, the distribution of the fine-grained component within the coarser framework becomes more important when mud is more abundant, and this character cannot be easily quantified and controlled during the preparation of the sample. An effect related to the distribution of clay with respect to sand is also supported by the comparison of the porosity values. Starting from an average porosity of 0.41±0.005 for M50-samples, an addition of clay firstly determines a decrease in porosity (0.38±0.01 for M5-samples) due to the filling of the pores associated with the coarse fraction, and later an increase in porosity (0.61±0.02 for M05-samples) justifiable with the loss of a grain-sustained framework and the development of a clay suspension (*Shevnin et al.*, 2007; Fig. 6.11).

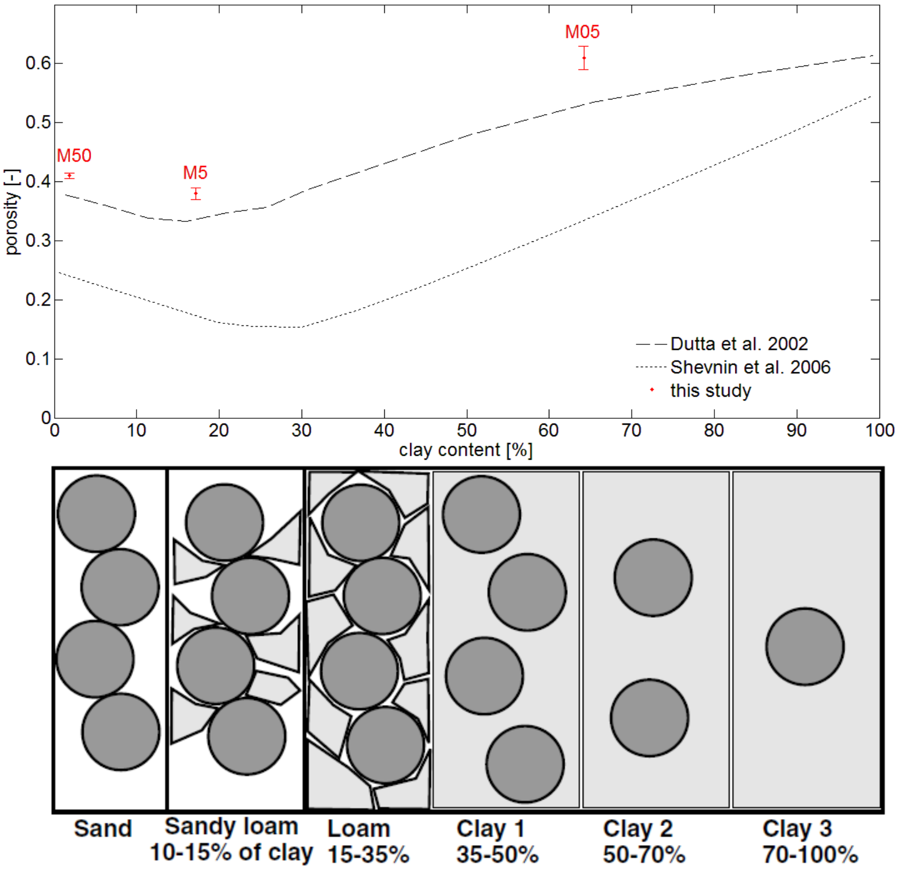

Fig. 6.11 - Average porosity for samples M50, M5, and M05 as a function of clay content. Experimental data of *Dutta et al.* (2002) are represented in dashed line and modelled data of *Shevnin et al.* (2006) in dotted line, with the corresponding diagram of the sand-clay arrangement (*Shevnin et al.*, 2007).

Clay distribution

An example of the importance of the clay distribution is provided by the comparison of spectral data of samples with a small fixed amount of clay (2%) concentrated in a single layer (Fig. 6.12a, b) or dispersed in the siliceous sandy framework. The dispersed system shows higher absolute phase values than the layered system for both the kaolinitic and the illitic cases (Figs. 6.13b and 6.14b), due to the increase in the amount of exposed surfaces bearing excess charges, whereas no significant differences appears on the amplitude component (Figs. 6.13a and 6.14a).

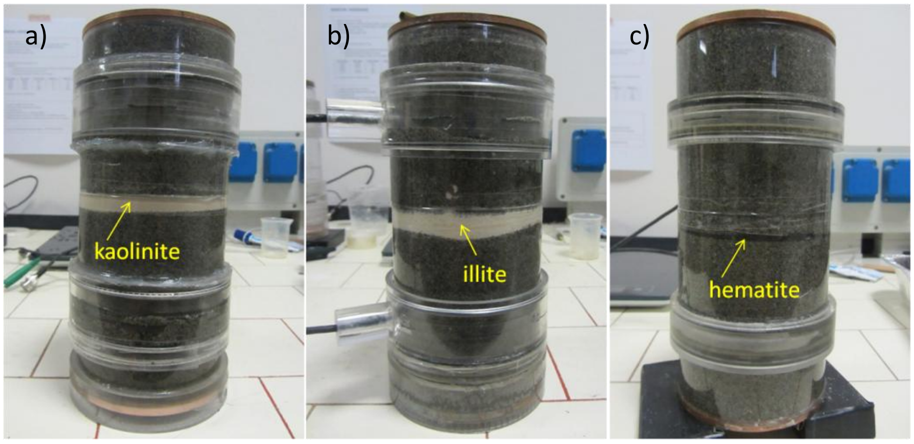

Fig. 6.12 - Samples KL-L-w2 (a), IL-L-w2 (b), and HE-L-w2 (c) in the sample holders for SIP measurements (ST.sip13 system).

The corresponding well-sorted sand spectra are also reported in the figures: even if a slight difference in the water resistivity prevents from a fully rigorous comparison, especially for the amplitude component that is strongly affected by water resistivity, the layered systems do not strongly deviate from the well-sorted sand as regards the phase. Also, no mineralogical effect is visible between KL-L-w2 and IL-L-w2, whereas for the corresponding dispersed samples a larger phase deviation from the sand spectrum is observed for the illitic case. This is coherent with the higher unbalanced electric charge per unit cell of illite as compared to kaolinite.

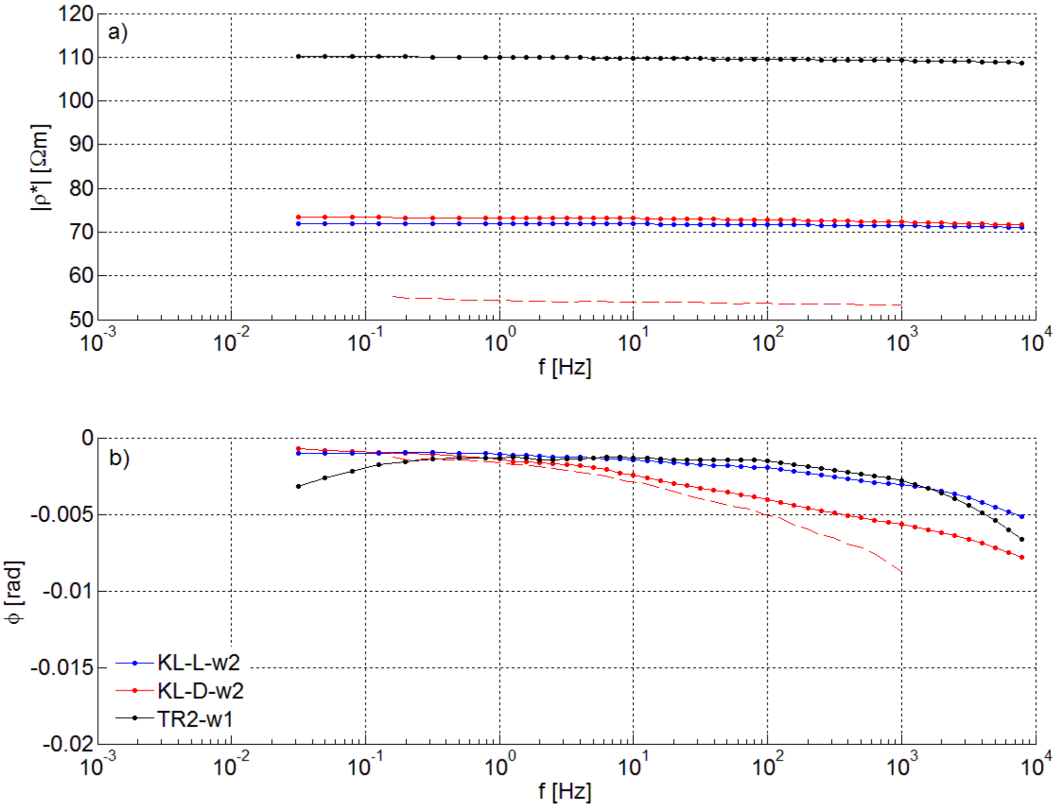

Fig. 6.13 - Resistivity amplitude (a) and phase (b) spectra of siliceous sand-kaolinite mixtures in layered (KL-L) and dispersed configuration (KL-D), saturated with water w2, and compared with the corresponding sand TR2, saturated with water w1. The dashed line refers to data of *Slater et al.* (2006) acquired on a mixture of Ottawa sand and 5% kaolinitic clay.

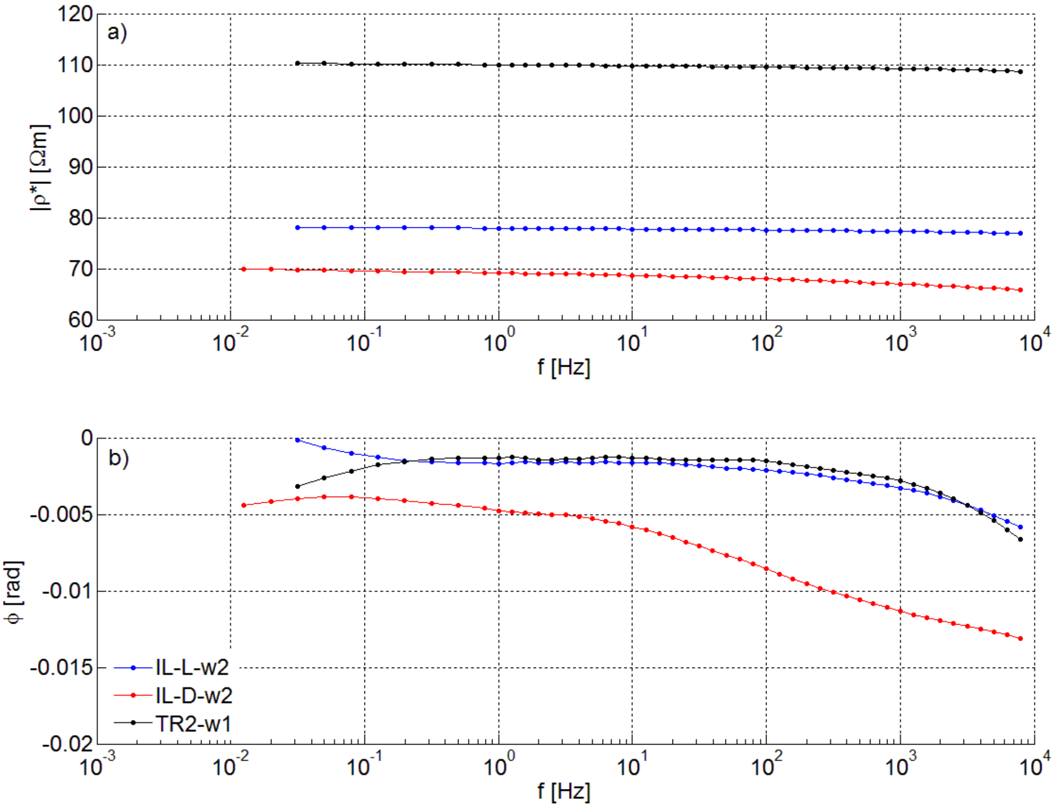

Fig. 6.14 - Resistivity amplitude (a) and phase (b) spectra of siliceous sand-illite mixtures in layered (IL-L) and dispersed configuration (IL-D), saturated with water w2, and compared with the corresponding clean sand TR2, saturated with water w1.

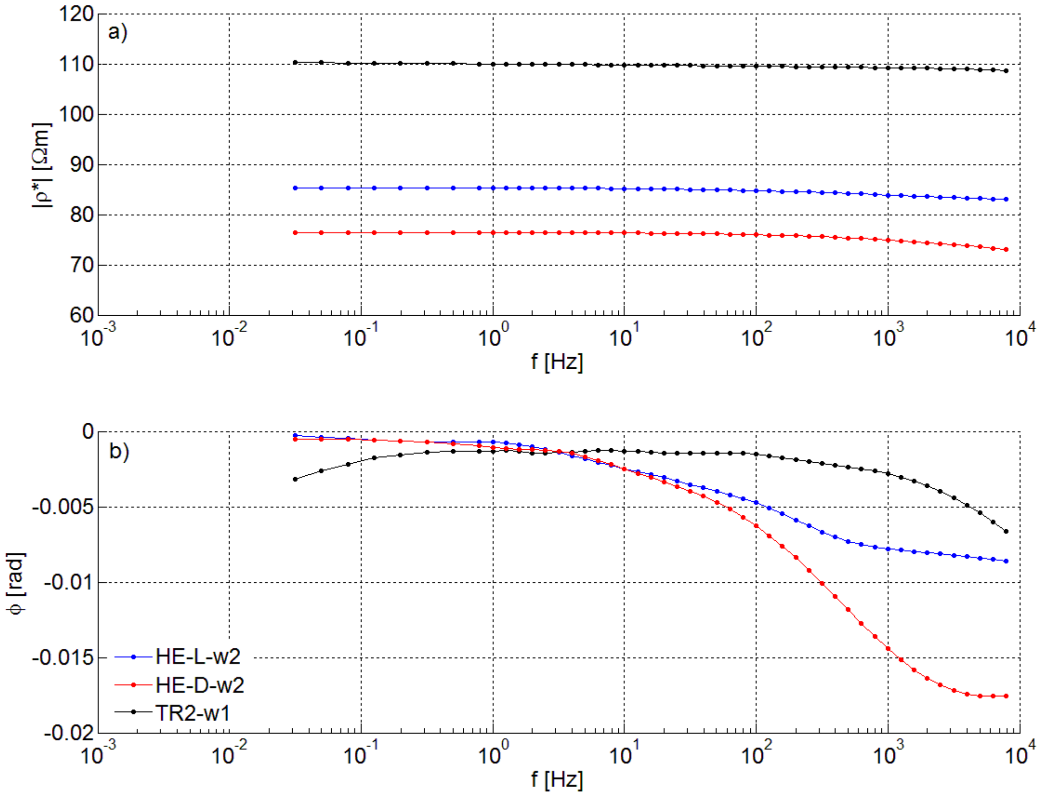

Fig. 6.15 - Resistivity amplitude (a) and phase (b) spectra of siliceous sand-hematite mixtures in layered (HE-L) and dispersed configuration (HE-D), saturated with water w2, and compared with the corresponding clean sand TR2, saturated with water w1.

Metal particles

The substitution of clay with hematite (Fig. 6.12c) produces an even greater polarization effect and a significant deviation from the clean sand case in the layered state, already (Fig 6.15b).

6.2 Preliminary results on the main dataset

The main dataset is composed by the samples collected in the sites of Orio Litta (O- and Ob-samples), Senna Lodigiana (S- and Sb-samples), Lozzolo (LZ-samples), and Landriano (LA-samples), and saturated with one to five different water solutions. Even if they are not undisturbed samples since they are repacked inside the sample holder for SIP measurements, they are addressed in the following as “natural samples” to highlight that they are analogous to the sediments of the study sites and to distinguish them from the well-sorted sands and sand-clay mixtures prepared with materials of the building industry (“artificial samples”). Each sample[8] is identified through a univocal code (ID) that allows gaining information on the type of sediment, the type of water, the experimental system, and the packing method, as it is shown by the following example:

Sb7j-w4

SEDIMENT: the letter stands for the location, whereas the number is just related to the sampling progression. (see sections 3.1 and 3.3.1)

SYSTEM: the letter j identifies samples investigated with the ZEL-SIP04-V02 system and prepared with the wetting packing with stirring. Otherwise the use of ST.sip13 system and the filling with tapping is implied. (see section 4.3)

WATER: the number is associated to a specific range of electrical resistivity, measured before the interaction with the solid phase. (see section 3.3.3)

In total, 66 samples are included in the dataset of natural samples. The results of the SIP measurements, partly performed with the ST.sip13 system and partly with the ZEL-SIP04-V02 system, are provided in the form of resistivity amplitude and phase spectra in Appendix B.

The direct current resistivity of the investigated samples was firstly approximated by the amplitude value measured at 10 mHz (ρ_a). It varies between 3 Ωm and 270 Ωm, and it

---

[8] From now on, the word sample will refer to the material investigated with the SIP technique, i.e., the system composed by both the solid and the fluid phase.

generally increases with ρ_w (Fig. 6.16). At low water resistivity, a linear relationship is observed, which is commonly expressed in the form of the Archie's law (*Archie*, 1942; see equation 2.7). In fact, electrolytic conduction in the fluid phase is the dominant conduction mechanism. At high water resistivity, data points are more dispersed because the surface conduction significantly contributes to the bulk electrical response. This conduction component is affected by the textural and mineralogical composition of the sample, causing a dual behaviour between samples with and without a non-negligible mud fraction.

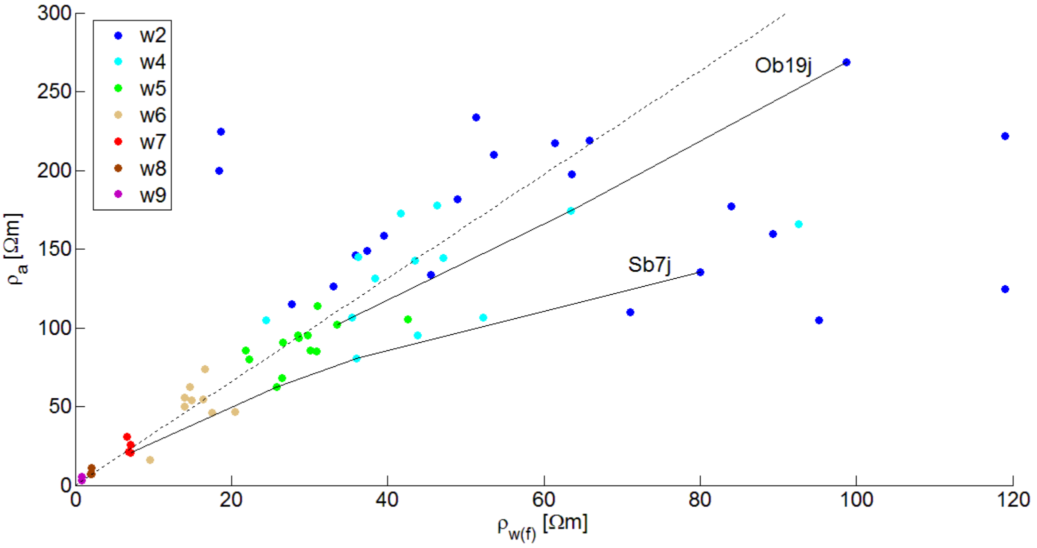

Fig. 6.16 - Approximated direct current resistivity as a function of the final water resistivity. Data points are coloured on the basis of the initial resistivity of the saturation water. The dashed line traces the Archie's law (*Archie*, 1942) for a porosity of 0.40 and a cementation exponent equal to 1.3. The solid lines highlight the trends of a sand (Ob19j) and a muddy sand (Sb7j).

The examples reported in Fig. 6.16 are representative for this difference. The sample Ob19j is a very slightly muddy sand (M=3%) and the data points corresponding to the tests performed with different waters lie on an almost straight line. On the opposite, the sample Sb7j with M=12% departs from the linear relationship and reduces the slope of the curve at increasing water resistivity. Of course, variations in porosity between experiments conducted with different water resistivity can contaminate the trends, but in general they are small and the observed behaviour is in accordance with previous studies (*de Lima et al.*, 2005; *Mele et al.*, 2014).

The dual behaviour becomes even more evident when observing the sand-clay mixtures (Fig. 6.17). Here, the sample M50 follows the linear Archie's law, whereas the samples M5 and M05 do not show significant differences in the DC resistivity for the different saturation waters. In addition, the highest the amount of clay in the sample, the highest is the reduction between the initial and the final water resistivity and the smallest is the difference among the final water resistivities.

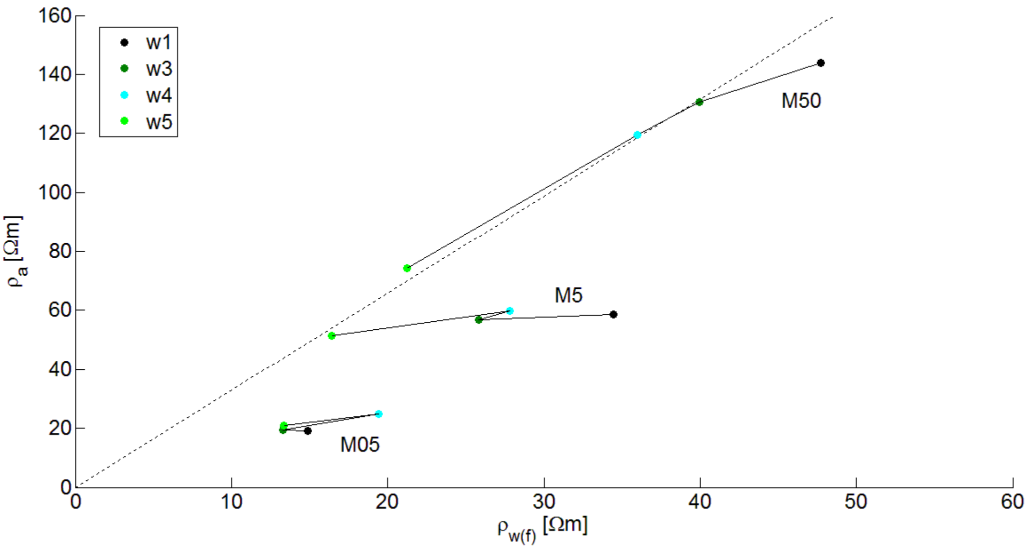

Fig. 6.17 - Approximated direct current resistivity as a function of the final water resistivity for sand-clay mixtures. Data points are coloured on the basis of the initial resistivity of the saturation water. The dashed line traces the Archie's law (*Archie*, 1942) for a porosity of 0.40 and a cementation exponent equal to 1.3.

Resistivity also decreases with increasing frequency (Fig. 6.18a). The relative reduction in resistivity amplitude between 10 mHz and 10 kHz varies from 1% to 42% for the investigated samples and it is directly correlated with the amount of silt and clay (Fig. 6.19). In fact, the fine-grained component is largely responsible for charge storage that in turn produces a frequency-dependent modification of the electrical field. However, some samples show an anomalous behaviour and deviate from the regression line of Fig. 6.19.

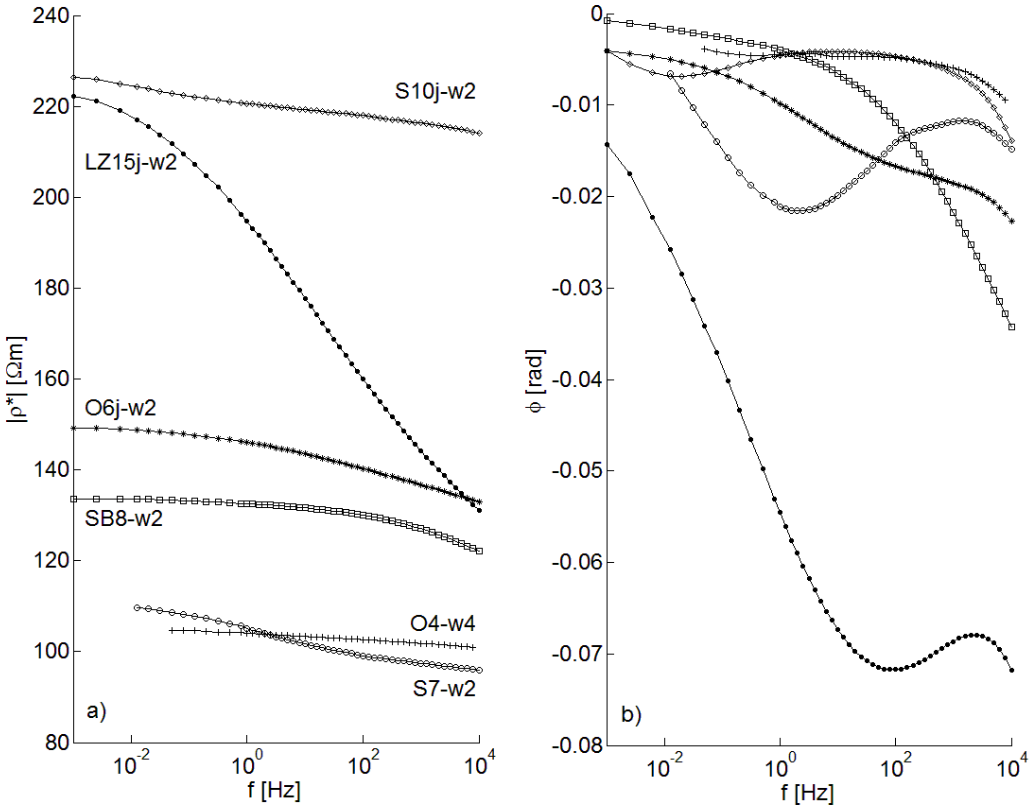

Fig. 6.18 - Resistivity amplitude (a) and phase (b) spectra for six illustrative samples of the natural samples.

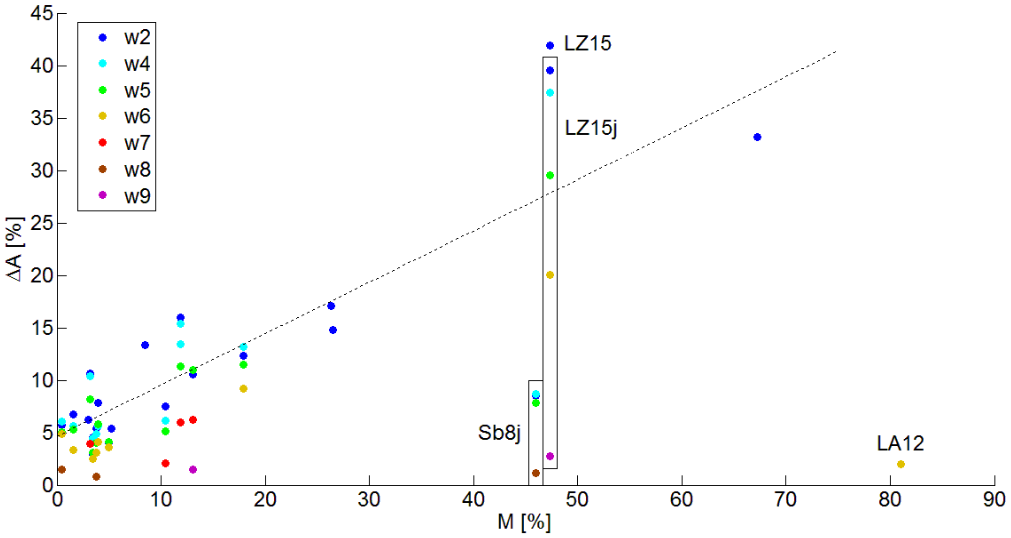

Fig. 6.19 - Relative resistivity amplitude reduction with frequency as a function of the mud content (silt and clay). Samples are coloured on the basis of the initial resistivity of the saturation water. The dashed line is the regression line for w2-samples (R^2=0.69 and R^2=0.87 excluding the samples LZ15, LZ15j, and Sb8j).

For example, the samples LZ15 and Sb8 have a similar mud content but they have different porosity (0.50±0.05 for LZ15; 0.36±0.05 for Sb8). Thus, a tentative explanation for their different behaviour can be searched in the effect of the fine fraction distribution within the sandy framework. In fact, the porosity of Sb8 is indicative of a grain-sustained structure, while the porosity of LZ15 suggests the presence of a significant amount of clay within the pores of a grain-sustained structure (Fig. 6.11). In addition, the mineralogical composition could also contribute to the observed difference. The amplitude reduction is also related to the water resistivity, with smaller variations between low and high frequency associated with low water resistivity, where electrolytic conduction, which is almost independent from frequency, dominates. This dependence is strongly emphasized by sample LZ15j.

Similar information are brought by the plot of the phase values or the imaginary component of conductivity at a fixed frequency against the mud content. For the investigated dataset, the best linear regression fitting was obtained with the imaginary component of electrical conductivity at 1 kHz and at 10 kHz (R^2=0.82, for the w2-saturated samples). A similar relationship was reported by *Slater et al.* (2006), and *Slater and Glaser* (2003), as a power-law dependence of the imaginary component of conductivity at 1 Hz on the specific surface area per unit pore volume, which is related to the fine-grained component content (and mineralogy). Instead, the power-law relationships reported by *Slater and Glaser* (2003) between the imaginary component of conductivity and the characterisitic gran diameters d_{50} and d_{90} for a set of 12 unimodal sandy samples were not observed. This can be due to the wider textural range of the present dataset.

The phase spectra showed a much larger behavioural variability than the amplitude spectra (Fig. 6.18b). In the following, the spectral behaviour of six samples is described in more detail to qualitatively highlight differences between samples:

- LZ15j-w2 is characterized by very high absolute phase values and by the presence of a phase minimum (peak) located between 10 Hz and 100 Hz. It is representative of LZ15, LZ15j (excluding LZ15j-w9) and LZ16 samples;
- S7-w2 shows a peak around 1 Hz, and so do O5-w2, O3-w2, and the other S7 samples, even though with different absolute values;
- S10j-w2 has a peak of relatively low magnitude in the lowest frequency region, i.e., around 10 mHz, and the samples O1, O2, Ob18j, S9, Sb9j, S10, Sb10j, S11 also show a phase peak below 1 Hz when saturated with resistive waters (w2, w4, and sometimes also w5 and w6). The ST.sip13 system does not provide data below 10 mHz and this low-frequency peak is therefore not properly recognized in some cases;
- O6j-w1 is representative of samples with a monotonic decrease of the phase, such as Ob19j, Sb17j, LZ13, LZ15j-w9, and Sb9j-w9;
- Sb8j, even if it shows a phase decrease without peaks, is peculiar and differentiates from the previous group since its phase spectrum has a pronounced downward concavity, so as LZ14;
- O4-w4 shows an almost constant phase spectrum which is similar to the behaviour of samples O1, O2, O4, Ob18j, S10, Sb10j, S11, when saturated with conductive waters, and LA13.

This large variability of the phase spectra suggests that it is possible to use the spectral information in order to achieve a more detailed characterization of the samples in terms of textural, structural, and mineralogical properties, and chemical properties of the fluid phase, and supports the added value of SIP as compared to DC analysis.

6.3 Fitting with Cole-type models

Measured SIP data were modelled with the Cole-Cole (CC) and the Generalized Cole-Cole (GCC) phenomenological models, as described in section 5.1.1. No samples were fitted over the whole measured frequency interval. In fact, even if a few samples (S7, LZ15, and LZ16) showed a type I behaviour in the Argand plot (i.e., a single negative curvature trend as in Fig. 5.1a), the high frequency range was not suited for the fitting with these simple models. The selected stopping frequency varied between 30 mHz and 800 Hz, where the highest values correspond to type I samples, the lowest to type III samples, and the intermediate to type II samples. In 36% cases also a starting frequency different from the first available measured point was selected, in order to remove anomalous values. In these cases, the starting frequency varied between 20 mHz and 126 mHz, with a mean value of 40 mHz.

The fitting quality was evaluated through the RMSE* (equation 5.7). A RMSE* < 1 ensures that the fitting error is lower than the measurement error. However, since the selection of the interval to be fitted was done manually for each analysed sample, it is possible that the measure of the fitting error partly includes also an error related to this choice, even if different selections were tested in order to limit this drawback. Anyway, the fitted interval is equal for the CC and GCC models and a comparison between them remains possible. RMSE* varies between 0.05 and 33.78 for the CC model and between 0.04 and 25.38 for the GCC model. On the average, RMSE* is equal to 2.07 and 1.30 for the CC and GCC case, respectively. RMSE* of GCC model is equal to the CC one for 13 samples and lower for 93 samples (Fig. 6.20), as it was expected from the higher flexibility of the GCC model due to the presence of 5 fitting parameters instead of 4.

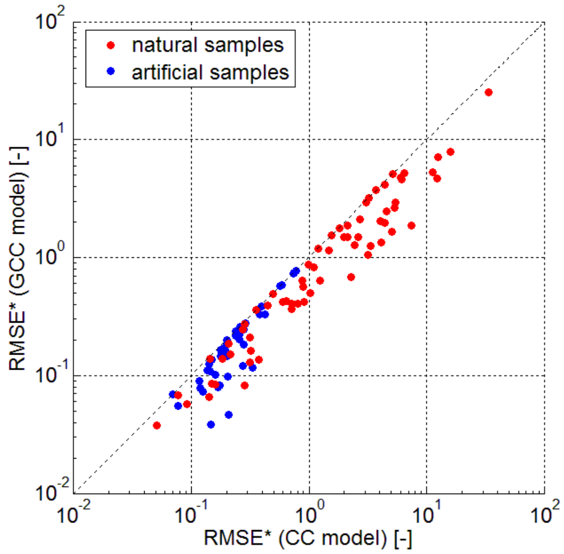

Fig. 6.20 - RMSE* of the GCC model as a function of the RMSE* of the CC model. Red dots correspond to the natural samples, blue dots to the well-sorted sands and sand-clay mixtures. The dashed line highlights the 1:1 ratio.

The distribution of the error among the samples does not follow a very regular trend, neither with the sample's type nor with the pore water resistivity, and is quite comparable between the two tested models (Fig. 6.21).

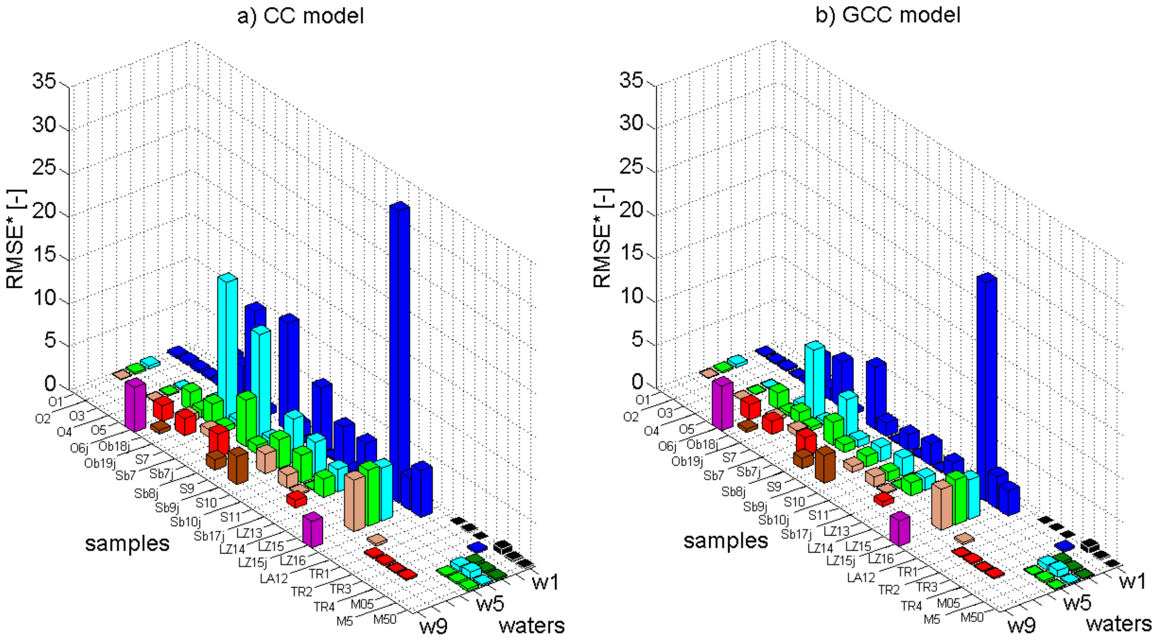

Fig. 6.21 - RMSE* of the CC model (a) and the GCC model (b) for each sample-water system.

In general, the fitting for the amplitude component is optimal for both models, with average errors of 0.52 for CC and 0.54 for GCC, and only 16 samples with RMSE* > 1 in both cases. The difference in the global error between CC and GCC models is mainly due to the phase component, with 30 samples not properly fitted with the former and 18 with the latter. For this component, the average errors are 1.65 and 1.30, respectively, with the maximum values associated to samples LZ15 and LZ15j.

The presence of samples properly fitted in the resistivity amplitude component, but not in the phase component, led to the evaluation of a multi-objective optimization as a tool to reduce the phase error to the detriment of the amplitude error. Thus, equations (5.8) and (5.9) were used as separated indicators of the goodness of fit. Among all the possible solutions, those belonging to the Pareto set were selected. The Pareto set resulted non-empty in 73 out of 106 cases with the CC model and in 84 cases with the GCC model, and included a number of solutions variable between 1 and 177 in the CC model, with an average value of 8 for natural samples and 24 for artificial samples, and between 1 and 1896 in the GCC model, with an average value of 33 for natural samples and 170 for artificial samples. As explained in section 5.1.1, the closest solution to the origin (RMSEam = 0; RMSEph = 0) was chosen as the representative one, whereas the others were used to determine the uncertainty of the model parameters. The representative solution of the Pareto set corresponds to the best fitting solution of the single-objective optimization for most of the samples. Furthermore, even when the two solutions are different, significant changes in the RMSE*, i.e., an error reduction below 1, never occur.

An improvement is observed for samples O6j-w5, Sb7j-w4, Sb10j-w4, Sb17j-w4, and LZ16-w2 for the GCC model, but related only to RMSEam or RMSEph and not to the corresponding bulk RMSE*. Actually, the key point of the multi-objective optimization lays in the parameter uncertainty estimation, rather than in a significant improvement of the fitting.

The direct current resistivity shows always a unimodal distribution in the solutions of the Pareto set and an average variability of only 1 Ωm. The representative values for CC and GCC model are also perfectly comparable (Fig. 6.22a). On average, ρ_0 is 2% higher than the resistivity at 10 mHz, which was previously used as the approximated value.

Chargeability is also usually unimodal along an interval of variability of 0.05 for the CC model and 0.07 for the GCC model. The values associated with the GCC model are equal or larger than the corresponding values of the CC model (Fig. 6.22b).

Within the Pareto set, the range of variation of the frequency exponent c is 0.18 on average for CC model and 0.35 for GCC model, and tends to be larger for artificial samples such as the well-sorted sands. Both unimodal and multimodal distributions are observed. Similar considerations apply also for the frequency exponent k of the GCC model, with an even higher variability (0.64 on average). In the comparison between the characteristic exponent c of the two tested models, similar values are observed between 0 and 0.25, whereas a steep increase of the GCC values occurs afterwards (Fig. 6.22d). For the CC model, $c \leq 0.6$, which is consistent with literature data (*Pelton et al.*, 1978; *Seigel et al.*, 1997). The presence of higher values in the case of GCC model is supported by data collected on a set of 13 mixtures of quartz sand and slag grains that differ in the size and amount of slag grains (*Nordsiek and Weller*, 2008), which are plotted in Fig. 6.22 for comparison.

The less constrained parameters is the relaxation time, which varies on average by two orders of magnitude with multimodal distributions. The larger variability is associated to the samples with a layer of clay or hematite. In general, the GCC values are higher than the corresponding CC values but a good proportionality is observed, except for some artificial samples with low τ_{CC}. Also in this case, the behaviour of data from *Nordsiek and Weller* (2008) and *Kruschwitz et al.* (2010) is well comparable with that of this study (Fig. 6.22c).

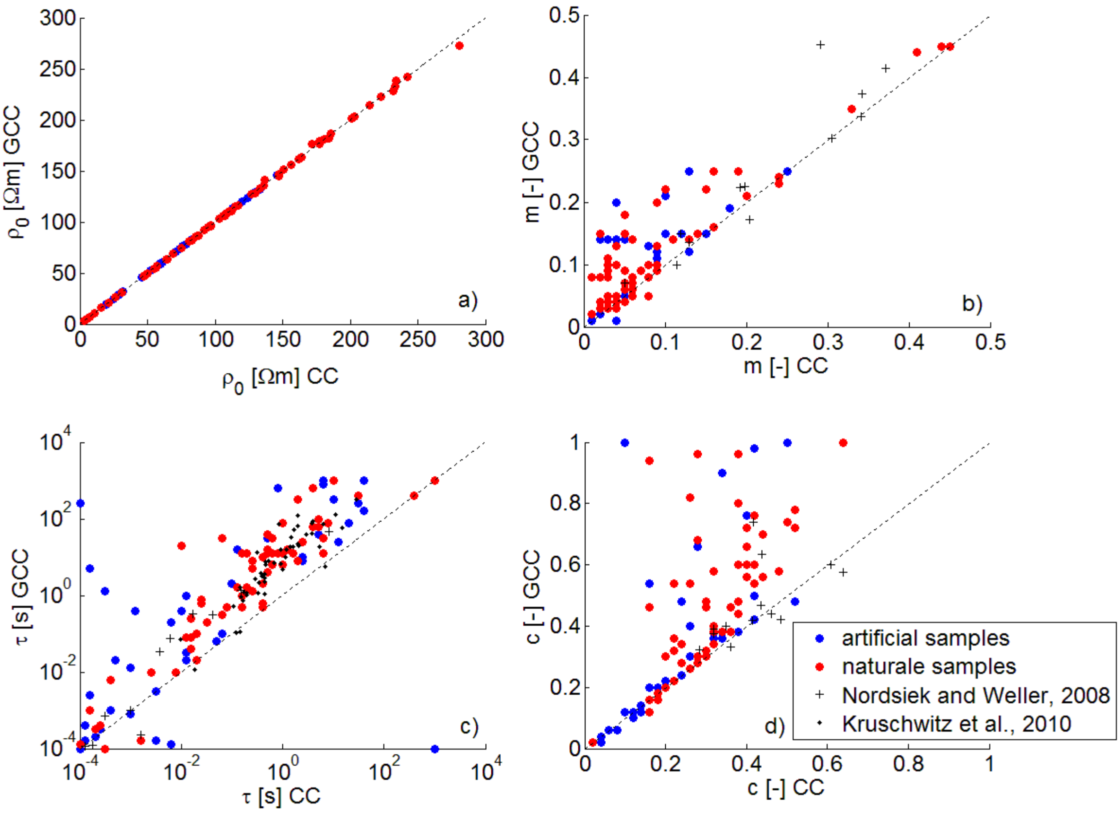

Fig. 6.22 - Comparison of model parameters obtained with the fitting through the CC and GCC models: a) direct current resistivity; b) chargeability; c) relaxation time; d) frequency exponent. Data points correspond to the representative solution of the Pareto set or to the best fitting solution of the single-objective optimization when the set is empty. The dashed lines highlight the 1:1 ratio.

6.4 Fitting with Debye decomposition

The fitting of SIP data from 10 mHz to 10 kHz with the DD approach was conducted with two algorithms, which provided a non-continuous and a continuous relaxation time distribution function, respectively (see section 5.1.2). In both cases, most of the samples have a RMSEam and a RMSEph lower than one (Fig. 6.23). The larger errors associated to the Tikhonov regularization method as compared to the *lsqnonneg* method are due to the regularization parameter. This allows to smooth the fitting curve in order to reduce the high frequency variability on data that is expected to be linked to measurement errors, but of course it results in an increase of the fitting error. In the investigated dataset, the regularization parameter varied between 2 and 15, with an average value of 6 in the natural samples subset and 8 in the artificial sample subset.

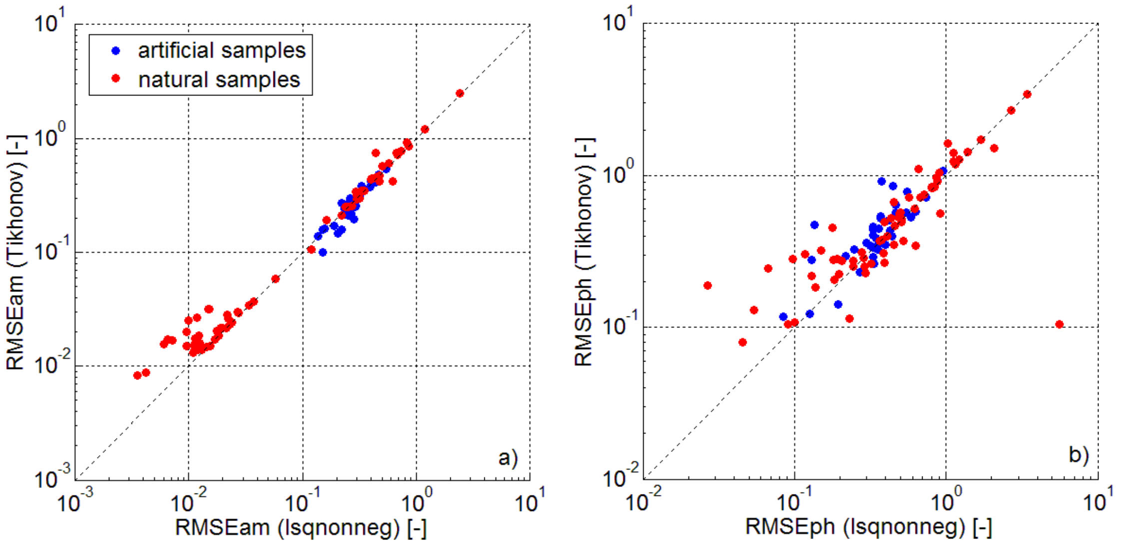

Fig. 6.23 - Comparison of the RMSEam (a) and the RMSEph (b) of the fitting with the Debye decomposition approach using the *lsqnonneg* and the Tikhonov regularization algorithm. The dashed line highlights the 1:1 ratio.

However, the differences in the values of the integrating parameters are mostly negligible, with only a few exceptions. The main example is constituted by Sb9j-w8, a sample with very low resistivity phase values, which cannot be fitted by the *lsqnonneg* method. This results in completely different cumulative chargeability curves and in turn completely different characteristic relaxation times. The remaining samples are gathered along the 1:1 line, with differences mostly included in the same order of magnitude (Fig. 6.24). This overall similarity supported the choice to utilize only the model parameters deriving from the Tikhonov regularization in the following discussion, due to the greater physical meaning of this method.

A direct comparison with the model parameters of the Cole-type models is possible only with ρ_0. The correspondence is satisfactory, with an average difference of 2±3%.

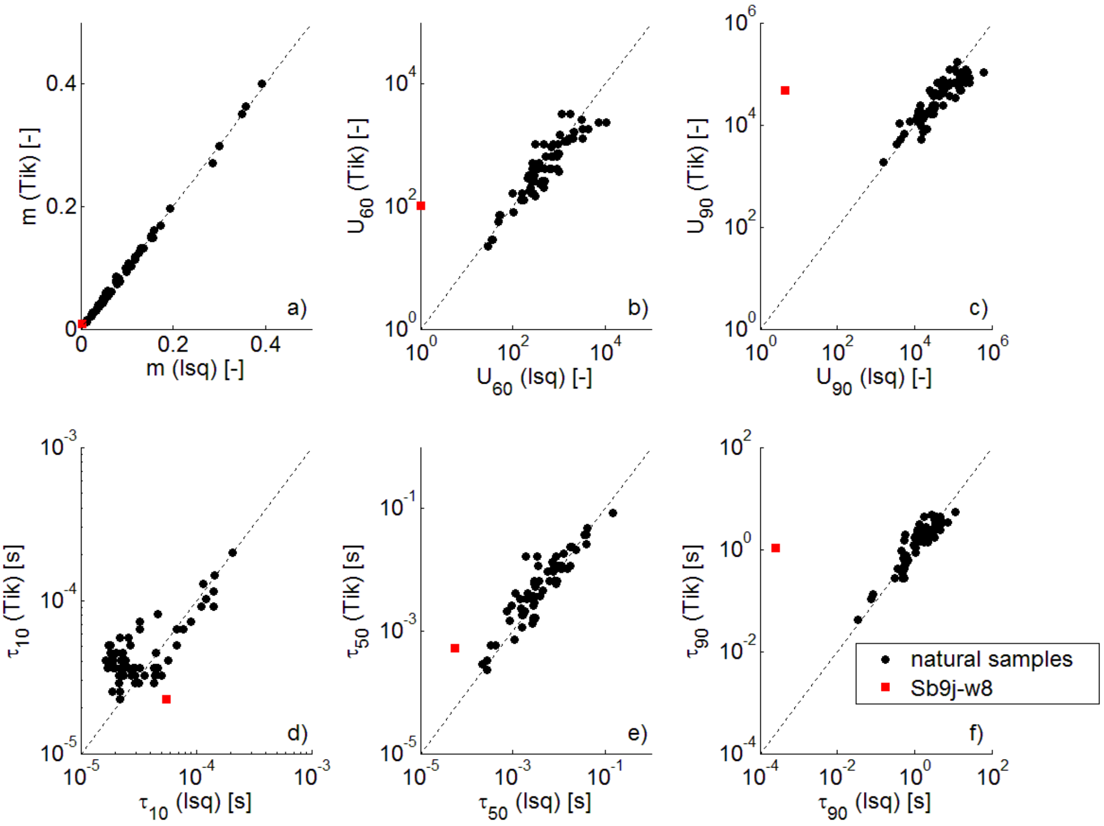

Fig. 6.24 - Comparison of chargeability (a), uniformity coefficients of chargeability curve (b, c), and characteristic relaxation times (d, e, f) obtained with the Debye decomposition approach using the *lsqnonneg* and the Tikhonov regularization algorithm. The dashed line highlights the 1:1 ratio.

The comparison between total chargeability of the DD model and the chargeability of CC or GCC models is equivalent at comparing the relative reduction in resistivity along an ideally infinite frequency range, i.e., the slope of the resistivity amplitude curve, and the relative reduction along a selected interval in the low frequency range where the Cole-type models are applied. Considering the CC model, 34 samples show a low-frequency chargeability higher than the total chargeability, and 32 samples lower; for the GCC model the number of samples are 52 and 14, respectively.

6.5 Multivariate analysis (PCA and CA)

The combination of PCA and CA was applied on the natural samples in order to obtain a samples' classification based on quantitative data rather than qualitative observations. The electrical response variability provided by 12 electrical parameters deriving from raw spectral data and from the fitting with the Debye decomposition approach (see section 5.2.1) was firstly investigated with the PCA. It provided three significant principal components (PCs) considering eigenvalues greater than 1 (Fig. 6.25a) and total explained variance greater than 80% (Fig. 6.25b). These PCs are responsible for about 40%, 37%, and 9% of the total variance of the system, respectively.

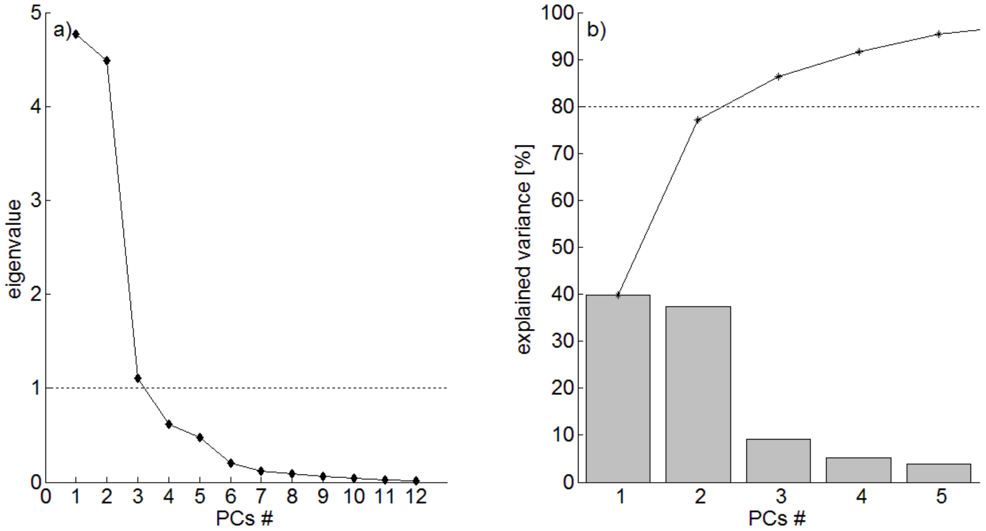

Fig. 6.25 - Eigenvalues of the principal components obtained with the PCA (a); fractional and cumulative percentage of explained variance on the total system variance for the first five PCs (b). Dashed lines represent the thresholds of the heuristic criteria used to determine the number of significant PCs.

Thus, the samples can be projected on new coordinate systems based on these PCs, which allow to deal with the highest variance of the system on a simple plot and to visualize the distribution of the samples with respect to the origin of the system (coordinate 0, 0), which represents the average characteristics of the whole investigated dataset. The relationships between each PC and the original electrical variables are identified through the Pearson correlation coefficient (Fig. 6.26):

- PC 1 is directly related to the curvature coefficient of the chargeability distribution, and inversely related to the relative phase differences at high frequency ($f > 100$ Hz);
- PC 2 is inversely related to the characteristic relaxation times describing the low frequency interval (τ_{50}, and τ_{90}, in 10-based logarithmic form), and to the relative phase difference between 1 Hz and 100 Hz;

- PC 3 is inversely related to the direct current resistivity, with a minor contribution from the total chargeability.

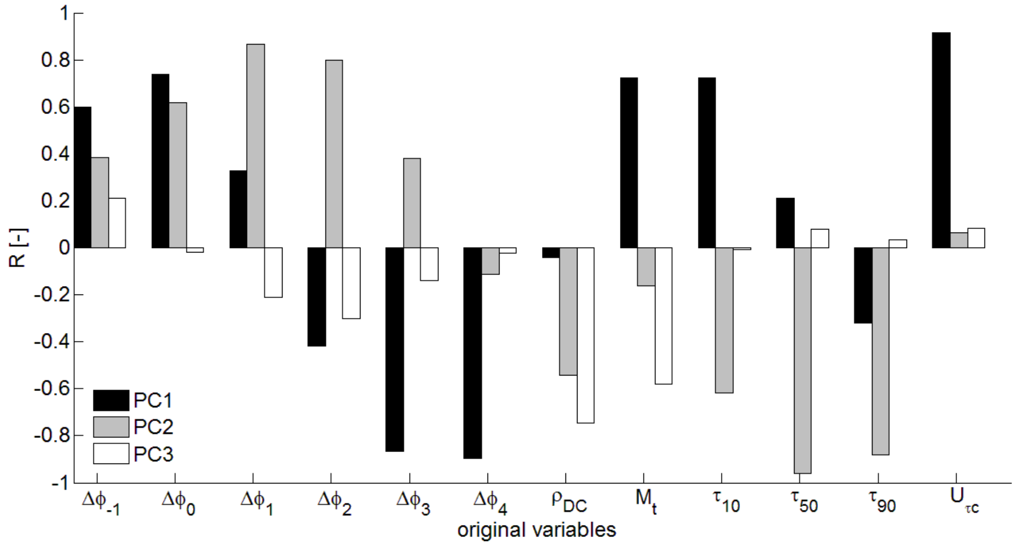

Fig. 6.26 - Pearson correlation coefficients between the original electrical variables and the first three PCs.

In general, all the variables with $R > 0.8$ can be effectively used to interpret the direction of increase of those specific variables, in the new coordinate systems (i.e., PC 1-PC 2 and PC 1-PC 3 in Fig. 6.27).

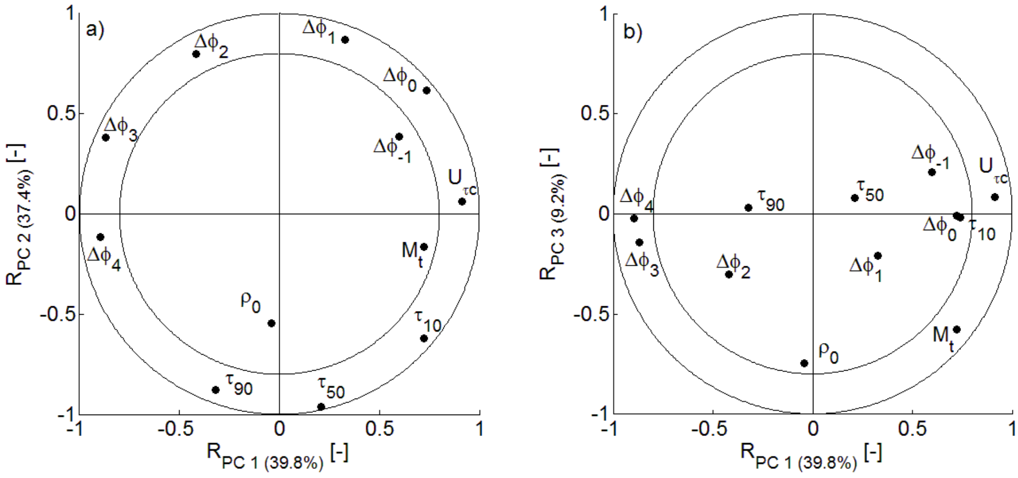

Fig. 6.27 - Position of the original variables in the correlation circles for the system PC 1-PC 2 (a) and PC 1-PC 3 (b). The external circumference draws the limit $R = 1$ and the internal one $R = 0.8$.

With the same input dataset of the PCA, a hierarchical CA with the average linkage method and the Ward's linkage method (equations 5.23 and 5.25, respectively) was performed, obtaining the dendrograms of Fig. 6.28. Here, individual samples are plotted on the left side and then are connected by nodes that are located at a distance proportional to the value of the dissimilarity between them. The subsequent levels of merging regards samples and clusters, up to the merging of all observations in a single cluster.

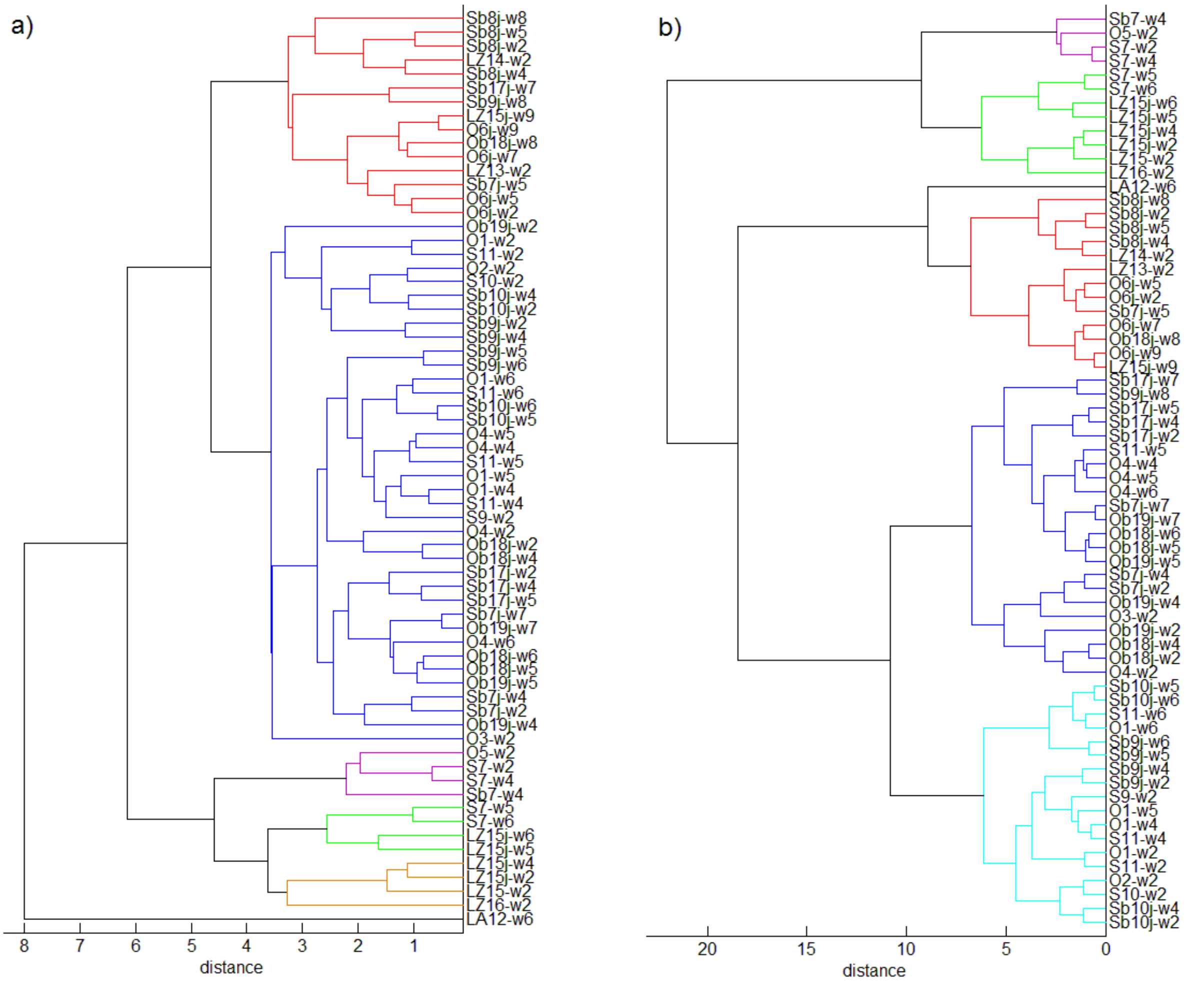

Fig. 6.28 - Dendrograms obtained by the average linkage method (a) and the Ward's minimum variance method (b). Colours refer to the solution with 6 clusters, and highlight the similarities between the clusters' content according to the two algorithms.

The results of the CA are then easily superimposed on the results of the PCA, so that clusters at a specific level of aggregation can be explained in terms of intervals of variability of PCs. In fact, clusters can be visualized in the coordinate systems made of PCs by the mean of different colours and even if they are plotted in systems that account for less than the total variance, the clustering is produced using the whole dataset, i.e., 100% variance. This is the reason for possible occurrences of overlaps among clusters when plotted in PCs systems.

7.5.1 Comparison of linkage methods

In general, the clustering obtained with the average linkage method and with the Ward's minimum variance method are quite similar. The first major difference regards sample LA12-w6, which constitutes a cluster by itself in the case of the average linkage method. Excluding this sample, and thus comparing the content of the clusters with an offset of one cluster (e.g., three clusters for the average method and two clusters for the Ward's method), other differences regard the samples located at the borders of the clusters represented in PCs systems. This is an expected result, due to the presence of a continuous range of variability in the electrical input data, which determines the occurrence of samples that can be associated to more than one cluster according to different calculations of the distance with respect to the other samples. The cophenetic coefficients are 0.80 and 0.71 for the average and the Ward's solution, respectively, and are both considered satisfactory.

Other commonly used linkage methods were also tested, such as the single and the complete methods. The latter is based on the maximum distance between the observations of two clusters and tends to produce clusters equally populated. It has a cophenetic coefficient equal to 0.62 and leads to cluster contents quite comparable with those described for the previous methods. The single linkage merges the objects with the shortest distance. For this dataset, it has a cophenetic coefficient of 0.61, but it is not suited for the aim of the work because it tends to isolate individual samples and maintain all the others in a unique highly populated cluster. Finally, median and centroid linkage methods were excluded because they provided non-monotonic dendrograms.

The cophenetic coefficient is an indicator of the overall distortion of the distances among the samples before and after the merging. However, it does not give any information on the effectiveness of the clustering at a specific level of aggregation. The mean silhouette values can add this information. In Fig. 6.29 it is plotted as a function of the total number of clusters and indicates a better solution related to the average linkage method for a number of clusters lower than 10. In particular, the most significant difference regards a subdivision into 3, 4, or 5 clusters. In fact, according to Tab. 5.1, the average methods provides a reasonable structure, whereas the Ward's method has a mean silhouette value representative of only a weak structure. For the other level of merging both methods are within the same interpretative category. However, a high number of clusters is not suited for a further statistical analysis of data contained in each group, because of the low number of samples that populate the clusters.

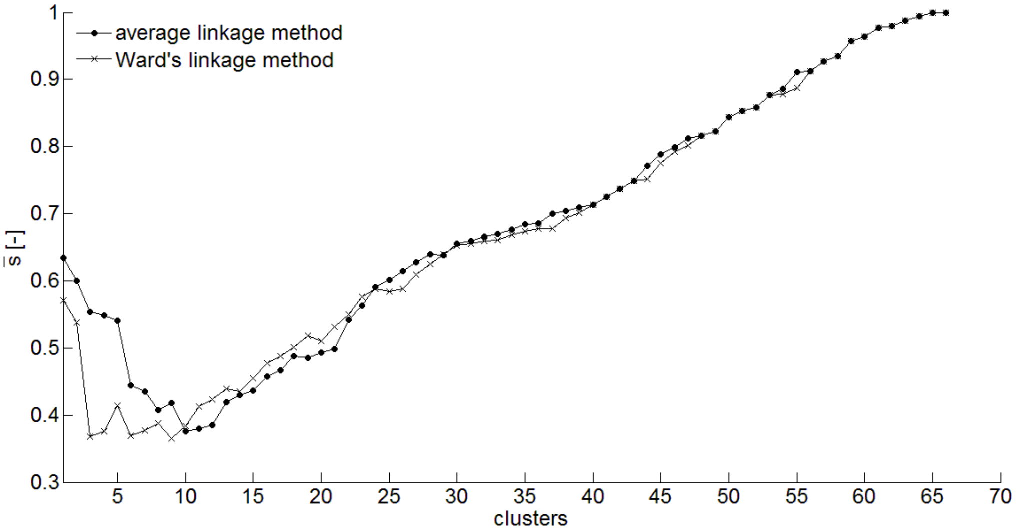

Fig. 6.29 - Mean silhouette value as a function of the total number of clusters selected from the hierarchical dendrogram, according to the average linkage method and the Ward's minimum variance method.

Despite the above considerations, the Ward's method was preferred because it gathers most of the samples of the same material in the same cluster. This means that this algorithm tends to emphasize the similarity of the general spectral behaviour rather than more peculiar characters that are instead considered at a later stage. The average method seems, instead, to reverse this order, firstly separating a smaller number of samples at a greater distance from an hypothetical average group. The clusters' content then converges for the two methods from about 10 clusters, with major differences regarding those samples with a low silhouette value. It is worthwhile noting that the solution with 6 clusters represented in Fig. 7.20b recognizes at least five of the six different spectral behaviours described in section 6.1, while the flat spectra are divided into two clusters and LA12-w6 constitutes a single cluster due to its anomalous phase spectrum. This supports the hypothesis that the CA allows a more consistent classification, especially for those samples that exhibit electrical spectra with intermediate characteristics with respect to more defined behaviours of other samples.

In order to stress the relevance of the classification of samples obtained with the CA, it is useful to observe that similar results cannot be achieved with simple cross plots of two variables, such as a polarization term (e.g., phase at a fixed frequency, characteristic relaxation time, total or normalized chargeability, etc.) vs. a conductive term (i.e., the DC resistivity). In fact, none of these graphs individually allowed to identify more than two groups of samples through definite threshold values. This remark supports the adoption of CA in order to obtain a higher resolution classification.

Chapter 7

Discussion

7.1 Empirical relationships

The advantage of fitting SIP data with simple equivalent circuit models is the opportunity to delineate empirical relationships between circuital elements (i.e., model parameters) and bulk properties of the investigated material, in the same way as the Archie's law describes the ohmic conduction in a porous medium. In the following, the discussion is focused on natural samples, with references to sand-clay mixtures when needed.

The relationship between direct current resistivity and water resistivity has already been addressed in section 6.2. The substitution of ρ_a with ρ_0 obtained by the fitting with the CC, GCC, or DD models does not produce significant changes. Power relationships with high correlation ($R^2 > 0.95$) between ρ_0 and $\rho_{w(f)}$ are observed for the samples of the same material analyzed with waters with different electrical resistivity. Only samples Ob18j-w2 and Sb10j-w2 present anomalous values of water resistivity, which are very low as compared to similar samples, and appear as outliers with respect to the trend determined by the other samples of the same material. No explanation for this anomaly is available at the moment, and also a contamination of the water sample cannot be excluded. For samples with a low amount of mud (O1, O4, O6j, Ob19j, Sb9j, Sb0j, S11, Sb17j) simple linear relationships are also suitable for the investigated interval of water resistivity. Using equation (2.7) and the porosity estimated from the water content at full saturation, the cementation exponent of these samples was calculated and varied between 1.3 and 1.5, in accordance with the values proposed by *Archie* (1942) for loosely consolidated sands. For muddy sands and sandy muds, the calculated exponent is addressed as an apparent cementation exponent (*Worthington*, 1993) and varies between 0.1 and 1.7. Similar ranges are reproduced by the sand-clay mixtures, with average cementation exponent of 1.4 for M50, 1.0 for M5, and 0.6 for M05.

Chargeability is related to the amount of polarisable objects, i.e., charged particles such as clay or metals. In Fig. 7.1, m and m_n for the CC, GCC, and DD models are plotted against the mud percentage, and regression lines are drawn for w2-saturated samples. This selection was made to limit the effect of water resistivity on chargeability, which is visible because data points tend to be ordered with decreasing chargeability at decreasing water resistivity, for the same material. A decrease of total chargeability and an increase of normalized chargeability at increasing water conductivity was observed also by *Titov et al.* (2010), and *Weller et al.* (2011).

Sample Sb8j strongly deviates from the regression lines of Figs. 7.1a, 7.1b, and 7.1c. It has a high mud content (46%) but shows a chargeability comparable to that of clean sands. This anomalous behaviour was already observed in Fig. 6.19, where the relative reduction in resistivity was plotted against the mud fraction. Actually, the relative reduction was calculated as

$$\Delta A = \frac{\rho_{10\,\mathrm{mHz}} - \rho_{10\,\mathrm{kHz}}}{\rho_{10\,\mathrm{mHz}}}, \tag{7.1}$$

which corresponds to the definition of chargeability reported in equation (2.24) if $\rho_{10\,\mathrm{mHz}} = \rho_0$ and $\rho_{10\,\mathrm{kHz}} = \rho_\infty$.

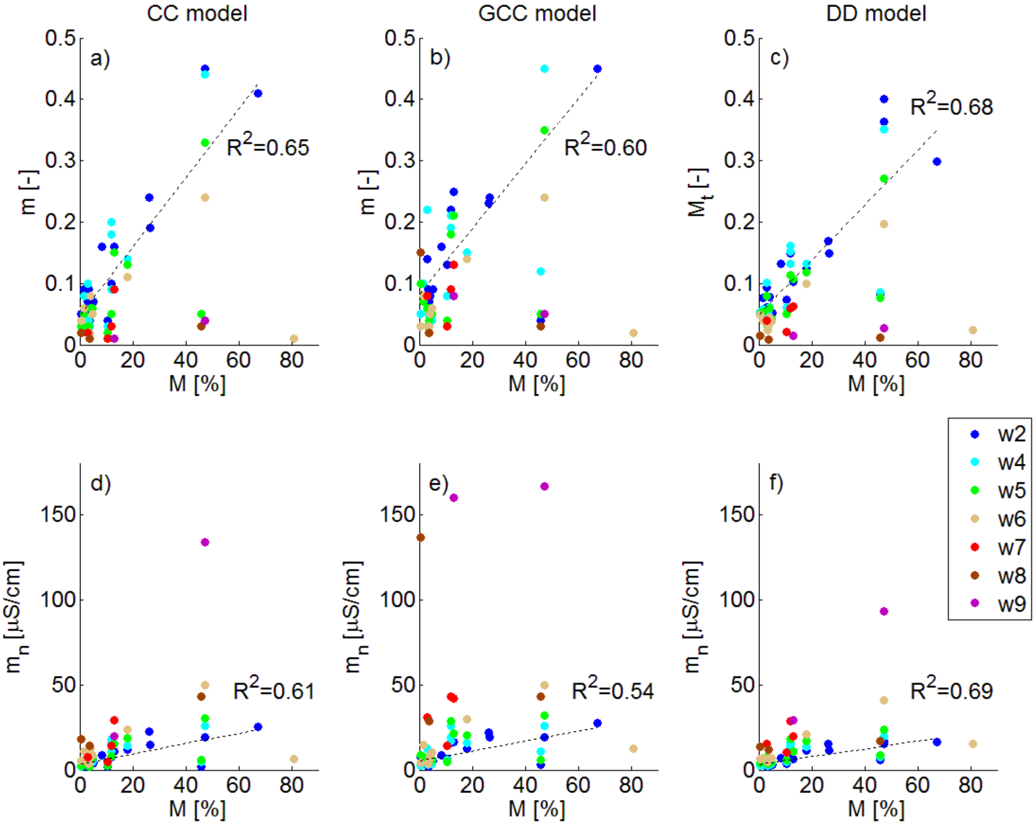

Fig. 7.1 - Chargeability as a function of the mud content for the CC model (a) and the GCC model (b); total chargeability as a function of the mud content for the DD model (c); normalized chargeability as a function of the mud content for the CC (d), GCC (e), and DD (f) models. Samples are coloured on the basis of the initial resistivity of the saturation water. The dashed lines are the regressions for w2-saturated samples.

The best correlation with the mud content is observed for the normalized chargeability of the DD model (Fig. 7.1f). When considering the sand-clay mixtures, R^2 increases to 0.99. This improvement can be associated either to the homogeneity of the clay mineralogy or to the dominance of clay in the mud fraction. A significant statistical correlation between m (or m$_n$) and clay content was reported also by *Titov et al.* (2010) for sandstones and by *Ustra et al.* (2012) for mixtures of Ottawa sand and montmorillonite. Alternatively, the quantification of the polarisable objects present in the investigated samples can be done through the characteristic diameter d$_{10}$. For the subset of natural samples, the coefficients of determination for the regression lines d$_{10}$-m$_n$ are 0.74, 0.71, and 0.73 for the CC, GCC, and DD models, respectively. In the latter case, good correlations are persistent at the decrease of water resistivity, at least till w6 (Fig. 7.2).

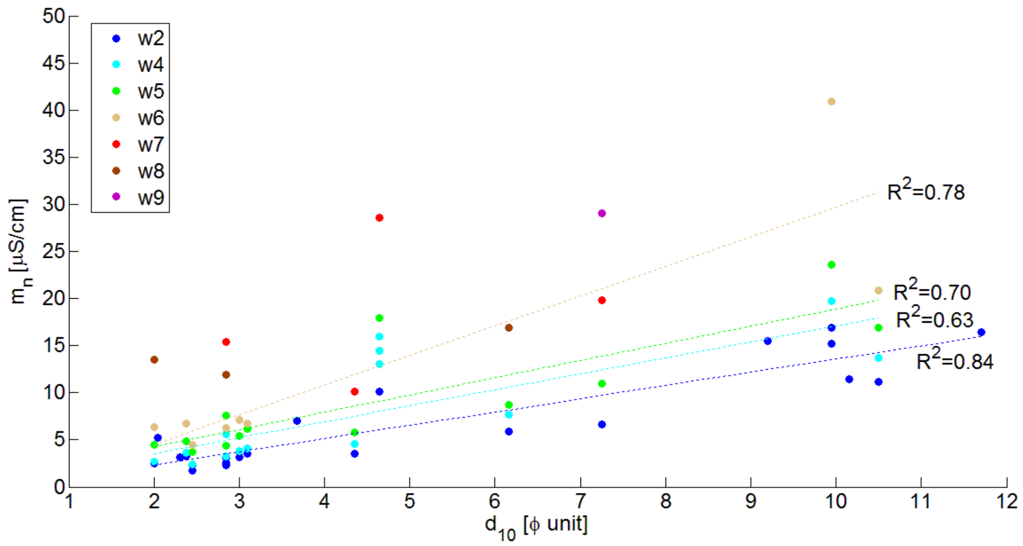

Fig. 7.2 - Normalized chargeability of DD model as a function of the characteristic grain diameter d_{10}. Samples are coloured on the basis of the initial resistivity of the saturation water and the dashed lines are the corresponding linear regressions for w2-, w4-, w5-, and w6-saturated samples.

In the literature, a linear relationship between m_n and surface-area-to-pore-volume ratio (S_p) was derived for organic-rich and iron-rich clay samples by *Mansoor and Slater* (2007), and for a database of unconsolidated and consolidated sandstones by *Kruschwitz et al.* (2010), and *Weller et al.* (2010), whereas *Slater et al.* (2006) identified a power-law dependence for metal-sand mixtures. Many authors substituted chargeability with the imaginary conductivity at 1 Hz: relationships between $\sigma''_{(1Hz)}$ and S_p were reported by *Slater and Lesmes* (2002), *Slater and Glaser* (2003), *Slater et al.* (2006), and *Revil* (2012) for a variable set of samples including sands, tills, and kaolinite-sand mixtures. A linear correlation between m_n and $\sigma''_{(1Hz)}$ was observed on bentonite-sand mixtures (*Slater and Lesmes*, 2002), peat (*Ponziani et al.*, 2012), and saprolite (*Revil et al.*, 2012), and also in the subsets of the present database (Fig. 7.3).

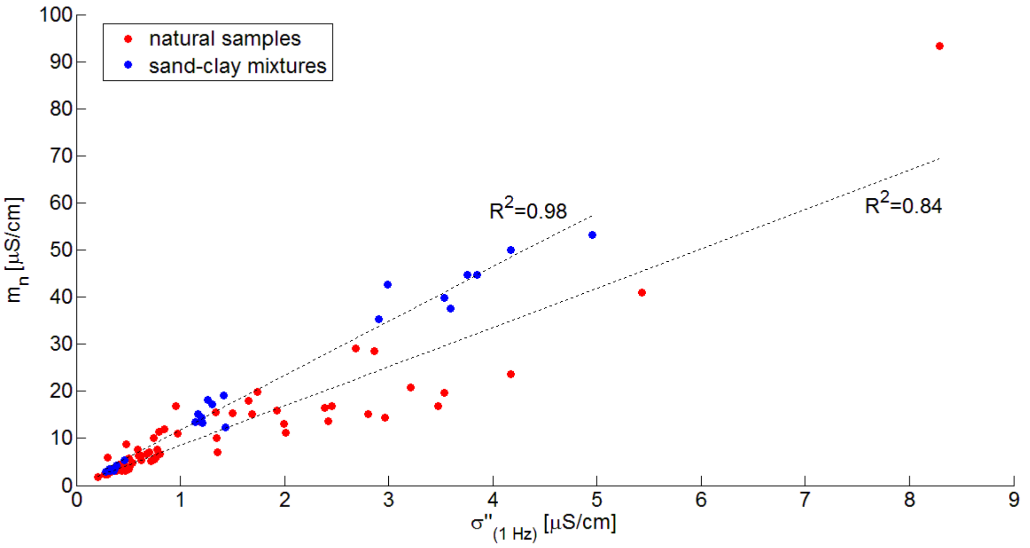

Fig. 7.3 - Correlations between normalized chargeability of DD model and imaginary conductivity at 1 Hz for natural samples and for sand-clay mixtures.

The dependence of τ on a characteristic length scale of the system has been thoroughly investigated in the literature, since it is of primary importance in order to use SIP as an indirect tool to estimate the hydraulic conductivity or permeability (*Binley et al.*, 2005; *Tong et al.*, 2006; *Revil and Florsch*, 2010; *Zisser et al.*, 2010; *Koch et al.*, 2011; *Koch et al.*, 2012; *Revil et al.*, 2012; *Attwa and Günther*, 2013; *Revil*, 2013; *Slater et al.*, 2014). A theoretical study by *Schwarz* (1962) on the relaxation time of a suspension of spherical particles with uniform size in an electrolyte solution, provided the relationship

$$\tau = \frac{r^2}{2uk_bT}, \tag{7.2}$$

where r is the particle radius, and u is the surface mobility of the counter-ions. Starting from this equation, other models were proposed and several empirical expressions were derived by researchers according to their dataset (Tab. 7.1). They are often based on the size of the pore rather than the size of the grain, which is however not available for the present dataset.

relation	**r [μm]**	**R^2**	**dataset**	references
$\tau_{CC} = 7 \cdot 10^{-8} r^{3.62}$	mean pore throat	n.a.	clean sands	*Revil*, 2013; *Revil et al.*, 2013; *Revil et al.*, 2014
$\tau_{CC} = 0.011 r^{1.04}$	pore throat	0.61	sandstones	*Binley et al.*, 2005
$\tau_{GCC} = r^{2.97}$	pore throat (> 5 μm)	0.55	sandstones and building-material	*Kruschwitz et al.*, 2010
$\tau_p = 0.064 e^{0.167r}$	dominant pore throat	0.94	15 sandstones with defined phase peak	*Scott and Barker*, 2003
$\tau_{IP} = 0.882 e^{0.059r}$	dominant pore throat	0.95	6 sandstones	*Titov et al.*, 2010
$\tau_{CC} = 0.007 r^{1.97}$ $\bar{\tau} = 0.008 r^{1.54}$	maximum slag grain mm	0.81 0.91	7 mixtures of sands and slag grains	*Nordsiek and Weller*, 2008

Tab. 7.1 - Empirical relationships between relaxation time and characteristic dimension of the sample' pores or grains, according to different authors. Legend: τ_{CC} relaxation time of the CC model; τ_{GCC} relaxation time of the GCC model; τ_p inverse of the frequency of the phase peak; τ_{IP} modal relaxation time of the distribution obtained by inversion of IP decays; $\bar{\tau}$ mean relaxation time of the DD model; D^S_+ diffusion coefficient of the counter-ions in the Stern layer; r is defined in the table.

In addition, most works were focused on highly homogeneous sets of samples, such as sandstones and sand-clay mixtures, and it is expected that the same relationships cannot be straightforwardly applied to the present database constituted by unconsolidated samples with very different grain-size-distributions and a possible occurrence of more than one characteristic length scale. Actually, the relaxation time of the CC and GCC models tends to increase with the characteristic grain diameter d_{10} (Fig. 7.4). The effect of water conductivity is not clear, because no regular trend is visible for all samples. The τ values of some samples are very similar for all tested waters, whereas big differences are evident for other samples. For this reason, the regression line was calculated only for the w2-saturated samples and has $R^2 = 0.62$. As in the case of chargeability, the variability of water resistivity is reduced by this selection, but is not completely eliminated, because different rates of dissolution of salts from the solid phase into the electrolyte were observed for the different samples, resulting in different values of final water resistivity. In addition, it is important to consider that for fine-grained samples, such as S7, Sb7, Sb8, LZ14, LZ15, and LZ16, d_{10} is an approximated value since the cumulative granulometric curve does not cross the corresponding threshold.

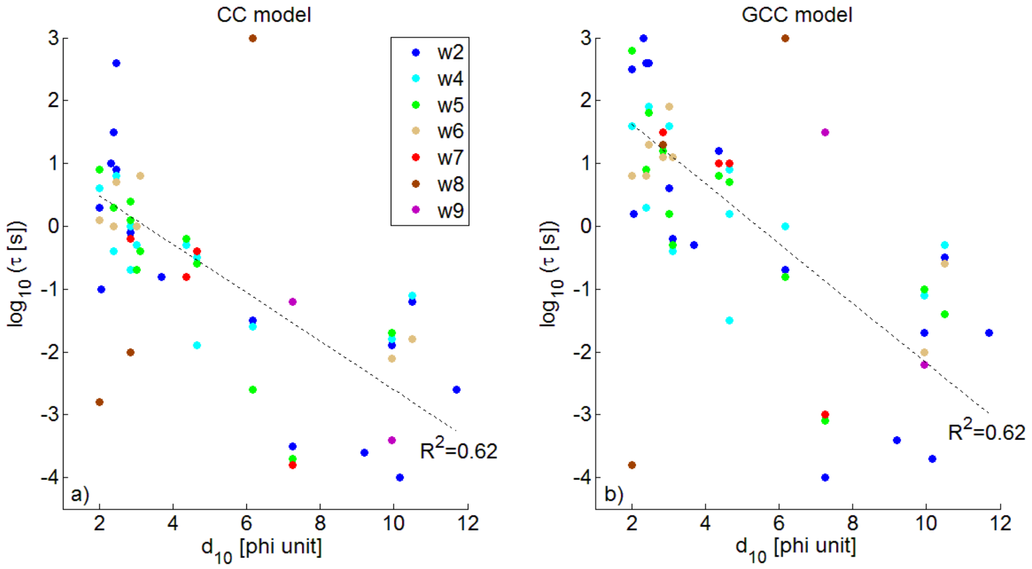

Fig. 7.4 - Relaxation time as a function of the characteristic grain diameter d_{10} for the CC (a) and the GCC (b) models. The diameter is expressed in phi units and is thus inversely ordered. Samples are coloured on the basis of the initial resistivity of the saturation water. The dashed lines are the regressions for w2-saturated samples.

A better correlation is observed between τ and U_{90} for the CC model (Fig. 7.5). Since the uniformity coefficient is calculated as the ratio between d_{90} and d_{10}, the approximation is persistent also in this case. Unfortunately, a cross reading of these graphs cannot be used to increase the predictive power of the relationships, because samples with a wide grain-size-distribution always include a non-negligible mud component, whereas samples with unimodal distribution are always sandy samples, in the analyzed database.

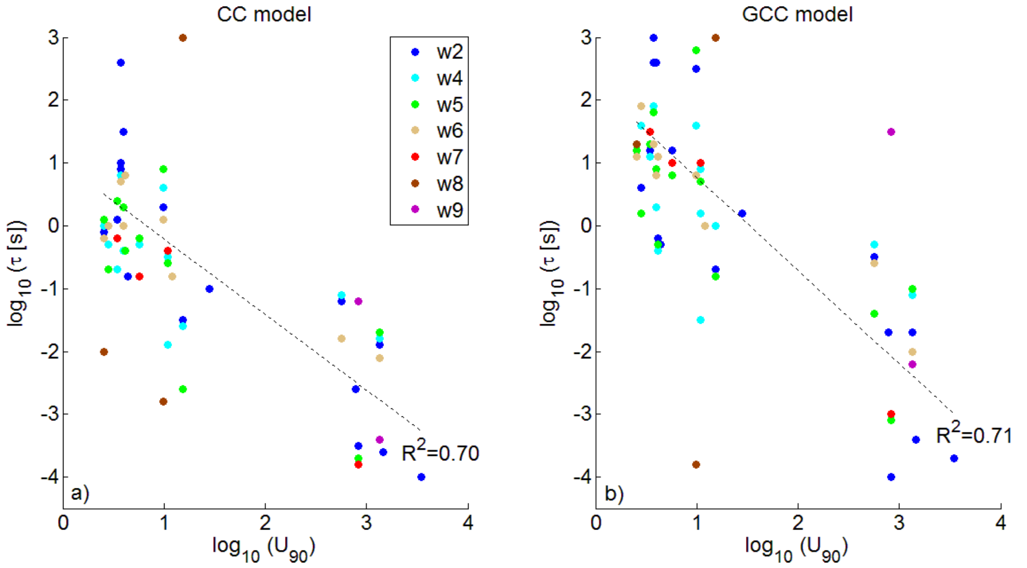

Fig. 7.5 - Relaxation time as a function of the uniformity coefficient U_{90} for the CC (a) and the GCC (b) models. Samples are coloured on the basis of the initial resistivity of the saturation water. The dashed lines are the regressions for w2-saturated samples.

In the case of the DD approach, several characteristic relaxation times are available for each sample. They are determined in correspondence of fixed thresholds on the cumulative chargeability curve, in such a direction that lower thresholds correspond to the high frequency and higher thresholds to the low frequency portion of the spectrum. Neither any of these value, nor the mean relaxation time defined in equation (5.18), is significantly correlated with a characteristic grain-size. However, the 10-based logarithm of the uniformity coefficient $U_{\tau 90}$ is inversely correlated with the 10-based logarithm of the coarse-to-fine ratio $\Gamma_{0.125}$ (Fig. 7.6). This means that the finer the sample the wider the chargeability distribution and the larger the uniformity coefficient relative to the relaxation times.

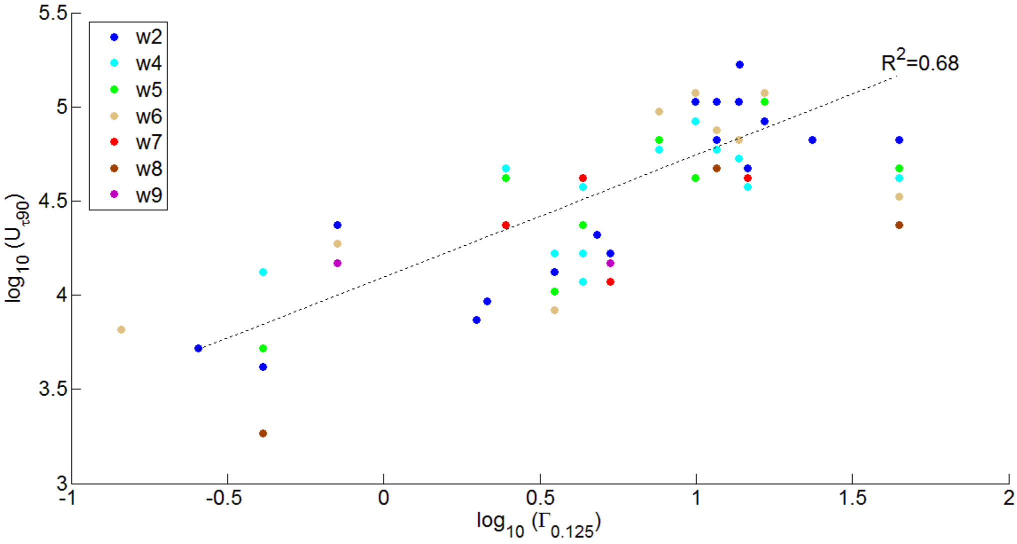

Fig. 7.6 - Uniformity coefficient relative to the relaxation time as a function of the coarse-to-fine ratio. Samples are coloured on the basis of the initial resistivity of the saturation water. The dashed line is the regression for w2-saturated samples.

The frequency exponents are not correlated with any of the available properties of the sediments and fluids. The theoretical correlation between $U_{\tau 60}$ and c of the CC model derived by *Nordsiek and Weller* (2008) was weakly supported by their experimental data ($R^2 = 0.52$). *Revil et al.* (2014) proposed a correlation between the CC exponent and the cementation exponent of the Archie's law for well-sorted sands and clay-rich materials. Neither this relation is suited for the investigated dataset.

7.2 Interpretation of clusters

The joint geophysical and sedimentological interpretation of the clusters strictly depends on the selection of the clustering level, which can be supported by a specific number of predefined clusters, or by a threshold distance for the maximum intra-cluster dissimilarity. The advantage of the hierarchical procedure is that the choice can be done after the analysis and can change according to the aim of the work. Once the clusters have been selected, a representative electrical and sedimentological characterization is determined for each of them. Of course, this result is related both to the linkage method and to the chosen total number of clusters, with the general consideration that children clusters are more homogeneous than parent clusters for each considered property. At one extreme, a single cluster gathers all the investigated samples and is characterized by the highest possible variability for each one of the considered electrical and sedimentological properties. At the other extreme, the number of clusters can be equal to the number of samples so that each cluster is perfectly informative about the data. Both extreme cases cannot be used in a predictive way to estimate properties of samples not included in the initial dataset.

In order to discuss the relationships between electrical and sedimentological properties, four cases were selected, namely two, five, eight, and eleven clusters. The first case represents the classification with the lowest resolution obtained for the investigated dataset, whereas the other cases constitute local maxima of the mean silhouette graph for the Ward's algorithm (Fig. 6.29). Finally, the last case (eleven clusters) is selected as the value with $\bar{s}$ exceeding the values of the previous cases, on the portion of curve with $\bar{s}$ monotonically increasing. A further increase in the number of clusters was not considered, in order to avoid the formation of many small clusters that strongly overlap in the PC 1-PC 2, PC 1-PC 3, and PC 2-PC 3 systems, meaning that principal component of minor importance should be considered to explain the separation of these clusters. For each analyzed case, Figs. 7.7, 7.8, 7.9, and 7.10 show:

a) the dendrogram, coloured in such a way to highlight the different clusters according to the case under analysis;

b) the sorted silhouette values of the samples within each cluster, with a dashed line at $s_i = 0.5$ to emphasize the threshold for a reasonable clusters' structure according to Tab. 5.1. The sorting helps to visualize the consistency of a cluster in terms of overall area: the greater the coloured area on the positive side and the smaller on the negative one, the greater the similarity of the samples with those belonging to the same cluster and the greater the dissimilarity with samples belonging to other clusters. However, this does not allow to maintain the same order of samples as in subplot (a);

c) the distribution of samples in the coordinate system PC 1-PC 2, with crosses identifying the centroid of each cluster;

d) the distribution of samples in the coordinate system PC 1-PC 3, with crosses as before;

e) the representative grain-size-distribution of each cluster, depicted through the median characteristic grain diameters and the 25th and 75th percentiles (i.e., first and third quartiles, Q1 and Q3, respectively) as horizontal error bars, and the percentage amount of gravel and mud with the corresponding vertical error bars;

f) the statistics concerning the final water resistivity, represented as box plots where the central mark is the median value, the edges of the box are Q1 and Q3, the whiskers extend to the most extreme data-points, excluding outliers, which are plotted as individual red crosses. Outliers are determined as data points larger than $Q3 + 1.5 \cdot (Q3 - Q1)$ or smaller than $Q1 - 1.5 \cdot (Q3 - Q1)$.

The clusters are identified by two numbers separated by a slash, where the first number is the cluster number, and the second is the clustering level identified by the total number of clusters (e.g., 4/5 indicates cluster 4 of the subdivision into five clusters). The first number might change among different clustering levels, even if the cluster's content does not change between two successive classification steps. In fact, the identification numbers are ordered in each case following the intra-cluster variability, i.e., lower numbers correspond to more homogeneous clusters in each specific level of merging.

<u>*1^{st} case: 2 clusters*</u>

The subdivision of the investigated dataset into two clusters distinguishes a group of 12 samples (05-w2, S7-w2,4,5,6, Sb7-w4, LZ15-w2, LZ15j-w2,4,5,6, LZ16-w2; cluster 1/2), mostly located in the fourth quadrant of the PC 1-PC 2 graph (Fig. 7.7c), with PC 1> 2, PC 2 < 2, and no differences with respect to the other cluster on PC 3 (Fig. 7.7d). From the interpretation of Fig. 7.7c with Fig. 6.27, these samples are characterized by high values of characteristic relaxation time τ_{10} ($\log \tau_{10} > -4.29$), i.e., the relaxation time that corresponds to the achievement of 10% of chargeability in the cumulative chargeability curve. This means that these samples demonstrate high chargeability due to polarization effects in the high frequency range. In addition, they are characterized by high values of total chargeability ($M_t > 0.09$) and curvature coefficient ($\log U_{\tau c} > -1.1$). However, these ranges are not completely different from the ranges characterizing cluster 2/2, because the clustering algorithm takes into account all the input electrical parameters. Nonetheless, these parameters strongly affect PC 1 and PC 2 and thus the clusters appear well separated on this plane (Figs. 7.7c, d). The mean silhouette value for the 2-clusters solution is 0.57 (Fig. 6.29). For cluster 1/2, 83% of the samples has $s_i > 0.5$, and 78% for cluster 2/2. Samples with $s_i < 0.5$ are located in the belt between the two clusters both in Fig. 7.7c and in Fig. 7.7d. Looking at the characteristic grain-size-distribution (Fig. 7.7e), the two clusters differ in particular for the percentage of mud, that determines a distinction of muddy sand or sandy mud (cluster 1/2) from sand (cluster 2/2). The error bars also show that (slightly gravelly)-slightly-muddy sand could belong to both clusters, but a difference still remains since the curve of cluster 1/2 is always below the 2/2 one, i.e., is representative of a finer-grained material. On the other hand, the coarse-grained component is similar for both groups of samples, meaning that it does not affect to a considerable extent the electrical data. A drawback of this subdivision regards samples Sb8, which are muddy sands but are located in cluster 2/2, due to the anomalous electrical behaviour already described in section 6.2. Finally, no significant differences in the electrical resistivity of water are observed in this case between the two clusters (Fig. 7.7f).

<u>*2^{nd} case: 5 clusters*</u>

The classification of samples within five clusters is represented in Fig. 7.8a. The clusters of the previous case are subdivided in two and three children clusters, respectively. $\bar{s}$ is lower (0.38), since a higher number of samples can be matched to different clusters. In fact, only 33% of samples have $s_i > 0.5$ (Fig. 7.8b), and mostly belong to the children clusters of cluster 1/2. This subdivision tends to separate the samples with a phase peak between 1 Hz and 10 Hz (cluster 1/5) from those with a phase peak between 10 Hz and 100 Hz (cluster 2/5) and has a strong counterpart in the grain-size curves (Fig. 7.8e).

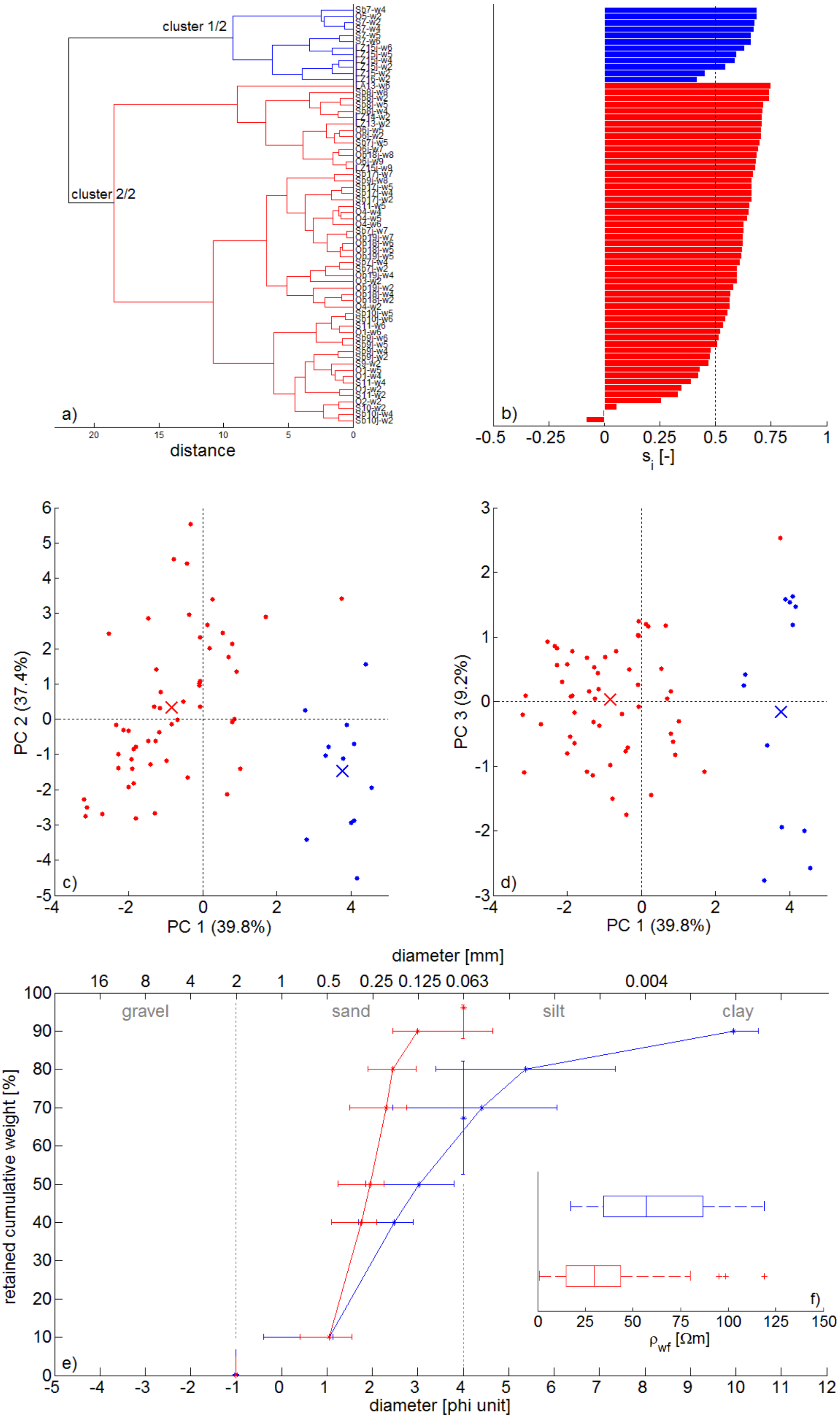

Fig. 7.7 - Dendrogram (a), silhouette values (b), clusters distribution on PCs' systems (c, d), average grain-size-distribution (e), and final water resistivity (f) for samples classified into two clusters.

Here, cluster 1/5 is represented by fine to medium sand with 26% of silt and clay as median value, whereas cluster 2/5 has a wider distribution, with about 7% gravel and 47% mud as median values. The granulometric distribution cannot be considered the unique factor responsible for the differences in the complex electrical behaviour, because, for example, samples S7 are present in both clusters. This is due to the fact that S7-w5 and S7-w6 have a phase peak shifted towards the high frequency with respect to S7-w2 and S7-w4. In general, however, the water resistivity is not significantly different between the two clusters (Fig. 7.8f). Clusters 3/5 and 4/5 have an almost identical characteristic grain-size-distribution, with the only difference in the variability range of the mud fraction, which is a bit larger for cluster 4/5. In the PCs system of Fig. 7.8c, cluster 4/5 is moved towards the third quadrant, whereas cluster 3/5 constitutes the group located around the origin of the system, i.e., the group with the average characteristic of the whole investigated dataset. In terms of original electrical input variables, they differ in the shape of the phase spectra in the frequency range below 10 Hz. In particular, cluster 3/5 has $\Delta\Phi_0$, $\Delta\Phi_1$, and/or $\Delta\Phi_{-1} < 0$, i.e., the samples has a phase peak in this low frequency region, whereas samples of cluster 4/5 have more flat spectra. These characters were already observed in the qualitative classification of samples of section 6.2, but do not find an explanation in the grain-size-distribution. An effect due to a different arrangement of grains is not expected for sandy samples, as it is shown in section 4.6 and also suggested by comparable porosity values. No significant differences in the organic matter content are observed, even if the data of this property are not available for all the samples. Some variations in the mineralogy, with particular reference to the phyllosilicates, are present, but it is not possible to recognize a specific mineralogical association able to explain the presence of a resistivity phase peak of relatively low magnitude in the low frequency domain. Cluster 5/5 is the most heterogeneous one, and is characterized by a highly uncertain grain-size-distribution (Fig. 7.8e). This cluster includes samples Sb8 and LZ14, which are those samples with a phase spectrum with a downward concavity, but also most of the samples saturated by waters with very low electrical resistivity (w8 and w9), independently from their textural composition. Fig. 7.8c shows that cluster 5/5 is characterized by high value of PC 2, which in turn means high value of $\Delta\Phi_1$ and $\Delta\Phi_2$ and low values of $\log\tau_{50}$ and $\log\tau_{90}$. The latter is the relaxation time that corresponds to the achievement of 90% of chargeability in the cumulative chargeability curve and it is thus related also to the polarization at low frequency. Both some fine-grained and coarse-grained materials saturated with conductive waters show low polarizability and flat phase spectra below 10 Hz and a high relative phase reduction between 1 Hz and 100 Hz. Possibly, the effect of water and texture on polarization is not easily distinguishable over a certain threshold of water electrical conductivity. In fact, even if a tendency toward low water resistivity is highlighted by the box plot of cluster 5/5 in Fig. 7.8f, this cluster is significantly different only from cluster 1/5. However, it should be noted that samples with low water resistivity are only a few and the role of water could be partly underestimated, for example avoiding the formation of a cluster only dependent on water resistivity.

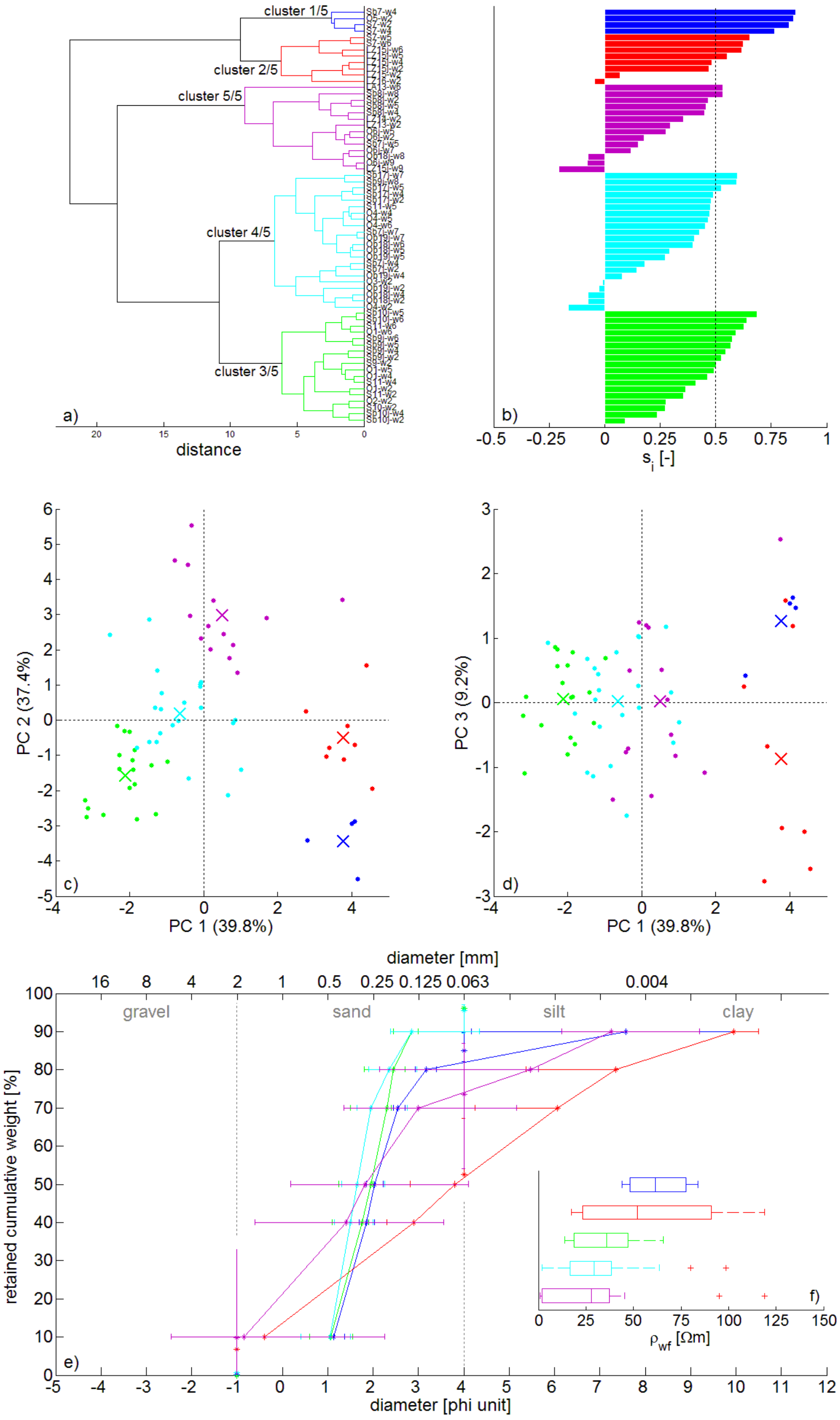

Fig. 7.8 - Dendrogram (a), silhouette values (b), clusters distribution on PCs' systems (c, d), average grain-size-distribution (e), and final water resistivity (f) for samples classified into five clusters.

3^{rd} case: 8 clusters

The subdivision of the dataset into eight clusters produces differences in clusters 4/5 and 5/5 of the previous clustering level. From cluster 4/5, two children clusters are separated mainly on the basis of the resistivity of the saturation water. In fact, all the samples characterized by $\rho_w < 50$ Ωm (i.e., waters w5, w6, w7, w8, and w9) are located in cluster 2/8, whereas most of the others constitute cluster 1/8 (Fig. 7.9a). As before, the separation of these clusters is not perfect in Fig. 7.9f, but the overlapping concerns only the whiskers and not the box edges. In this 8-clusters subdivision, the averaged grain-size-distribution of clusters 1/8, 2/8, and 8/8 is very similar, and if the water can be considered a key factor to interpret the clustering result as far as the separation between clusters 1/8 and 2/8, no explanation was found for cluster 8/8. In this regard, all the observations reported in the previous case for clusters 3/5 and 4/5 apply also here. From cluster 5/5 of the previous classification step, instead, three children clusters are formed: one composed by a single sample (LA12-w6, cluster 5/8), one composed by the samples with a downward concavity of the phase spectrum (Sb8-w2,w4,w5,w8 and LZ14-w2, cluster 3/8), and one with samples O6j-w2,w5,w7,w9, LZ13-w2, Sb7j-w5, and LZ15j-w9 (cluster 4/8). This subdivision helps to reduce the textural uncertainty previously observed. In fact, cluster 4/8 has a median gravel content of 24%, whereas it is negligible for cluster 3/8 (Fig. 7.9e). On the opposite, cluster 3/8 has a median mud value of 46%, whereas the other only 13%, and show non-overlapping variability bars. All the characteristic grain diameters also differ between the two clusters, with cluster 3/8 shifted toward the fine fraction. It is worthwhile noting that the grain-size-distribution of cluster 3/8 drawn from the union of the median values of the characteristic grain diameters is non-monotonic. However, the error bars limit a physically realistic area, where individual monotonic curves can be traced. Cluster 5/8, for which $s_i = 0$ by definition (Fig. 7.9b), identifies the anomalous sample with increasing phase values above 500 Hz, which was separated from the rest of the dataset at the first step of clustering already, when using the average algorithm (Fig. 6.28). This increasing phase value is probably caused by very low water resistivity due to a considerable dissolution of ions in the pore water after the sample preparation, responsible for a decrease in water resistivity which is not perfectly compatible with the proper range of the instrument (see section 4.4). Since other samples have a bulk resistivity lower than the bulk resistivity of sample LA12-w6, the problem is expected to be related to the water itself, i.e., the medium that provide the effective contact between the sample and the electrodes.

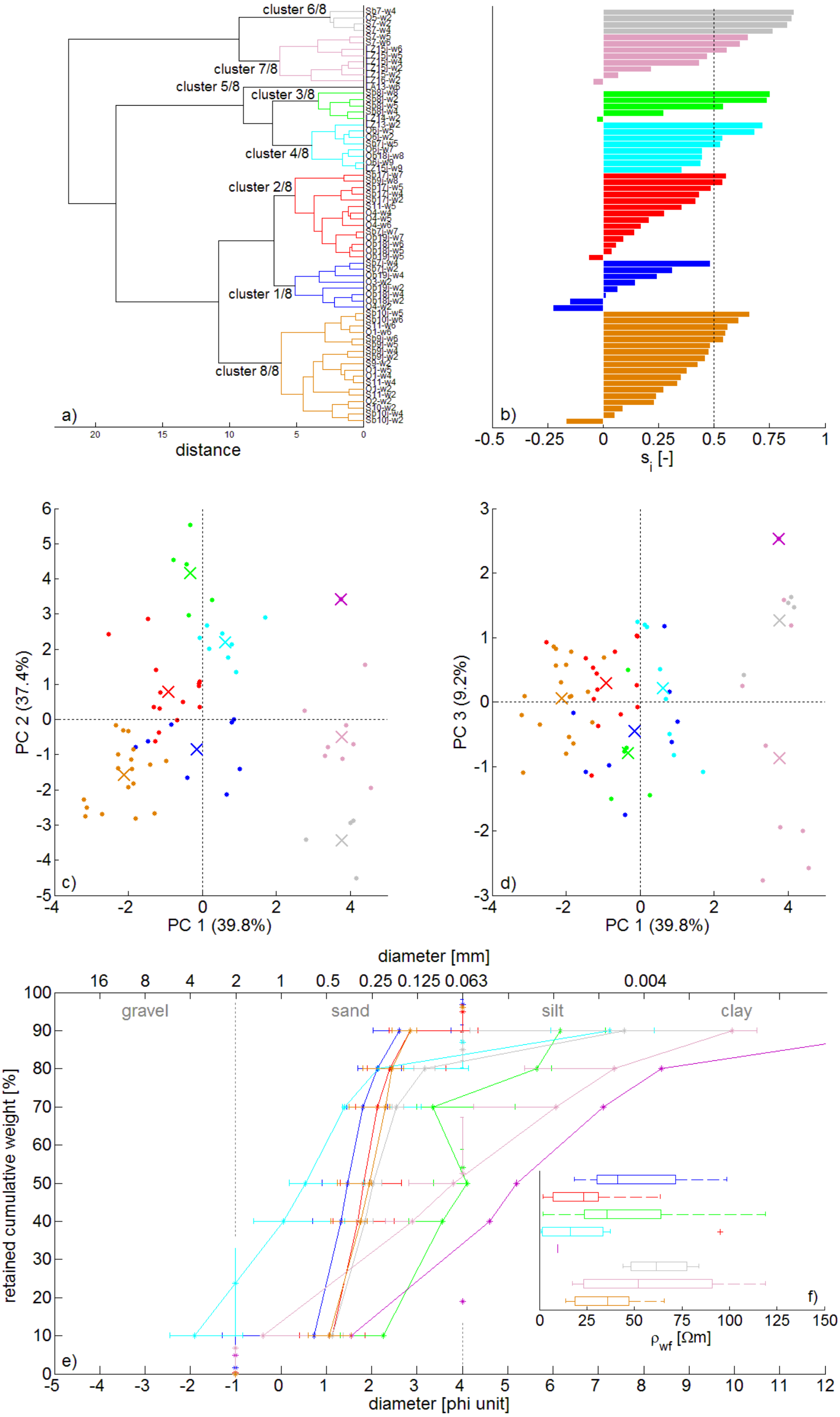

Fig. 7.9 - Dendrogram (a), silhouette values (b), clusters distribution on PCs' systems (c, d), average grain-size-distribution (e), and final water resistivity (f) for samples classified into eight clusters.

4th case: 11 clusters

The next level of aggregation with $\bar{s}$ greater than that of the 8-clusters solution is represented by the 11-clusters solution. The three new clusters are constituted by the samples with low water resistivity within each parent cluster. This difference can be observed in Fig. 7.10e when comparing clusters 1/11 and 2/11, 3/11 and 4/11, 5/11 and 6/11. Box edges (i.e., 25th and 75th percentiles) are never overlapping, and also whiskers include similar values only in one case. The distribution of the clusters in the PCs systems also supports this evidence. In fact, these pairs of clusters are well separated along the PC 3 (Fig. 7.10d), that strongly depends on ρ_0 which is in turn related to ρ_w as shown in Fig. 6.16. It is interesting to note that, at this clustering level, the less consistent clusters are those with the high water resistivity, especially in the case of sandy samples (clusters 2/11, 4/11 and 7/11; Fig. 7.10b).

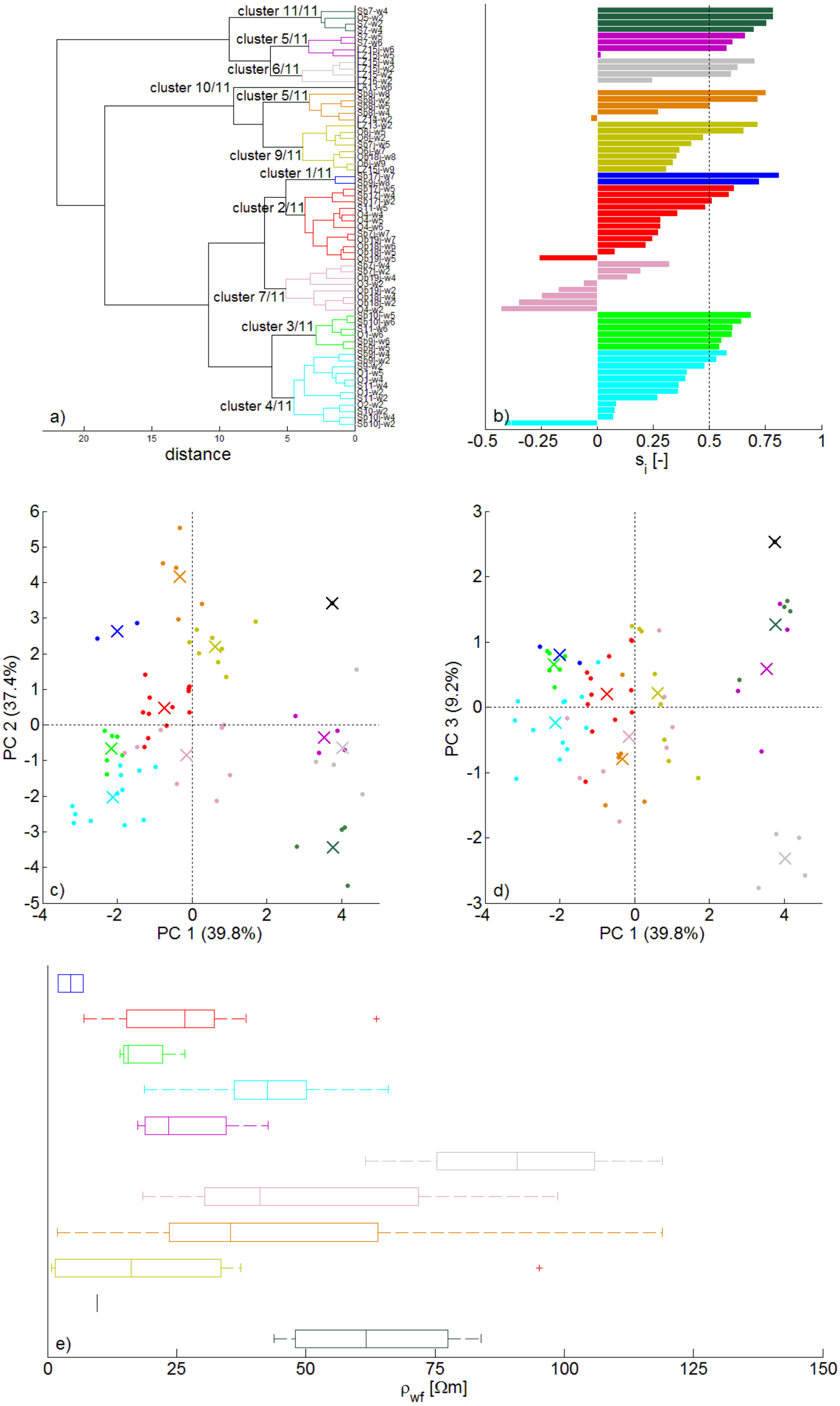

Fig. 7.10 - Dendrogram (a), silhouette values (b), clusters distribution on PCs' systems (c, d), and final water resistivity (e) for samples classified into eleven clusters. The figure of the granulometric distribution is not reported, because the new clusters simply duplicates existing curves of the previous case.

7.3 Validation

The results discussed in the previous section were used to estimate the grain-size-distribution of samples not included in the initial dataset, in order to assess the validity of the joint approach of CA and PCA as a tool for the indirect determination of samples' properties from SIP data. In particular, both a validation on a set of independent samples from the literature and an internal validation performed by removing three samples from the calibration dataset, are discussed[9]. The workflow considers four steps:

- data modelling with DD approach, in the frequency range from 10 mHz to 10 kHz, and with a procedure as much similar as possible to that used for the modelling of the main dataset;
- the determination of the set of electrical parameters constituting the input dataset;
- the assignment of the sample to a cluster, after the selection of a specific level of aggregation, on the basis of the similarity of most of the electrical input parameters;
- the estimation of the grain-size-distribution, water electrical resistivity, and eventually other properties such as porosity, organic matter content, etc., from the cluster identified in the previous step.

The contribution of the CA in this application is clear, whereas a few words are needed in regard to the PCA. It is expected that not all the input electrical parameters leads to the same cluster of assignment, especially when a sample is quite different from those investigated before. PCA provides an order of importance of the input variables, that is useful to support the assignment of a sample to a specific cluster, in addition to the comparison between the calculated values of the PCs and the typical ranges of the clusters. The relative importance of each variable was established by considering the sum of the absolute value of the eigenvectors of each parameter for the first three PCs, weighted on their explained variance. The list so far obtained, in order of decreasing importance, is: $\Delta\Phi_0$, $\Delta\Phi_2$, $\log\tau_{10}$, $\Delta\Phi_3$, $\Delta\Phi_1$, $\log\tau_{90}$, $\log\tau_{50}$, M_t, $\Delta\Phi_{-1}$, $\Delta\Phi_4$, $\log U_{\tau c}$, and ρ_0. As in the case of the textural parameters, the range of variability of the electrical quantities within the clusters are expressed through the percentiles, in the form 25th (50th) 75th percentiles.

---

[9] PCA and CA referring to the complete calibration dataset (66 samples) were used for the validation with external samples and are discussed in the previous section, whereas all the phases of the elaboration were repeated on a reduced calibration dataset of 63 samples for the validation with internal samples.

7.3.1 Validation with literature samples

For the validation of the joint PCA-CA approach with samples independent from the calibration dataset, four examples are presented in the following. Their resistivity amplitude and phase spectra are represented in Fig. 7.11.

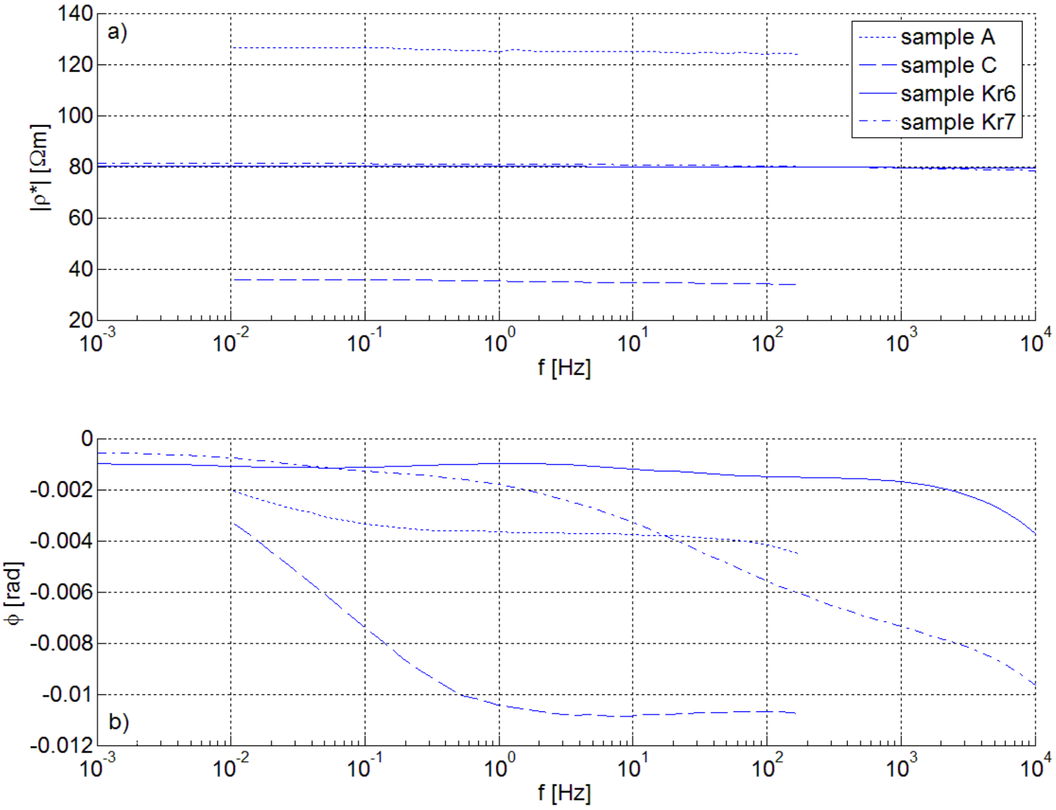

Fig. 7.11 - Resistivity amplitude (a) and phase (b) spectra of unconsolidated sediment samples reported by *Bairlein et al.* (2014; sample A and C) and obtained from Forschungszentrum Jülich GmbH (samples Kr6 and Kr7).

Since no SIP data are available for samples A and C (*Bairlein et al.*, 2014) above 200 Hz, the lacking points were approximated by linearly extrapolating amplitude and phase spectral data with the slope of the last available points. Even though it is not trivial to establish the error associated with this extrapolation, the result was proven to be relatively insensitive to different reasonable simulations of the lacking data. The set of input electrical parameters of each sample was compared with the characteristic range of variability of the corresponding parameters in each cluster, according to the different clustering solutions (Appendix G). A cluster was considered acceptable when the value was included between the 25th and the 75th percentiles (direct compatibility), whereas it was considered possible when the value was outside the range but close to it (indirect compatibility). The cluster, which the validation samples belong to, was chosen by considering the highest number of direct and indirect compatibilities for each cluster, and their position, because the input parameters are ordered with decreasing importance. The litho-textural characterization of the samples was then inferred from the interquartile range (IQR) of the properties of the sediment and the fluid of the selected clusters (Appendix G). For each sample, the table with the values of the input parameters is reported in Appendix H with the corresponding direct and indirect compatibilities of the clusters. Also, the table with the comparison between the measured and inferred textural and fluid properties is reported in Appendix H.

<u>*Example 1*</u>: sample A (*Bairlein et al.*, 2014), i.e., sandy soil sample of the sedimentary basin of Braunschweig (Germany).

In the case of only two clusters the assignment does not present any problem. In fact, cluster 2/2 is directly identified by eight indicators out of twelve and indirectly by other three, whereas cluster 1/2 only by three plus one. Furthermore, the sample is located near the centroid of cluster 2/2 in the PCs system and far from cluster 1/2 (Fig. 7.12a).

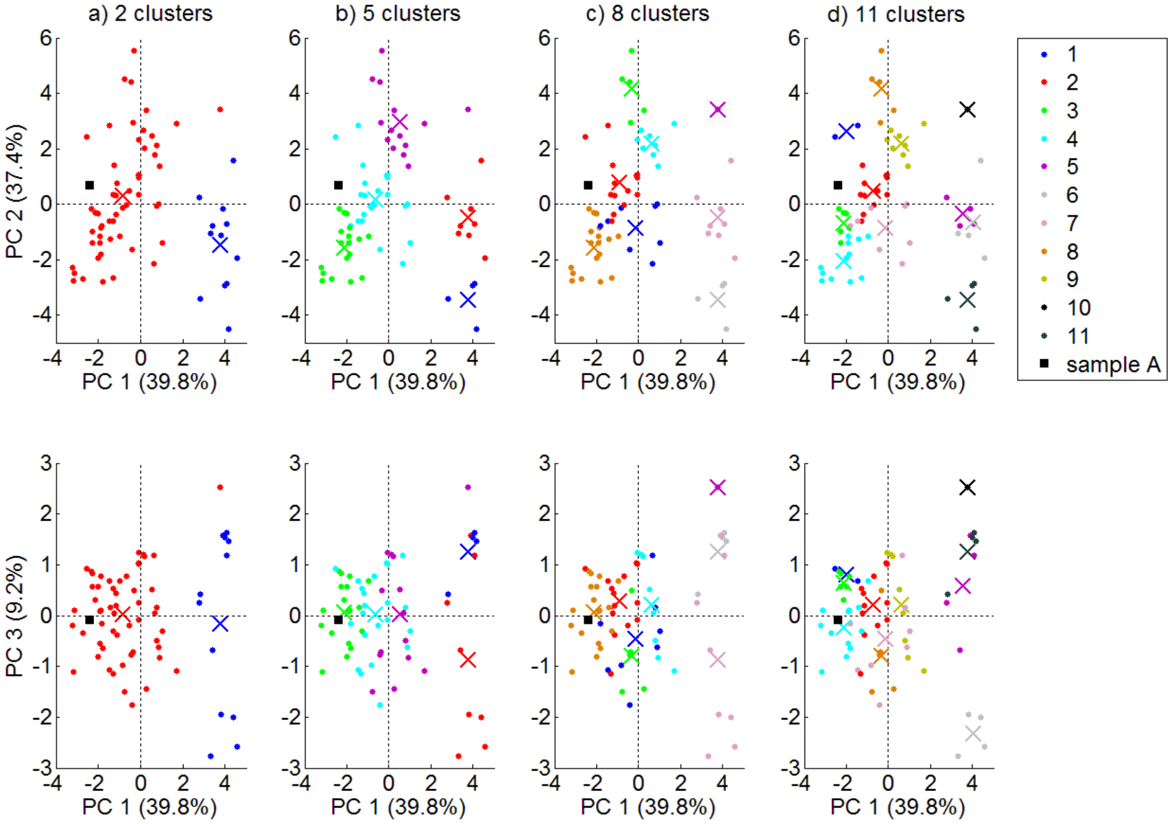

Fig. 7.12 - Position of sample A in the coordinate systems PC 1-PC 2 (upper row) and PC 1-PC 3 (lower row), according to the solutions with a total number of clusters equal to two (a), five (b), eight (c), and eleven (d). The legend refers to the number of clusters and is valid for all the subplots.

In the subdivision with five clusters, cluster 4/5 is identified by six direct and three indirect indicators and none of the other clusters has a similar compatibility. In this case, the importance of PCA to determine the best cluster is apparent, whereas it is not trivial to decide simply by the observation of Fig. 7.12b where the sample is located at the border between cluster 3/5 and cluster 4/5. With the increase of the total number of clusters, the assignment becomes more and more difficult, since more than one cluster is usually acceptable for each input parameter. For example, cluster 1/8 is identified by six direct and two indirect indicators, whereas cluster 2/8 is identified by four and five, respectively. Here, it is not trivial to establish which one should be selected and in fact both these clusters are children of the cluster 4/5 and are characterized by low s_i (Fig. 7.9b), thus meaning that a strong similarity between the samples of each cluster is present. Cluster 2/8 was preferred over cluster 1/8 from Fig. 7.12c. Similar remarks apply for the selection of cluster 2/11 over cluster 7/11.

The characteristic grain-size-distributions of the selected clusters are compared with the measured grain-size-distribution of sample A in Fig. 7.13.

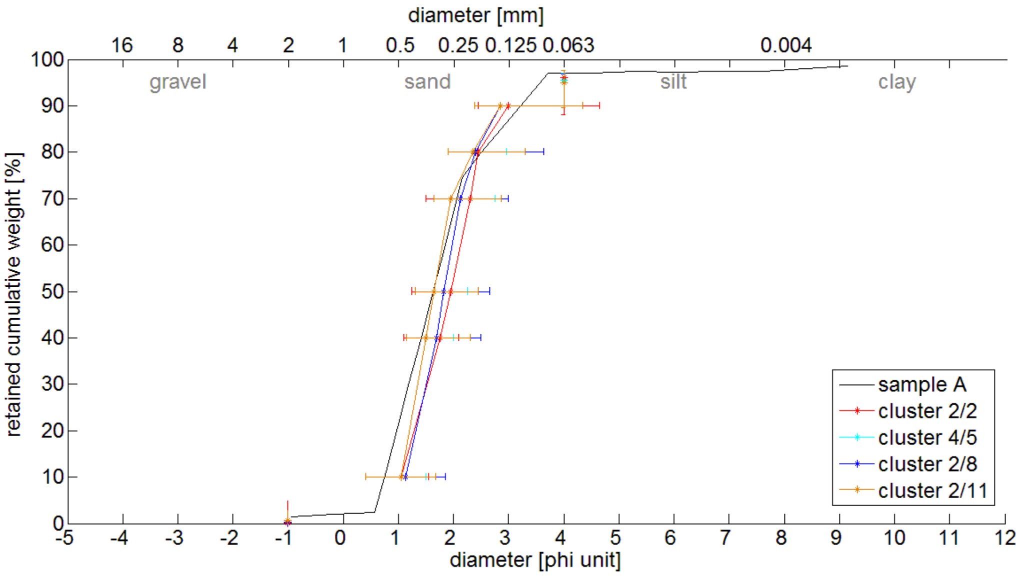

Fig. 7.13 - Comparison of the measured grain-size-distribution curve of sample A with the estimated curves, according to the selected clusters of different merging cases. The grain-size curve of cluster 4/5 is fully hidden by the curve 2/11, so as some portions of the error bars.

All the curves drawn on the basis of the median characteristic diameters are quite similar and well representative for the measured data. The estimated textural composition of the sample ranges between a fine and a medium sand, with a well constrained small amount of gravel. A small overestimation of the amount of silt and clay is instead possible from the interquartile range (IQR) of the mud fraction (i.e., the vertical error bar at diameter equal to 4 phi units in Fig. 7.13) and the characteristic grain diameter d_{10} (i.e., the horizontal error bar at 90% retained cumulative weight in Fig. 7.13). In general, the smallest IQR ranges around the median values of characteristic diameters are related to the solution 4/5. A good accordance is observed for almost all the granulometric-related parameters in all cases (Appendix H). The resistivity of the saturation water reported by *Bairlein et al.* (2014) for sample A is about 33 Ωm. The estimated value agrees, but it should be noted that it represents water resistivity after an interval of time that allows dissolution of ions from the solid phase, whereas measured value is reported at the beginning of the test and can thus be an overestimation of the true resistivity of water during the SIP measurement. Estimated porosity is higher than the measured value in all cases, possibly due to the lacking of lower porosity values in the calibration dataset.

*Example 2*: sample C (*Bairlein et al.*, 2014), i.e., slightly-sandy mud of the sedimentary basin of Braunschweig (Germany).

The selection of the cluster to which this sample belongs to in the four cases of merging is straightforward from Fig. 7.14: the relevant clusters are 1/2, 2/5, 7/8, and 5/11.

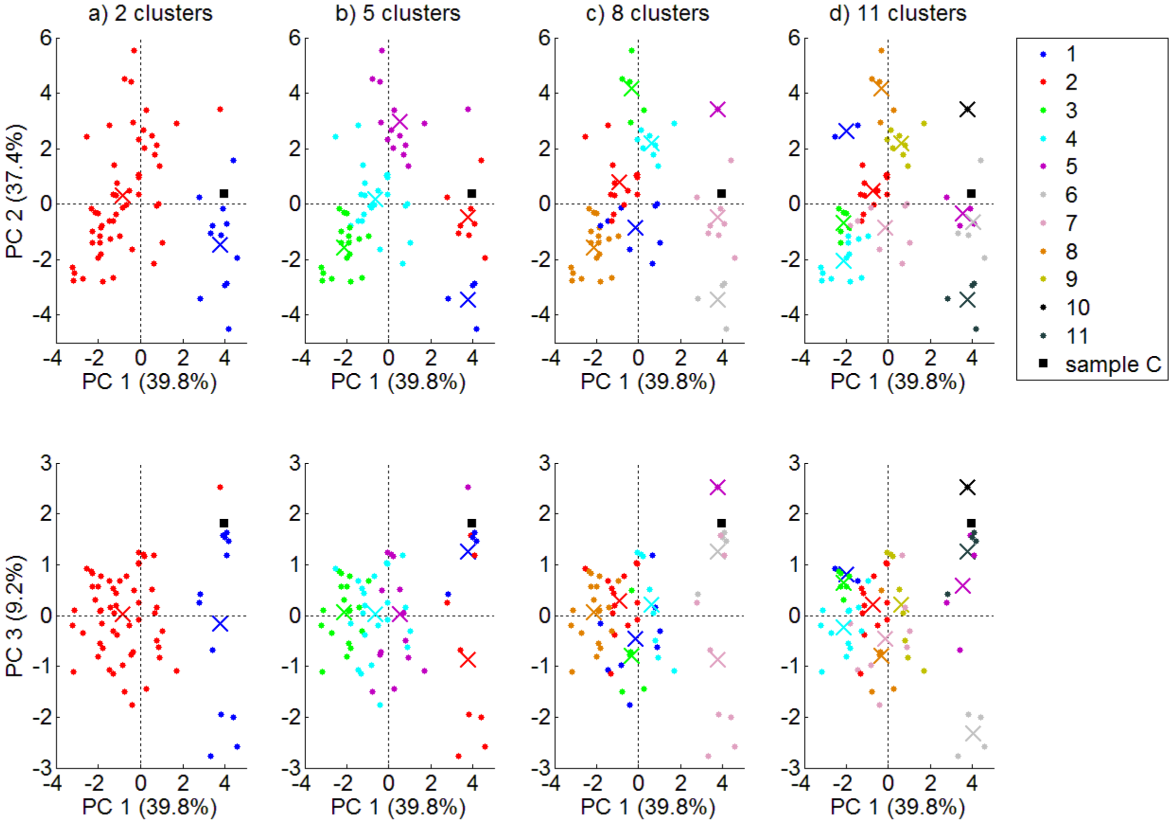

Fig. 7.14 - Position of sample C in the coordinate systems PC 1-PC 2 (upper row) and PC 1-PC 3 (lower row), according to the solutions with a total number of clusters equal to two (a), five (b), eight (c), and eleven (d). The legend refers to the number of clusters and is valid for all the subplots.

Nonetheless, the estimated textural parameters and grain-size-distribution curves (Fig. 7.15) are quite distant from the measured values. Actually, sample C strongly differs from all the samples of the calibration dataset, except from LA12, and in fact the latter constitutes a cluster by itself from a classification into six clusters onward. The position of the investigated samples in the PCs systems is not far from the position of sample LA12. The problem arises from the fact that the procedure of assignment of a sample to a specific cluster is based on the comparison of the electrical parameters with the corresponding IQR ranges of the clusters. The assignment to a cluster made of only one sample is thus possible only when the two values are identical. In addition, LA12 showed an anomalous phase spectrum at the extreme frequency decade, which could possibly distort the calculated PCs with respect to the remaining samples.

Correct granulometric constrains concern only the very coarse sand fraction and gravel fraction, which are both negligible. Porosity is also correctly estimated in cases 1/2, 2/5, and 7/8. The tendency of the estimated curves to reflect the clay content of the measured one, even in absence of accurate values determination, suggests that the bulk electrical behaviour is strongly affected by this component. In fact, excluding the cluster with only one sample, the material under analysis is always assigned to the available cluster with the finest granulometric composition. Unfortunately, the values of the PCs do not give rise to any evidence for the lacking of really comparable samples in the dataset and the result is an underestimation of the mud content. Water resistivity is correctly estimated, especially in the case 5/11. This is expected because this high-resolution classification specifically addresses this parameter, as it was explained in section 7.2.

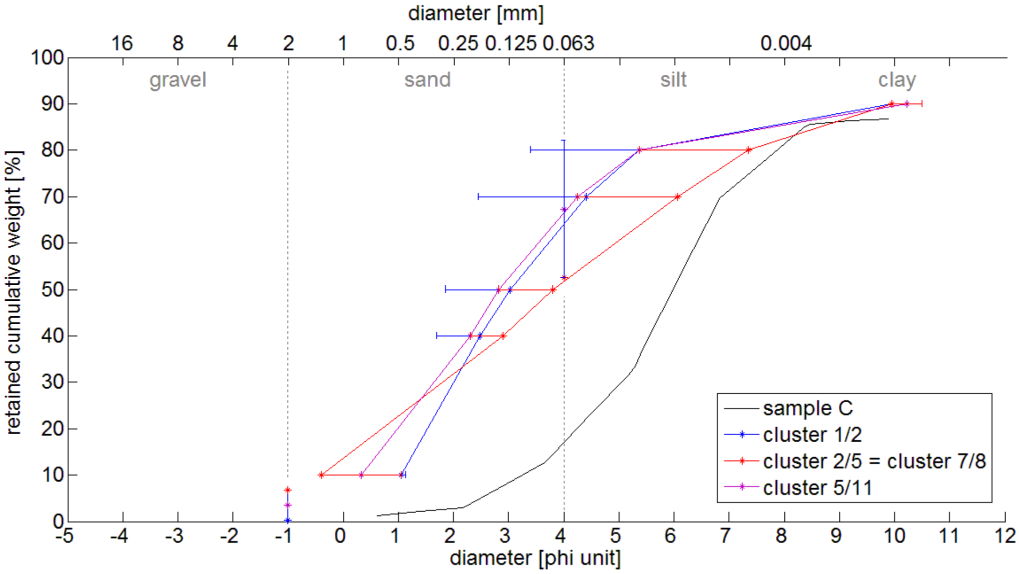

Fig. 7.15 - Comparison of the measured grain-size-distribution curve of sample C with the estimated curves, according to the selected clusters of different merging cases. Some portions of the error bars are hidden below others.

<u>*Example 3*</u>: sample Kr6 (personal communication of data, see *Vereecken et al.*, 2000 for site description), i.e., sandy gravel sample from Krauthausen test site (Germany).

This example constitutes another case of sample with very different textural parameters as compared to the calibration dataset. In fact, it is mainly composed by G (57%) followed by *vc*S and *c*S (34%), whereas the coarser of the investigated samples is made by only 27% G (sample O3). Sample O6 has a higher amount of G (35%), but also 15% M. The textural estimation expected by the use of the clustering approach cannot be a detailed one for sample Kr6, due to the lacking of similar samples and as already discussed for the previous example. The set of electrical parameters allows to assign the sample to clusters 2/2, 4/5, 2/8, and 2/11, which are exactly the same clusters selected for sample A. As in that case, some ambiguity arise in the classifications with more than two clusters, due to the position of the sample under investigation at the border between more than one cluster (Fig. 7.16b, 7.16c, and 7.16d).

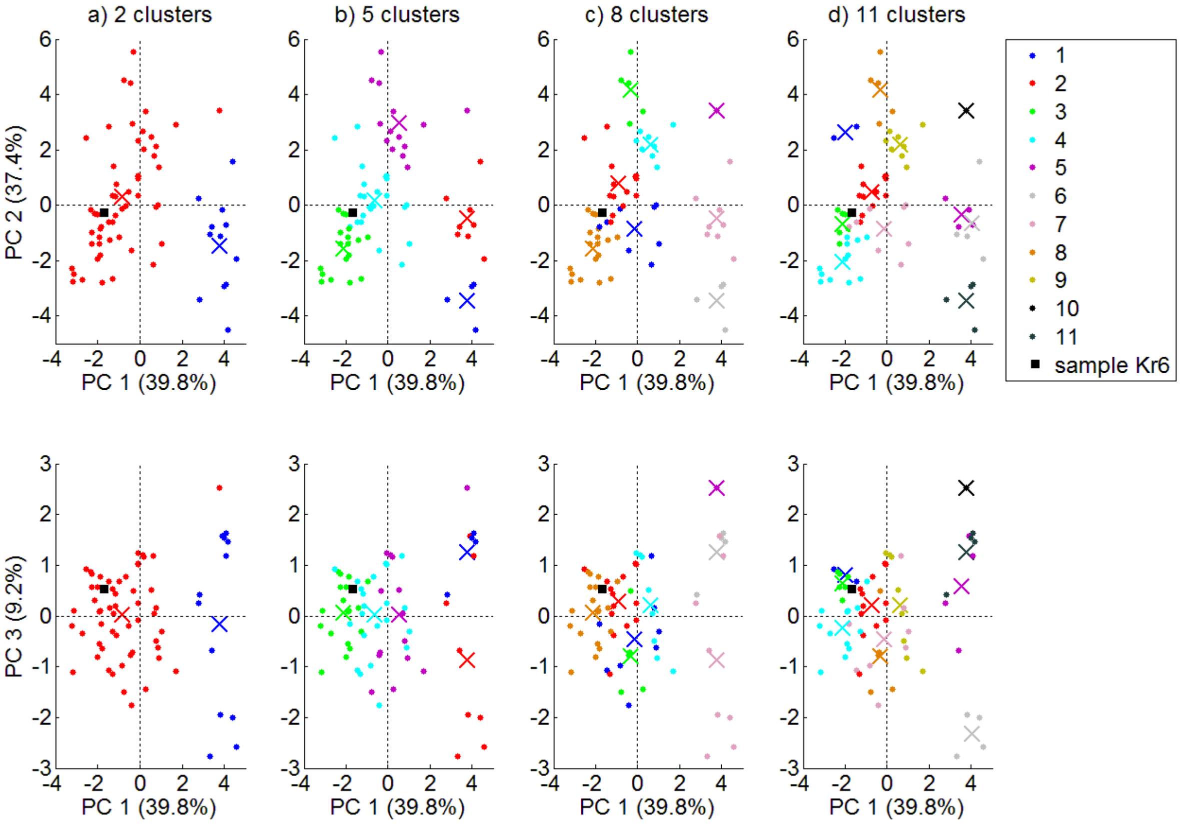

Fig. 7.16 - Position of sample Kr6 in the coordinate systems PC 1-PC 2 (upper row) and PC 1-PC 3 (lower row), according to the solutions with a total number of clusters equal to two (a), five (b), eight (c), and eleven (d). The legend refers to the number of clusters and is valid for all the subplots.

The comparison of the measured and estimated individual properties of the sample is bad, so as the determination of the grain-size-distribution (Fig. 7.17).

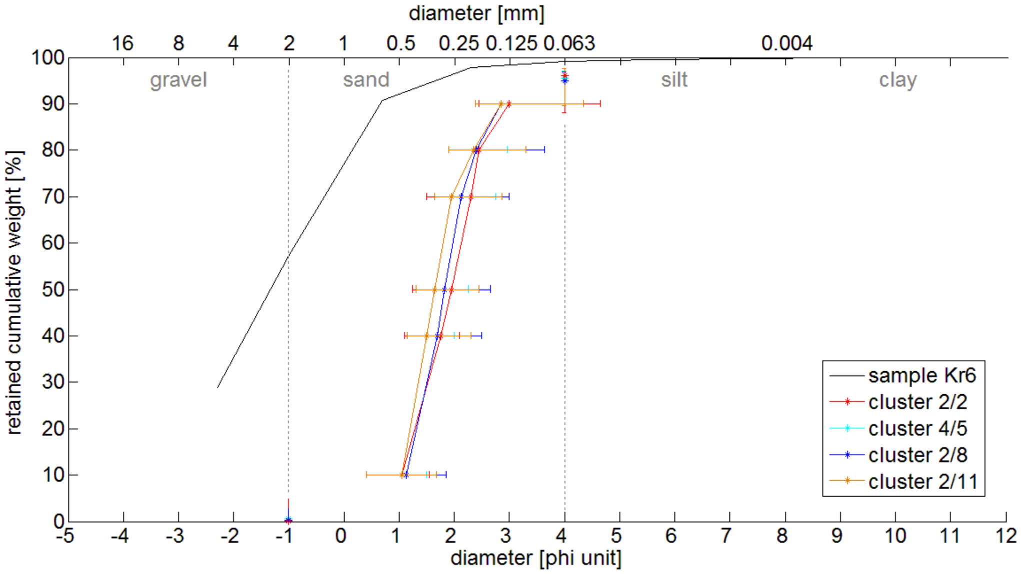

Fig. 7.17 - Comparison of the measured grain-size-distribution curve of sample Kr6 with the estimated curves, according to the selected clusters of different merging cases. Some portions of the error bars are hidden below others.

The good point is that the sample is allocated within the most similar available group, i.e., the cluster including clean sands with a phase spectrum without local peaks. The drawback is that no specific hints of the difference of the sample from the available dataset arise from Fig. 7.16, where the sample point is close to the available data, thus meaning that the electrical parameters are effectively similar. This remark have already been expressed for the previous case, but here is much more pronounced because the sample is located near the centroid of cluster 2/2, whereas sample C was located toward an extreme of cluster 1/2 and the presence of additional samples in the initial dataset could have affected the merging of samples into clusters.

Example 4: sample Kr7 (personal communication of data, see *Vereecken et al.*, 2000 for site description), i.e., slightly-muddy gravelly sand from Krauthausen test site (Germany).

The cumulative grain-size-distribution of sample Kr7 is quite similar to that of sample O6j and an assignment to the cluster including this sample was expected. In fact, it is joined to clusters 2/2 and 5/5, even if a high number of indicators are only close to the corresponding variability intervals of the clusters and not completely included (indirect indicators). Instead, expected cluster 9/11 is not identified by any indicator, whereas cluster 4/8 is directly indicated by four parameters and indirectly by three, but it is not selected. Figs. 7.18c and 7.18d also support this choice, especially when considering the PC 1-PC 2 plane.

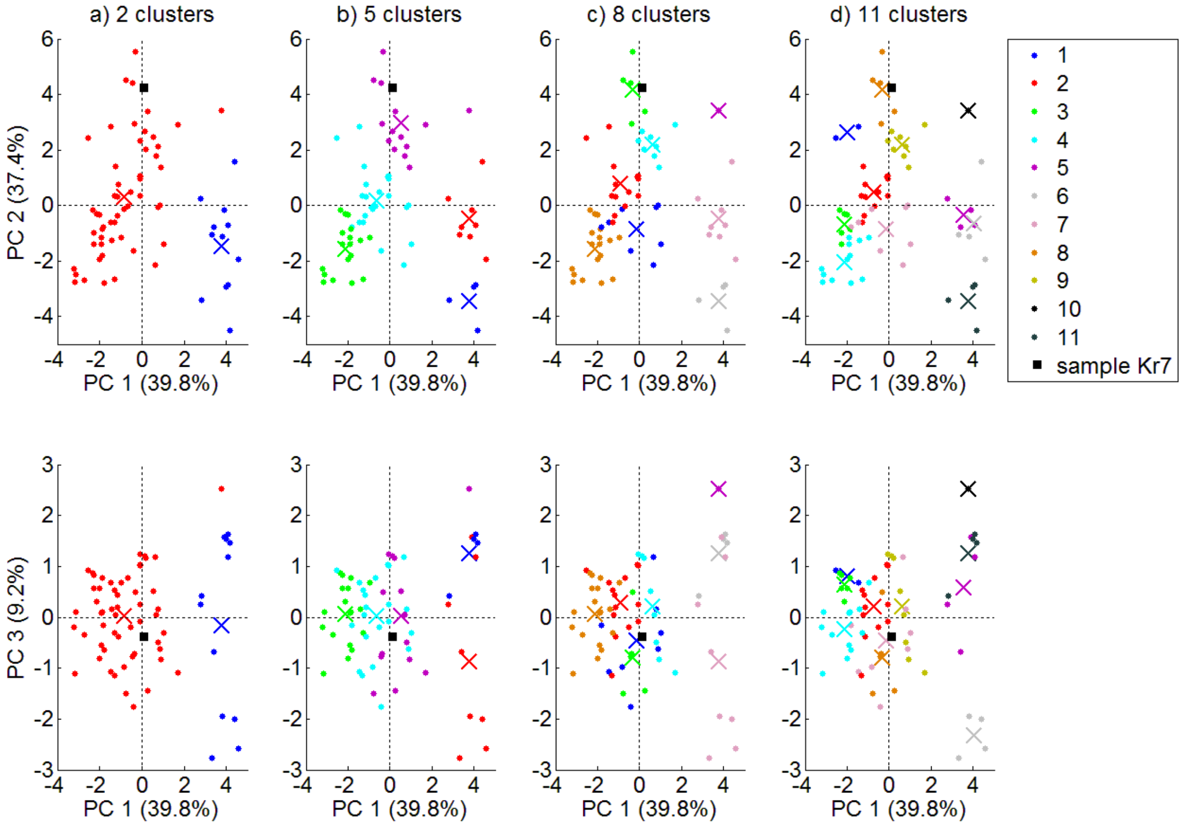

Fig. 7.18 - Position of sample Kr7 in the coordinate systems PC 1-PC 2 (upper row) and PC 1-PC 3 (lower row), according to the solutions with a total number of clusters equal to two (a), five (b), eight (c), and eleven (d). The legend refers to the number of clusters and is valid for all the subplots.

This result is well explained by considering that the phase spectrum of sample Kr7 (Fig. 7.11) reflects the typical shape of the phase spectra of samples Sb8j (i.e., a downward concave trend, as that represented in Fig. 6.18b). The clustering approach recognizes this similarity and assigns the sample Kr7 to the clusters including Sb8j, which only during the initial phases of subdivision correspond to the clusters containing also sample O6j. As a consequence, the estimation of textural properties does not provide good results in these cases. On the opposite, the inferred cumulative grain-size-distribution includes the measured one in the case 5/5 and partly in the case 2/2 (Fig. 7.19). In particular, the latter better approximates the fine-grained portion of the curve.

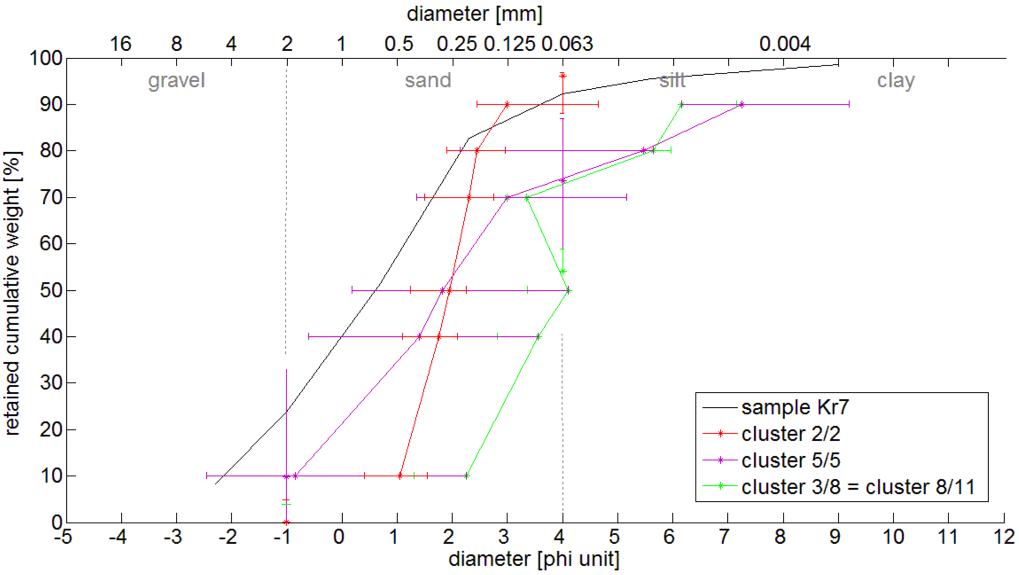

Fig. 7.19 - Comparison of the measured grain-size-distribution curve of sample Kr7 with the estimated curves, according to the selected clusters of different merging cases. Some portions of the error bars are hidden below others.

The drawback of cluster 5/5 is that it is not very informative. In fact, the IQR of its characteristic diameters are large, and this is due to the small number of different samples included in the cluster. This high heterogeneity, accompanied by a small statistical significance, does not allow to achieve a detailed textural characterization of the sample, as it was done for sample A, but only to determine that the sample under investigation has a non-uniform grain-size-distribution, spanning from gravel to mud. In the PCs graphs of Fig. 7.18, sample Kr7 occupy a region characterized by a low density of data points. This suggests that the inclusion of more samples in the calibration dataset for that particular region of space, could help reducing the uncertainty in the estimates. In addition, samples containing at least 10% of mud show a higher spectral differentiation with respect to clean samples. In fact, the fine-grained samples were subdivided into a larger number of clusters with respect to the coarse-grained samples already in the initial dataset (e.g., five vs. three clusters in the case with eight total clusters). This is interpreted as an indirect demonstration that other factors beside textural composition affect the complex electrical behaviour of sediments, and these factors are mainly related to the fine-grained sediment fraction. An example was already given in section 4.5, with the discussion of the differences in the phase spectra of samples

Sb7 and Sb7j that were related to the distribution of the different granulometric classes determined by the packing method. In the example described here, factors as the mineralogy of the polarisable components, and the properties related both to the texture and the mineralogy, such as the cation exchange capacity or the specific surface area could be of interest, since an effect due to the instrument can be excluded because SIP data of samples O6j, Sb8j, and Kr7 were all acquired with the ZEL-SIP04-V02 experimental system. In addition, a local validity of the relationships between electrical and sedimentological parameters can be expected, as it happen, for example, with the exponent of the Archie's law. In fact, the calibration database covers a reasonably wide range of samples representative for the Quaternary alluvial sedimentary facies of the interfluve between Adda and Lambro rivers in the Po plain, whereas the tested sample belong to the sediments of Rur and upper Rhine (*Vereecken et al.*, 2000).

7.3.2 Validation with internal samples

A secondary phase of the validation was based on a set of samples removed from the calibration dataset. This constitutes a simplification of the previous case because it limits the possible occurrence of contaminations related to local factors. The selected samples are a sand (S9-w2), a slightly-muddy sand (Sb17j-w5), and a sandy mud (LZ15j-w6). Of course, the acquisition parameters and the Debye decomposition were perfectly equal to those of the calibration samples. The PCA and CA were executed without these samples and produced very similar results to those of the complete dataset. Therefore, they are not represented and discussed in detail. A major difference in the clustering regards the classification of samples between clusters 3/5 and 4/5. This is due to the high similarity between these clusters, which can thus be affected even by minor changes in the initial dataset. In addition, the discussion is proposed for the clustering solutions with two, five, and ten clusters. The latter replaces the eight- and eleven-solution described in the previous section, on the basis of the analysis of the mean silhouette trend as a function of the total number of clusters for this reduced dataset.

In the subdivision with two clusters, samples S9-w2 and Sb17j-w5 are assigned to cluster 2/2 by nine and ten out of twelve direct indicators, respectively, whereas sample LZ15j-w6 is assigned to cluster 1/2 by six direct indicators and two indirect indicators. The grain-size-distribution of sample S9-w2 is correctly identified; the measured grain-size-distribution of sample LZ15j-w6 is also included in the estimated range, even if on the finest-grained extreme term (Fig. 7.20). Major problems seem to regard sample Sb17j-w5, that is assigned to cluster 2/2 but whose measured textural properties (e.g., d_{20}, d_{30}, d_{50}, d_{60}) are similar to the median values of cluster 1/2 and external to the IQR ranges of cluster 2/2. However, this constitutes a good result when considering that for such a low-resolution classification only a rough subdivision into sandy samples ($M < 12\%$) and samples containing a non negligible percentage of mud ($M > 18\%$) can be obtained. Effectively, the sample Sb17j-w5 is made by about 15% mud, but this is possibly an overestimate due to the lacking of data related to the 90 μm sieve. In addition, the IQR ranges relative to cluster 2/2 show smaller dimension as compared to cluster 1/2 due to the major number of samples belonging to cluster 2/2. As a matter of fact, all the samples Sb17j are part of cluster 2/2 and the assignment of the investigated sample to this cluster is thus correct.

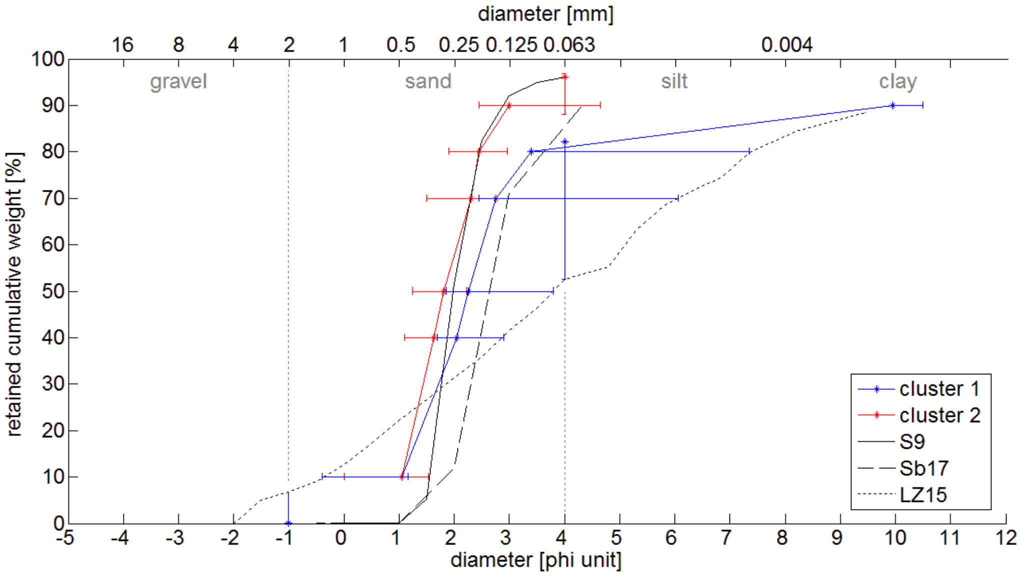

Fig. 7.20 - Comparison of the measured grain-size-distributions with the estimated curves, according to a subdivision into two clusters.

In the classification into five clusters, the samples S9-w2, Sb17j-w5, and LZ15j-w6 are joined to clusters 4/5, 5/5, and 1/5, respectively. The representative grain-size-distribution curve of sample LZ15j-w6 perfectly matches the measured distribution, thanks to the high internal homogeneity of this cluster. A nice correspondence is also obtained for sample S9-w2. In fact, the deviation of the representative distribution of cluster 4/5 from the measured one is more apparent towards the coarse-grained portion as compared to the previous classification, but is however restricted within the same textural class (i.e., medium sand). This apparent deterioration is due to the change in the number of objects included in each cluster and the subsequent modification of the IQR of the textural properties. Nonetheless, the fine-grained portion is dominant in determining the complex electrical properties, and this is reproduced with much better accuracy (e.g., stronger constraint on the mud content). The estimation of the grain-size-distribution for sample Sb17j-w5 is also improved, especially by reducing the amount of mud and the characteristic diameter d_{10}. However, the range of variability is quite high and the textural description of the sample cannot be very detailed. This can be explained by considering that this cluster tends to gather the samples saturated with waters with low resistivity. In this conditions, despite important textural differences among the samples, the electrical parameters related to the phase spectra are less characteristic (e.g., flat phase spectra without local peaks), and this constitutes the similarity element that associate the samples. A secondary assignment for this sample is to cluster 4/5, on the basis of five direct and two indirect indicators, often present in association with cluster 5/5. Cluster 4/5 is a fine-medium sand. The occurrence of such different plausible characterizations helps to avoid an excessive confidence in the results.

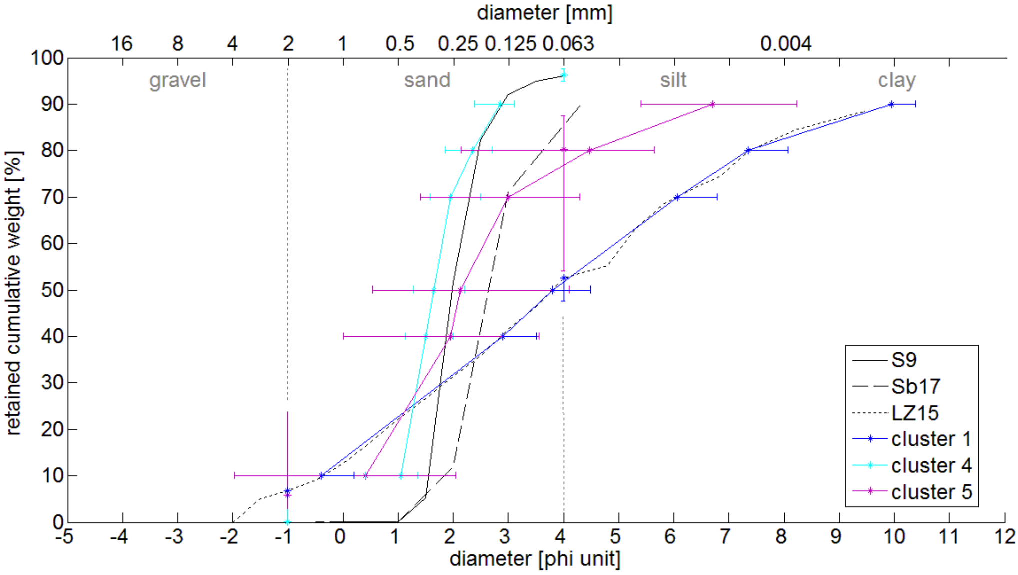

Fig. 7.21 - Comparison of the measured grain-size-distributions with the estimated curves, according to a subdivision into five clusters.

Finally, the assignment to a cluster in the solution with ten groups of samples is still straightforward for samples S9-w2 (ten out of twelve direct indicators correspond to cluster 7/10) and LZ15j-w6 (seven direct and one indirect correspond to cluster 9/10). The characteristic grain-size-distributions estimated for these samples perfectly match the measured curves (Fig. 7.22).

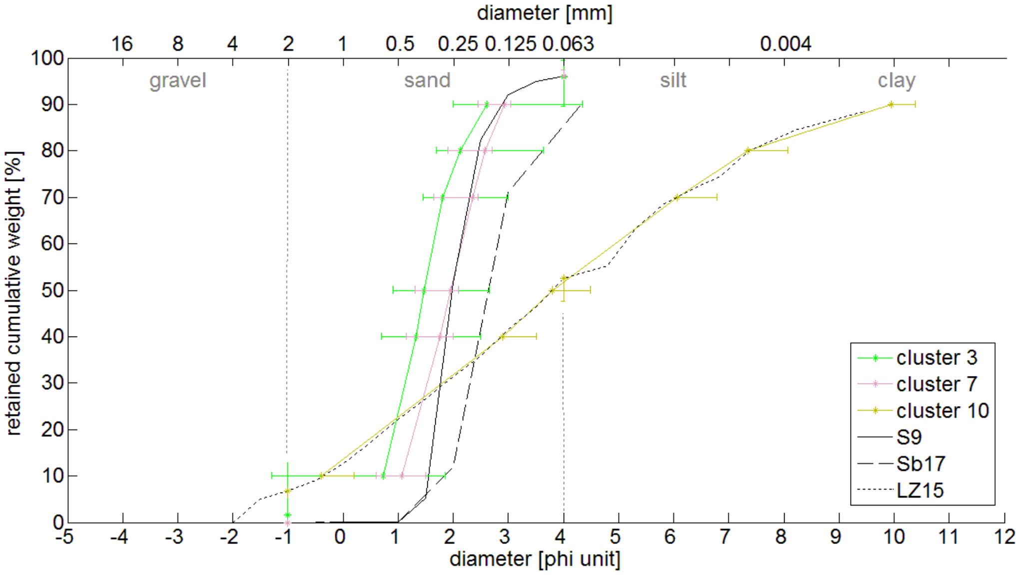

Fig. 7.22 - Comparison of the measured grain-size-distributions with the estimated curves, according to a subdivision into ten clusters.

For sample Sb17j-w5, the assignment is more difficult among clusters 3/10, 4/10, and 7/10, both in the comparison between the measured electrical parameters and the corresponding IQR of the clusters and in the location of the investigated samples on the PCs planes (Fig. 7.23).

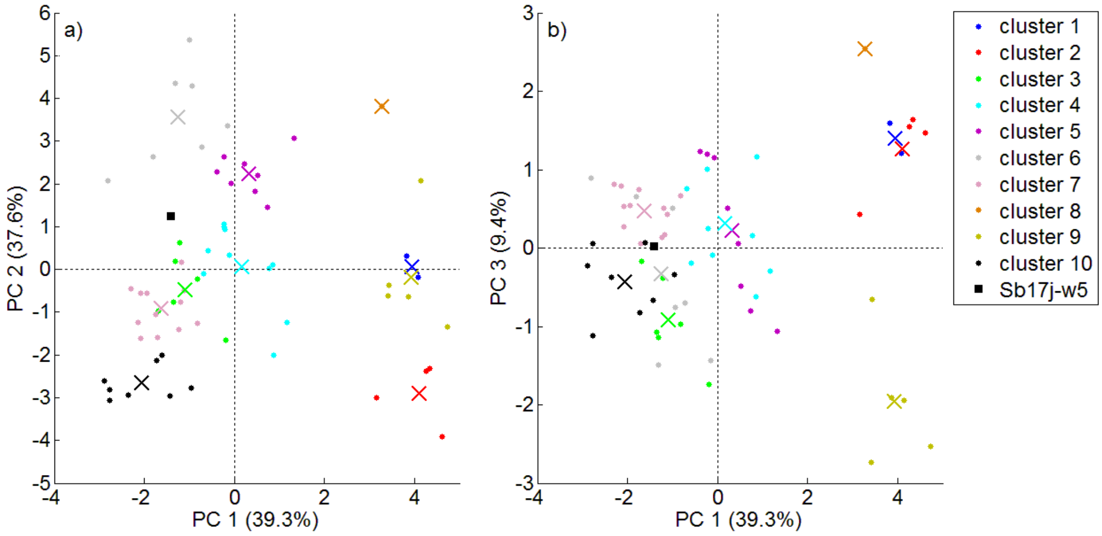

Fig. 7.23 - Position of sample Sb17j-w5 in the coordinate systems PC 1-PC 2 (a) and PC 1-PC 3 (b), according to the ten-clusters solution.

The measured values of the most important electrical parameter in the list ordered in descending importance ($\Delta\varphi_0$) is close to clusters 3/10 and 4/10. After this, cluster 3/10 shows the first direct occurrence in the parameter $\Delta\varphi_3$, whereas cluster 4/10 in the subsequent $\Delta\varphi_1$. For this reason, the former was selected as the most appropriate. It is important noting that a different selection would not have caused significant differences in the textural estimation, due to the large overlapping of the characteristic grain-size-distributions of these clusters. The investigated sample is described as mostly composed by medium or fine sand, with $M < 12\%$ and $G < 12\%$. This is almost the same result obtained with the solution with two clusters. As a general trend, cluster 3/10 gathers samples with high water resistivity as compared to cluster 4/10, and according to this parameter the best assignment would have been to cluster 4/10. However, also in this case, the IQR are slightly overlapping and the difference cannot be considered completely significant.

7.4 Field counterpart

In this section, electrical impedance tomography (EIT) measurements performed in the field are discussed. The work was conducted in August 2014 as part of a collaboration between the Department of Earth Sciences (Università degli Studi di Milano, Italy), the Institut für Bio- und Geowissenschaften (IBG-3, Forschungszentrum Jülich GmbH, Germany), and the Zentralinstitut für Engineering, Elektronik und Analytik (ZEA-2, Forschungszentrum Jülich GmbH, Germany). It was mainly aimed at testing the EIT system designed and constructed at ZEA-2 and evaluating the type and quality of results that can be obtained in real field case studies, i.e., in absence of a detailed characterization of the subsurface, and in non-ideal acquisition conditions. The details concerning the data processing and inversion are beyond the scope of this section, since they constitute a big work by themselves. In fact, the complex resistivity imaging is a relatively new geophysical technique, which still requires big efforts toward the understanding of the data correction steps needed to obtain high accuracy results and the application of proper forward and inverse modelling methods to correctly map the spatial variability of absolute phase values. Here, only an overview of the field counterpart of the laboratory SIP measurements, extensively addressed within the text, is presented with some preliminary observations.

Three sites were selected, with different sedimentological characteristics and as close as possible to the outcrops where the sampling for laboratory SIP measurements was performed:

- Landriano (see section 3.1.3);
- Senna Lodigiana (see section 3.1.2);
- Lozzolo (see section 3.1.4).

The acquisitions were performed with a linear array of 30 metal electrodes (Fig. 7.24a) at 1 m separation. The cables connecting the system to the electrodes were laid on the ground along straight lines and with a radial symmetric geometry. The portion of the cable in excess with respect to the distance between the electrode and the system was arranged as in Fig. 7.24b, in order to suppress the electromagnetic coupling related to this portion by summation of two equal terms with opposite sign. Two “fast” measurements (6 Hz-10 kHz) were used to calibrate the experimental system and to correct the data. An open circuit measurement allowed to determine the cables capacitance (ranging between 1000 pF and 2000 pF), that depends on the cable length and cable connections and is independent from the array geometry. A close circuit measurement allowed to determine the parasitic capacitance between cables and ground (ranging between 8000 pF and 12000 pF), that is strictly related to the contact between them and thus on the cable configuration.

Fig. 7.24 - Radial and symmetric distribution of connecting cables between the EIT system and the electrodes (a); detail of an electrode and the corresponding amplifier unit (b); closed cable loop beyond the electrode position (c).

The former calibration also permitted to evaluate the contact impedances between electrodes and ground. Low ($< 1000\ \Omega$) and constant values for all the electrodes are desirable to reduce phase errors, and thus saline water was added in correspondence of electrodes with higher contact impedance. An interference around 1 Hz was observed in the phase section acquired in Landriano and was attributed to an additional security switch that checked the system voltage at that frequency. The switch was removed for the following acquisitions. The sinusoidal input signal had a peak-to-peak amplitude of 18 V. The frequency series was composed of 15 logarithmically spaced values from 100 mHz to 10 kHz[10] (3 points per decade). The series was determined as the optimal one to be filtered to remove the 50 Hz noise and the correlated interferences. However, data above 1 kHz are not considered in the following due to potentially unknown or uncorrected capacitive and inductive errors. For each frequency, three sinusoidal cycles were measured and used to calculate the impedance as the mean value of the three repetitions. 30 pairs of electrodes were used for the current injection, whereas potential was measured at all other electrodes simultaneously. The injection pairs were determined by hypothetically ordering the electrodes in a circular arrangement and considering a distance between the current electrodes in this arrangement equal to 17 (i.e., electrodes 1-18, 2-19,…, 13-30, 14-1,…, 29-16, 30-17). The effective skip in the linear configuration did not always correspond to this number. This approach allowed to obtain a combination of the results of all the common electrode configurations used in ERGI surveys (Wenner, Schlumberger, dipole-dipole) with a relatively short data acquisition.

---

[10] The exact frequency series is 0.1, 0.2, 0.5, 1, 3, 6, 14, 31, 71, 164, 367, 850, 1950, 4400, 10000 Hz.

The inversion grid was composed of 39 cells in the x-direction, with a constant length of 1 m, and 29 cells in the z-direction, with an increasing height from about 0.2 m to about 0.7 m. The sensitivity map was calculated in the inversion grid to estimate a plausible area where a reliable interpretation of the model is expected (Fig. 7.25). The sensitivity describes the change in the model response due to a variation in the model parameter (i.e., the complex resistivity). This means that high values of sensitivity correspond to regions with larger influence on the measurement and lower uncertainty in the model. Sensitivity decreases exponentially from surface to depth and with increasing distance from the electrode array. On this basis, the inversion results are examined only for a qualitatively-established semi-circular region included between the electrode array and a depth of about 5 m (dashed line in Fig. 7.25).

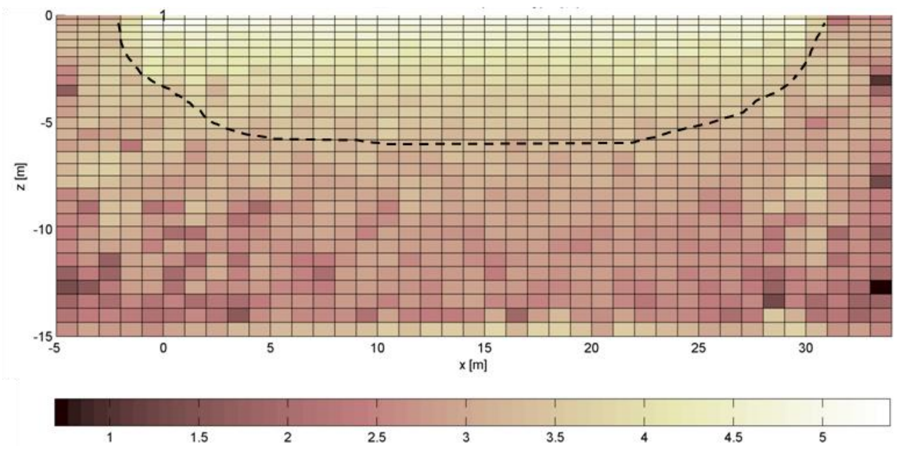

Fig. 7.25 - Sensitivity (S) map in the inversion grid, represented as a logarithmic colour scale ($1/2 \log_{10} S$). The dashed line qualitatively identifies the region where a reliable interpretation of the model is expected.

7.4.1 Landriano

At the Landriano site, the acquisition was done along a profile N60E, parallel to the short side of the maize crop (Fig. 7.26), at a distance of 1.7 m from the first row and less than a meter from the hose for the distribution of the irrigation water.

Fig. 7.26 - EIT acquisition in Landriano; the electrode array is arranged along a N60E profile.

The resistivity amplitude sections (Fig. 7.27) show a resistive layer ($\rho > 120\ \Omega$m) above a conductive layer, with an interface at about 1 m depth, between x = 0 m and x = 13 m. Beyond this point, the upper layer is less continuous and also less resistive, especially at high frequency. The horizontal interface is interpreted as the water table extensively risen by the irrigation water during the summer period. This can explain the difference of depth from DC measurements by *Ortuani et al.* (2015; Fig. 3.7) that were conducted after the harvest. The lateral transition of resistivity is also an expected feature that confirms the results of previous measurements.

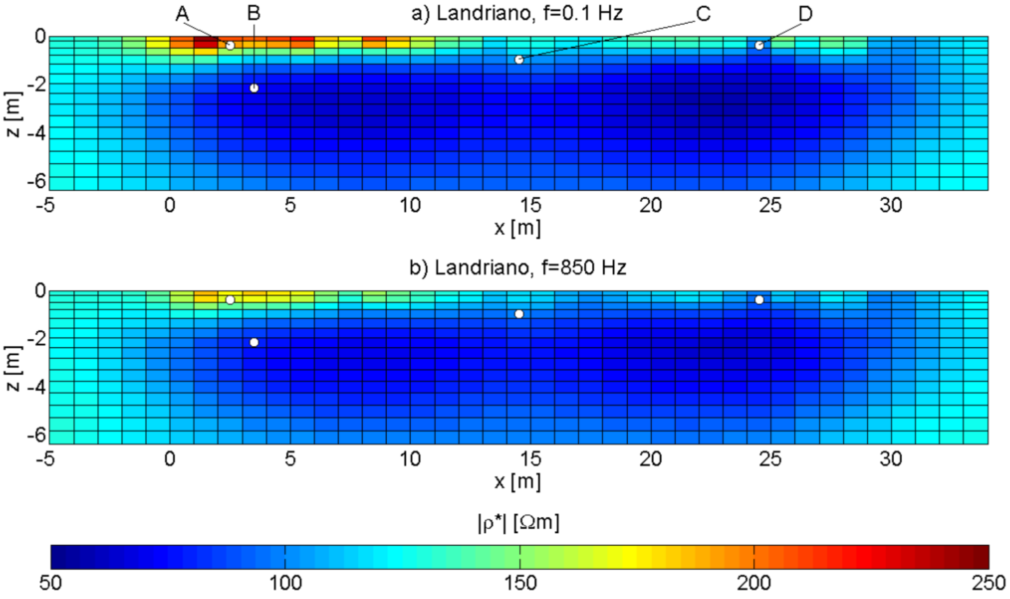

Fig. 7.27 - Resistivity amplitude sections at 0.1 Hz (a) and 850 Hz (b) in the upper part of the inversion grid. The electrode array is located between x = 0 m and x = 29 m. White dots represent the points selected for the spectra representation.

Below 1 Hz, the highest absolute phase values are located between x = 13 m and x = 18 m, and migrate toward the surface from $z = -2$ m (Fig. 7.28a). On the opposite, the lowest values are located in two surface spots around the extreme of the electrode array. Above 1 Hz, the phase sections reproduce a similar structure to the amplitude sections (Figs. 7.28b, 7.28c, and 7.28d), with an upper layer characterized by high absolute phase values that decrease in the x-direction, and a bottom layer with lower phase values ($\varphi < -8$ mrad). The absolute phase usually reaches the highest value at high frequency. However, at a depth of about 3 m, the opposite behaviour is observed (point B; Fig. 7.27). In the laboratory, such an anomalous behaviour was obtained in presence of high saline waters that badly affect the electromagnetic coupling. A low electrical resistivity was actually measured on water samples taken from a well providing irrigation water ($\rho_w = 32\ \Omega$m), but it does not seem sufficiently low to justify this behaviour, unless a strong contribution of salts is added by the agricultural soil after the irrigation.

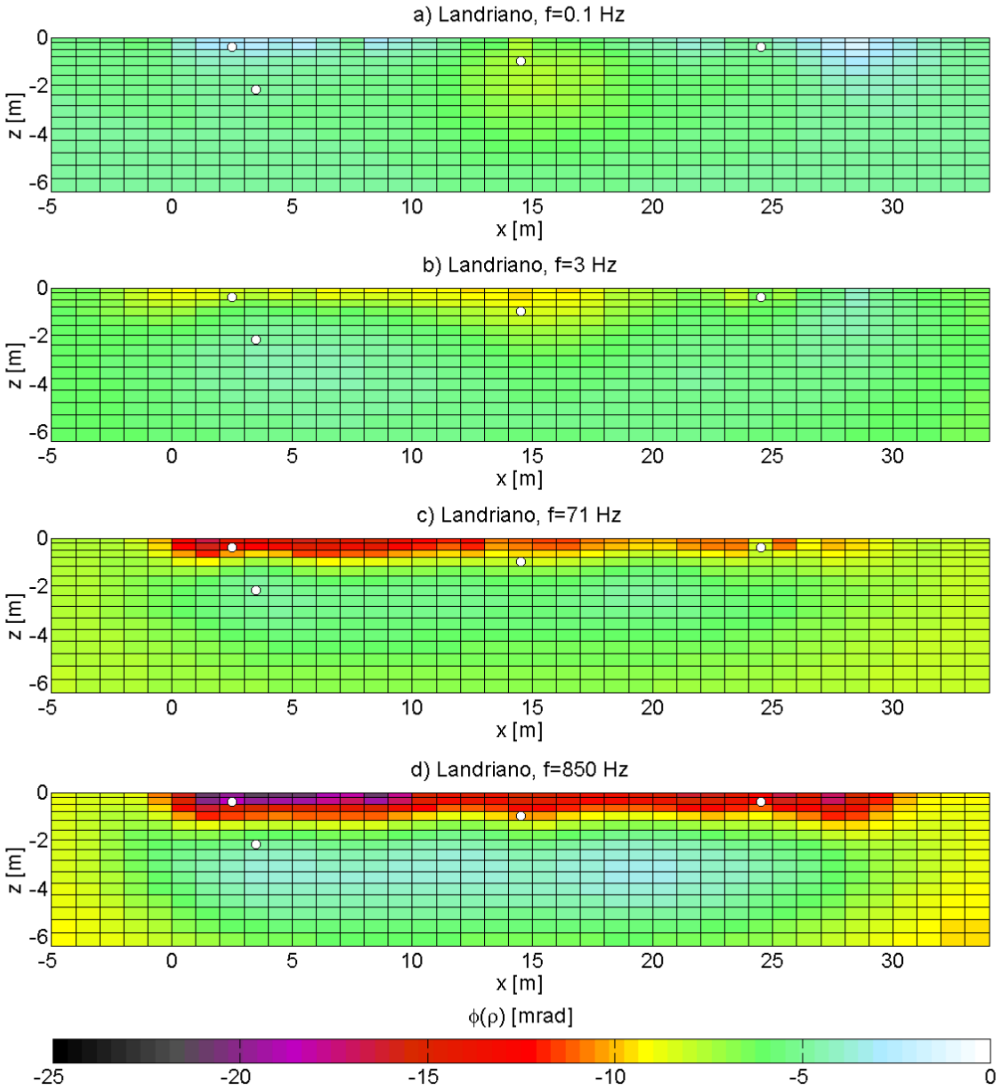

Fig. 7.28 - Resistivity phase sections at 0.1 Hz (a), 3 Hz (b), 71 Hz (c), and 850 Hz (b) in the upper part of the inversion grid. The electrode array is located between $x = 0$ m and $x = 29$ m. White dots represent the points selected for the spectra representation.

The sample LA12-w6, i.e., the sample prepared with sediments collected at this site (Fig. 7.29) was characterized by a similar behaviour.

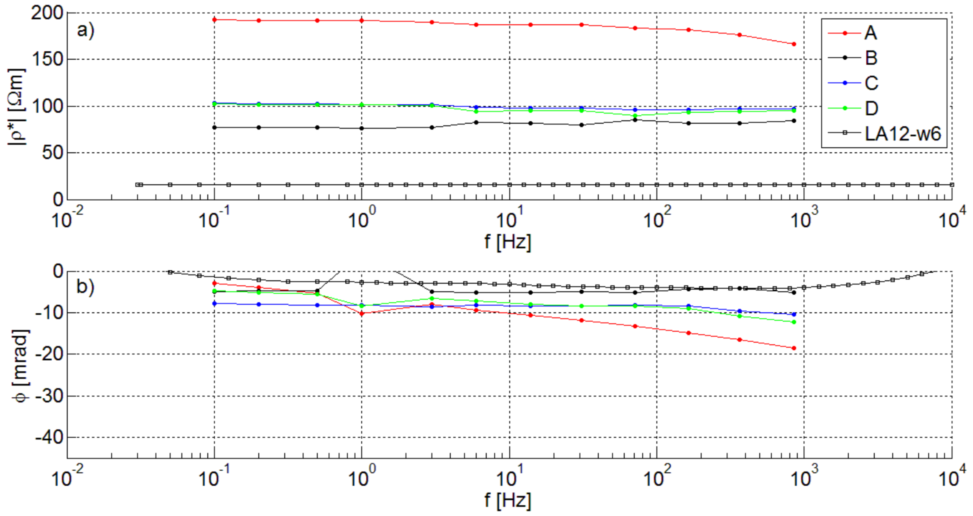

Fig. 7.29 - Resistivity amplitude and phase spectra of selected points of the EIT measurements in Landriano. The location of the points is represented in Fig. 7.27a.

For the sake of completeness, it should also be considered that the relative reduction in resistivity, calculated in the whole inversion grid considering 0.1 Hz and 850 Hz as the low and high frequency terms in equation (7.1), highlights only a surface region where it is positive (Fig. 7.30). This is possibly an indicator that only this portion of the whole inversion grid can be properly interpreted, whereas elsewhere a larger uncertainty is expected on the model.

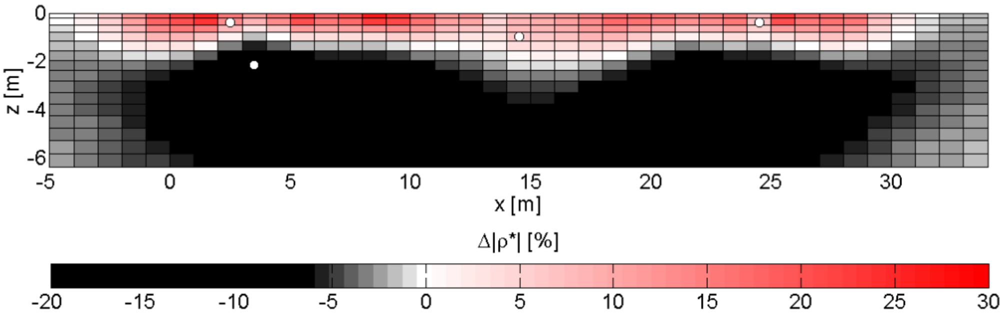

Fig. 7.30 - Relative reduction of resistivity amplitude between 0.1 Hz and 850 Hz in the upper part of the inversion grid. The electrode array is located between $x = 0$ m and $x = 29$ m. White dots represent the points selected for the spectra representation.

7.4.2 Senna Lodigiana

The EIT acquisition at the Senna Lodigiana site was performed along a profile N167E, at a distance of about 6.5 m from the sampling wall described in section 3.1.2 and of about 2 m from the upper quarry level (Fig. 7.31). The presence of this non-flat morphology could affect the results because the inversion was conducted with a 2D-approximation. However, the quantification of this error can only be achieved with a comparison with a 3D-inversion, which is currently not available. A further error could arise from the high contact impedances (from 1000 Ω to 5000 Ω) measured between the electrodes and the ground, even after the wetting with saline water.

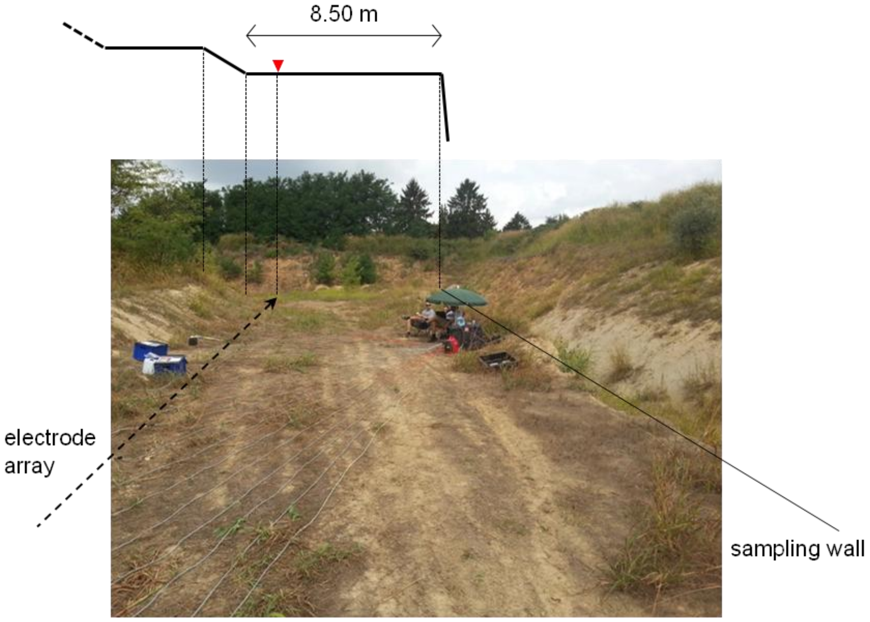

Fig. 7.31 - EIT acquisition in Senna Lodigiana: the electrode array is arranged along a N167E profile. The beach umbrella near the EIT system was used to shade the laptop and guarantee a constant monitoring of the measurement. The morphology of the area is sketched above.

The resistivity amplitude image is represented in Fig. 7.32 for the lowest and highest considered frequencies (i.e., 0.1 Hz and 850 Hz). The electrode array is located between x = 0 m and x = 29 m. The position x = 0 m of the following sections also corresponds to the position x = 1 m of Fig. 3.5a.

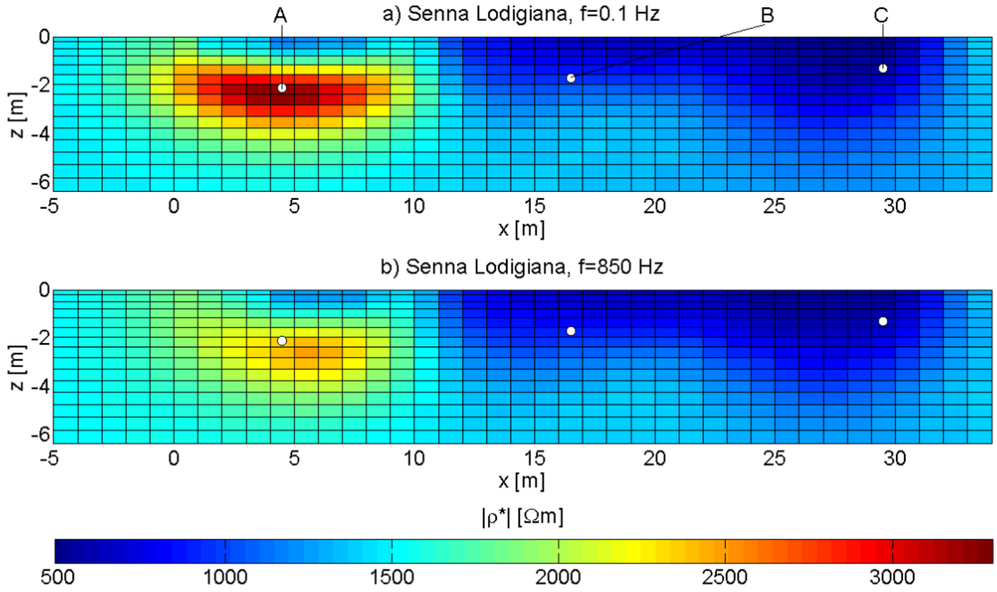

Fig. 7.32 - Resistivity amplitude sections at 0.1 Hz (a) and 850 Hz (b) in the upper part of the inversion grid. The electrode array is located between x = 0 m and x = 29 m. White dots represent the selected points for the spectra representation.

The main feature is a high resistivity zone located between x = −1 m, x = 10 m, z = −1 m, and z = −5 m, which is separated from the surface by a relatively conductive layer that extends laterally. In the remaining part of the section, a homogeneous region with ρ < 1500 Ωm is observed. In analogy to the previous DC and GPR surveys (Fig. 3.5), the high resistivity zone is interpreted as the depocentral region of the sandy unit with a channel shape that cuts the horizontal stratification. However, its lateral persistence as a layer extending from the surface to about 1 m depth cannot be observed; the same remark applies to the conductive layer between 1 m and 3 m depth. This is possibly related to the larger electrode separation of this acquisition as compared to the DC survey and the consequent lower resolution. The differences in the absolute values are expected to be determined by differences in the water content. The more conductive spot on the surface, between x = 24 m and x = 30 m can be associated to the interruption of the resistive layer of Figs. 3.5a and 3.5b. The sections at the different frequencies show similar characters, with a tendency to a resistivity decrease. This has already been observed in the laboratory tests and it is a physically acceptable solution implying a positive chargeability. However, the relative reduction in resistivity highlights region with an opposite behaviour (Fig. 7.33). These are especially located at z < −5 m, but also near the surface above the resistive feature, and in correspondence of the right side of the conductive spot.

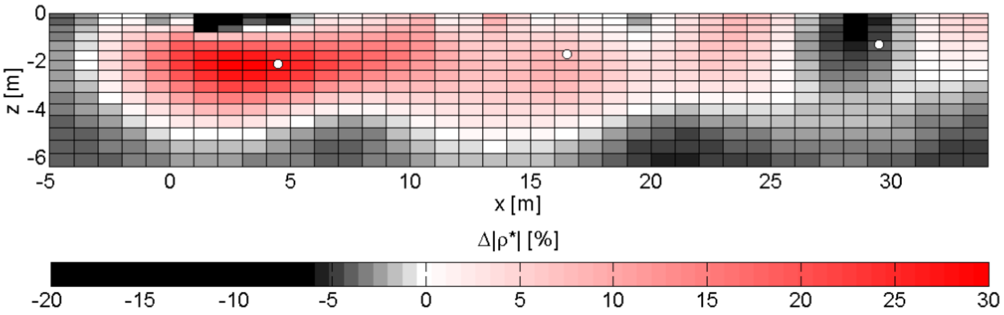

Fig. 7.33 - Relative reduction of resistivity amplitude between 0.1 Hz and 850 Hz in the upper part of the inversion grid. The electrode array is located between x = 0 m and x = 29 m. White dots represent the points selected for the spectra representation.

In the phase images a region with large polarizability as compared to the background, is present between x = 0 m and x = 10 m, at a depth of about 2.5 m.

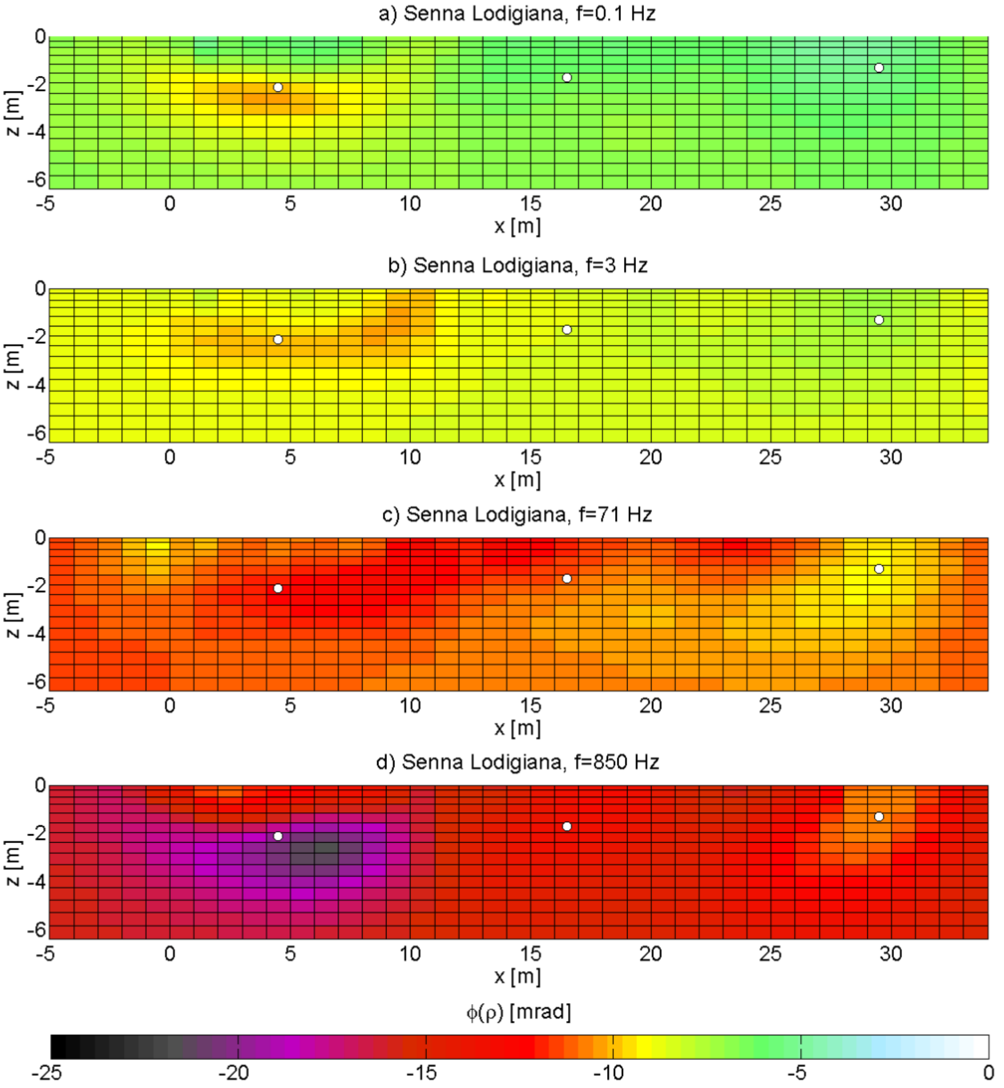

Fig. 7.34 - Resistivity phase sections at 0.1 Hz (a), 3 Hz (b), 71 Hz (c), and 850 Hz (d) in the upper part of the inversion grid. The electrode array is located between x = 0 m and x = 29 m. White dots represent the selected points for the spectra representation.

Increasing the frequency from 0.1 Hz to 3 Hz (Fig. 7.34a, 7.34b), this region tends to extend laterally with a concave-up shape and intersects the surface at x = 10 m. From f = 14 Hz, a low polarizability feature becomes more evident. It has an oblique shape, extending from the surface at $x = 30$ m to 4 m depth at $x = 25$ m (Fig. 7.34c). From $f = 367$ Hz, the high polarizability region stands out again from the background as a spot with $\phi < -15$ mrad (Fig. 7.34d). The high polarizability associated to the sandy channel appears at a first sight as a strange feature. A possible interpretation of this phenomenon might be related to the presence of oxidative reddish mottling in the sand and in the mud clasts at the base of this unit (Fig. 7.35), characterized by a higher metal content. Of course, the electrode and grid spacings are not sufficient to allow a good resolution of the shape of this polarisable object.

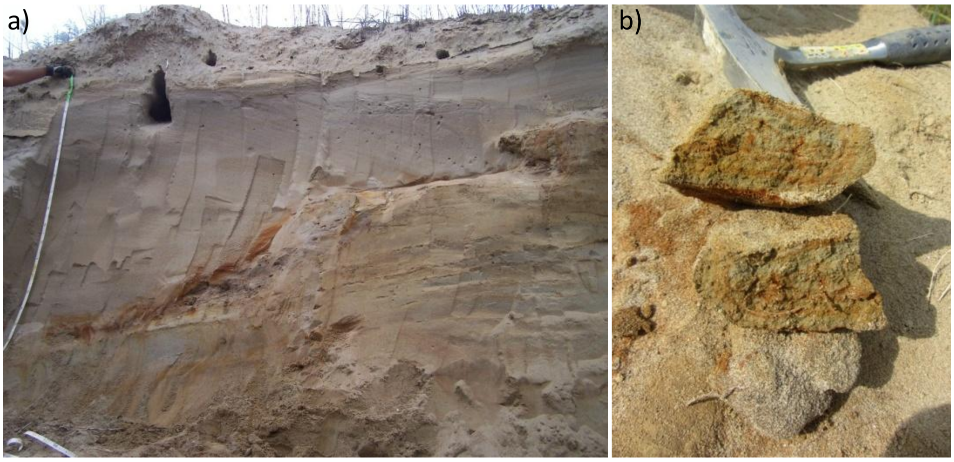

Fig. 7.35 - Sandy channel with the reddish level at the basis (a); mud clast with reddish mottling (b).

On the other hand, the more conductive and less polarisable spot is interpreted as a more humid region eventually associated with a coarser-grained zone.

On the basis of these observations, three points were selected (A, B, C, see Fig. 7.32a for their location) to represent the SIP spectra in the considered frequency range (Fig. 7.36). Phase spectra of points B and C are almost parallel and monotonically decrease with frequency. Point A seems to delineate a local phase peak toward the lowest investigated frequency, which, even if not completely sampled, results comparable to the spectral shape of the laboratory samples collected in that unit (S9 and Sb9j). However, a proper comparison with laboratory results is not feasible, due to the large difference in the saturation ($S_w = 1$ in laboratory, $S_w \ll 1$ in the field), which affects both the real and the imaginary part of resistivity. The real part increases by about one order of magnitude with a decrease of the saturation degree, whereas the imaginary part varies with a more irregular trend. In particular, *Breede et al.* (2012) observed an increase of the imaginary component (and of chargeability) followed by a reduction for clean sands and sand-clay mixtures with a low clay content, whereas only a reduction for sand-clay mixtures with high clay content. *Jougnot et al.* (2010) observed instead an increase of the absolute phase values and of chargeability associated to an increase of the saturation decrease for mudstones.

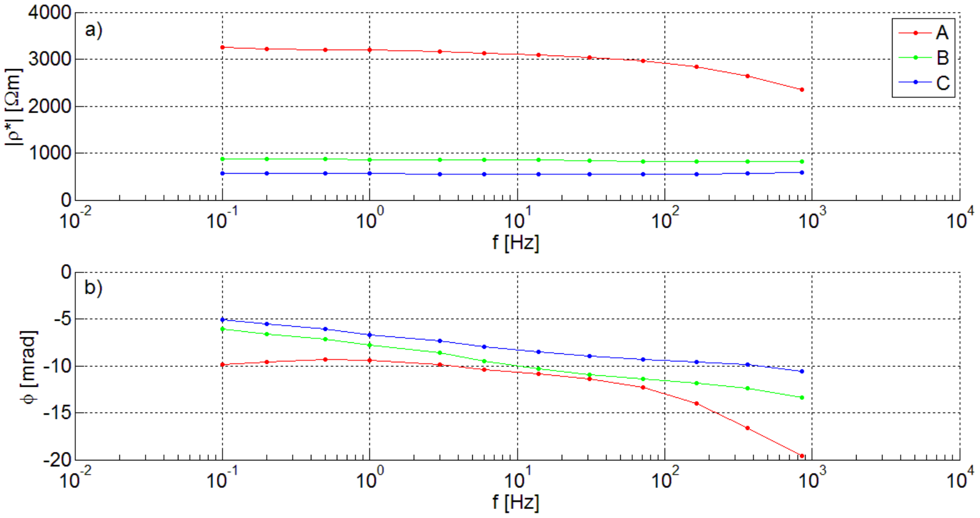

Fig. 7.36 - Resistivity amplitude and phase spectra of selected points of the EIT measurements in Senna Lodigiana. The location of the points is represented in Fig. 7.32a.

This behaviour is explained through the rearrangement of clay particles along the grain surfaces and the subsequent reduction of the total surface area and through the modification of the region mainly interested by current flow (large pores at high saturation, narrow pores at medium saturation, and water films at low saturation). This modification of the characteristic length scale also affect the distribution of relaxation times, with a shift of the phase peak toward higher frequency (*Binley et al.*, 2005).

7.4.3 Lozzolo

At the Lozzolo site, the electrode array was laid along a profile N129E, located on the second terrace of the mine from the lake (Fig. 7.37), at a distance of about 7 m from the front wall. As in the previous case, a non-flat morphology could affect the accuracy of the subsurface reconstruction. In addition, also the electrode were not laid on a plane, but a difference of a couple of meters was present between electrodes 1 and 30. Instead, the measured contact impedance was very low and constant among the electrodes (from 300 Ω to 600 Ω).

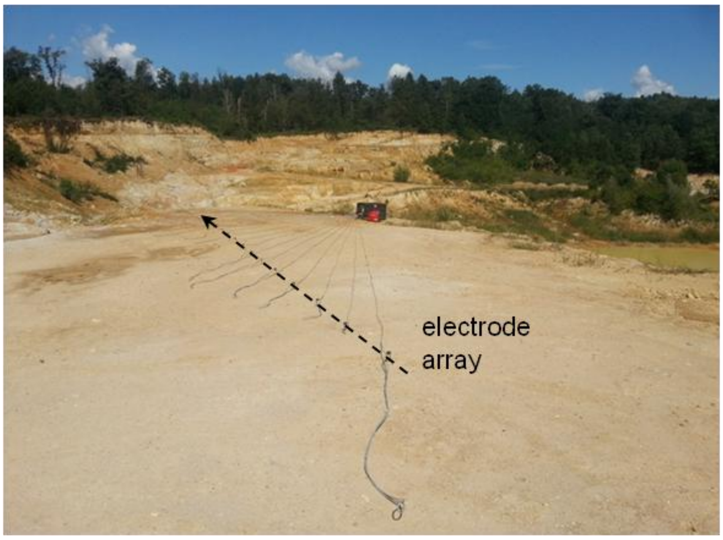

Fig. 7.37 - EIT acquisition in Lozzolo: the electrode array is arranged along a N129E profile.

The electrode array is located between x = 0 m and x = 29 m.

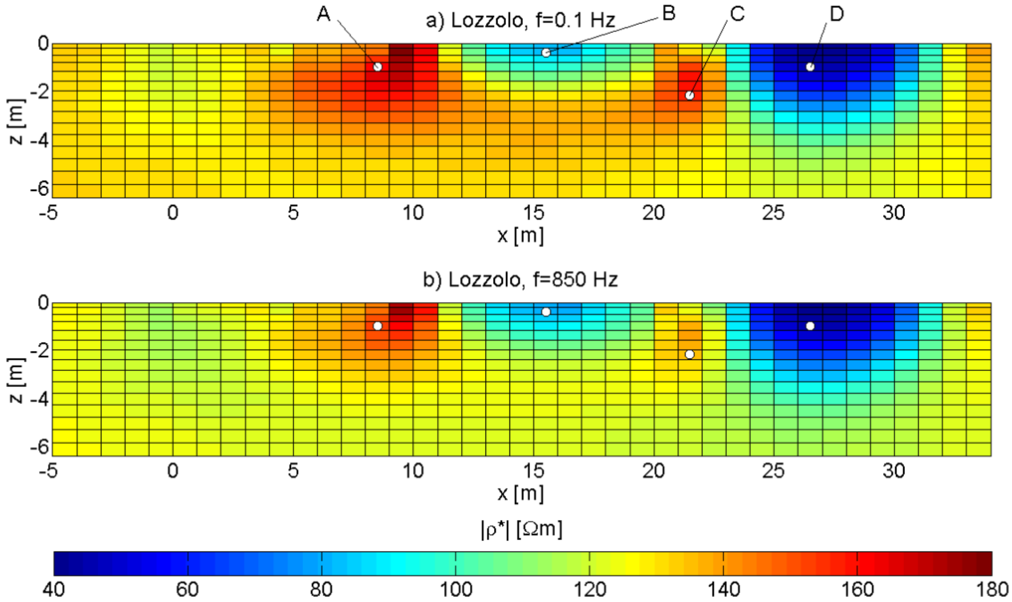

Fig. 7.38 - Resistivity amplitude sections at 0.1 Hz (a) and 850 Hz (b) in the upper part of the inversion grid. The electrode array is located between x = 0 m and x = 29 m. White dots represent the points selected for the spectra representation.

At 0.1 Hz three semi-circular regions of low resistivity that affect the first one or two meters depth are located in an average background resistivity of about 150 Ωm. The resistivity of these regions decreases in the x-direction (Fig. 7.38)a. The latter is well correlated with the occurrence of a brownish-yellowish silty-sand body (*Volpina*?) with a thickness of at least 2 m, with lithic rounded pebbles (maximum dimension 8 cm) and partially consolidated pebbles of muddy-sand rich in micas, with fine gravel (Fig. 7.38a). These are light grey in colour and have an elliptic shape up to 30 cm length; they probably correspond to *Caolino* that outcrop in a lenticular body on the wall of the upper terrace (Fig. 7.39b) and as pebbles on the surface where electrodes 1 to 10 are fixed. The front wall in correspondence of electrodes 10 to 30 was partially collapsed in the months prior the acquisition and thus covered. Silty-sandy sediments with gravel (*Complesso Basale*) are expected also in that portion.

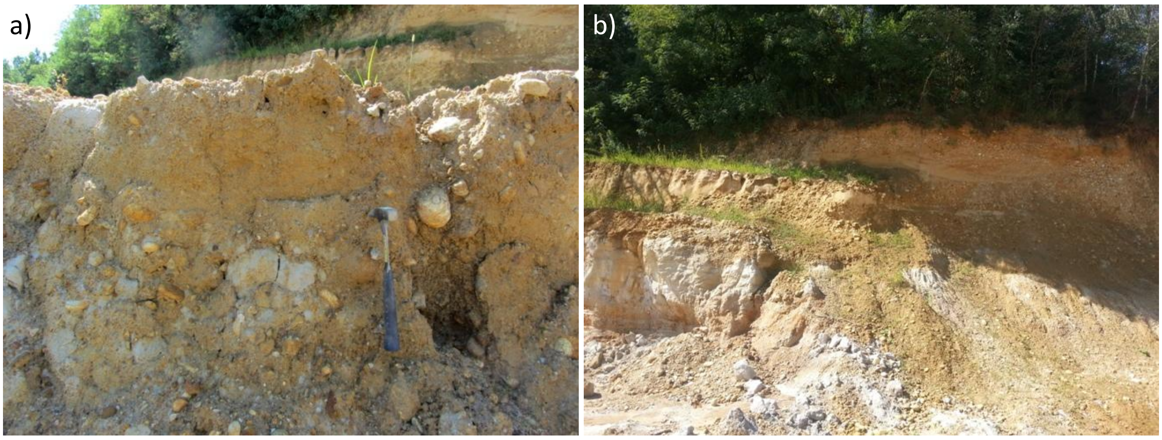

Fig. 7.39 - Silty-sand with lithic and partially consolidated pebbles of muddy-sand rich in micas (*Volpina*?) outcropping on the front wall of the quarry terrace between x = 20 m and x = 29 m (a); white lens of muddy sand (*Caolino*?) outcropping on the front wall of the upper terrace.

In general, the resistivity decreases with frequency in the whole inversion grid (Fig. 7.40). The only small region with an opposite behaviour corresponds to the region with the lowest resistivity, as in the case of Senna Lodigiana, but it shows a negligible increase (maximum 1.5%). A layer with a high reduction of resistivity (i.e., a high chargeability) is located between x = 3 m and x = 24 m, and between 1 m and 4 m depth. This layer corresponds to the zone of high absolute phase values (Fig. 7.41).

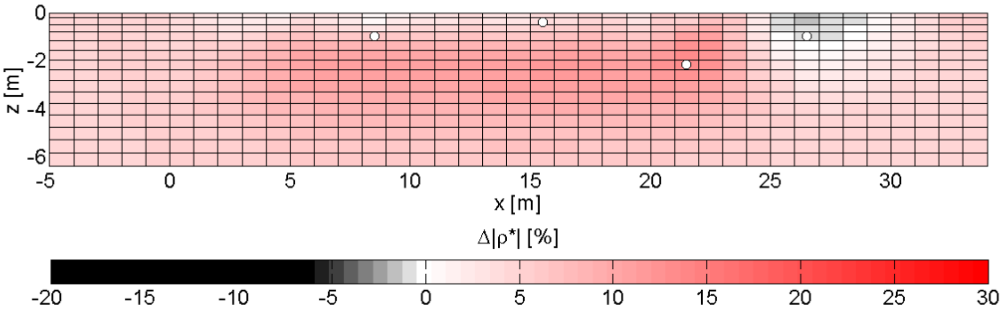

Fig. 7.40 - Relative reduction of resistivity amplitude between 0.1 Hz and 850 Hz in the upper part of the inversion grid. The electrode array is located between x = 0 m and x = 29 m. White dots represent the points selected for the spectra representation.

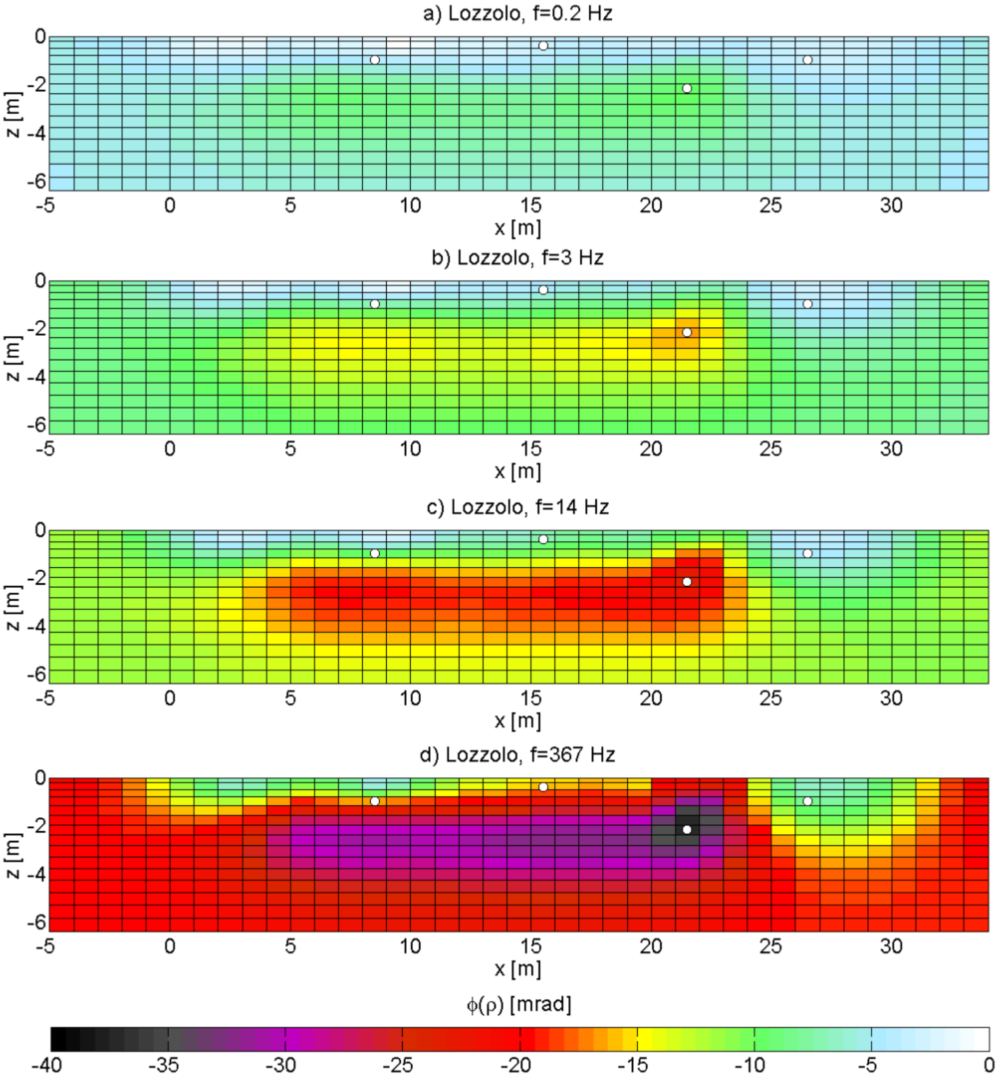

Fig. 7.41 - Resistivity phase sections at 0.2 Hz (a), 3 Hz (b), 14 Hz (c), and 367 Hz (d) in the upper part of the inversion grid. The electrode array is located between x = 0 m and x = 29 m. White dots represent the points selected for the spectra representation.

The phase images thus show a different structure as compared to the amplitude images. More conductive and less polarisable regions (points B and D) typically occur on the surface, where both a compaction and re-orientation of clay particles and eluviations could have contributed to a reduction of the surface area. However, also differences in the saturation degree, easily supported by different rate of drainage due to a heterogeneous distribution of sand and clay can explain this result. This is suggested also by the presence of small pools (ρ_w = 476 Ωm on the average) in different positions on the terrace. Below the surface level, a more resistive and more polarisable material occurs (point C). The phase spectrum of this point is strongly similar to that obtained with the laboratory measurement performed on the *Volpina* sample (LZ13), as it can be seen in Fig. 7.42. Points A, B, and D have instead a characteristic downward concave spectrum, which was observed only in samples LZ14 (slightly-gravelly muddy sand) and Sb8j (sandy mud).

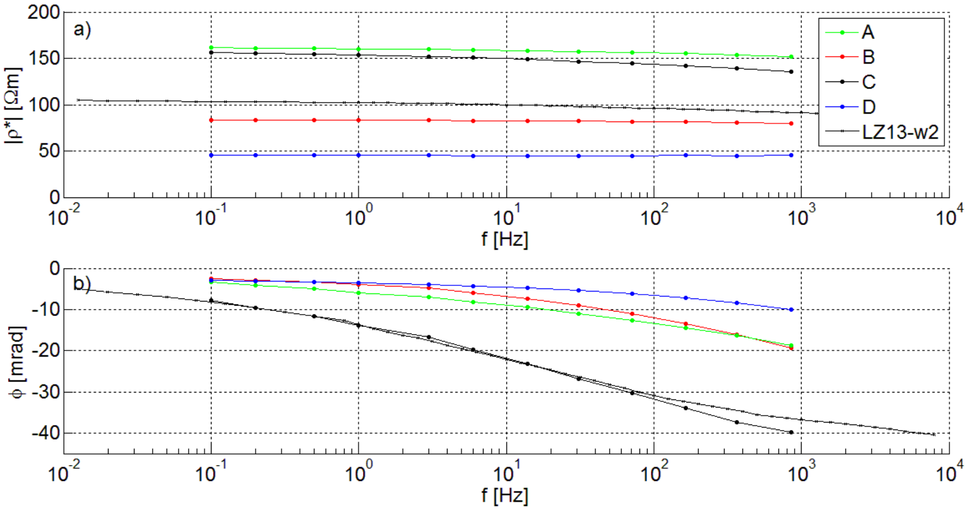

Fig. 7.42 - Resistivity amplitude and phase spectra of selected points of the EIT measurements in Lozzolo. The location of the points is represented in Fig. 7.38a.

Chapter 8

Conclusions

This Ph.D. research concerned the design and realization of an experimental apparatus to measure complex electrical resistivity (amplitude and phase) of unconsolidated samples, the compilation of a local reference SIP database for saturated sediments representative of alluvial environments, and the investigation of the petrophysical relationships between electrical properties and solid and fluid properties of the samples.

For the first item, the prescriptions derived from the literature and the characteristics of the sample holder previously used for DC analysis were joined. This resulted in an experimental apparatus composed of an ADC card, an amplifier unit with high input impedance, and a cylindrical sample holder with a volume of about 540 cm^3. The potential electrodes were created by coating a silver wire with AgCl, which permitted to avoid electrode polarization effects even with the placement of these electrodes within the cylinder. On the other hand, this expedient guaranteed a high contact area and thus a low contact impedance also at high frequency. Several design choices and acquisition protocols were tested in order to improve the accuracy, especially on the phase; the final system was characterized by systematic average errors of about 1% on the amplitude and <1 mrad on the phase from 10 mHz to 10 kHz. The measurement repeatability and the comparison with a qualified instrument was satisfactory, with major differences related to the packing method of the solid and fluid phases into the holder and not to the system itself.

SIP measurements were executed on a set of 19 unconsolidated materials collected in four sites of the Po plain south of Milan (Orio Litta, Senna Lodigiana, Landriano, and Lozzolo), and saturated with seven NaCl-water solutions with electrical resistivity varying from 0.9 Ωm to 315 Ωm. The textural composition of the samples varied between slightly-sandy mud and gravelly sand, and the porosity of the repacked samples between 0.26 and 0.63. Additional samples of well-sorted sands and sand-clay mixtures were analyzed to determine the individual complex electrical response of grain-size, water resistivity, clay content, etc. This SIP database constitutes a wide reference system for unconsolidated materials, which are not prepared as mixtures of sorted classes of grain-size but derive from the sampling of sedimentary layers. This main difference from the previous literature is essential to evaluate the weight of contaminating factors, such as variations in mineralogy, organic matter, grain-size-distribution curve, etc., on the measured SIP response.

The resistivity amplitude and phase spectra were modelled with single-relaxation models (Cole-Cole and generalized Cole-Cole) in a limited low-frequency interval and with a multi-relaxation model (Debye decomposition) on the whole investigated frequency range. For the Cole-type, single-relaxation models, a single-optimization was used to determine the best fitting parameters and an original multi-optimization approach was tested to obtain a set of optimal solutions (*Inzoli and Giudici*, 2015). The best fitting parameters were very similar to the representative values of the solutions' set, but the second method also provided an uncertainty interval for each model parameter, which was a valuable additional indicator to avoid the misinterpretation of petrophysical relationships with scarcely reliable parameters. For the DD multi-relaxation model, the fitting was conducted with two algorithms, i.e., non-negative least square and Tikhonov, which provided comparable results in terms of integral model parameters and non-continuous and continuous relaxation time distributions, respectively. The latter was then selected due the higher physical meaning of the continuous and smoothed relaxation time distribution.

Significant direct relationships were identified between DC resistivity of all models and water resistivity, and between chargeability (or normalized chargeability) and mud content. The 10-based logarithm of the relaxation time of the Cole-type models was inversely correlated with a characteristic diameter, whereas no such a relationship was identified with any of the relaxation times derived from the DD model. The loss of this relation was attributed to the intrinsic differences between the models. In fact, CC and GCC models describe only the complex electrical behaviour at low frequency, in a specific interval determined for each sample by the identification of a curve with negative curvature on the Argand plot, as a single polarization process. On the other hand, the DD approach takes into consideration the whole frequency interval and the occurrence of several polarization processes characterized by different relaxation times. In order to maintain the whole spectral information also in the search for electrical-textural relationships, the application of multivariate statistical tools was introduced, in the form of a combination of cluster analysis and principal component analysis. This constituted a new approach to relate spectral electrical behaviour to litho-textural properties (*Inzoli et al.*, submitted), avoiding the selection of individual parameters or individual frequency. The CA permitted to classify the samples on the basis of their electrical behaviour, and the PCA allowed to interpret the variability within the database in terms of a series of parameters ordered by importance. A textural characterization (expressed through the quartiles of the grain-size-distribution and of the gravel and mud contents) was associated to each cluster based on the characteristics of the corresponding samples. Analogously, a typical range of water resistivity was attributed to each cluster.

The association of variability ranges of electrical and sedimentological properties was then used to infer the sediments' properties of samples external to the input database, with satisfactory results. The high flexibility of the hierarchical clustering also allowed evaluating the differences in the inferred properties according to the number of selected clusters.

As an answer to the key problem of distinguishing the electrical response due to texture and water, the SIP measurements, integrated by the CA-PCA approach, provided better results than those obtained with DC measurements. In fact, the clustering separates the samples on the basis of their grain-size-distribution at low level of classification (i.e., low number of clusters) and on the basis of water resistivity at higher level of classification.

Competing effects were also recognized, such as the arrangement of grains, clay particles and pores and the mineralogy of the fine-grained component; they increased the uncertainty in litho-textural estimations by enlarging the intra-cluster variability (i.e., by joining samples to a specific cluster, even in absence of textural similarity). However, properties or samples that were not considered in this work can be easily added in the future within the same workflow in order to improve the cluster characterization.

Finally, some preliminary SIP tests were performed in three field sites. Field and laboratory results were not completely comparable, due to the differences in porosity, water content, and scale of investigation. However, some peculiar characters of the laboratory spectra were recognized in the corresponding field spectra, such as the low-phase in Landriano, and the high-phase in Lozzolo. A qualitative interpretation of the resistivity amplitude and phase distribution from the surface to a depth of about 5 m also provided a subsurface model in accordance with geological observations and previous geophysical surveys.

References

Abdel Aal, G. Z., Atekwana E. A., Rossbach S., and Werkema D. D. (2010), Sensitivity of geoelectrical measurements to the presence of bacteria in porous media. Journal of Geophysical Research, 115, G03017.

Agip (1994), Acque dolci sotterranee: inventario dei dati raccolti dall'Agip durante la ricerca di idrocarburi in Italia dal 1971 al 1990. Agip S.p.a., 515 pp., Roma.

Alfano L., and Mancuso M. (1996), Sull'applicabilità del metodo dipolo-polare continuo nelle ricerche idriche a media profondità in aree di pianura. Acque Sotterranee, 13(2-50), 61-71.

Anfossi G., Desio A., Gelati R., Laureri S., Petrucci F., and Venzo S. (1967), Note Illustrative della Carta Geologica d'Italia alla scala 1:100.000, Foglio 60 Piacenza, Servizio Geologico d'Italia, Roma.

Arca S., and Beretta G. P. (1985), Prima sintesi geodetica-geologica sui movimenti verticali del suolo nell'Italia Settentrionale (1897-1957). Bollettino di Geodesia e Scienze Affini, 2.

Archie G. E. (1942), Electrical resistivity log as an aid in determining some reservoir characteristics. Transaction of American Institute of Mining Metallurgical and Petroleum Engineers, 146, 54-62.

Atekwana E. A., Atekwana E. A., Rowe R. S., Werkema D. D., and Legall F. D. (2004), The relationship of total dissolved solids measurements to bulk electrical conductivity in an aquifer contaminated with hydrocarbon. Journal of Applied Geophysics, 56(4), 281-294.

Attwa M., and Günther T. (2013), Spectral induced polarization measurements for predicting the hydraulic conductivity in sandy aquifers. Hydrology and Earth System Sciences, 17(10), 4079-4094.

Bairlein K., Hördt A., and Nordsiek S. (2014), The influence on sample preparation on spectral induced polarization of unconsolidated sediments. Near Surface Geophysics, 12(2036), 667-677.

Baio M., Bersezio R., Bini A., Cavalli E., Cantone M., Mele M., Pavia F., Losi E., Rigato V., Rodondi C., Sommariga M., and Zembo I. (2009), Geological and geomorphological map of the Lodi alluvial Plain: the contribution of surface geology to hydrostratigraphic reconstruction. Epitome, 3(5), ISSN 1972-1552.

Baratelli F., Giudici M. and Vassena C. (2011), Single and dual-domain models to evaluate the effects of preferential flow paths in alluvial sediments. Transport in Porous Media 87, 465-484.

Barsoukov E., and Macdonald J. R. (2005), Impedance Spectroscopy, Theory Experiment and Applications. Wiley-Interscience, John Wiley and Sons, Hoboken, New Jersey.

Bersezio R., Cavalli E., and Cantone M. (2010), Aquifer building and Apennine tectonics in a Quaternary foreland: the southernmost Lodi plain of Lombardy. Memorie Descrittive Carta Geologica d'Italia, XC, 21-30.

Bersezio R., Giudici M., and Mele M. (2007), Combining sedimentological and geophysical data for high-resolution 3-D mapping of fluvial architectural elements in the Quaternary Po plain (Italy). Sedimentary Geology, 202(1-2), 230-248.

Bini A. (1987), L'apparato glaciale Würmiano di Como. Ph.D. thesis, Università degli Studi di Milano (Italy).

Bini A. (1997), Problems and methodologies in the study of the Quaternary deposits of the Southern side of the Alps. Geologia Insubrica, 2(2), 11-20.

Bini A., Strini A., Violanti D., and Zuccoli L. (2004), Geologia di sottosuolo dell'alta pianura a NE di Milano. Il Quaternario, 17, 343-354.

Binley A., Cassiani G., and Deiana R. (2010), Hydrogeophysics: opportunities and challenges. Bollettino di Geofisica Teorica ed Applicata, 51(4), 267-284.

Binley A., Slater L. D., Fukes M., and Cassiani G. (2005), Relationship between spectral induced polarization and hydraulic properties of saturated and unsaturated sandstone. Water Resources Research, 41(12).

Binley A., Hubbard S. S., Huisman J. A., Revil A., Robinson D. A., Singha K., and Slater L. D. (2015), The emergence of hydrogeophysics for improved understanding of subsurface processes over multiple scales. Water Resources Research, 51(6), 3837-3866.

Blasone R. S., Madsen H., and Rosbjerg D. (2007), Parameter estimation in distributed hydrological modelling: comparison of global and local optimisation techniques. Nordic Hydrology, 38, 451-476.

Blott S. J., and Pye K. (2012), Particle size scales and classification of sediment types based on particle size distributions: review and recommended procedures. Sedimentology, 59(7), 2071-2096.

Boadu F. K., and Seabrook B. C. (2006), Effects of clay content and salinity on the spectral electrical response of soils. Journal of Environmental and Engineering Geophysics, 11(3), 161-170.

Boni A. (1967), Note Illustrative della Carta Geologica d'Italia alla scala 1:100.000, Foglio 59 Pavia, Servizio Geologico d'Italia, Roma.

Bottino G. (1973), Studio geologico e mineralogico delle argille di Lozzolo (Biellese). Estratto dai Rendiconti della Società Italiana di Mineralogia e Petrologia, XXIX.

Boyle D. P., Gupta H. V., and Sorooshian S. (2000), Toward improved calibration of hydrologic models: combining the strengths of manual and automatic methods. Water Resources Research, 36, 3663.

Boyle D. P., Gupta H. V., Sorooshian S., Koren V., Zhang Z., and Smith M. (2001), Toward improved streamflow forecasts: value of semidistributed modeling. Water Resources Research, 37, 2749.

Breede K., Kemna A., Esser O., Zimmermann E., Vereecken H., and Huisman J. A. (2012), Spectral induced polarization measurements on variably saturated sand-clay mixtures. Near Surface Geophysics, 10(6), 479-489.

Bresciani I., and Perotti C. R. (2014), An active deformation structure in the Po Plain (N Italy): The Romanengo anticline. Tectonics, 33, 2059-2076.

Cantone M. (2008), Geologia e idrostratigrafia della pianura lodigiana a sud di Lodi. Ph.D tesi, Università degli Studi di Milano (Italy).

Carminati E. (2003), Influence of glacial cycles and tectonics on natural subsidence in the Po Plain (Northern Italy): Insights from 14 C ages. Geochemistry Geophysics Geosystems, 4(10).

Carraro F., Bortolami G., and Sacchi R. (1967), Note Illustrative della Carta geologica d'Italia alla scala 1:100000, Foglio 43 Biella, Servizio Geologico d'Italia, Roma.

Carroll D. (1959), Ion exchange in clays and other minerals. Geological Society of America Bulletin, 70(6), 749-779.

Casati C. (2012), Revisione della successione geologica presente nella miniera di argille "Fornaccio" presso Lozzolo (VC) al fine dell'attività estrattiva. M.Sc. thesis, Università degli Studi di Milano (Italy).

Cassiani G., Kemna A., Villa A., and Zimmermann E. (2009), Spectral induced polarization for the characterization of free-phase hydrocarbon contamination of sediments with low clay content. Near Surface Geophysics, 7, 547-562.

Castiglioni G. B., Biancotti A., Bondesan M., Castaldini B., Ciabatti M., Cremaschi M., Favero V., Pellegrini G. B., et al. (1997), Carta geomorfologica della Pianura Padana / Geomorphological map of the Po plain. 1:250.000. S.E.L.C.A., Firenze.

Castiglioni G. B., and Pellegrini G. B. (2001), Note illustrative della carta geomorfologica della Pianura Padana / Illustrative notes of the geomorphological map of Po Plain (Italy). Supplementi di Geografia Fisica e Dinamica Quaternaria, 4, 207 pp.

Chen J., Hubbard S. S., Williams K. H., Flores Orozco A., and Kemna A. (2012), Estimating the spatiotemporal distribution of geochemical parameters associated with biostimulation using spectral induced polarization data and hierarchical Bayesian models. Water Resources Research, 48(5), W05555.

Clavier C., Coates G., and Dumanoir J. (1984), Theoretical and experimental bases for the dual-water model for interpretation of shaly sands. Society of Petroleum Engineers Journal, 24, 153-168.

Cole K. S., and Cole R. H. (1941), Dispersion and absorption in dielectrics I - Alternating current characteristics. The Journal of Chemical Physics, 9(4), 341-351.

Cremaschi, M. (1987), Paleosols and vetusols in the Central Po Plain (Northern Italy). A study in Quaternary geology and soil development. Ph.D. thesis, Università degli Studi di Milano (Italy).

Dahlin T. (2000), Short note on electrode charge-up effects in DC resistivity data acquisition using multi-electrode arrays. Geophysical Prospecting, 48, 181-187.

Dahlin T., and Leroux V. (2012), Improvement in time-domain induced polarization data quality with multi-electrode systems by separating current and potential cables. Near Surface Geophysics, 10(6), 545-565.

Dahlin T., Leroux V., and Nissen J. (2002), Measuring techniques in induced polarisation imaging. Journal of Applied Geophysics, 50(3), 279-298.

Dal Moro G. (2010), Insights on surface wave dispersion and HVSR: Joint analysis via Pareto optimality. Journal of Applied Geophysics, 72, 129

Dal Moro G., and Pipan M. (2007), Joint inversion of surface wave dispersion curves and reflection travel times via multi-objective evolutionary algorithms. Journal of Applied Geophysics, 61, 39-55.

Davis J. C. (1973), Statistics and data analysis in geology. John Wiley & Sons, ISBN 0-471-83743-1.

De Donno G. (2013), 2D tomographic inversion of complex resistivity data on cylindrical models. Geophysical Prospecting, 61, 586-601.

De Donno G., and Cardarelli E. (2014), 3D complex resistivity tomography on cylindrical models using EIDORS. Near Surface Geophysics, 12(2036).

de Lima O. A. L., and Sharma M. M. (1990), A grain conductivity approach to shaly sandstones. Geophysics, 55(10), 1347-1356.

de Lima O. A. L., Clennel M. B., Nery G. G., and Niwas S. (2005), A volumetric approach for the resistivity response of freshwater shaly sandstones. Geophysics, 70(1), F1-F10.

dell'Arciprete D., Bersezio R., Felletti F., Giudici M., Comunian A., and Renard P. (2011), Comparison of three geostatistical methods for hydrofacies simulation: a test on alluvial sediments. Hydrogeology Journal, 20(2), 299-311.

Desio A. (1965), I rilievi isolati della pianura lombarda e i movimenti tettonici del Quaternario. Rendiconti Istituto Lombardo di Scienze e Lettere, 99, 881-894.

Dias C. A. (2000), Developments in a model to describe low-frequency electrical polarization of rocks. Geophysics, 65(2), 437-451.

Dutta N., Mukerji T., Prasad M., and Dvorkin J. (2002), Seismic detection and estimation of overpressures Part I: rock physics basis. CSEG Recorder, 27(7).

Efstratiadis A., and Koutsoyiannis D. (2010), One decade of multi-objective calibration approaches in hydrological modelling: a review. Hydrological Sciences Journal, 55(1), 58-78.

Fantoni R., Bersezio R., and Forcella F. (2004), Alpine structure and deformation chronology at the southern Alps-Po Plain border in Lombardy. Bollettino Della Societa Geologica Italiana, 123(3), 463-476.

Fiandaca G., Auken E., Christiansen A. V., and Gazoty A. (2012), Time-domain-induced polarization: Full-decay forward modeling and 1D laterally constrained inversion of Cole-Cole parameters. Geophysics, 77(3), E213-E225.

Flores Orozco A., Kemna A., and Zimmermann E. (2012), Data error quantification in spectral induced polarization imaging. Geophysics, 77(3), E227-E237.

Florsch N., Revil A., and Camerlynck C. (2014), Inversion of generalized relaxation time distributions with optimized damping parameter. Journal of Applied Geophysics, 109, 119-132.

Florsch N., Camerlynck C., and Revil A. (2012), Direct estimation of the distribution of relaxation times from induced-polarization spectra using a Fourier transform analysis. Near Surface Geophysics, 10(6), 517-531.

Gazoty A., Fiandaca G., Pedersen J., Auken E., and Christiansen A. V. (2012), Mapping of landfills using time-domain spectral induced polarization data: the Eskelund case study. Near Surface Geophysics, 10(6), 575-586.

Ghorbani A., Cosenza P., Revil A., Zamora M., Schmutz M., Florsch N., and Jougnot D. (2009), Non-invasive monitoring of water content and textural changes in clay-rocks using spectral induced polarization: A laboratory investigation. Applied Clay Science, 43(3-4), 493-502.

Giudici M., Mele M., Inzoli S., Comunian A., and Bersezio R. (2015), The application of hydrogeophysics to study water-based ecosystem services in alluvial plains. First break EAGE, 33(8), 55-60.

Gomaa M. M. (2009), Saturation effect on electrical properties of hematitic sandstone in the audio frequency range using non-polarizing electrodes. Geophysical Prospecting, 57(6), 1091-1100.

Gomaa M. M., and Alikaj P. (2010), Effect of electrode contact impedance on A.C. electrical properties of a wet hematite sample. Marine Geophysical Researches, 30(4), 265-276.

Grunat D. A., Slater L. D., and Wehrer M. (2013), Complex electrical measurements on an undisturbed soil core: evidence for improved estimation of saturation degree from imaginary conductivity. Vadose Zone Journal, 12(4).

Guggenheim S., and Martin R. T. (1995), Definition of clay and clay mineral: joint report of the AIPEA nomenclature and CMS nomenclature committees. Clays and Clay Minerals, 43(2), 255-256.

Gupta H. V., Sorooshian S., and Yapo P. O. (1998), Toward improved calibration of hydrologic models: multiple and non commensurable measures of information. Water Resources Research, 34, 751-763.

Hadzick Z. Z., Guber A. K., Pachepsky Y. A., and Hill R. L. (2011), Pedotransfer functions in soil electrical resistivity estimation. Geoderma, 164(3-4), 195-202.

Honig M., and Tezkan B. (2007), 1D and 2D Cole-Cole-inversion of time-domain induced-polarization data. Geophysical Prospecting, 55, 117-133.

Hördt A., and Milde S. (2012), Studies with gel-filled sandstone samples with implications for the origin of induced polarization. Near Surface Geophysics, 10(6), 469-478.

Hubbard S., and Rubin Y. (2000), Hydrogeological parameter estimation using geophysical data: a review of selected techniques. Journal of Contaminant Hydrology, 45, 3-34.

Huisman J. A., Zimmermann E., Esser O., Haegel F.-H., Treichel A., and Vereecken H. (2015), Evaluation of a novel correction procedure to remove electrode impedance effects from broadband SIP measurements. Journal of Applied Geophysics, *in press*.

Hwang C. L., and Masud A. S. M. (1979), Multiple objective decision making - Methods and applications. A state-of-the-art survey. Springer-Verlag, ISBN 978-3-540-09111-0.

Hördt A., Hanstein T., Hönig M., and Neubauer F. M. (2006), Efficient spectral IP-modelling in the time domain. Journal of Applied Geophysics, 59, 152-161.

Inzoli S. (2012), Analisi sperimentale della conducibilità elettrica di sedimenti alluvionali in relazione alle proprietà tessiturali e dei fluidi. M.Sc. thesis, Università degli Studi di Milano (Italy).

Inzoli S., and Giudici M. (2015), A comparison between single- and multi-objective optimization to fit spectral induced polarization data from laboratory measurements on alluvial sediments. Journal of Applied Geophysics, 122, 149-158.

Inzoli S., Giudici M., and Huisman J. A., Estimation of sediment texture from spectral induced polarization data using cluster and principal component analysis. Near Surface Geophysics, *under revision*.

Jones S. B., and Friedman S. P. (2000), Particle shape effects on the effective permittivity of anisotropic or isotropic media consisting of aligned or randomly oriented ellipsoidal particles. Water Resources Research, 36(10), 2821-2833.

Jougnot D., Ghorbani A., Revil A., Leroy P., and Cosenza P. (2010), Spectral induced polarization of partially saturated clay-rocks: a mechanistic approach. Geophysical Journal International, 180(1), 210-224.

Joyce R. A., Glaser II D. R., Werkema Jr D. D., and Atekwana E. A. (2012), Spectral induced polarization response to nanoparticles in a saturated sand matrix. Journal of Applied Geophysics, 77(0), 63-71.

Kadhim F. S., Samsuri A., and Kamal A. (2013), A review in correlations between cementation factor and carbonate rocks properties. Life Science Journal, 10(4), 2451-2458.

Kaufman L., and Rousseeuw P. J. (2005), Finding groups in data: an introduction to cluster analysis. John Wiley & Sons, Hoboken, New Jersey, ISBN 978-0471735786.

Kavian M., Slob E. C., and Mulder W. A. (2012a), Measured electric responses of unconsolidated layered and brine-saturated sand and sand-clay packs under continuous fluid flow conditions. Journal of Applied Geophysics, 80, 83-90.

Kavian M., Slob E. C., and Mulder W. A. (2012b), A new empirical complex electrical resistivity model. Geophysics, 77(3), E185-E191.

Keery J., Binley A., Elshenawy A., and Clifford J. (2012), Markov-chain Monte Carlo estimation of distributed Debye relaxations in spectral induced polarization. Geophysics, 77(2), E159-E170.

Keller G. V., and Frischknecht F. C. (1966), Electrical methods in geophysical prospecting. Pergamon Press.

Kemna A. (2000), Tomographic inversion of complex resistivity. Theory and application. Ph.D. thesis, Rhur-Universität Bochum (Germany).

Kemna A., Binley A., Cassiani G., Niederleithinger E., Revil A., Slater L., Williams K. H., Flores Orozco A., Haegel F. H., Hördt A., Kruschwitz S., Leroux V., Titov K., and Zimmermann E. (2012), An overview of the spectral induced polarization method for near-surface applications. Near Surface Geophysics, 10(6), 453-468.

Koch K., A. Kemna, J. Irving, and K. Holliger (2011), Impact of changes in grain-size and pore space on the hydraulic conductivity and spectral induced polarization response of sand, Hydrology Earth System Science, 15(6), 1785-1794.

Koch, K., Revil A., and Holliger K. (2012), Relating the permeability of quartz sands to their grain-size and spectral induced polarization characteristics. Geophysical Journal International, 190(1), 230-242.

Krumbein W. C. (1936), Application of logarithmic moments to size frequency distributions of sediments. Journal of Sedimentary Research, 6(1), 35-47.

Kruschwitz S., Binley A., Lesmes D., and Elshenawy A. (2010), Textural controls on low-frequency electrical spectra of porous media. Geophysics, 75(4), WA113-WA123.

Leroy P., and Revil A. (2009), A mechanistic model for the spectral induced polarization of clay materials. Journal of Geophysical Research: Solid Earth, 114(B10), B10202.

Lesmes D. P., and Morgan F. D. (2001), Dielectric spectroscopy of sedimentary rocks. Journal of Geophysical Research, 106(B7), 13329-13346.

Lesmes D. P., and Frye K. M. (2001), Influence of pore fluid chemistry on the complex conductivity and induced polarization responses of Berea sandstone. Journal of Geophysical Research, 106(B3), 4079-4090.

Livio F., Berlusconi A., Michetti A. M., Sileo G., Zerboni A., Trombino L., Cremaschi M., Mueller K., Vittori E., Carcano C., and Rogledi S. (2009), Active fault-related folding in the epicentral area of the December 25, 1222 (Io = IX MCS) Brescia earthquake (Northern Italy): Seismotectonic implications. Tectonophysics, 476(1-2), 320-335.

Madsen H. (2003), Parameter estimation in distributed hydrological catchment modelling using automatic calibration with multiple objectives. Advances in Water Resources 26, 205.

Magill M. T. (2010), Geoelectrical response of surfactant solutions in a quartzitic sand analog aquifer. United States Environemntal Protection Agency, EPA/600/R-10/041.

Mansoor N., and Slater L. (2007), On the relationship between iron concentration and induced polarization in marsh soils. Geophysics, 72(1), A1-A5.

Marler R. T., and Arora J. S. (2004), Survey of multi-objective optimization methods for engineering. Structural and Multidisciplinary Optimization, 26(6), 369-395.

Martinho E., Almeida F., and Senos Matias M. J. (2006), An experimental study of organic pollutant effects on time domain induced polarization measurements. Journal of Applied Geophysics, 60(1), 27-40.

Mele M. (2008), L'architettura degli acquiferi alluvionali: una metodologia integrata geologico-geofisica per la caratterizzazione a diverse scale,. Ph.D. thesis, Università degli Studi di Milano (Italy).

Mele M., Bersezio R., and Giudici M. (2012), Hydrogeophysical imaging of alluvial aquifers: electrostratigraphic units in the quaternary Po alluvial plain (Italy). International Journal of Earth Sciences, 101(7), 2005-2025.

Mele M., Bersezio R., Giudici M., Inzoli S., Cavalli E., and Zaja A. (2013), Resistivity imaging of Pleistocene alluvial aquifers in a contractional tectonic setting: A case history from the Po plain (Northern Italy). Journal of Applied Geophysics, 93(0), 114-126.

Mele M., Bersezio R., Giudici M., Rusnighi Y., and Lupis D. (2010), The architecture of alluvial aquifers: an integrated geological-geophysical methodology for multiscale characterization. Memorie Descrittive Carta Geologica d'Italia, XC, 209-224.

Mele M., Ceresa N., Bersezio R., Giudici M., Inzoli S., and Cavalli E. (2015), Resolving electrolayers from VES: A contribution from modelling the electrical response of a tightly constrained alluvial stratigraphy. Journal of Applied Geophysics, 119, 25-35.

Mele M., Inzoli S., Giudici M., and Bersezio R. (2014), Relating electrical conduction of alluvial sediments to textural properties and pore-fluid conductivity. Geophysical Prospecting, 62(3), 631-645.

Menke W. (2012), Geophysical data analysis: discrete inverse theory. MATLAB edition. Elsevier, 293 pp, ISBN 978-0-12-397160-9.

Meunier A. (2005), Clays. Springer Berlin Heidelberg, New York, 472 pp., ISBN 3-540-21667-7.

Muttoni G., Carcano C., Garzanti E., Ghielmi M., Piccin A., Pini R., Rogledi S., and Sciunnach D. (2003), Onset of Major Pleistocene glaciations in the Alps. Geology, 31, 989-992.

Nassar M. K., and Ginn T. R. (2014), Impact of numerical artifact of the forward model in the inverse solution of density-dependent flow problem. Water Resources Research, 50, 6322–6338.

Nordsiek S., and Weller A. (2008), A new approach to fitting induced-polarization spectra. Geophysics, 73(6), F235-F245.

Oh M., Kim Y., and Park J. (2007), Factors affecting the complex permittivity spectrum of soil at a low frequency range of 1 kHz–10 MHz. Environmental Geology, 51(5), 821-833.

Ortuani B., Chiaradia E. A., Priori S., L'Abate G., Canone D., Mele M., Comunian A., Giudici M., and Facchi A. (2015), Comparing EM38 and Profiler-EMP400 for the delineation of homogeneous management zones within agricultural fields. Extended abstract, Near Surface Geoscience 2015, Turin (Italy).

Ortuani B., Benedetto A., Giudici M., Mele M., and Tosti F. (2013), A non-invasive approach to monitor variability of soil water content with electromagnetic methods. Procedia Environmental Sciences, 19, 446-455.

Pellegrini L., Boni P., and Carton A. (2003), Hydrographic evolution in relation to neotectonics aided by data processing and assessment: some examples from the Northern Apennines (Italy). Quaternary International, 101-102, 211-217.

Pelton W., Ward S., Hallof P., Sill W., and Nelson P. (1978), Mineral discrimination and removal of inductive coupling with multifrequency IP. Geophysics, 43(3), 588-609.

Penk A., Bruckner E. (1909), Die Alpen im Eiszeitalter. Erster Band. Die Eiszeiten in den Nördlichen Ostalpen. Leipzig.

Pettinelli E., Vannaroni G., Cereti A., Pisani A. R., Paolucci F., Del Vento D., Dolfi D., Riccioli S., and Bella F. (2005), Laboratory investigations into the electromagnetic properties of magnetite/silica mixtures as Martian soil simulants. Journal of Geophysical Research, 110, E04013.

Pieri M., and Groppi G. (1981), Subsurface geological structure of the Po Plain, Italy. Publ. 414, P.F. Geodinamica, CNR, 23 pp., Roma.

Ponziani M., Slob E. C., Ngan-Tillard D. J. M., and Vanhala H. (2011), Influence of water content on the electrical conductivity of peat. International Water Technology Journal, 1(1), 14-21.

Ponziani M., Slob E. C., Vanhala H., and Ngan-Tillard D. J. M. (2012), Influence of physical and chemical properties on the low-frequency complex conductivity of peat. Near Surface Geophysics, 10(6), 491,501.

Rao S. M., and Thyagaraj T. (2007), Role of direction of salt migration on the swelling behaviour of compacted clays. Applied Clay Science, 38(1–2), 113-129.

Regione Emilia-Romagna, and Eni-Agip (1998), Riserve idriche sotterranee della Regione Emilia-Romagna. Servizio Geologico, Sismico e dei Suoli, Bologna.

Regione Lombardia, and Eni-Agip (2001), Geologia degli acquiferi Padani della Regione Lombardia. A cura di Carcano C. e Piccin A., S.E.L.C.A., Firenze.

Revil A. (2012), Spectral induced polarization of shaly sands: Influence of the electrical double layer, Water Resources Research, 48(2).

Revil A. (2013), Effective conductivity and permittivity of unsaturated porous materials in the frequency range 1 mHz–1GHz, Water Resources Research, 49(1), 306-327.

Revil A., and Florsch N. (2010), Determination of permeability from spectral induced polarization in granular media. Geophysical Journal International, 181, 1480-1498.

Revil A., and Skold M. (2011), Salinity dependence of spectral induced polarization in sands and sandstones, Geophysical Journal International, 187(2), 813-824.

Revil A., Eppehimer J. D., Skold M., Karaoulis M., Godinez L., and Prasad M. (2013), Low-frequency complex conductivity of sandy and clayey materials. Journal of Colloid and Interface Science, 398(0), 193-209.

Revil A., Florsch N., and Camerlynck C. (2014), Spectral induced polarization porosimetry. Geophysical Journal

Revil A., Koch K., and Holliger K. (2012), Is it the grain-size or the characteristic pore size that controls the induced polarization relaxation time of clean sands and sandstones?. Water Resources Research, 48, W05602.

International, 198(2), 1016-1033.

Reynolds J. M. (2011), An introduction to applied and environmental geophysics. John Wiley & Sons, 710 pp., ISBN 978-0-471-48535-3.

Robinson D. A., and Friedman S. P. (2001), Effect of particle-size distribution on the effective dielectric permittivity of saturated granular media. Water Resources Research, 37(1), 33-40.

Rousseeuw P. J. (1987), Silhouettes: a graphical aid to the interpretation and validation of cluster analysis. Journal of Computational and Applied Mathematics, 20, 53.

Salem H. S., and Chilingarian G. V. (1999), The cementation factor of Archie's equation for shaly sandstone reservoirs. Journal of Petroleum Science and Engineering, 23, 83-93.

Sarstedt M., and Mooi E. (2011), A concise guide to market research - The process, data, and methods using IBM SPSS statistics. Springer, ISBN 978-3642125409.

Saltas V., Vallianatos F., Soupios P., Makris J. P., and Triantis D. (2007), Dielectric and conductivity measurements as proxy method to monitor contamination in sandstone. Journal of Hazardous Material, 142(1-2), 520-525.

Scardia G., Muttoni G., and Sciunnach D. (2006), Subsurface magnetostratigraphy of Pleistocene sediments from the Po Plain (Italy): Constraints on rates of sedimentation and rock uplift. Geological Society of America Bulletin, 118, 1299-1312.

Scardia G., De Franco R., Muttoni G., Rogledi S., Caielli G., Carcano C., Sciunnach D., and Piccin A. (2012), Stratigraphic evidence of a Middle Pleistocene climate-driven flexural uplift in the Alps. Tectonics, 31, TC6004.

Schwartz N., Huisman J. A., and Furman A. (2012), The effect of NAPL on the electrical properties of unsaturated porous media, Geophysical Journal International, 188(3), 1007-1011.

Schwarz G. (1962), A theory of the low-frequency dielectric dispersion of colloidal particles in electrolyte solution 1,2. The Journal of Physical Chemistry, 66(12), 2636-2642.

Scott J. B. T., and Barker R. D. (2003), Determining pore-throat size in Permo-Triassic sandstones from low-frequency electrical spectroscopy, Geophysical Research Letters, 30(9), 1450.

Seigel H. (1959), Mathematical formulation and type curves for induced polarization. Geophysics, 24(3), 547-565.

Seigel H. O., Vanhala H., and Sheard S. N. (1997), Some case histories of source discrimination using time-domain spectral IP. Society of Exploration Geophysicists, Tulsa, OK, ETATS-UNIS.

Sen P. N., Goode P. A., and Sibbit A. (1988), Electrical conduction in clay bearing sandstones at low and high salinities. Journal of Applied Physics, 63(10), 4832.

Shevnin V., Mousatov A., Ryjov A., and Delgado-Rodriguez O. (2007), Estimation of clay content in soil based on resistivity modelling and laboratory measurements. Geophysical Prospecting, 55, 265-275.

Shevnin V., Delgado-Rodriguez O., Mousatov A., and Ryjov A. (2006), Estimation of hydraulic conductivity on clay content in soil determined from resistivity data. Geofisica Internacional, 45(3), 195-207.

Shivola A. (1999), Electromagnetic mixing formulas and applications. Institution of Electrical Engineers, Electromagnetic Waves Series, 47, 296 pp, London, ISBN 0852967721.

Shlens J. (2014), A tutorial on principal component analysis. arXiv preprint arXiv:1404.1100

Skold M., Revil A., and Vaudelet P. (2011), The pH dependence of spectral induced polarization of silica sands: Experiment and modeling. Geophysical Research Letters, 38(12), L12304.

Slater L. D. (2007), Near surface electrical characterization of hydraulic conductivity: from petrophysical properties to aquifer geometries - A review. Surveys in Geophysics, 28(2-3), 169-197.

Slater L. D., and Binley A. (2003), Evaluation of permeable reactive barrier (PRB) integrity using electrical imaging methods. Geophysics, 68(3), 911-921.

Slater L. D., and Glaser D. R. (2003), Controls on induced polarization in sandy unconsolidated sediments and application to aquifer characterization. Geophysics, 68(5), 1547-1558.

Slater L. D., and Lesmes D. P. (2002), Electrical-hydraulic relationships observed for unconsolidated sediments. Water Resources Research, 38(10).

Slater L. D., Barrash W., Montrey J., and Binley A. (2014), Electrical-hydraulic relationships observed for unconsolidated sediments in the presence of a cobble framework. Water Resources Research, 50(7), 5721-5742.

Slater L. D., Choi J., and Wu Y. (2005), Electrical properties of iron-sand columns: implications for induced polarization investigation and performance monitoring of iron-wall barriers. Geophysics, 70(4), G87-G94.

Slater L. D., Ntarlagiannis D., and Wishart D. (2006), On the relationship between induced polarization and surface area in metal-sand and clay-sand mixtures. Geophysics, 71(2), A1-A5.

Sokal R. R., and Michener C. D. (1958), A statistical method for evaluating systematic relationships. University of Kansas Scientific Bulletin, 28, 1409-1438.

Steuer R.E. (1986), Multiple criteria optimization: theory, computation, and application. John Wiley & Sons, ISBN 0894643932.

Tarasov A., and Titov K. (2007), Relaxation time distribution from time domain induced polarization measurements. Geophysical Journal International, 170(1), 31-43.

Tarasov A., and Titov K. (2013), On the use of the Cole-Cole equations in spectral induced polarization. Geophysical Journal International, 195(1), 352-356.

Titov K., Tarasov A., Ilyin Y., Seleznev N., and Boyd A. (2010), Relationships between induced polarization relaxation time and hydraulic properties of sandstone. Geophysical Journal International, 180(3), 1095-1106.

Tong M., Li L., Wang W. N., and Jiang Y. (2006), A time-domain induced-polarization method for estimating permeability in a shaly sand reservoir. Geophysical Prospecting, 54, 623-631.

Tronicke J., Holliger K., Barrash W., and Knoll M. D. (2004), Multivariate analysis of cross-hole georadar velocity and attenuation tomograms for aquifer zonation. Water Resources Research, 40, W01519.

Ulrich C., and Slater L. D. (2004), Induced polarization measurements on unsaturated, unconsolidated sands. Geophysics, 69(3), 762-771.

Ustra A., Slater L. D., Ntarlagiannis D., and Elis V. (2012), Spectral Induced Polarization (SIP) signatures of clayey soils containing toluene. Near Surface Geophysics, 10(6), 503-515.

Vanhala H. (1997), Mapping oil-contaminated sand and till with the spectral induced polarization (SIP) method. Geophysical Prospecting, 45, 303-326.

Vaudelet P., Revil A., Schmutz M., Franceschi M., and Bégassat P. (2011a), Induced polarization signatures of cations exhibiting differential sorption behaviors in saturated sands. Water Resources Research, 47(2), W02526.

Vaudelet P., Revil A., Schmutz M., Franceschi M., and Bégassat P. (2011b), Changes in induced polarization associated with the sorption of sodium, lead, and zinc on silica sands. Journal of Colloid and Interface Science, 360(2), 739-752.

Vereecken H., Döring U., Hardelauf H., Jaekel U., Hashagen U., Neuendorf O., Schwarze H., and Seidemann R. (2000), Analysis of solute transport in a heterogeneous aquifer: the Krauthausen field experiment. Journal of Contaminant Hydrology, 45(3–4), 329-358.

Volkmann J., and Klitzsch N. (2010), Frequency-dependent electric properties of microscale rock models for frequencies from one millihertz to ten kilohertz. Vadose Zone Journal, 9(4), 858-870.

Volkmann J., and Klitzsch N. (2015), Wideband impedance spectroscopy from 1mHz to 10MHz by combination of four- and two-electrode methods. Journal of Applied Geophysics, 114, 191-201.

Vrugt J. A., Gupta H. V., Bastidas L. A., Bouten W., and Sorooshian S. (2003), Effective and efficient algorithm for multiobjective optimization of hydrologic models. Water Resources Research, 39, 1214.

Walkley A., and Black I. A. (1934), An examination of the Degtjareff method for determining soil organic matter, and proposed modification of the chromic acid titration method. Soil Science, 37, 1, 29.

Ward Jr J. H. (1963), Hierarchical grouping to optimize objective function. Journal of the American Statistical Association, 58, 301, 236-244.

Waxman M. H., and Smits L. J. M. (1968), Electrical conductivities in oil-bearing shaly sands. Society of Petroleum Engineers Journal, 8, 107-122.

Weller A., and Slater L. D. (2012), Salinity dependence of complex conductivity of unconsolidated and consolidated materials: Comparisons with electrical double layer models. Geophysics, 77(5), D185-D198.

Weller A. Breede K., Slater L., and Nordsiek S. (2011), Effect of changing water salinity on complex conductivity spectra of sandstones. Geophysics, 76(5), F315-F327.

Weller A., Slater L., Nordsiek S., and Ntarlagiannis D. (2010), On the estimation of specific surface per unit pore volume from induced polarization: A robust empirical relation fits multiple data sets. Geophysics, 75(4), WA105-WA112.

Wentworth C. K. (1922), A scale of grade and class terms for clastic sediments. The Journal of Geology, 30(5), 377-392.

Werkema Jr D. D., Glaser D., Joyce R., Hawkins D., Atekwana E., and Abdel Aal G. Z. (2010), A feasibility study on the geophysical response to nanoparticles in the subsurface. United States Environmental Protection Agency, EPA/600/R-10/105.

Whitney D. L., and Evans B. W. (2010), Abbreviations for names of rock-forming minerals. American Mineralogist, 95, 185-187.

Worthington P. F. (1993), The uses and abuses of the Archie equations, 1: the formation factor-porosity relationship. Journal of Applied Geophysics, 30, 215-228.

Yapo P. O., Gupta H. V., and Sorooshian S. (1998). Multi-objective global optimization for hydrologic models. Journal of Hydrology 204, 83-97.

Zhao Y., Zimmermann E., Huisman J. A., Treichel A., Wolters B., van Waasen S., and Kemna A. (2013), Broadband EIT borehole measurements with high phase accuracy using numerical corrections of electromagnetic coupling effects. Measurement Science and Technology, 24(8), 085005.

Zimmermann E., Huisman J. A., Kemna A., Berwix J., Glaas W., Meier H., Wolters B., and Esser O. (2010), Advanced electrical impedance tomography system with high phase accuracy. Extended Abstract, 6th World Congress on Industrial Process Tomography, Beijing, China.

Zimmermann E., Kemna A., Berwix J., Glaas W., and Vereecken H. (2008a), EIT measurement system with high phase accuracy for the imaging of spectral induced polarization properties of soils and sediments. Measurement Science and Technology, 19(9), 094010.

Zimmermann E., Kemna A., Berwix J., Glaas W., Münch H. M., and Huisman J. A. (2008b), A high-accuracy impedance spectrometer for measuring sediments with low polarizability. Measurement Science and Technology, 19(10), 105603.

Zisser N., SERfit. A MATLAB package and GUI for quantification of spectral electrical response, *unpublished*.

Zisser N., Kemna A., and Nover G. (2010), Relationship between low-frequency electrical properties and hydraulic permeability of low-permeability sandstones. Geophysics, 75(3), E131-E141.

Appendices

Appendix A

Textural and mineralogical characterization of materials collected in the sites of Orio Litta (O- and Ob-samples), Senna Lodigiana (S- and Sb-samples), Landriano (LA-samples), and Lozzolo (LZ-samples).

The cumulative grain size distributions are gathered according to the sampling site. The diffractograms are provided for the mud (d < 0.063 mm) and clay (d < 0.002 mm) fractions; the identified mineralogical phases are indicated with the symbols and abbreviations of *Kretz* (1983).

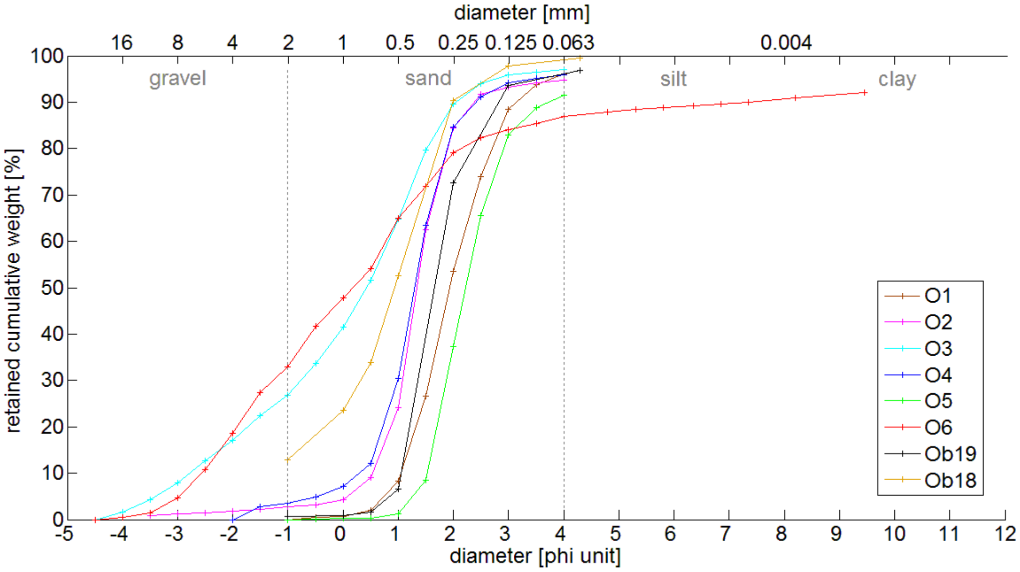

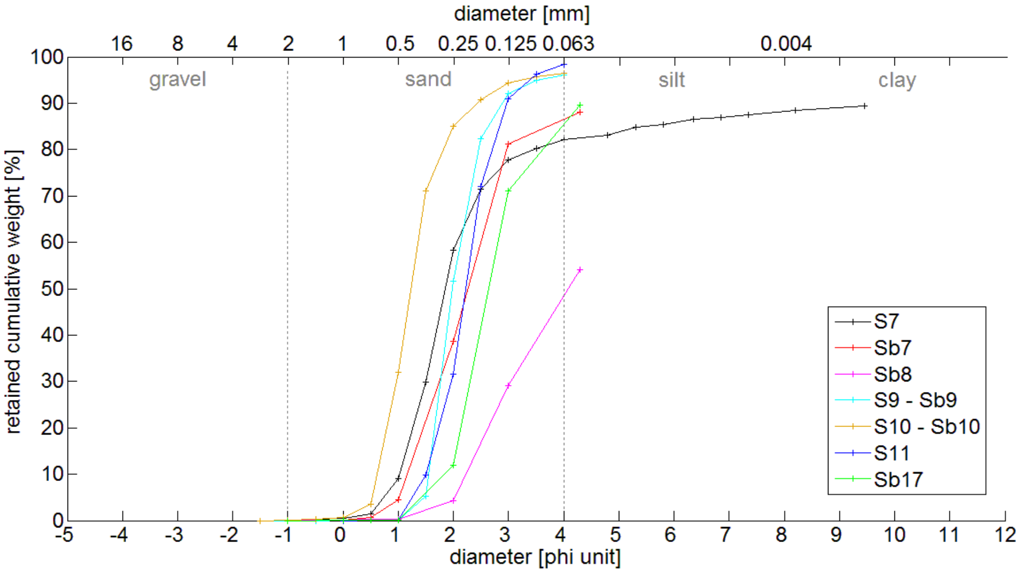

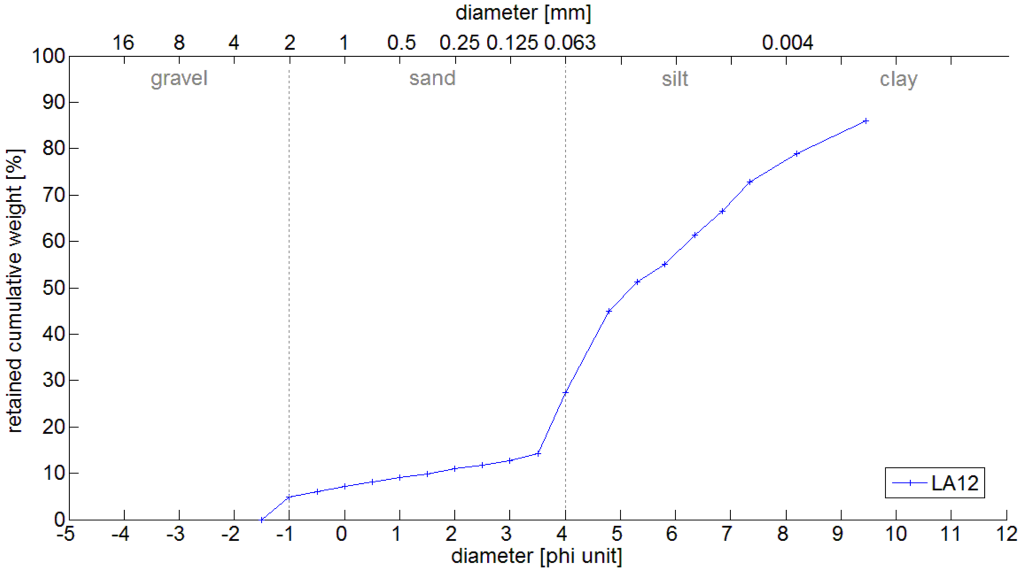
diameter [mm]
16
8
4
2
1
0.5
0.25
0.125
0.063
0.004
gravel
sand
silt
clay
retained cumulative weight [%]
100
90
80
70
60
50
40
30
20
10
0
LA12
-5
-4
-3
-2
-1
0
1
2
3
4
5
6
7
8
9
10
11
12
diameter [phi unit]

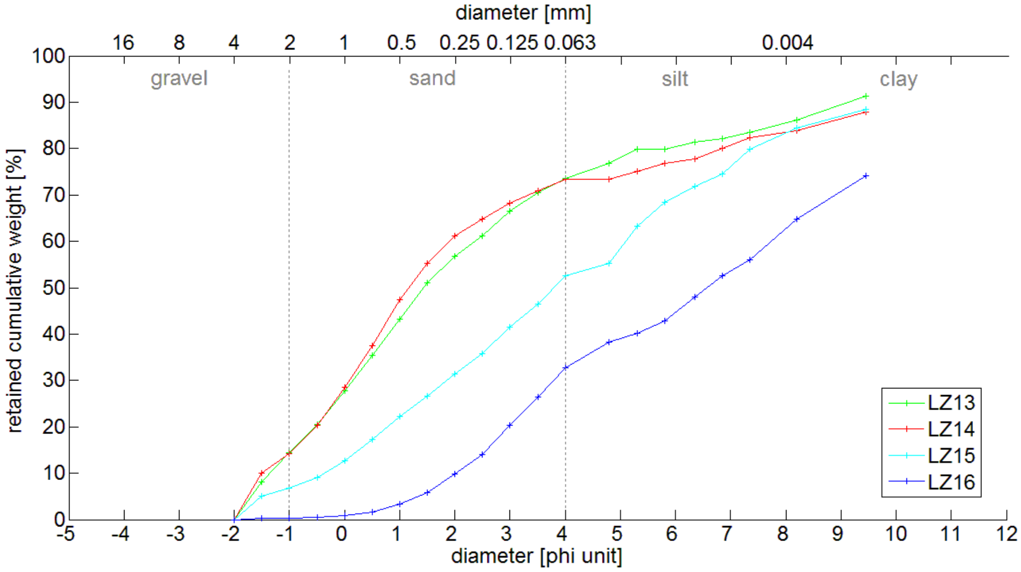
diameter [mm]
16
8
4
2
1
0.5
0.25
0.125
0.063
0.004
gravel
sand
silt
clay
retained cumulative weight [%]
100
90
80
70
60
50
40
30
20
10
0
LZ13
LZ14
LZ15
LZ16
-5
-4
-3
-2
-1
0
1
2
3
4
5
6
7
8
9
10
11
12
diameter [phi unit]

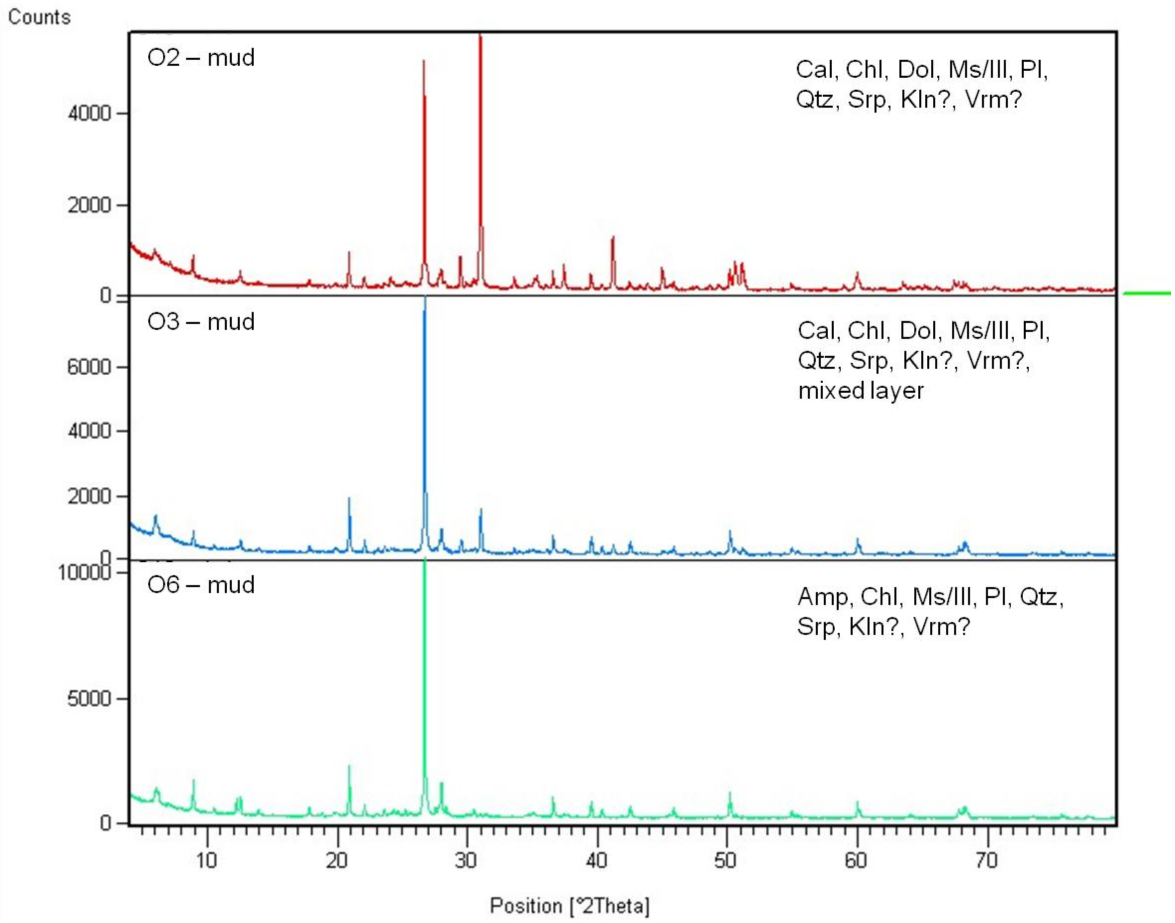
Counts
O2 – mud
Cal, Chl, Dol, Ms/Ill, Pl, Qtz, Srp, Kln?, Vrm?
4000
2000
0
O3 – mud
Cal, Chl, Dol, Ms/Ill, Pl, Qtz, Srp, Kln?, Vrm?, mixed layer
6000
4000
2000
0
10000
O6 – mud
Amp, Chl, Ms/Ill, Pl, Qtz, Srp, Kln?, Vrm?
5000
0
10
20
30
40
50
60
70
Position [°2Theta]

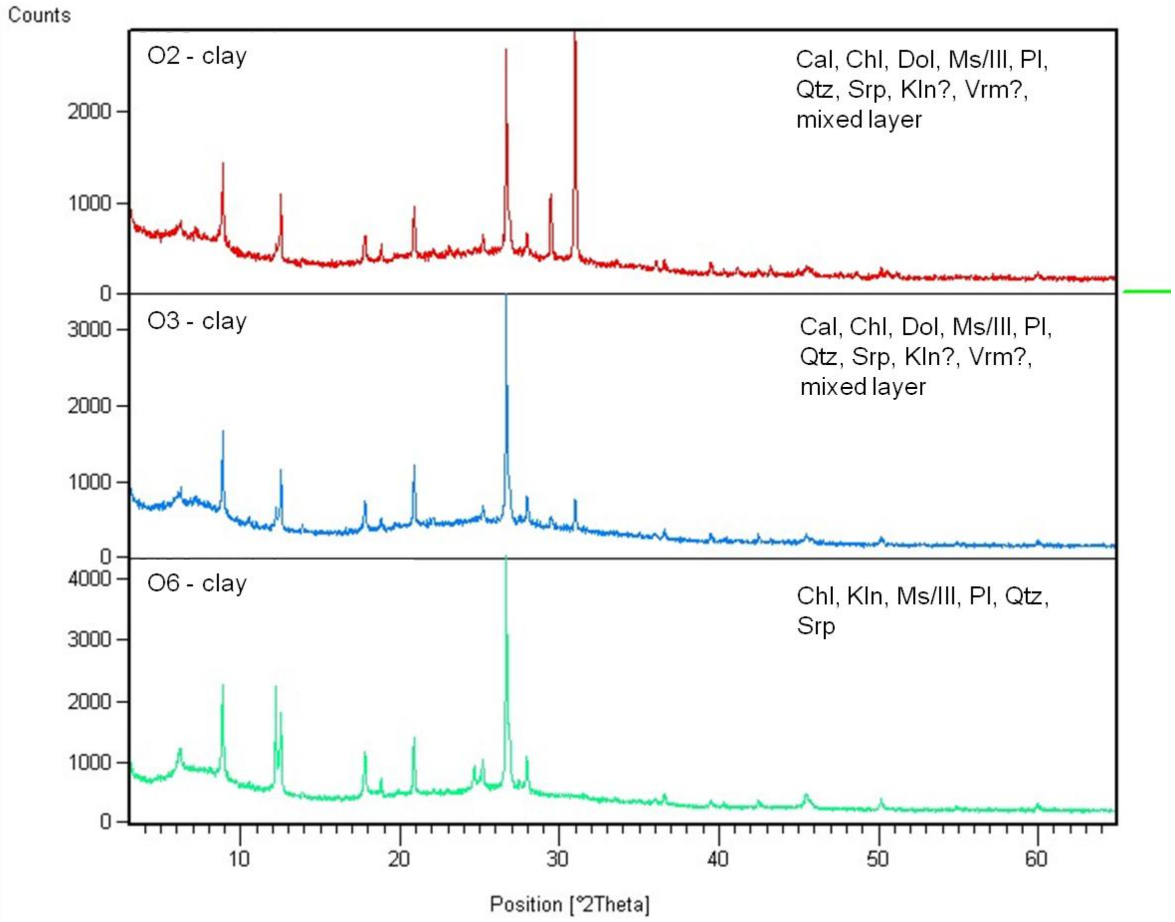
Counts
O2 - clay
Cal, Chl, Dol, Ms/Ill, Pl, Qtz, Srp, Kln?, Vrm?, mixed layer
2000
1000
0
O3 - clay
Cal, Chl, Dol, Ms/Ill, Pl, Qtz, Srp, Kln?, Vrm?, mixed layer
3000
2000
1000
0
4000
O6 - clay
Chl, Kln, Ms/Ill, Pl, Qtz, Srp
3000
2000
1000
0
10
20
30
40
50
60
Position [°2Theta]

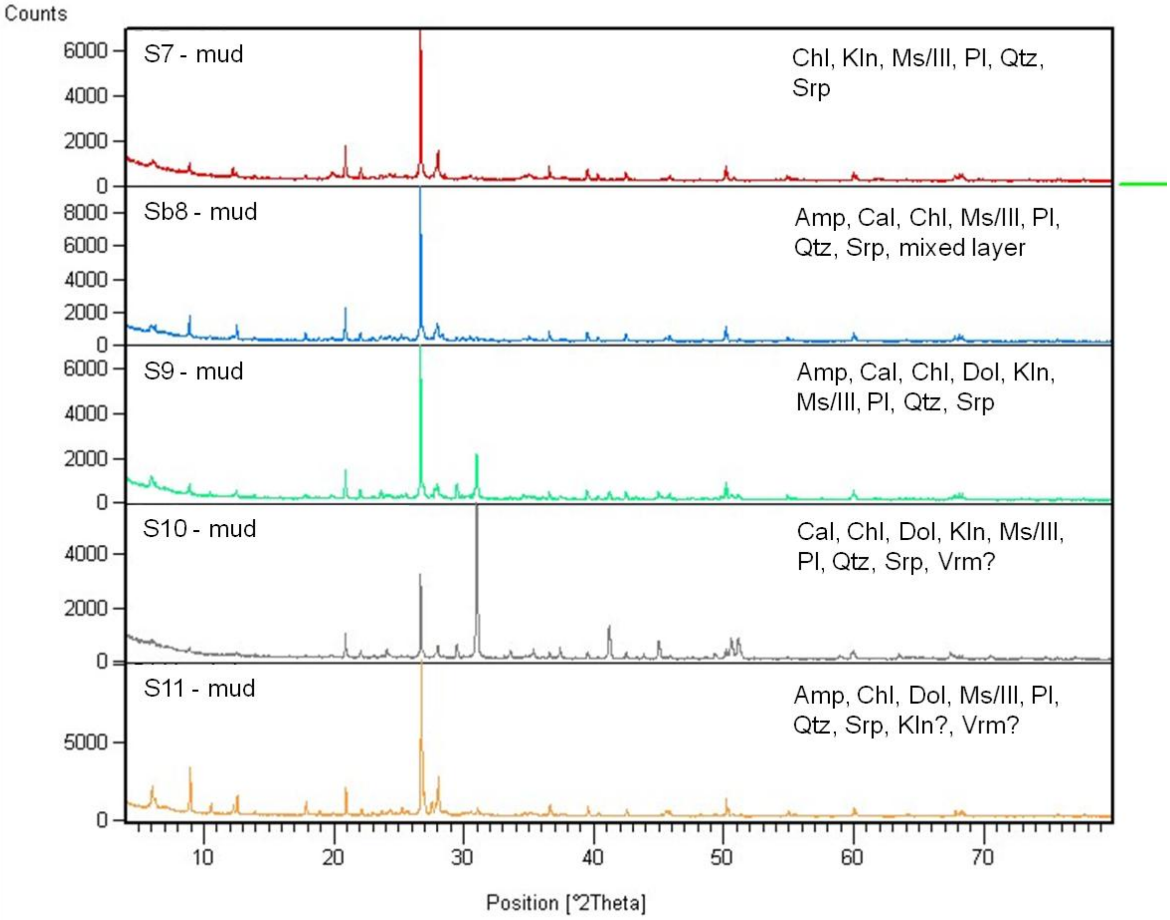
Counts
S7 - mud
Chl, Kln, Ms/Ill, Pl, Qtz, Srp
6000
4000
2000
0
Sb8 - mud
Amp, Cal, Chl, Ms/Ill, Pl, Qtz, Srp, mixed layer
8000
6000
4000
2000
0
S9 - mud
Amp, Cal, Chl, Dol, Kln, Ms/Ill, Pl, Qtz, Srp
6000
4000
2000
0
S10 - mud
Cal, Chl, Dol, Kln, Ms/Ill, Pl, Qtz, Srp, Vrm?
4000
2000
0
S11 - mud
Amp, Chl, Dol, Ms/Ill, Pl, Qtz, Srp, Kln?, Vrm?
5000
0
10
20
30
40
50
60
70
Position [°2Theta]

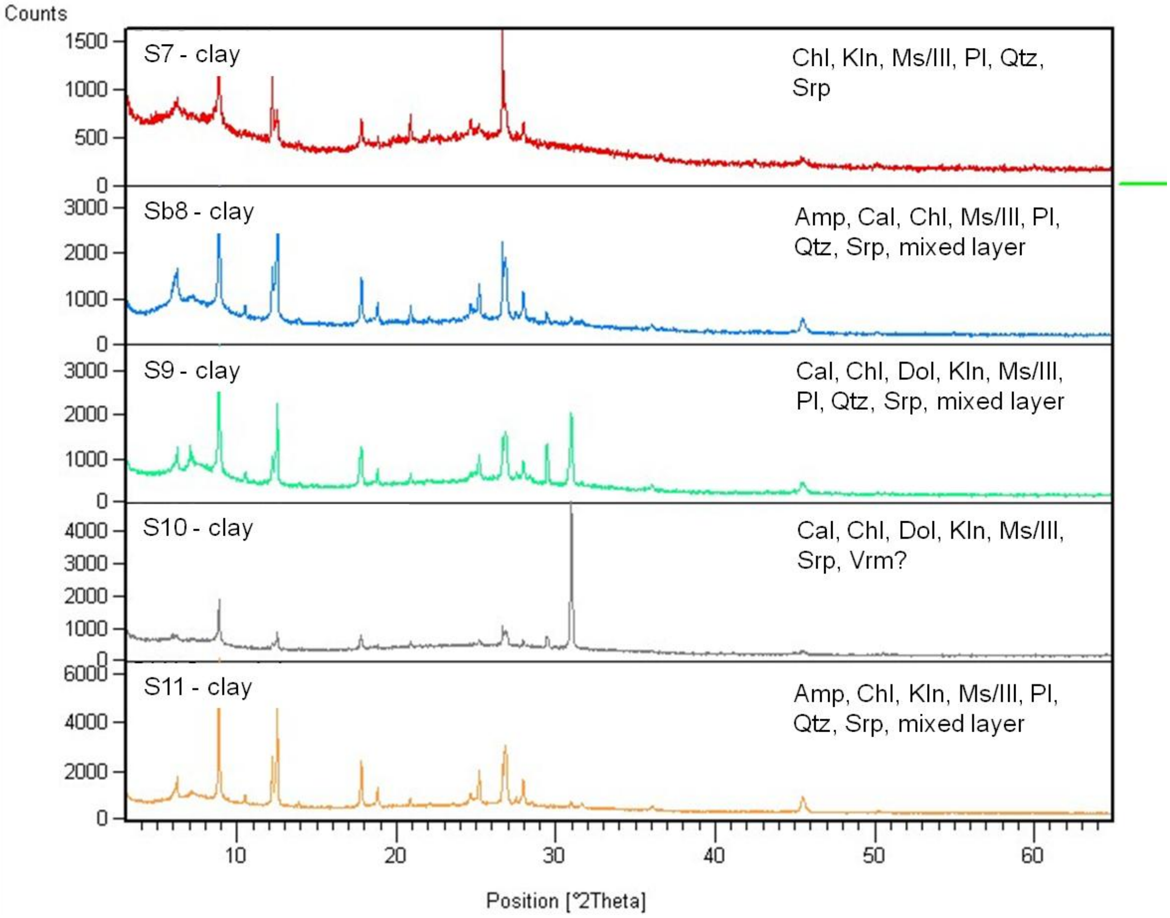
Counts
S7 - clay
Chl, Kln, Ms/Ill, Pl, Qtz, Srp
1500
1000
500
0
Sb8 - clay
Amp, Cal, Chl, Ms/Ill, Pl, Qtz, Srp, mixed layer
3000
2000
1000
0
S9 - clay
Cal, Chl, Dol, Kln, Ms/Ill, Pl, Qtz, Srp, mixed layer
3000
2000
1000
0
S10 - clay
Cal, Chl, Dol, Kln, Ms/Ill, Srp, Vrm?
4000
3000
2000
1000
0
S11 - clay
Amp, Chl, Kln, Ms/Ill, Pl, Qtz, Srp, mixed layer
6000
4000
2000
0
10
20
30
40
50
60
Position [°2Theta]

Appendix B

SIP measurements on natural samples, represented as resistivity amplitude and phase as a function of frequency.

All the tests performed on the same material saturated with different waters are gathered in the same graph in order to highlight the general trend of amplitude and phase absolute values reduction passing from resistive water (w2) to conductive water (different for each sample). Vertical scales are adapted to each sample to better visualize the spectral behaviour; curves' colours are kept constant to identify the initial water resistivity. The table associated to the graphs collects the values of porosity (θ), initial and final water resistivity at 20°C ($\rho_{w(i)}$ and $\rho_{w(f)}$) of each investigated sample. The results of the chemical analysis on the water extracted from the sample at the end of the SIP measurement are also reported when available.

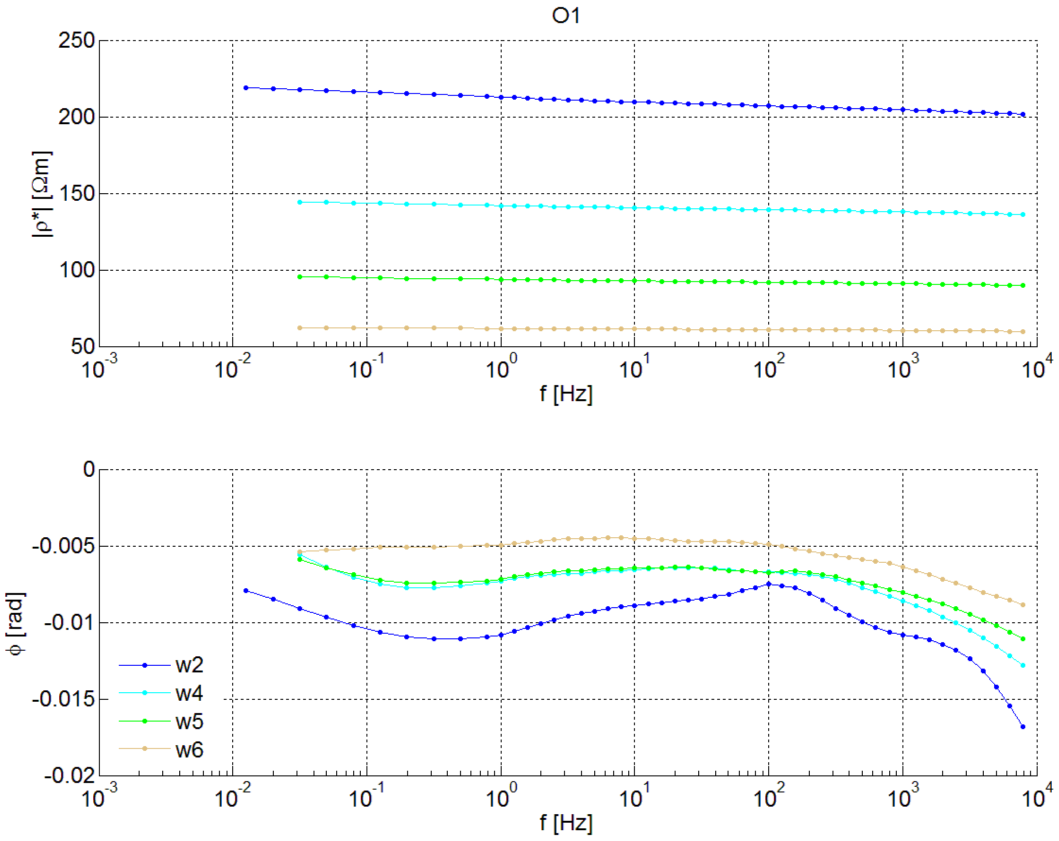

	θ [m^3m^{-3}]	$\rho_{w(i)}$ [Ωm]	$\rho_{w(f)}$ [Ωm]	chemical analysis of final water (Na; K; Mg; Ca; Mn; Fe [ppm])
O1-w2	0.41	270	66	7.32; 1.20; 2.32; 16.12; 0.00; 0.12
O1-w4	0.40	103	47	n.a.
O1-w5	0.37	45	29	n.a.
O1-w6	0.37	22	15	n.a.

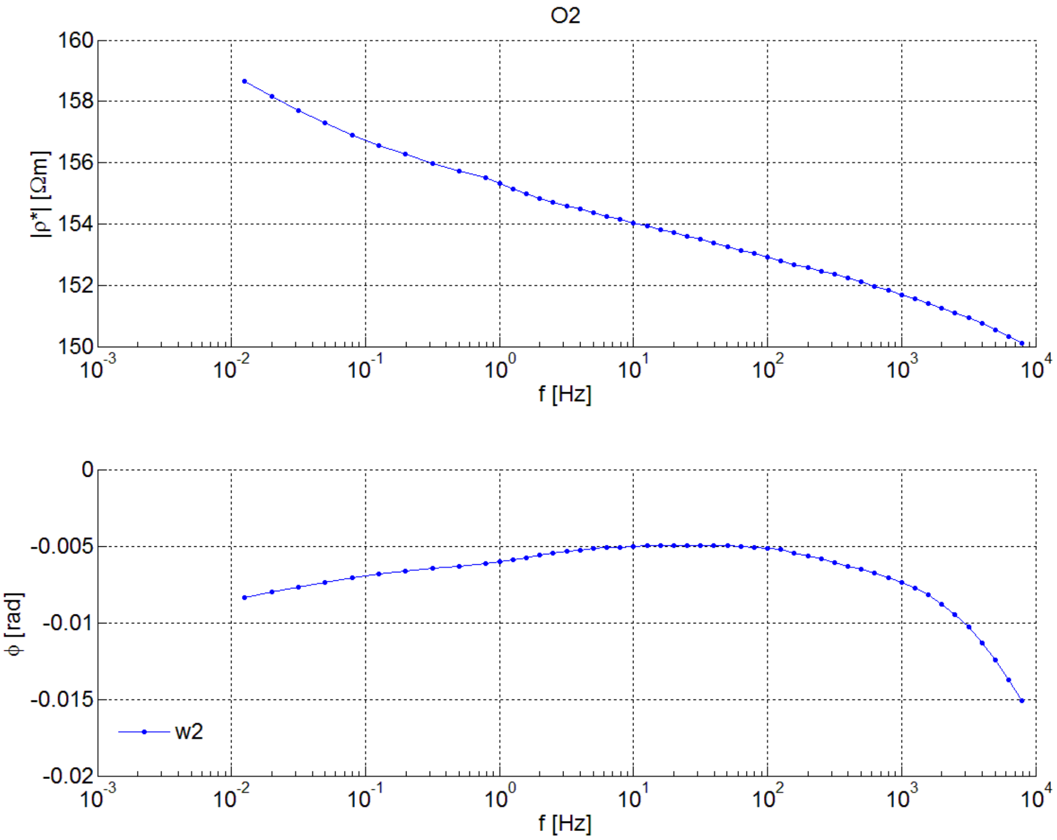

	θ [m^{3}m^{-3}]	**$\rho_{w(i)}$ [Ωm]**	**$\rho_{w(f)}$ [Ωm]**	chemical analysis of final water (Na; K; Mg; Ca; Mn; Fe [ppm])
O2-w2	0.38	283	39	n.a.

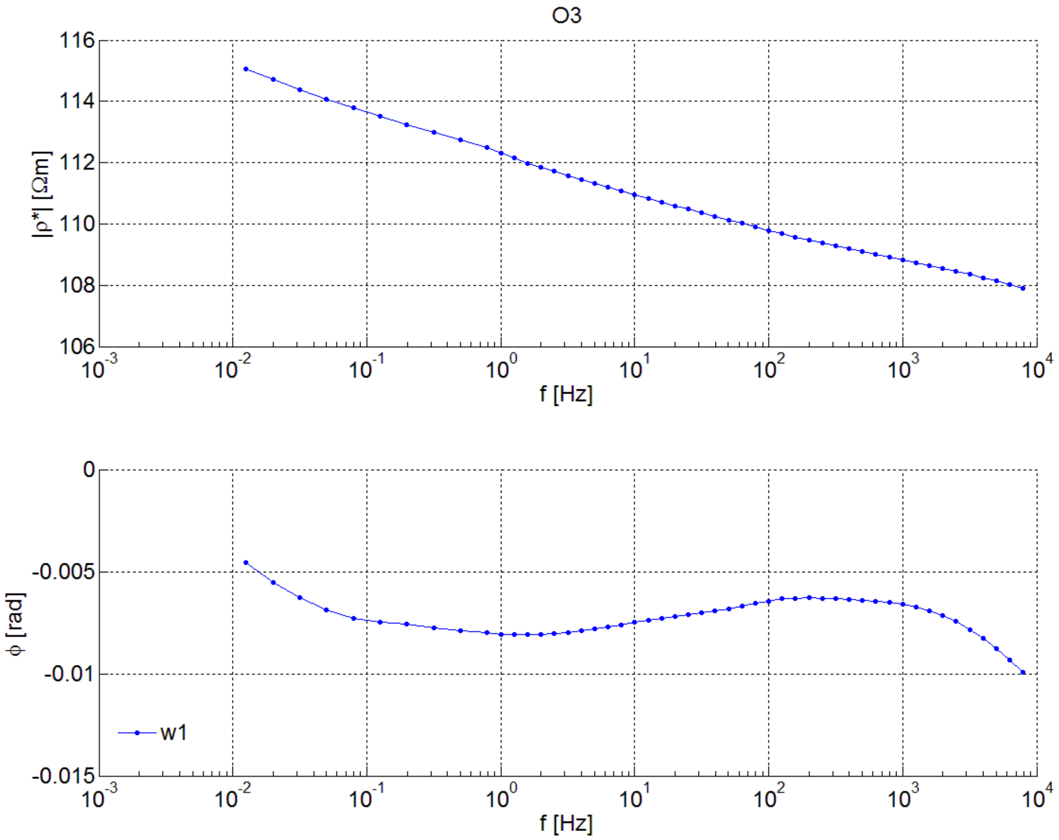

	θ [m^{3}m^{-3}]	**$\rho_{w(i)}$ [Ωm]**	**$\rho_{w(f)}$ [Ωm]**	chemical analysis of final water (Na; K; Mg; Ca; Mn; Fe [ppm])
O3-w2	0.34	283	28	n.a.

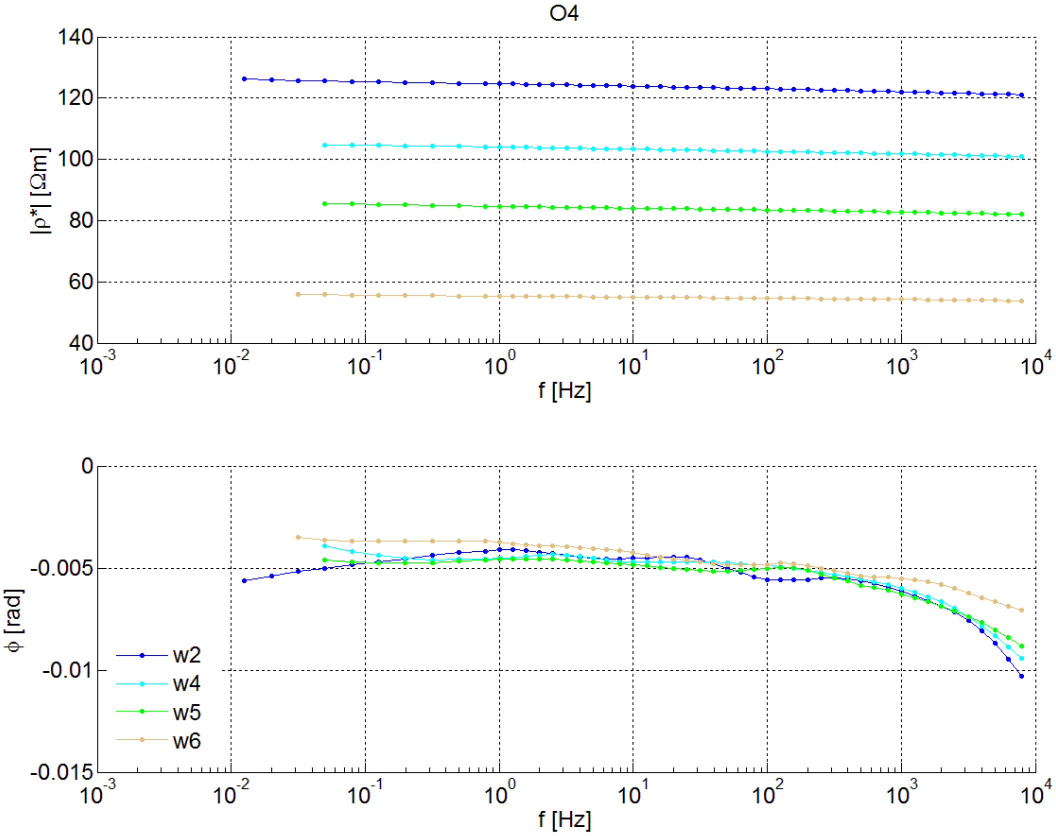

	θ [m^3m^{-3}]	$\rho_{w(i)}$ [Ωm]	$\rho_{w(f)}$ [Ωm]	chemical analysis of final water (Na; K; Mg; Ca; Mn; Fe [ppm])
O4-w2	0.40	302	33	11.42; 0.89; 6.68; 39.14; 0.03; 0.0
O4-w4	0.38	103	24	n.a.
O4-w5	0.39	45	22	n.a.
O4-w6	0.37	22	14	n.a.

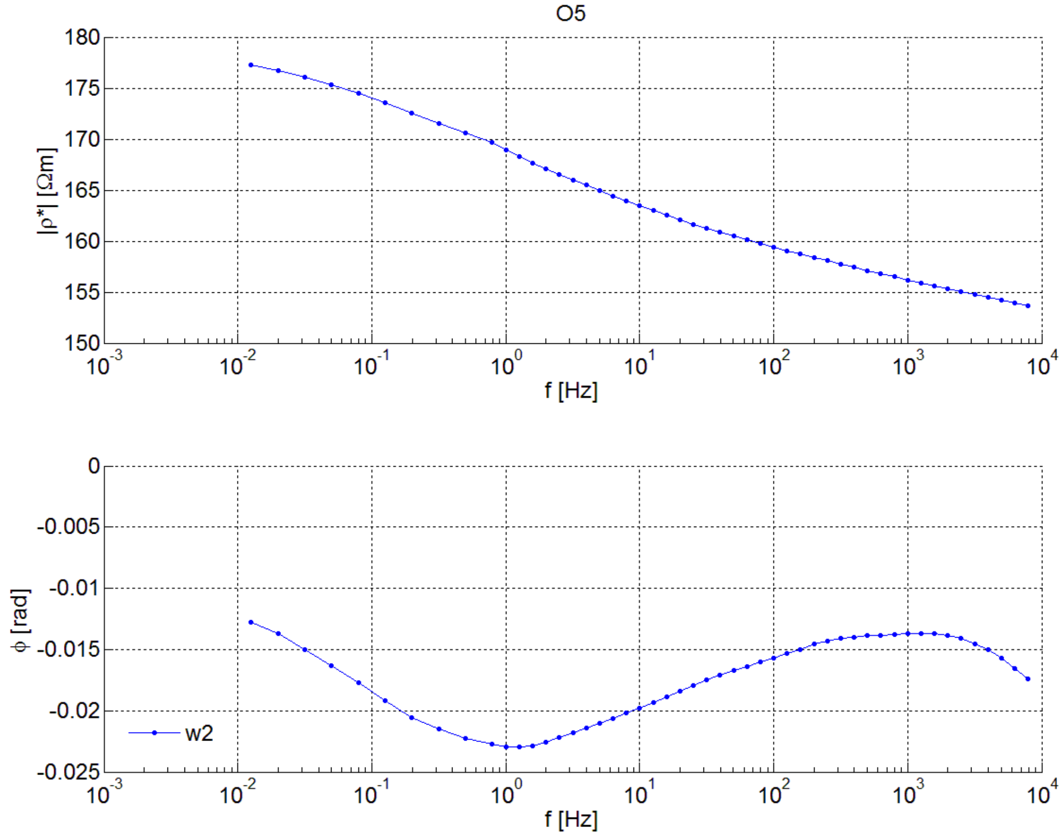

	θ $[m^3m^{-3}]$	$\rho_{w(i)}$ [Ωm]	$\rho_{w(f)}$ [Ωm]	chemical analysis of final water (Na; K; Mg; Ca; Mn; Fe [ppm])
O5-w2	0.39	270	84	7.55; 0.80; 1.62; 9.10; 0.04; 0.00

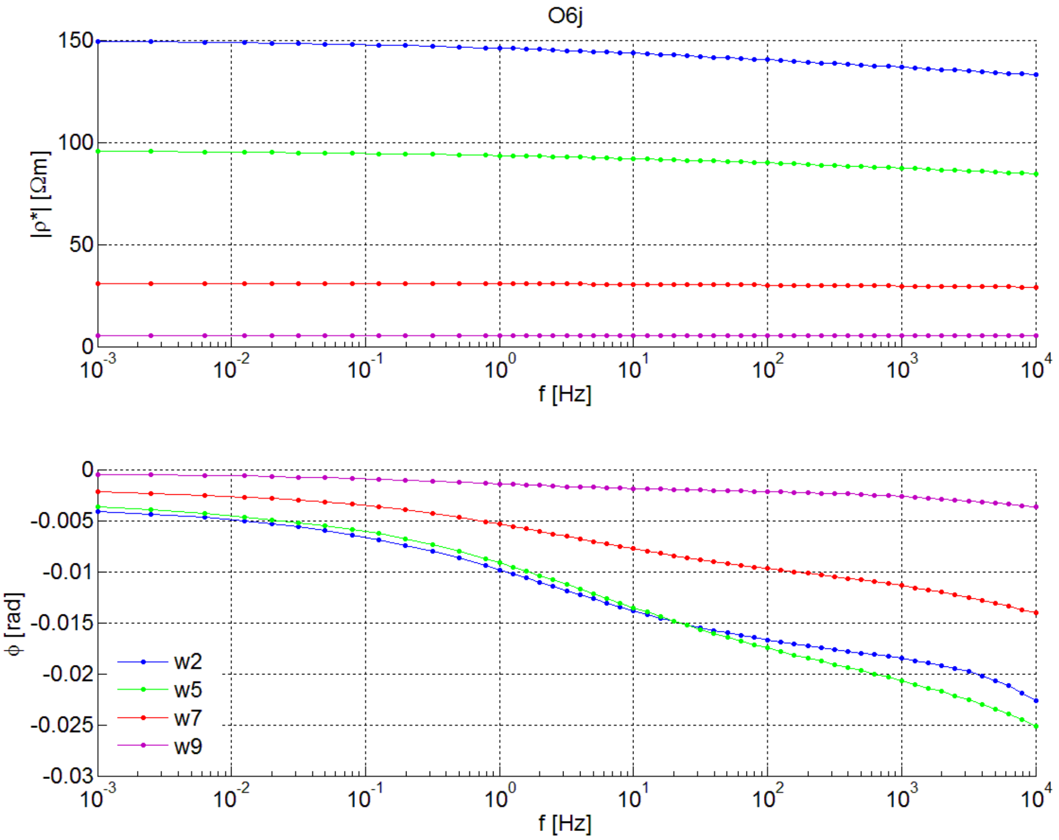

	θ [m^3m^{-3}]	**$\rho_{w(i)}$ [Ωm]**	**$\rho_{w(f)}$ [Ωm]**	chemical analysis of final water (Na; K; Mg; Ca; Mn; Fe [ppm])
O6j-w2	0.38	319	37	n.a.
O6j-w5	0.37	43	30	n.a.
O6j-w7	0.37	7	7	n.a.
O6j-w9	0.26	1	1	n.a.

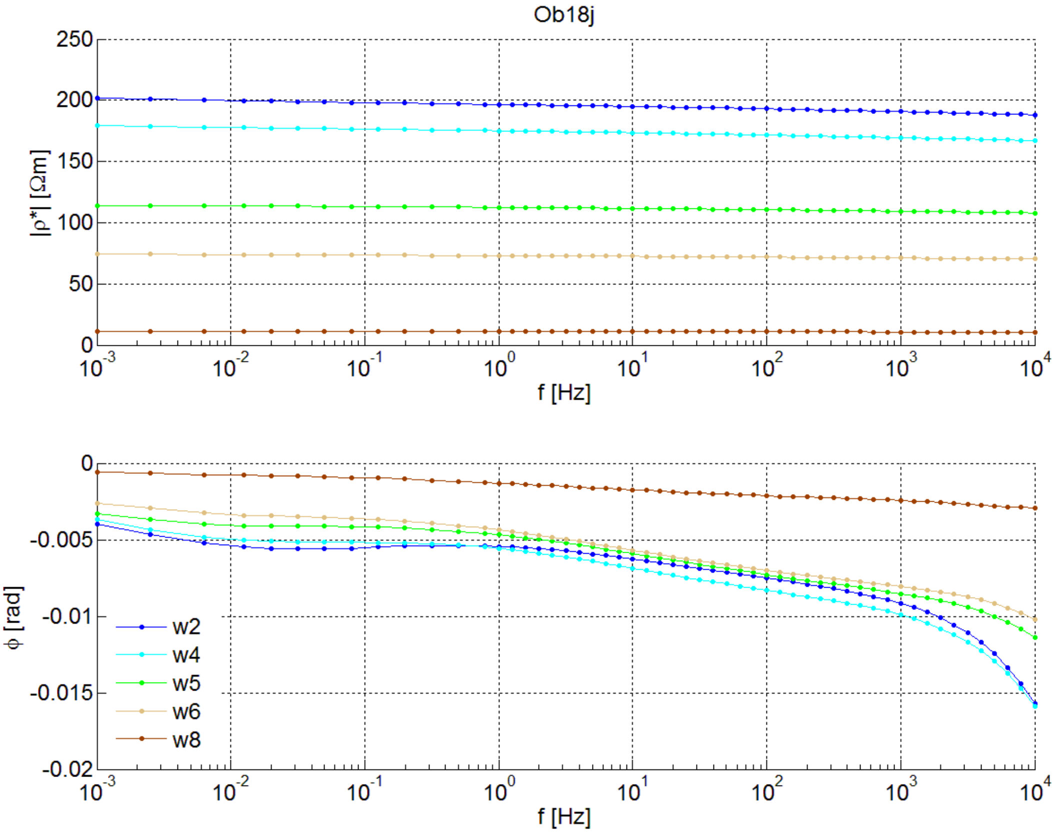

	θ [m^3m^{-3}]	$\rho_{w(i)}$ [Ωm]	$\rho_{w(f)}$ [Ωm]	chemical analysis of final water (Na; K; Mg; Ca; Mn; Fe [ppm])
Ob18j-w2	0.34	319	18	n.a.
Ob18j-w4	0.35	97	46	n.a.
Ob18j-w5	0.35	43	31	n.a.
Ob18j-w6	0.36	21	17	n.a.
Ob18j-w8	0.36	2	2	n.a.

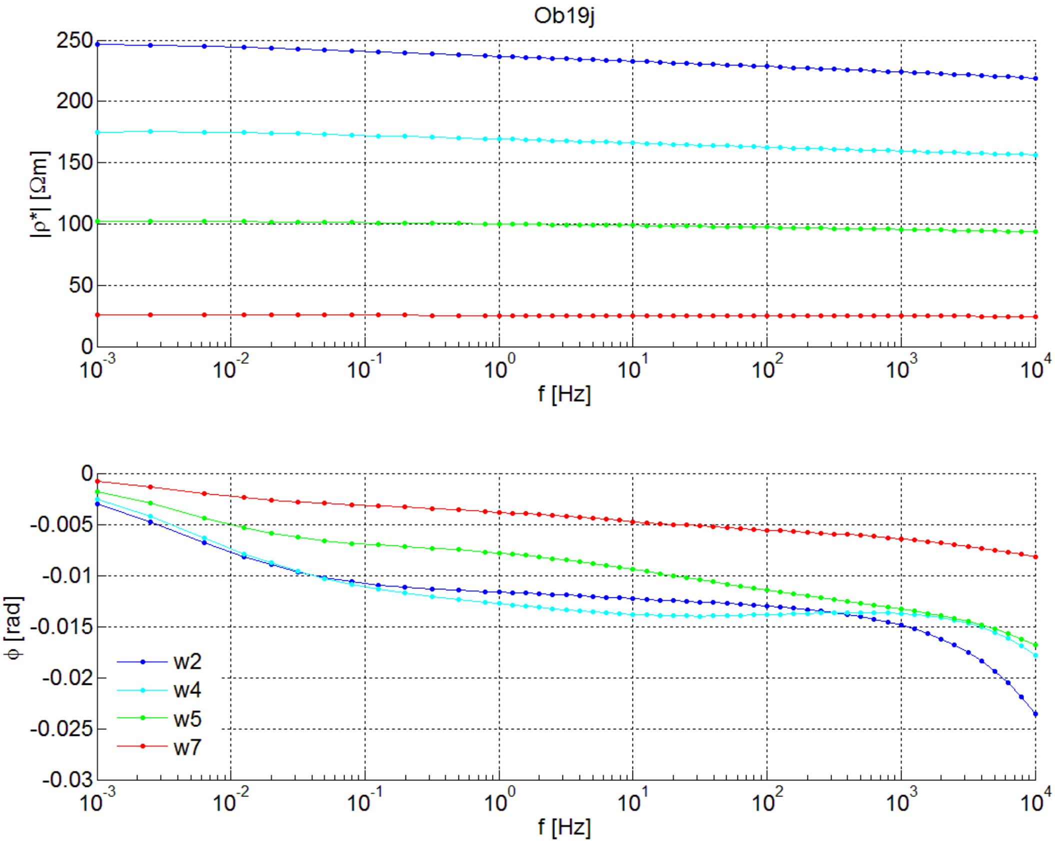

	θ [m^3m^{-3}]	$\rho_{w(i)}$ [Ωm]	$\rho_{w(f)}$ [Ωm]	chemical analysis of final water (Na; K; Mg; Ca; Mn; Fe [ppm])
Ob19j-w2	0.41	319	99	n.a.
Ob19j-w4	0.42	98	63	n.a.
Ob19j-w5	0.41	44	34	n.a.
Ob19j-w7	0.40	7	7	n.a.

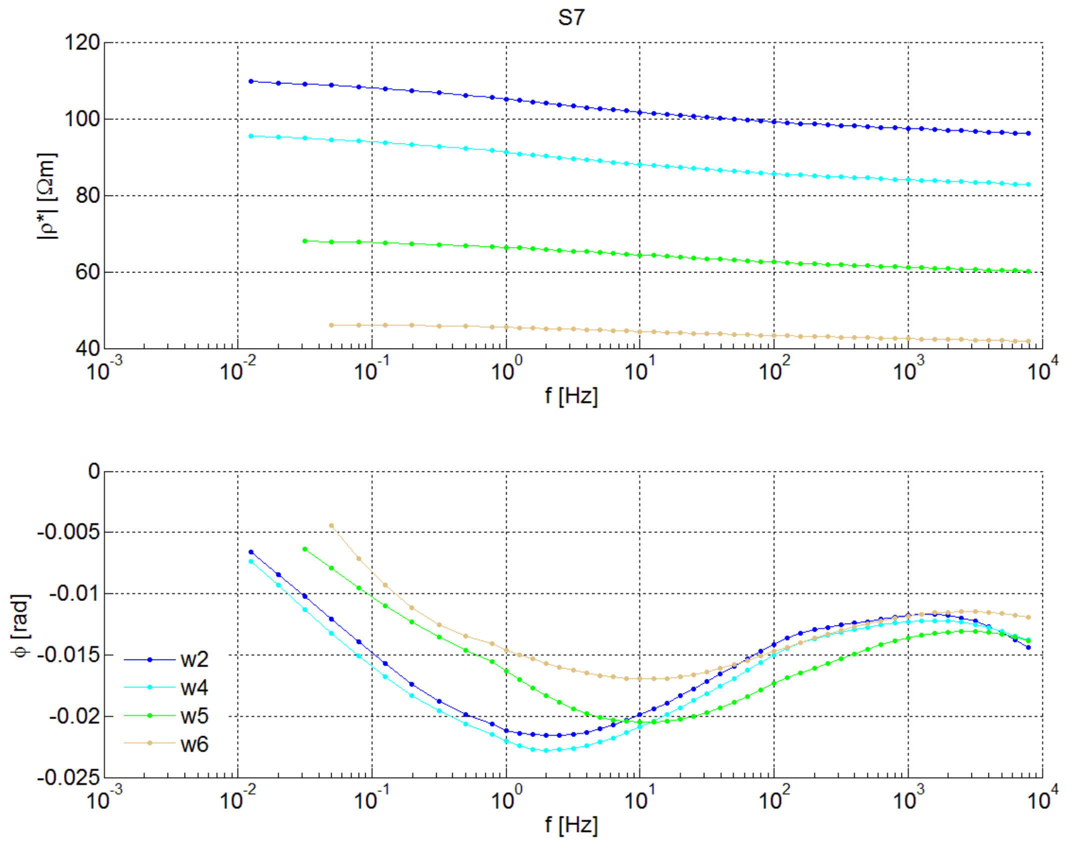

	θ [m³m⁻³]	$\rho_{w(i)}$ [Ωm]	$\rho_{w(f)}$ [Ωm]	chemical analysis of final water (Na; K; Mg; Ca; Mn; Fe [ppm])
S7-w2	0.44	302	51	8.22; 1.85; 2.38; 16.55; 0.08; 0.00
S7-w4	0.45	103	43	n.a.
S7-w5	0.41	45	29	n.a.
S7-w6	0.38	23	16	n.a.

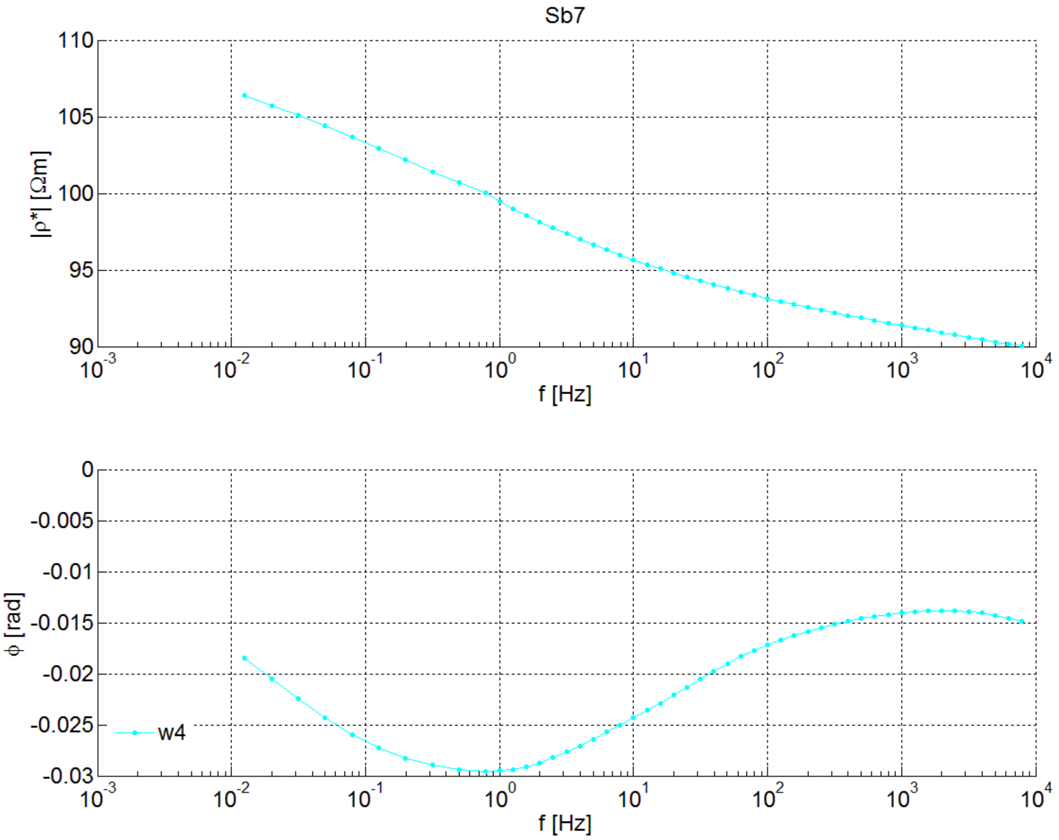

	θ [m³m⁻³]	**$\rho_{w(i)}$ [Ωm]**	**$\rho_{w(f)}$ [Ωm]**	chemical analysis of final water (Na; K; Mg; Ca; Mn; Fe [ppm])
Sb7-w4	0.42	97	52	n.a.

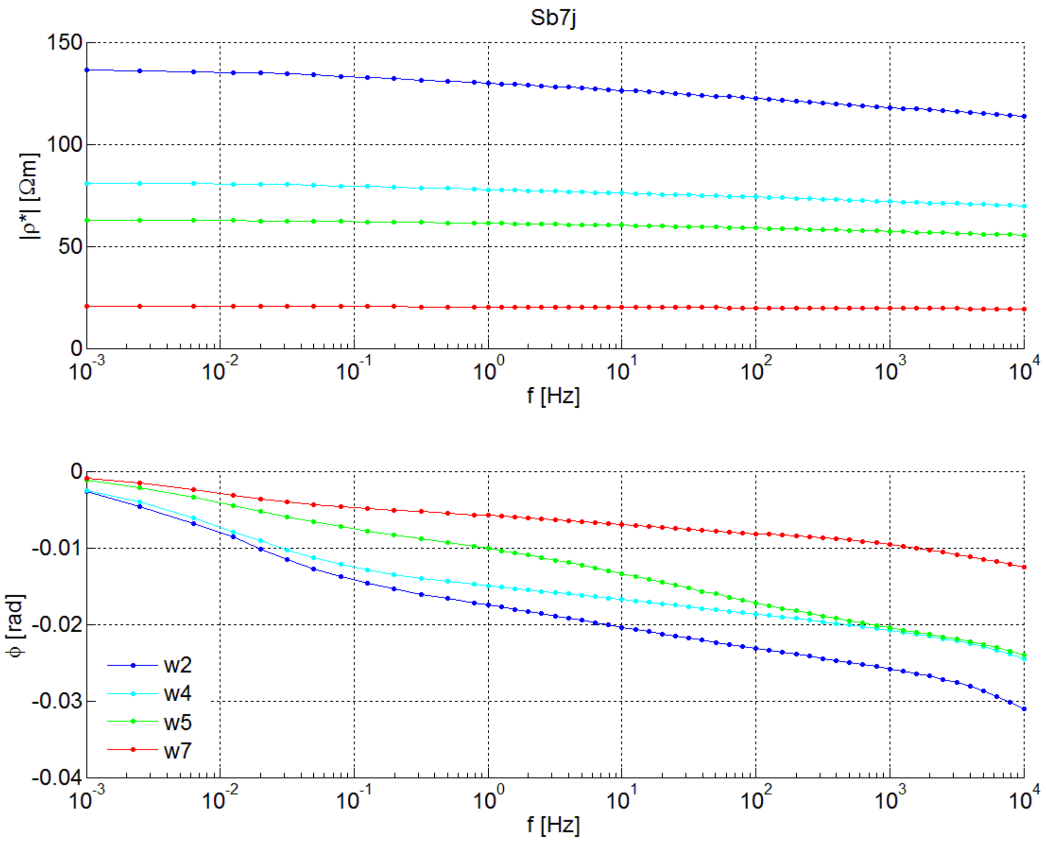

	θ [m^3m^{-3}]	$\rho_{w(i)}$ [Ωm]	$\rho_{w(f)}$ [Ωm]	chemical analysis of final water (Na; K; Mg; Ca; Mn; Fe [ppm])
Sb7j-w2	0.37	315	80	n.a.
Sb7j-w4	0.45	98	36	n.a.
Sb7j-w5	0.42	44	26	n.a.
Sb7j-w7	0.44	7	7	n.a.

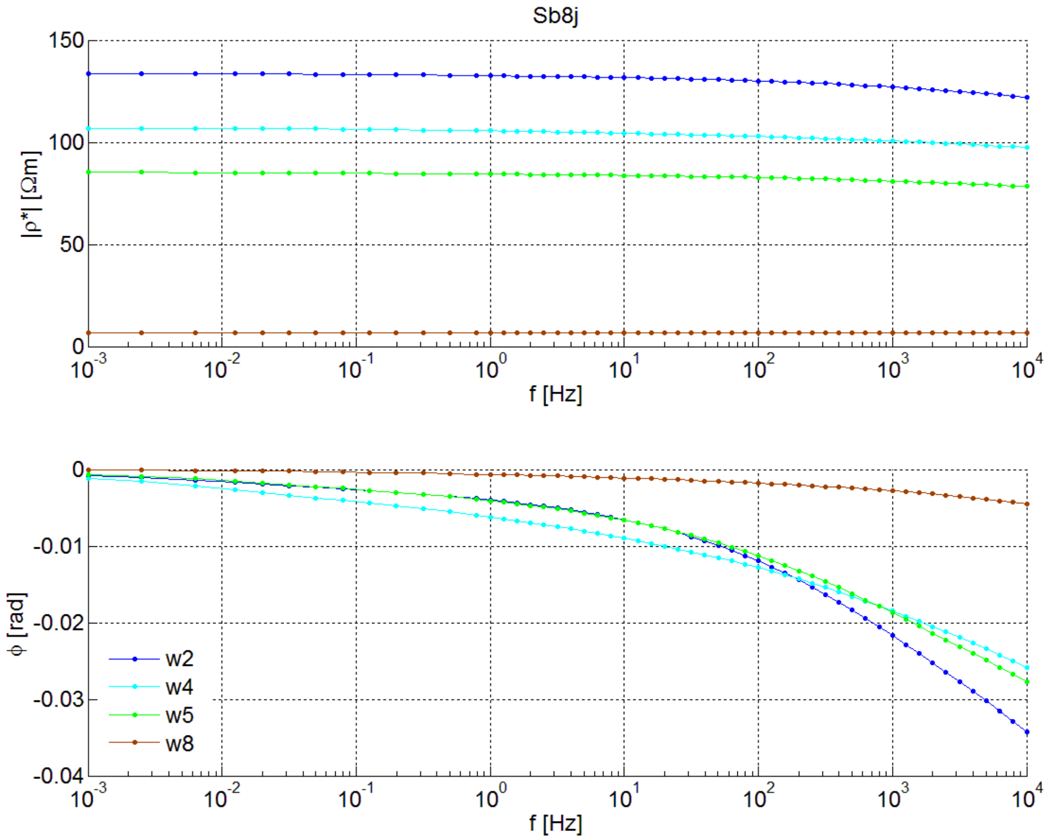

	θ [m³m⁻³]	$\rho_{w(i)}$ [Ωm]	$\rho_{w(f)}$ [Ωm]	chemical analysis of final water (Na; K; Mg; Ca; Mn; Fe [ppm])
Sb8j-w2	0.31	322	46	n.a.
Sb8j-w4	0.39	97	35	n.a.
Sb8j-w5	0.39	45	31	n.a.
Sb8j-w8	0.47	2	1,9542	n.a.

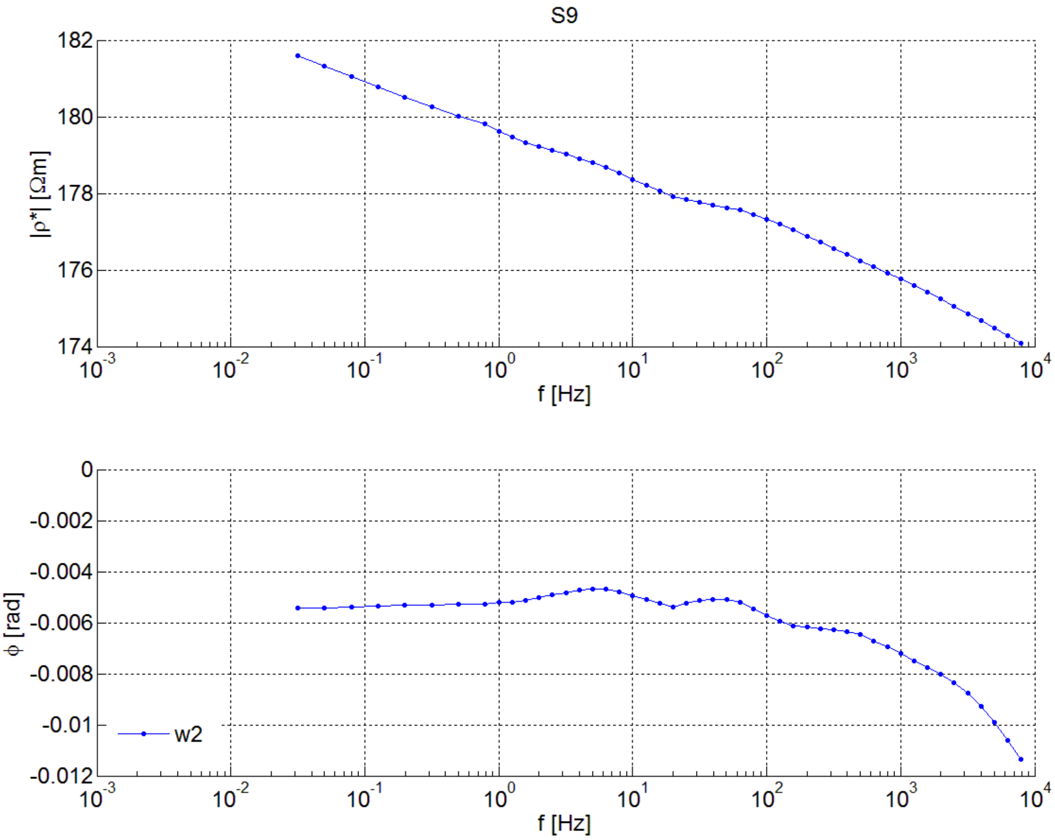

	θ [m^3m^{-3}]	$\rho_{w(i)}$ [Ωm]	$\rho_{w(f)}$ [Ωm]	chemical analysis of final water (Na; K; Mg; Ca; Mn; Fe [ppm])
S9-w2	0.37	304	49	7.16; 1.43; 4.37; 29.93; 0.06; 0.00

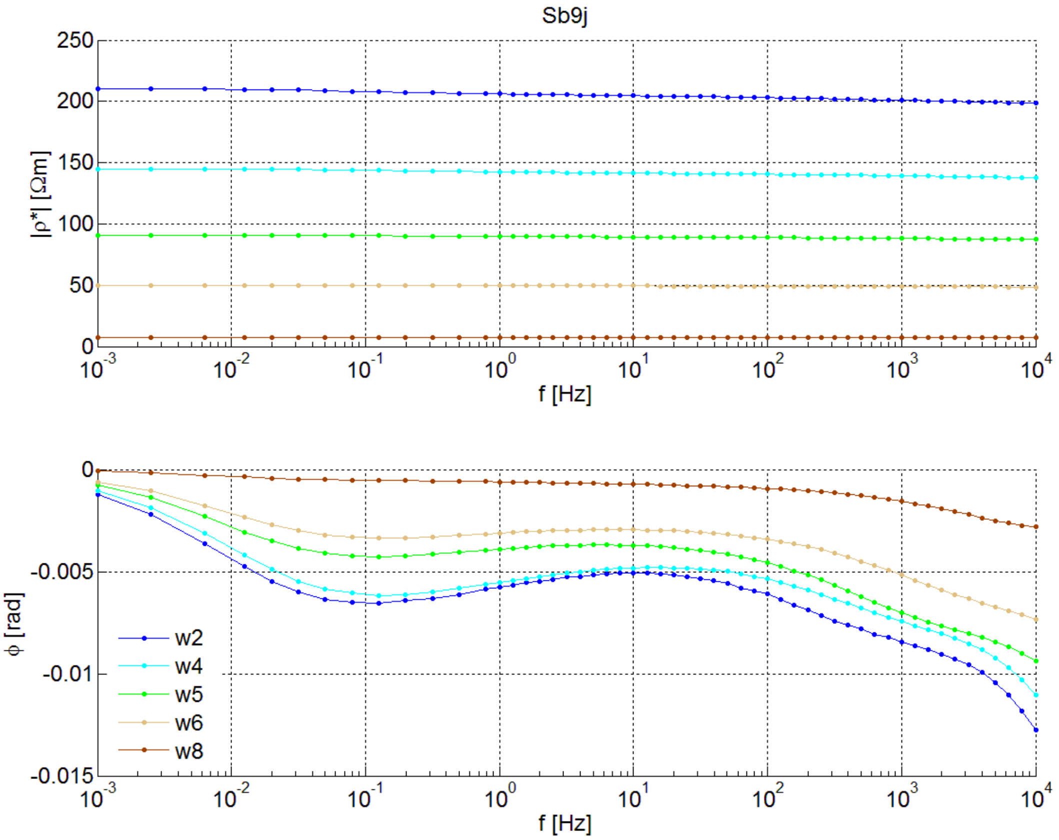

	θ [m^{3}m^{-3}]	$\rho_{w(i)}$ [Ωm]	$\rho_{w(f)}$ [Ωm]	chemical analysis of final water (Na; K; Mg; Ca; Mn; Fe [ppm])
Sb9j-w2	0.39	319	54	n.a.
Sb9j-w4	0.37	97	36	n.a.
Sb9j-w5	0.40	45	27	n.a.
Sb9j-w6	0.39	18	14	n.a.
Sb9j-w8	0.40	2	2	n.a.

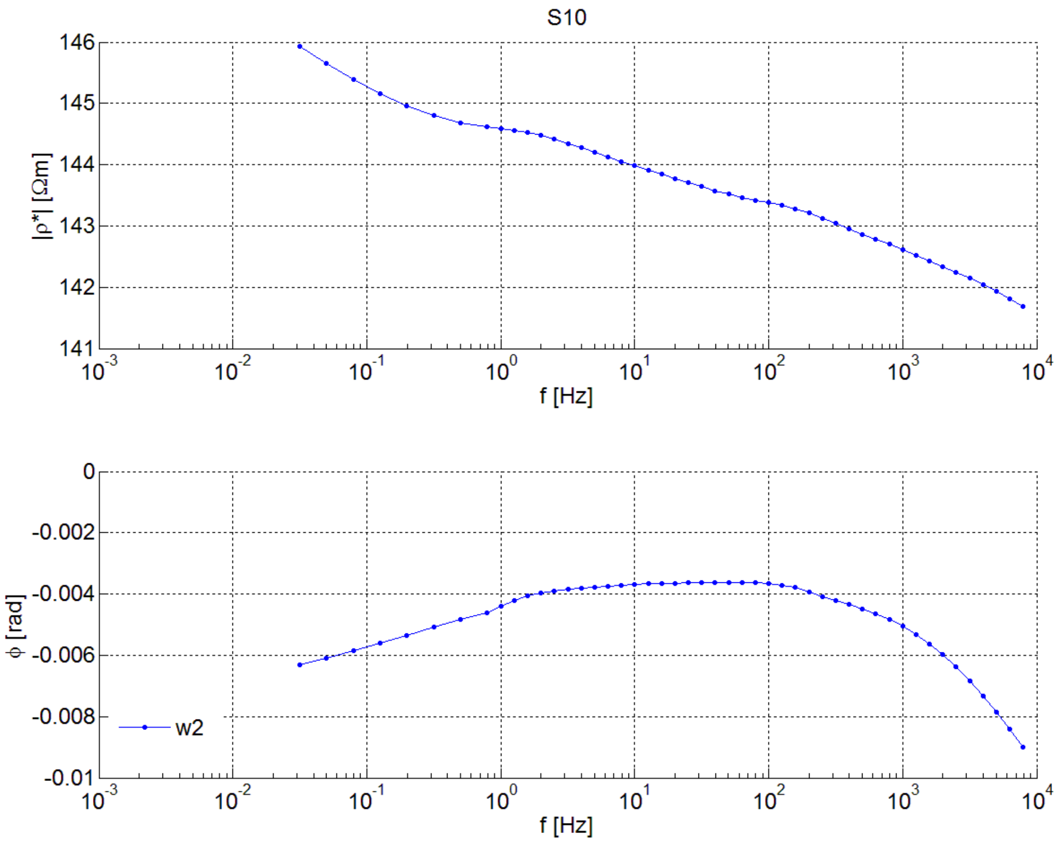

	θ $[m^3m^{-3}]$	**$\rho_{w(i)}$ [Ωm]**	**$\rho_{w(f)}$ [Ωm]**	chemical analysis of final water (Na; K; Mg; Ca; Mn; Fe [ppm])
S10-w2	0.40	283	36	n.a.

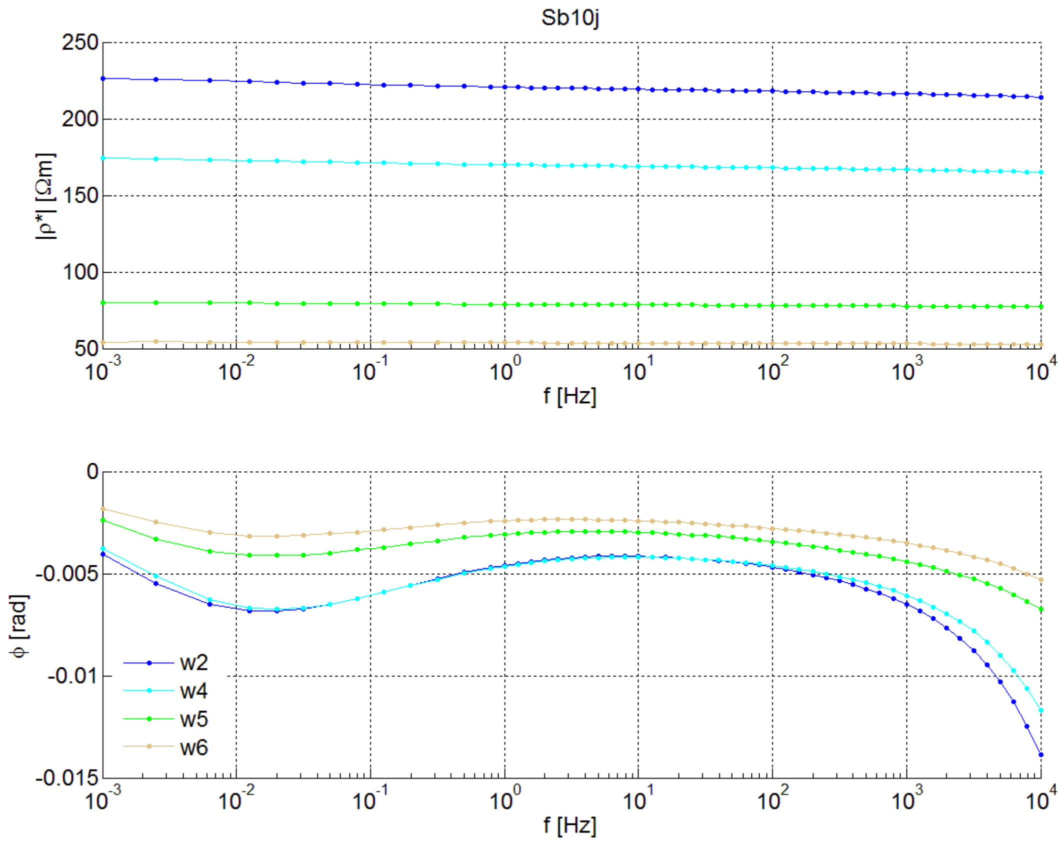

	θ $[m^3m^{-3}]$	$\rho_{w(i)}$ [Ωm]	$\rho_{w(f)}$ [Ωm]	chemical analysis of final water (Na; K; Mg; Ca; Mn; Fe [ppm])
Sb10j-w2	0.37	315	19	n.a.
Sb10j-w4	0.35	97	42	n.a.
Sb10j-w5	0.38	45	22	n.a.
Sb10j-w6	0.37	18	15	n.a.

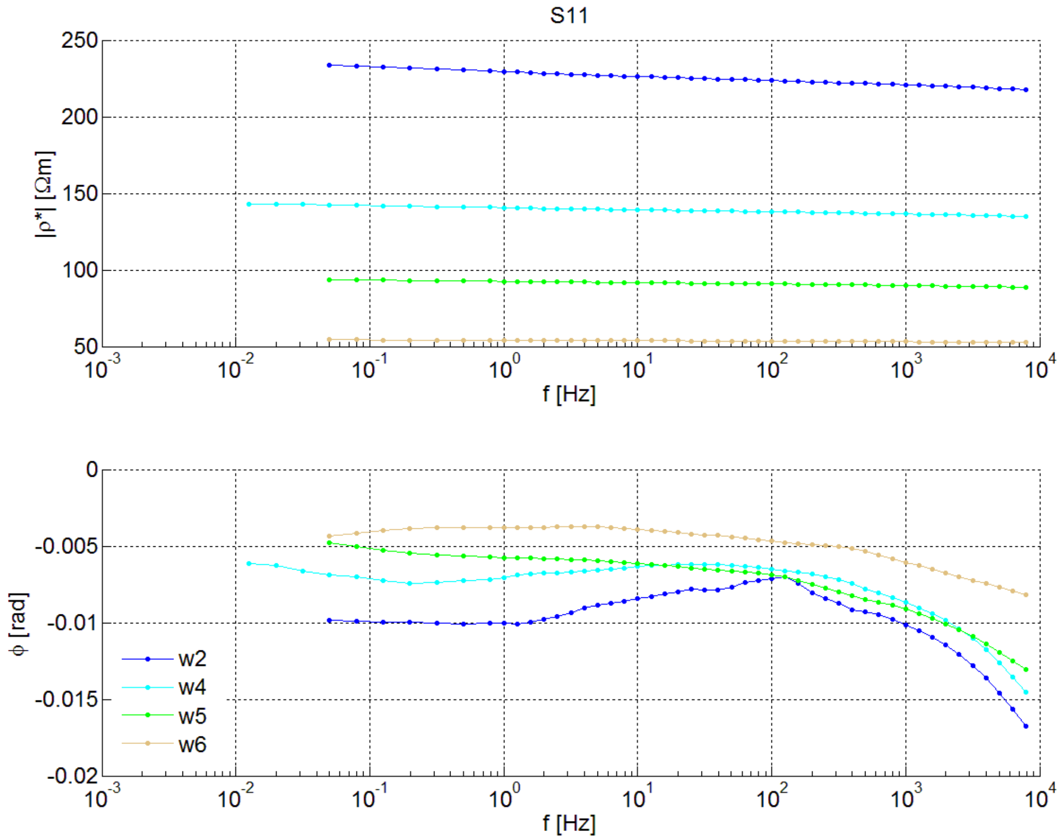

	θ [m^3m^{-3}]	$\rho_{w(i)}$ [Ωm]	$\rho_{w(f)}$ [Ωm]	chemical analysis of final water (Na; K; Mg; Ca; Mn; Fe [ppm])
S11-w2	0.44	302	51	7.80; 0.79; 4.55; 24.66; 0.00; 0.00
S11-w4	0.45	103	43	n.a.
S11-w5	0.41	45	29	n.a.
S11-w6	0.38	23	16	n.a.

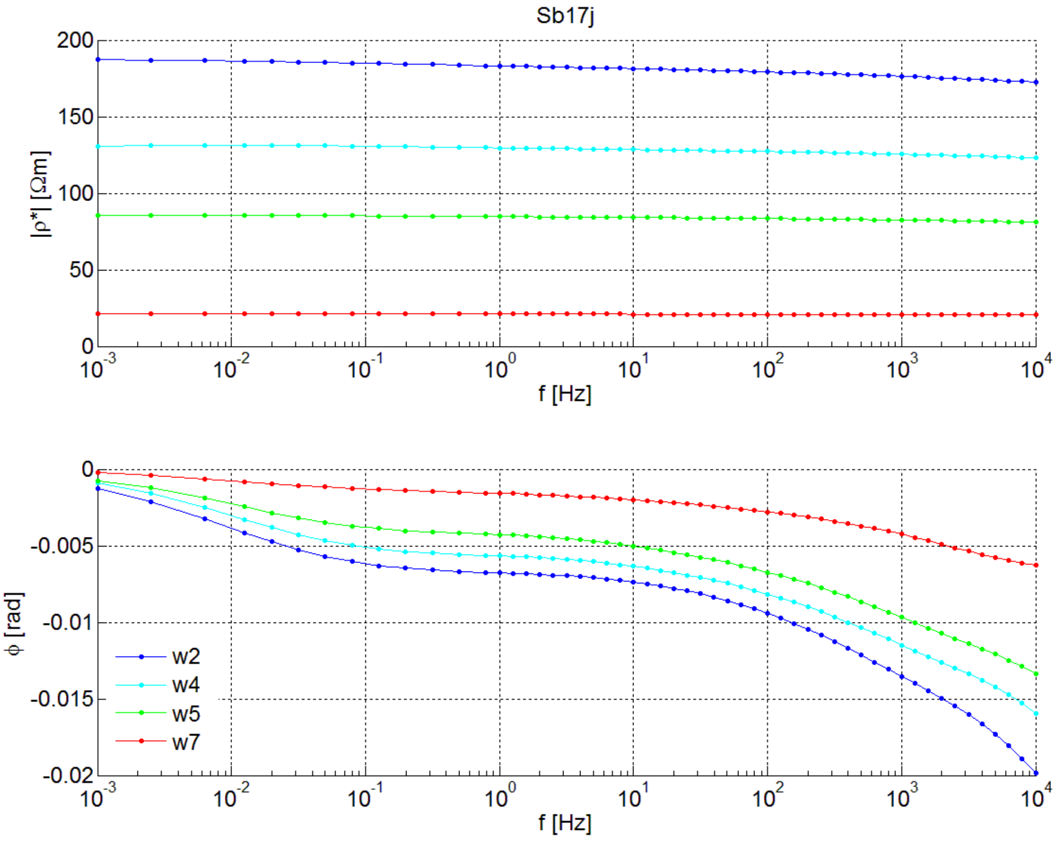

	θ [m^{3}m^{-3}]	**$\rho_{w(i)}$ [Ωm]**	**$\rho_{w(f)}$ [Ωm]**	chemical analysis of final water (Na; K; Mg; Ca; Mn; Fe [ppm])
Sb17j-w2	0.40	319	64	n.a.
Sb17j-w4	0,41	98	38	n.a.
Sb17j-w5	0.42	45	30	n.a.
Sb17j-w7	0,43	7	7	n.a.

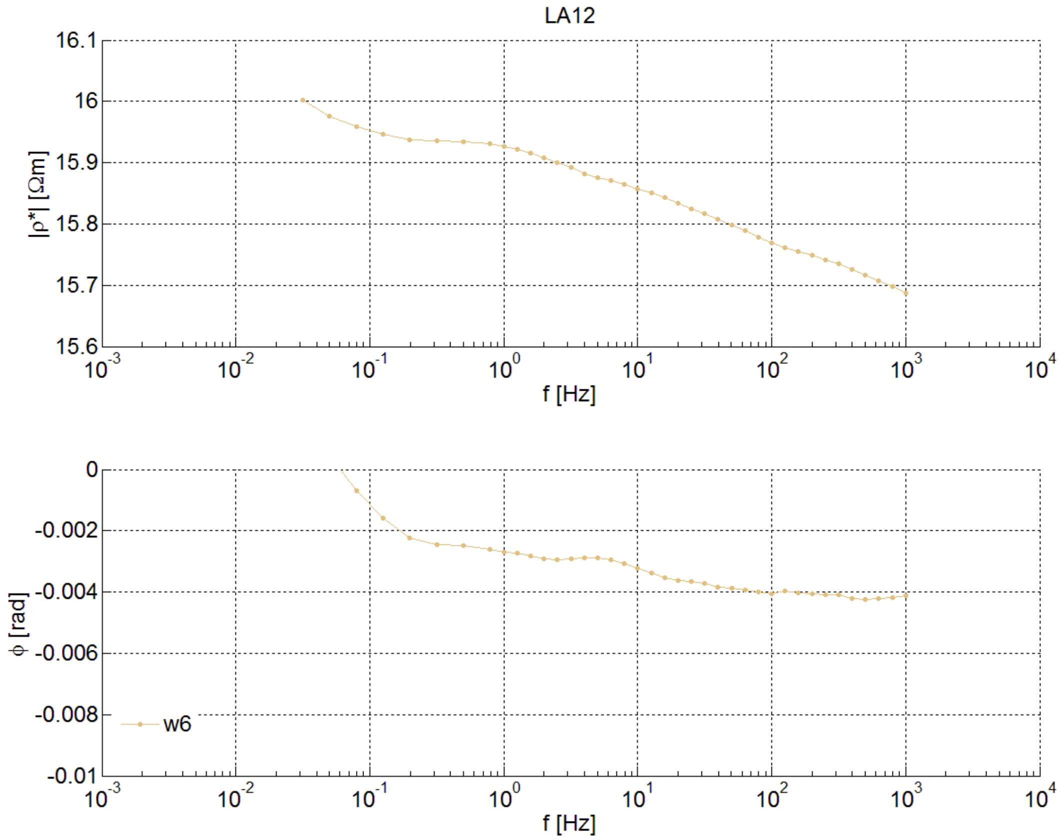

	θ **[m^{3}m^{-3}]**	**$\rho_{w(i)}$** **[Ωm]**	**$\rho_{w(f)}$** **[Ωm]**	chemical analysis of final water (Na; K; Mg; Ca; Mn; Fe [ppm])
LA12-w6	0.53	40	10	n.a.

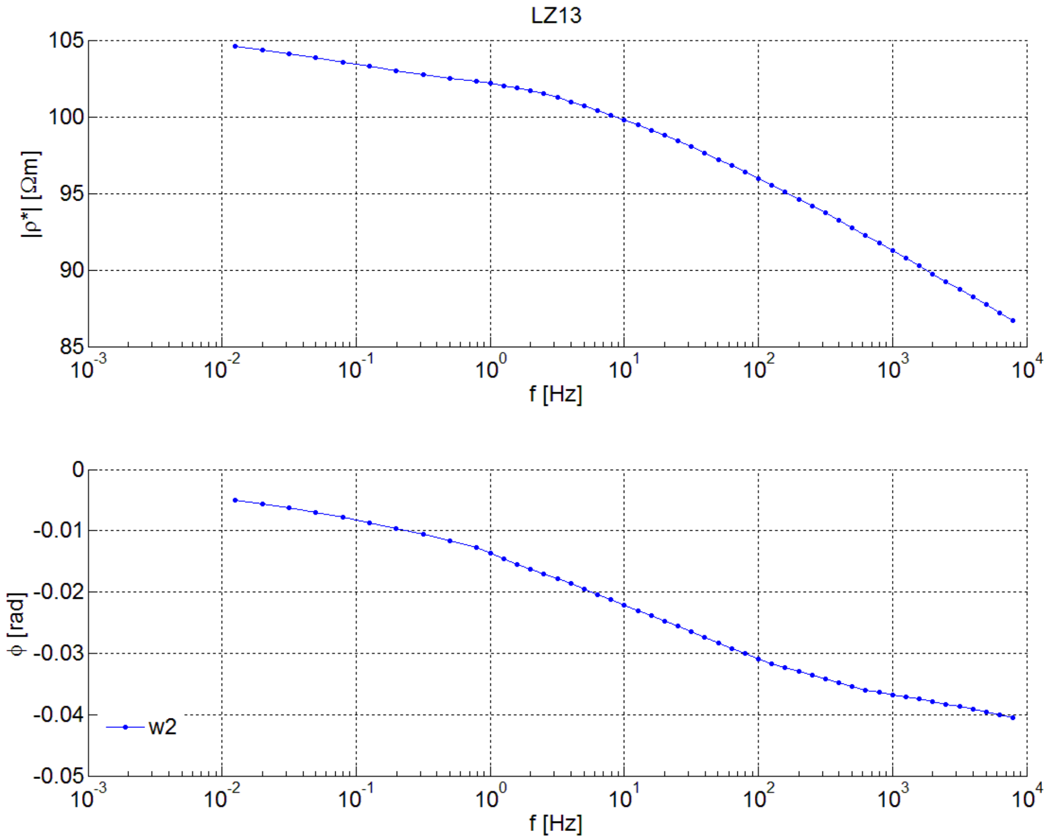

	θ [m³m⁻³]	**$\rho_{w(i)}$ [Ωm]**	**$\rho_{w(f)}$ [Ωm]**	chemical analysis of final water (Na; K; Mg; Ca; Mn; Fe [ppm])
LZ13-w2	0.35	304	95	n.a.

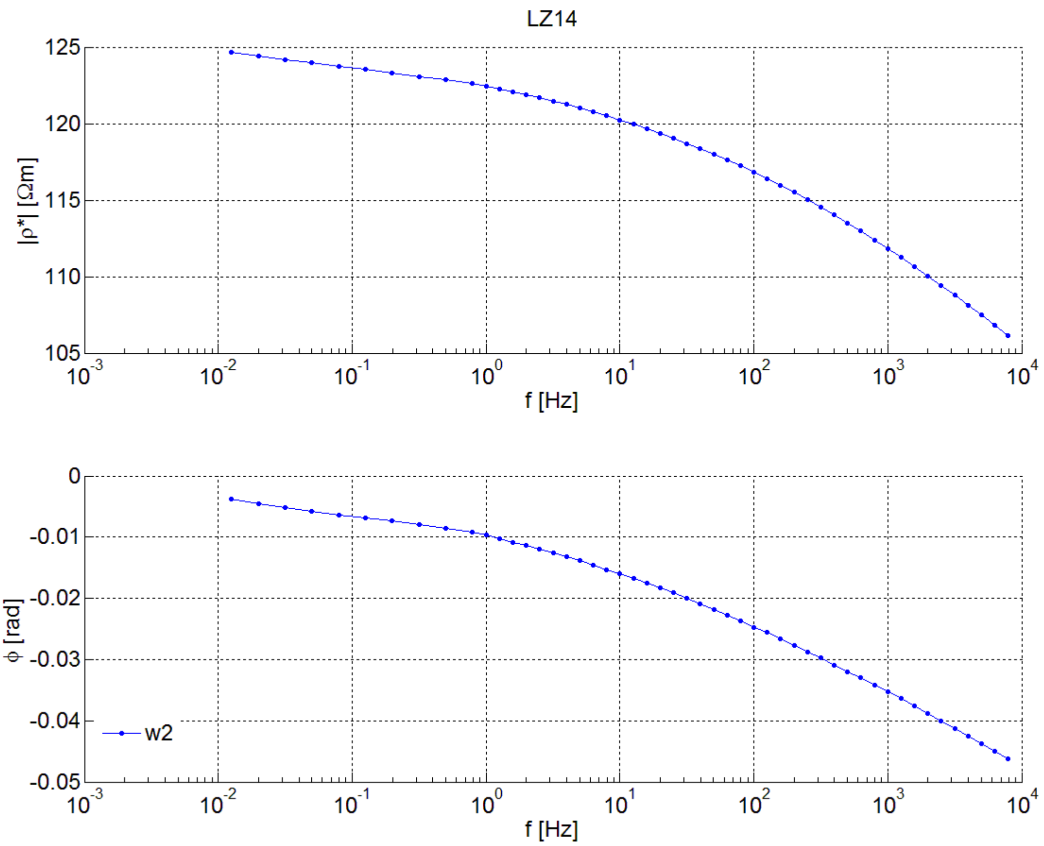

	θ [m^3m^{-3}]	**$\rho_{w(i)}$ [Ωm]**	**$\rho_{w(f)}$ [Ωm]**	chemical analysis of final water (Na; K; Mg; Ca; Mn; Fe [ppm])
LZ14-w2	0.38	270	119	n.a.

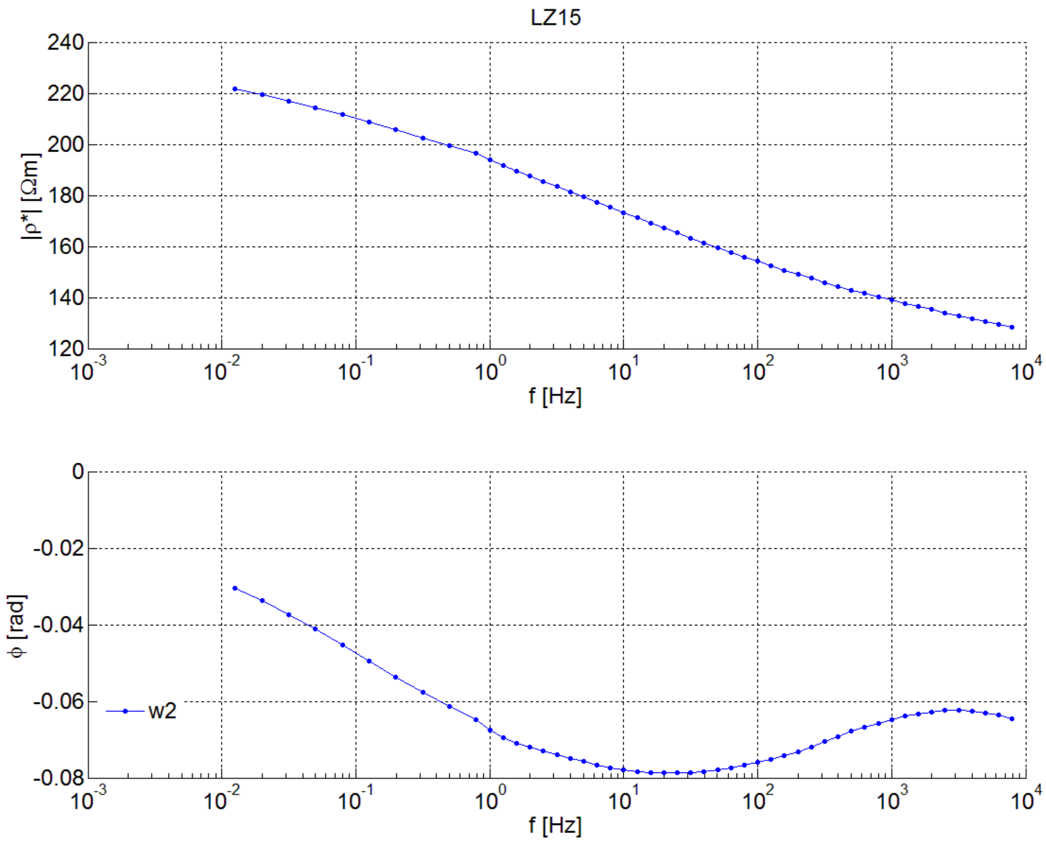

	θ $[m^3m^{-3}]$	**$\rho_{w(i)}$ [Ωm]**	**$\rho_{w(f)}$ [Ωm]**	chemical analysis of final water (Na; K; Mg; Ca; Mn; Fe [ppm])
LZ15-w2	0.51	270	119	12.21; 0.85; 1.45; 0.17; 0.06; 0.23

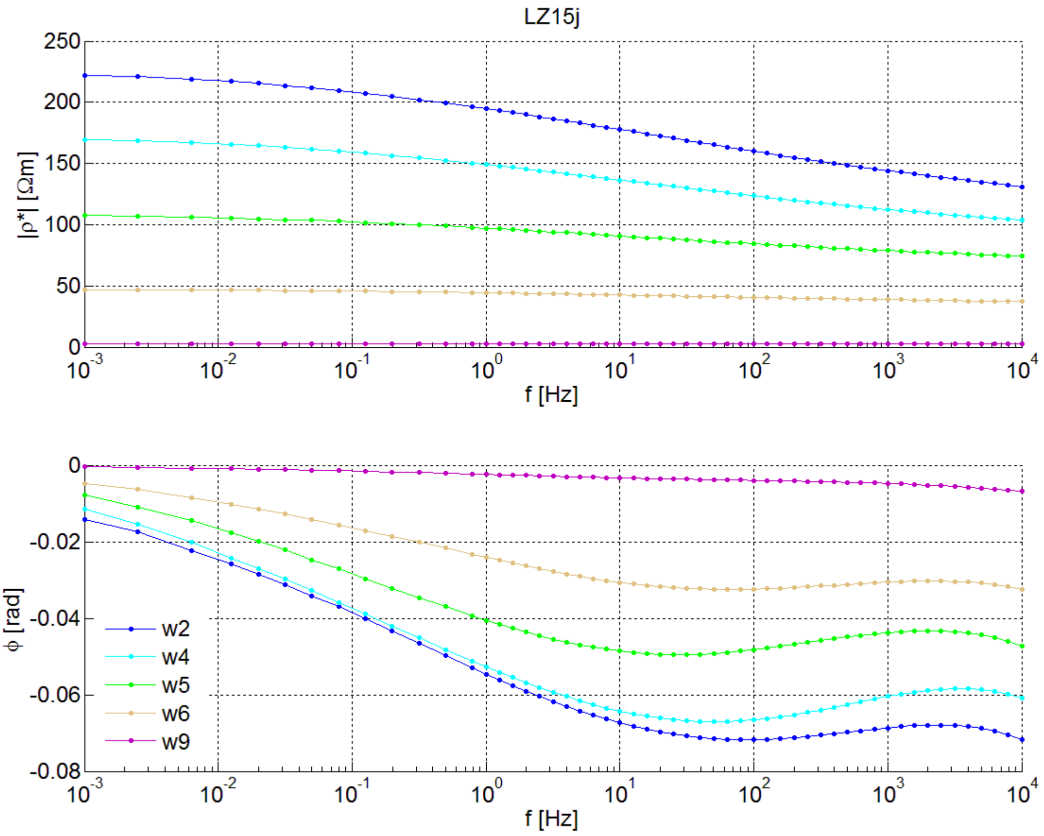

	θ [m³m⁻³]	$\rho_{w(i)}$ [Ωm]	$\rho_{w(f)}$ [Ωm]	chemical analysis of final water (Na; K; Mg; Ca; Mn; Fe [ppm])
LZ15j-w2	0.45	319	61	n.a.
LZ15j-w4	0.54	97	93	n.a.
LZ15j-w5	0.54	44	43	n.a.
LZ15j-w6	0.45	18	20	n.a.
LZ15j-w9	0.45	1	0,9	n.a.

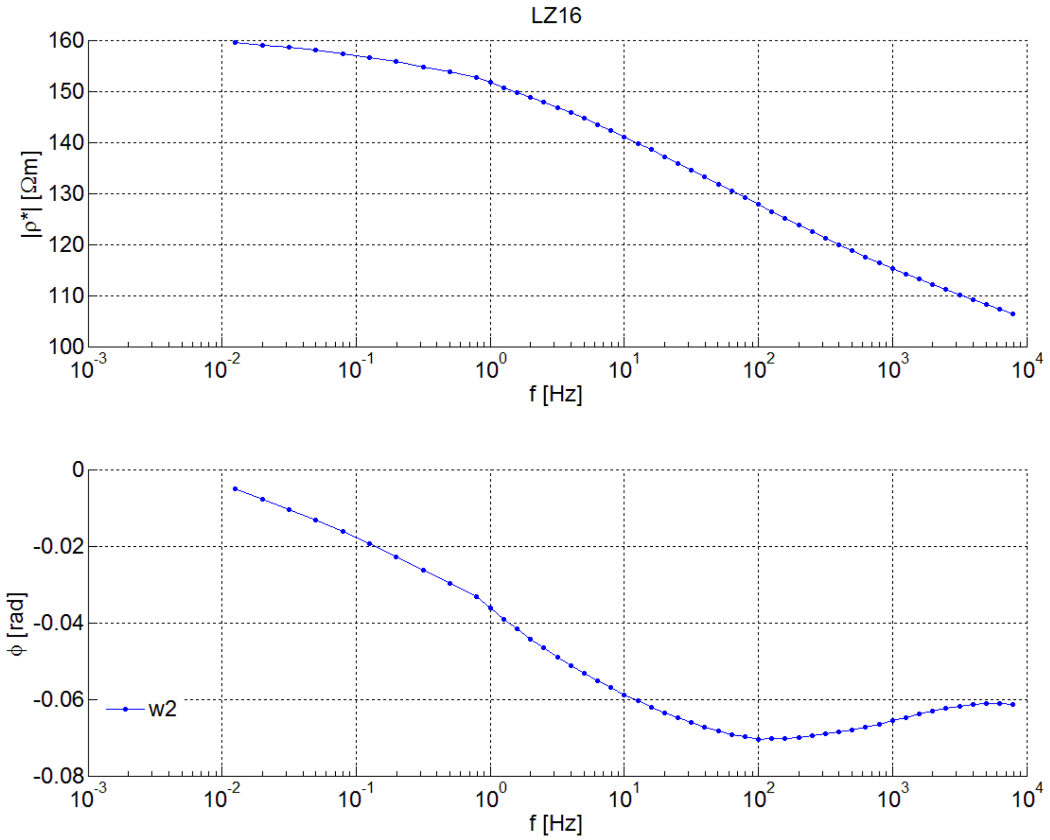

	θ [m^3m^{-3}]	**$\rho_{w(i)}$ [Ωm]**	**$\rho_{w(f)}$ [Ωm]**	chemical analysis of final water (Na; K; Mg; Ca; Mn; Fe [ppm])
LZ16-w2	0.63	269	89	10.18; 3.92; 1.95; 7.81; 0.00; 0.23

Appendix C

Comprehensive table of numerical values of the sedimentological and electrical properties of the natural samples, the parameters of CC, GCC, and DD (Tikhonov) models, and the corresponding RMSE.

Sampling site	Samples	**Grain-size distribution** (Wentworth's classification); in red the values measured with a cut-off diameter between sand and mud equal to 0.050 mm (phi scale = -4.3).								**Characteristic grain diameters**; in red the approximated values obtained by extrapolation from the grain-size distribution curve.					**Uniformity coefficients**; in red the values calculated from approximated grain diameters values.			**Coarse-to-fine ratios**; in red the values calculated from data with a cut-off diameter between sand and mud equal to 0.050 mm.			**Porosity**	**Organic matter content**; n.a. not available	**Initial water resistivity**	**Final water resistivity**; n.a. not available
	ID	**clay [%]**	**silt [%]**	***vf*S [%]**	***f*S [%]**	***m*S [%]**	***c*S [%]**	***vc*S [%]**	**G [%]**	**d$_{10}$ [mm]**	**d$_{30}$ [mm]**	**d$_{50}$ [mm]**	**d$_{60}$ [mm]**	**d$_{90}$ [mm]**	**U$_{60}$ [-]**	**U$_{90}$ [-]**	**U$_{c}$ [-]**	**$\Gamma_{0.063}$ [-]**	**$\Gamma_{0.125}$ [-]**	**$\Gamma_{0.250}$ [-]**	**θ [m^{3}m^{-3}]**	**OM [%]**	**$\rho_{w(i)}$ [Ωm]**	**$\rho_{w(f)}$ [Ωm]**
Orio Litta	**O1-w2**	4.0		7.6	34.8	45.3	7.6	0.7	0.0	0.117	0.189	0.259	0.297	0.480	2.5	4.1	1.0	24.1	7.6	1.2	0.41	0.05	270	66
	O1-w4																				0.40		103	47
	O1-w5																				0.37		45	29
	O1-w6																				0.37		22	15
	O2-w2	5.3		1.5	8.9	60.2	19.9	1.6	2.7	0.203	0.319	0.392	0.435	0.707	2.3	3.7	1.2	18.0	14.0	5.5	0.38	*n.a.*	283	39
	O3-w2	3.1		1.0	6.3	24.8	23.2	14.8	26.8	0.241	0.435	0.758	1.072	6.727	4.4	27.9	0.7	31.8	27.1	10.0	0.34	*n.a.*	283	28
	O4-w2	5.0		1.8	9.6	54.2	23.3	3.5	2.7	0.192	0.319	0.406	0.451	0.758	2.3	3.9	1.2	19.1	13.7	5.1	0.40	0.00	302	33
	O4-w4																				0.38		103	24
	O4-w5																				0.39		45	22
	O4-w6																				0.37		22	14
	O5-w2	8.5		8.7	45.6	36.0	1.1	0.2	0.0	0.078	0.159	0.218	0.241	0.342	3.1	4.4	1.3	10.8	4.8	0.6	0.39	0.04	270	84
	O6j-w2	9.1	3.9	2.8	5.1	14.0	17.2	14.8	32.9	0.007	0.392	0.886	1.516	5.464	230.7	831.8	15.4	6.7	5.3	3.8	0.38	*n.a.*	319	37
	O6j-w5																				0.37		43	30
	O6j-w7																				0.37		7	7
	O6j-w9																				0.26		1	1
	Ob18j-w2	0.5		1.7	7.4	37.9	28.9	10.7	12.8	0.250	0.366	0.536	0.616	2.460	2.5	9.9	0.9	211.8	44.7	9.4	0.34	*n.a.*	319	18
	Ob18j-w4																				0.35		97	46
	Ob18j-w5																				0.35		43	31
	Ob18j-w6																				0.36		21	17
	Ob18j-w8																				0.36		2	2
	Ob19j-w2	3.2		3.2	20.9	66.0	5.8	0.2	0.7	0.139	0.259	0.319	0.354	0.483	2.6	3.5	1.4	30.8	14.7	2.7	0.41	*n.a.*	319	99
	Ob19j-w4																				0.42		98	63
	Ob19j-w5																				0.41		44	34
	Ob19j-w7																				0.40		7	7
Senna Lodigiana	**S7-w2**	11.6	6.3	4.2	19.6	49.2	8.6	0.3	0.1	0.001	0.183	0.277	0.308	0.483	362.0	568.1	157.6	4.6	3.5	1.4	0.40	0.12	302	71
	S7-w4																				0.41		103	44
	S7-w5																				0.38		45	27
	S7-w6																				0.40		23	18
	Sb7-w4	11.9		6.9	42.6	34.1	4.4	0.1	0.0	0.040	0.149	0.210	0.250	0.435	6.3	10.9	2.2	7.4	4.3	0.6	0.42	*n.a.*	97	52
	Sb7j-w2																				0.37		315	80
	Sb7j-w4																				0.45		98	36
	Sb7j-w5																				0.42		44	26
	Sb7j-w7																				0.44		7	7
	Sb8j-w2	46.0		24.9	24.8	4.0	0.2	0.1	0.1	0.014	0.028	0.058	0.085	0.210	6.3	15.5	0.7	1.2	0.4	0.0	0.31	*n.a.*	322	46
	Sb8j-w4																				0.39		97	35
	Sb8j-w5																				0.39		45	31
	Sb8j-w8																				0.47		2	2
	S9-w2	3.8		4.1	40.4	51.5	0.2	0.0	0.0	0.139	0.203	0.250	0.268	0.342	2.0	2.5	1.1	25.2	11.6	1.1	0.37	0.04	304	49
	Sb9j-w2																				0.39		319	54
	Sb9j-w4																				0.37		97	36
	Sb9j-w5																				0.40		45	27
	Sb9j-w6																				0.39		18	14
	Sb9j-w8																				0.40		2	2
	S10-w2	3.5		2.3	9.3	53.1	31.2	0.7	0.1	0.183	0.354	0.420	0.467	0.660	2.6	3.7	1.5	27.9	16.5	5.7	0.40	*n.a.*	283	36
	Sb10j-w2																				0.37		315	19
	Sb10j-w4																				0.35		97	42
	Sb10j-w5																				0.38		45	22
	Sb10j-w6																				0.37		18	15
	S11-w2	1.6		7.5	59.3	31.4	0.2	0.0	0.0	0.125	0.177	0.218	0.233	0.354	1.9	2.8	1.1	61.5	10	0.5	0.44	0.37	302	51
	S11-w4																				0.45		103	43
	S11-w5																				0.41		45	29
	S11-w6																				0.38		23	16
	Sb17j-w2	10.4		18.5	59.1	11.8	0.1	0.0	0.0	0.049	0.125	0.159	0.177	0.277	3.6	5.7	1.8	8.6	2.5	0.1	0.40	*n.a.*	319	64
	Sb17j-w4																				0.41		98	38
	Sb17j-w5																				0.42		45	30
	Sb17j-w7																				0.43		7	7
Landriano	**LA12-w6**	37.1	43.9	6.3	1.7	1.9	1.9	2.3	4.8	0.0001	0.007	0.027	0.041	0.342	7.3	11.9	19.7	0.2	0.1	0.1	0.53	*n.a.*	40	10
Lozzolo	**LZ13-w2**	13.9	12.5	7.2	9.7	13.6	15.4	13.4	14.4	0.002	0.092	0.379	0.574	2.549	326.3	1448.2	8.7	2.8	2.0	1.3	0.35	0.34	304	*n.a.*
	LZ14-w2	16.2	10.4	5.3	7.1	13.6	18.9	14.3	14.3	0.001	0.098	0.451	0.660	2.828	803.4	3444.3	16.5	2.8	2.1	1.6	0.38	0.13	270	*n.a.*
	LZ15-w2	15.5	31.9	11.1	10.2	9.1	9.6	5.9	6.8	0.001	0.015	0.072	0.134	1.320	137.2	1351.2	1.7	1.1	0.7	0.5	0.51	0.31	270	*n.a.*
	LZ15j-w2																				0.63		269	89
	LZ15j-w4																				0.45		319	61
	LZ15j-w5																				0.54		97	93
	LZ15j-w6																				0.54		44	43
	LZ15j-w9																				0.45		18	20
	LZ16-w2	35.3	31.9	12.5	10.6	6.4	2.5	0.6	0.3	0.0003	0.002	0.011	0.025	0.250	78.8	776	0.5	0.5	0.3	0.1	0.45	0.15	1	*n.a.*

	variables indicated with * are used as input variables for the cluster analysis and the principal component analysis																										
Samples	**Relative amplitude variations**						**Relative phase variations**; in red an anomalous value associated to a positive phase value						**Direct current resistivity** (DD model)	**Total chargeability** (DD model)	**Normalized chargeability** (DD model)	**Characteristic relaxation times** (DD model)									**Uniformity coefficients** relative to the relaxation time (DD model)		
ID	**ΔA_{-1} [-]**	**ΔA_0 [-]**	**ΔA_1 [-]**	**ΔA_2 [-]**	**ΔA_3 [-]**	**ΔA_4 [-]**	**$^*\Delta\varphi_{-1}$ [-]**	**$^*\Delta\varphi_0$ [-]**	**$^*\Delta\varphi_1$ [-]**	**$^*\Delta\varphi_2$ [-]**	**$^*\Delta\varphi_3$ [-]**	**$^*\Delta\varphi_4$ [-]**	**$^*\rho_0$ [Ωm]**	**$^*M_t$ [-]**	**m_n [μS/cm]**	**$^*\tau_{10}$ [s]**	**τ_{20} [s]**	**$^*\tau_{30}$ [s]**	**τ_{40} [s]**	**$^*\tau_{50}$ [s]**	**τ_{60} [s]**	**τ_{70} [s]**	**τ_{80} [s]**	**$^*\tau_{90}$ [s]**	**$U_{\tau60}$ [-]**	**$U_{\tau90}$ [-]**	**$U_{\tau c}$ [-]**
O1-w2	0.01	0.01	0.01	0.01	0.01	0.01	0.26	0.02	-0.21	-0.19	0.31	0.36	225	0.08	0.0003	4.55E-05	2.05E-04	6.52E-04	5.87E-03	2.35E-02	1.06E-01	3.00E-01	9.55E-01	3.04E+00	2327	66699	0.09
O1-w4	0.01	0.01	0.01	0.01	0.01	0.01	0.26	-0.03	-0.11	0.02	0.22	0.33	148	0.06	0.0004	3.61E-05	1.15E-04	4.10E-04	2.07E-03	1.05E-02	4.71E-02	2.12E-01	6.75E-01	2.15E+00	1305	59411	0.10
O1-w5	0.01	0.01	0.01	0.01	0.01	0.01	0.18	-0.01	-0.11	0.04	0.16	0.27	97	0.06	0.0006	3.61E-05	1.29E-04	5.17E-04	2.33E-03	1.18E-02	5.29E-02	2.38E-01	7.58E-01	2.41E+00	1465	66699	0.14
O1-w6	0.01	0.01	0.01	0.01	0.01	0.01	-0.05	-0.03	-0.10	0.08	0.23	0.28	65	0.04	0.0007	3.22E-05	9.12E-05	3.26E-04	1.30E-03	6.59E-03	3.74E-02	1.89E-01	7.58E-01	3.04E+00	1162	94379	0.09
O2-w2	0.01	0.01	0.01	0.01	0.01	0.01	-0.22	-0.13	-0.20	0.03	0.30	0.51	164	0.05	0.0003	2.87E-05	1.02E-04	4.61E-04	2.61E-03	1.66E-02	9.44E-02	3.78E-01	1.35E+00	4.82E+00	3293	168318	0.08
O3-w2	0.01	0.01	0.01	0.01	0.01	0.01	0.39	0.07	-0.08	-0.16	0.02	0.33	116	0.06	0.0005	5.11E-05	3.26E-04	1.64E-03	7.40E-03	2.64E-02	9.44E-02	3.00E-01	1.07E+00	3.41E+00	1846	66699	0.56
O4-w2	0.01	0.00	0.01	0.01	0.01	0.01	-0.20	-0.14	0.09	0.19	0.09	0.40	129	0.04	0.0003	3.22E-05	1.15E-04	4.61E-04	1.46E-03	5.23E-03	2.97E-02	1.34E-01	8.50E-01	3.41E+00	922	105956	0.22
O4-w4	0.00	0.00	0.01	0.01	0.01	0.01	0.11	0.03	0.04	0.03	0.19	0.36	109	0.04	0.0004	3.22E-05	1.02E-04	3.65E-04	1.30E-03	5.87E-03	2.10E-02	1.19E-01	4.25E-01	1.70E+00	652	52920	0.20
O4-w5	0.00	0.01	0.01	0.01	0.01	0.01	0.03	-0.04	0.06	0.04	0.20	0.29	89	0.04	0.0005	3.61E-05	1.15E-04	3.65E-04	1.85E-03	6.59E-03	2.64E-02	1.34E-01	6.01E-01	2.41E+00	732	66699	0.14
O4-w6	0.00	0.00	0.01	0.01	0.01	0.01	0.05	0.01	0.12	0.12	0.12	0.22	57	0.04	0.0007	3.61E-05	1.15E-04	3.65E-04	1.46E-03	4.66E-03	1.87E-02	9.44E-02	4.77E-01	2.41E+00	517	66699	0.20
O5-w2	0.02	0.03	0.03	0.02	0.02	0.02	0.34	0.17	-0.16	-0.26	-0.15	0.21	187	0.13	0.0007	1.15E-04	7.32E-04	3.70E-03	1.48E-02	4.71E-02	1.19E-01	3.00E-01	7.58E-01	2.41E+00	1035	20970	1.00
O6j-w2	0.01	0.01	0.02	0.02	0.03	0.03	0.27	0.30	0.29	0.17	0.10	0.18	154	0.10	0.0007	4.06E-05	1.15E-04	2.90E-04	8.21E-04	2.33E-03	7.40E-03	2.35E-02	9.44E-02	6.75E-01	183	16638	0.28
O6j-w5	0.01	0.01	0.02	0.02	0.03	0.03	0.26	0.31	0.33	0.23	0.15	0.18	98	0.11	0.0011	3.61E-05	9.12E-05	2.30E-04	5.81E-04	1.64E-03	4.66E-03	1.48E-02	6.67E-02	5.35E-01	129	14820	0.31
O6j-w7	0.00	0.01	0.01	0.01	0.02	0.02	0.26	0.32	0.31	0.2	0.15	0.19	31	0.06	0.0020	3.61E-05	8.12E-05	2.05E-04	5.81E-04	1.46E-03	4.66E-03	1.48E-02	5.94E-02	4.25E-01	129	11758	0.25
O6j-w9	0.00	0.00	0.00	0.00	0.00	0.00	0.32	0.33	0.25	0.14	0.17	0.28	5	0.02	0.0029	3.22E-05	7.23E-05	1.83E-04	5.81E-04	1.64E-03	5.23E-03	1.87E-02	7.49E-02	4.77E-01	163	14820	0.20
Ob18j-w2	0.01	0.01	0.01	0.01	0.01	0.01	0.00	-0.01	0.13	0.17	0.18	0.42	211	0.05	0.0003	4.06E-05	1.29E-04	3.65E-04	1.16E-03	4.15E-03	1.66E-02	8.41E-02	4.77E-01	2.70E+00	410	66699	0.20
Ob18j-w4	0.01	0.01	0.01	0.01	0.01	0.01	0.03	0.07	0.19	0.17	0.16	0.38	198	0.05	0.0003	4.55E-05	1.15E-04	3.65E-04	1.04E-03	3.29E-03	1.18E-02	5.29E-02	2.67E-01	1.91E+00	258	41987	0.25
Ob18j-w5	0.01	0.01	0.01	0.01	0.01	0.01	0.03	0.10	0.21	0.19	0.15	0.25	115	0.05	0.0004	4.06E-05	1.15E-04	2.90E-04	9.22E-04	2.61E-03	9.33E-03	4.20E-02	2.12E-01	1.91E+00	230	47138	0.22
Ob18j-w6	0.01	0.01	0.01	0.01	0.01	0.01	0.08	0.16	0.23	0.19	0.13	0.21	75	0.05	0.0006	4.06E-05	1.15E-04	2.90E-04	8.21E-04	2.61E-03	8.31E-03	3.33E-02	1.89E-01	1.35E+00	205	33313	0.25
Ob18j-w8	0.00	0.00	0.00	0.00	0.00	0.00	0.20	0.24	0.25	0.18	0.13	0.17	11	0.01	0.0013	3.22E-05	8.12E-05	2.30E-04	6.52E-04	1.64E-03	5.23E-03	2.10E-02	9.44E-02	7.58E-01	163	23543	0.31
Ob19j-w2	0.02	0.02	0.02	0.02	0.02	0.02	0.26	0.05	0.04	0.05	0.13	0.38	306	0.09	0.0003	5.11E-05	1.83E-04	6.52E-04	2.61E-03	9.33E-03	3.74E-02	1.68E-01	6.75E-01	2.41E+00	732	47138	0.22
Ob19j-w4	0.01	0.02	0.02	0.02	0.02	0.02	0.31	0.11	0.08	0.00	-0.01	0.23	180	0.10	0.0006	6.44E-05	2.58E-04	9.22E-04	3.29E-03	1.18E-02	4.20E-02	1.50E-01	6.01E-01	2.41E+00	652	37399	0.31
Ob19j-w5	0.01	0.01	0.01	0.01	0.02	0.02	0.23	0.10	0.17	0.18	0.14	0.21	105	0.08	0.0008	4.55E-05	1.15E-04	3.26E-04	1.04E-03	3.29E-03	1.18E-02	5.29E-02	3.00E-01	1.91E+00	258	41987	0.20
Ob19j-w7	0.00	0.00	0.01	0.01	0.01	0.01	0.25	0.16	0.19	0.15	0.13	0.22	26	0.04	0.0015	3.61E-05	1.02E-04	2.90E-04	9.22E-04	2.61E-03	9.33E-03	3.74E-02	1.89E-01	1.52E+00	258	41987	0.25
S7-w2	0.02	0.02	0.03	0.03	0.02	0.01	0.58	0.26	-0.06	-0.40	-0.20	0.18	112	0.12	0.0011	1.45E-04	9.22E-04	4.66E-03	1.48E-02	3.74E-02	9.44E-02	2.12E-01	6.01E-01	1.91E+00	652	13201	1.59
S7-w4	0.02	0.03	0.04	0.03	0.02	0.01	0.56	0.24	-0.06	-0.39	-0.22	0.11	97	0.13	0.0014	1.29E-04	9.22E-04	4.15E-03	1.32E-02	3.74E-02	9.44E-02	2.38E-01	6.75E-01	2.15E+00	732	16638	1.41
S7-w5	0.01	0.02	0.03	0.03	0.02	0.02	0.42	0.32	0.21	-0.18	-0.28	0.02	70	0.12	0.0017	9.12E-05	4.61E-04	1.64E-03	4.66E-03	1.18E-02	2.97E-02	7.49E-02	2.38E-01	9.55E-01	326	10474	1.00
S7-w6	0.00	0.01	0.02	0.02	0.02	0.01	0.52	0.36	0.14	-0.15	-0.24	0.00	47	0.10	0.0021	7.23E-05	3.65E-04	1.30E-03	4.15E-03	1.05E-02	2.64E-02	6.67E-02	1.89E-01	6.01E-01	365	8310	0.89
Sb7-w4	0.03	0.03	0.04	0.03	0.02	0.02	0.32	0.08	-0.21	-0.42	-0.23	0.06	111	0.16	0.0014	2.05E-04	1.64E-03	8.31E-03	2.97E-02	8.41E-02	2.12E-01	5.35E-01	1.35E+00	3.41E+00	1035	16638	1.59
Sb7j-w2	0.02	0.02	0.03	0.03	0.04	0.04	0.41	0.16	0.14	0.12	0.10	0.17	146	0.15	0.0010	4.55E-05	1.45E-04	4.61E-04	1.46E-03	5.23E-03	1.87E-02	7.49E-02	3.37E-01	1.70E+00	410	37399	0.25
Sb7j-w4	0.02	0.02	0.02	0.03	0.03	0.03	0.39	0.14	0.11	0.10	0.10	0.15	83	0.13	0.0016	5.11E-05	1.45E-04	4.61E-04	1.64E-03	5.87E-03	2.10E-02	8.41E-02	3.78E-01	1.91E+00	410	37399	0.20
Sb7j-w5	0.01	0.01	0.02	0.02	0.03	0.03	0.42	0.23	0.24	0.22	0.16	0.15	63	0.11	0.0018	3.61E-05	1.02E-04	2.58E-04	6.52E-04	1.85E-03	6.59E-03	2.35E-02	1.19E-01	8.50E-01	183	23543	0.28
Sb7j-w7	0.01	0.01	0.01	0.01	0.01	0.02	0.36	0.15	0.17	0.14	0.15	0.24	21	0.06	0.0029	3.61E-05	9.12E-05	2.90E-04	9.22E-04	2.93E-03	1.05E-02	4.71E-02	2.38E-01	1.52E+00	290	41987	0.22
Sb8j-w2	0.00	0.00	0.01	0.01	0.02	0.04	0.39	0.31	0.39	0.45	0.45	0.37	139	0.08	0.0006	2.55E-05	4.06E-05	7.23E-05	1.15E-04	2.30E-04	5.81E-04	1.64E-03	8.31E-03	1.06E-01	23	4150	0.35
Sb8j-w4	0.00	0.01	0.01	0.02	0.02	0.03	0.40	0.29	0.31	0.30	0.31	0.29	111	0.08	0.0008	2.87E-05	5.74E-05	1.15E-04	2.58E-04	7.32E-04	2.07E-03	7.40E-03	4.20E-02	3.78E-01	72	13201	0.22
Sb8j-w5	0.00	0.00	0.01	0.01	0.02	0.03	0.44	0.33	0.38	0.41	0.40	0.32	88	0.08	0.0009	2.55E-05	4.55E-05	8.12E-05	1.45E-04	3.26E-04	7.32E-04	2.33E-03	1.18E-02	1.34E-01	29	5231	0.35
Sb8j-w8	0.00	0.00	0.00	0.00	0.00	0.01	0.52	0.43	0.41	0.38	0.36	0.37	7	0.01	0.0017	2.27E-05	4.06E-05	7.23E-05	1.29E-04	2.90E-04	6.52E-04	1.85E-03	6.59E-03	4.20E-02	29	1846	0.35
S9-w2	0.00	0.01	0.01	0.01	0.01	0.01	-0.01	-0.03	-0.06	0.14	0.21	0.36	186	0.05	0.0003	3.22E-05	1.02E-04	3.65E-04	1.30E-03	6.59E-03	3.33E-02	1.68E-01	7.58E-01	3.41E+00	1035	105956	0.12
Sb9j-w2	0.01	0.01	0.01	0.01	0.01	0.01	0.28	-0.13	-0.14	0.17	0.28	0.34	222	0.05	0.0002	5.74E-05	1.63E-04	4.61E-04	1.85E-03	1.05E-02	6.67E-02	3.37E-01	1.20E+00	3.83E+00	1162	66699	0.06
Sb9j-w4	0.01	0.01	0.01	0.01	0.01	0.01	0.32	-0.11	-0.15	0.10	0.28	0.33	149	0.05	0.0003	5.74E-05	1.45E-04	4.61E-04	2.07E-03	1.32E-02	7.49E-02	3.00E-01	1.07E+00	3.41E+00	1305	59411	0.05
Sb9j-w5	0.01	0.01	0.01	0.01	0.01	0.01	0.28	-0.09	-0.05	0.19	0.35	0.25	93	0.04	0.0004	4.06E-05	9.12E-05	2.05E-04	6.52E-04	3.29E-03	2.10E-02	1.34E-01	7.58E-01	3.04E+00	517	74881	0.05
Sb9j-w6	0.00	0.00	0.00	0.00	0.01	0.01	0.30	-0.08	-0.05	0.14	0.34	0.29	51	0.03	0.0006	3.61E-05	7.23E-05	1.83E-04	7.32E-04	3.70E-03	2.35E-02	1.34E-01	6.75E-01	2.70E+00	652	74881	0.04
Sb9j-w8	0.00	0.00	0.00	0.00	0.00	0.00	0.32	0.13	0.16	0.22	0.40	0.44	7	0.01	0.0012	2.27E-05	3.61E-05	6.44E-05	1.63E-04	5.17E-04	2.33E-03	1.32E-02	1.06E-01	1.07E+00	102	47138	0.08
S10-w2	0.01	0.00	0.00	0.00	0.01	0.01	-0.13	-0.27	-0.20	-0.01	0.27	0.44	159	0.04	0.0002	3.22E-05	1.02E-04	4.61E-04	2.93E-03	1.66E-02	1.06E-01	4.25E-01	1.35E+00	3.83E+00	3293	118953	0.06
Sb10j-w2	0.01	0.01	0.01	0.01	0.01	0.01	-0.16	-0.29	-0.11	0.11	0.28	0.53	242	0.04	0.0002	5.11E-05	1.45E-04	5.81E-04	2.93E-03	1.66E-02	9.44E-02	4.77E-01	1.70E+00	4.30E+00	1846	84067	0.07
Sb10j-w4	0.01	0.01	0.01	0.01	0.01	0.01	-0.14	-0.27	-0.10	0.09	0.24	0.48	177	0.04	0.0002	5.11E-05	1.63E-04	7.32E-04	3.70E-03	2.10E-02	1.19E-01	5.35E-01	1.91E+00	5.42E+00	2327	105956	0.09
Sb10j-w5	0.01	0.00	0.00	0.00	0.01	0.01	-0.11	-0.20	-0.03	0.13	0.22	0.35	81	0.03	0.0004	4.06E-05	1.29E-04	4.61E-04	1.85E-03	9.33E-03	5.29E-02	3.00E-01	1.20E+00	4.30E+00	1305	105956	0.10
Sb10j-w6	0.00	0.00	0.00	0.00	0.00	0.01	-0.11	-0.18	0.00	0.13	0.21	0.34	54	0.02	0.0004	3.61E-05	1.15E-04	3.65E-04	1.46E-03	6.59E-03	3.74E-02	1.89E-01	1.07E+00	4.30E+00	1035	118953	0.10
S11-w2	0.01	0.01	0.01	0.01	0.01	0.01	0.01	0.00	-0.19	-0.18	0.30	0.40	243	0.08	0.0003	3.61E-05	1.63E-04	5.81E-04	5.23E-03	2.35E-02	9.44E-02	3.00E-01	1.07E+00	3.83E+00	2613	105956	0.10
S11-w4	0.01	0.01	0.01	0.01	0.01	0.01	0.15	-0.02	-0.12	0.02	0.25	0.40	151	0.06	0.0004	3.22E-05	1.15E-04	4.10E-04	2.07E-03	1.18E-02	5.29E-02	2.12E-01	7.58E-01	2.70E+00	1645	84067	0.10
S11-w5	0.00	0.01	0.01	0.01	0.01	0.01	0.09	0.08	0.06	0.11	0.24	0.30	99	0.05	0.0005	3.22E-05	8.12E-05	2.58E-04	7.32E-04	3.29E-03	1.32E-02	6.67E-02	3.00E-01	1.35E+00	410	41987	0.16
S11-w6	0.00	0.00	0.01	0.01	0.01	0.01	-0.10	-0.05	0.03	0.16	0.23	0.26	55	0.04	0.0007	3.22E-05	8.12E-05	2.30E-04	1.04E-03	4.15E-03	2.10E-02	1.19E-01	7.58E-01	3.83E+00	652	118953	0.08
Sb17j-w2	0.01	0.01	0.01	0.01	0.02	0.02	0.34	0.07	0.08	0.22	0.30	0.32	205	0.07	0.0004	3.61E-05	8.12E-05	2.05E-04	5.17E-04	2.07E-03	9.33E-03	5.29E-02	3.00E-01	1.70E+00	258	47138	0.12
Sb17j-w4	0.01	0.01	0.01	0.01	0.01	0.02	0.37	0.08	0.11	0.22	0.29	0.28	135	0.06	0.0005	3.61E-05	8.12E-05	1.83E-04	5.17E-04	1.85E-03	7.40E-03	4.20E-02	2.67E-01	1.70E+00	205	47138	0.12
Sb17j-w5	0.00	0.01	0.01	0.01	0.01	0.02	0.37	0.09	0.15	0.25	0.30	0.28	88	0.05	0.0006	3.22E-05	7.23E-05	1.45E-04	4.10E-04	1.30E-03	5.23E-03	2.64E-02	1.89E-01	1.35E+00	163	41987	0.12
Sb17j-w7	0.00	0.00	0.00	0.00	0.00	0.01	0.39	0.16	0.22	0.28	0.35	0.32	21	0.02	0.0010	2.55E-05	4.55E-05	8.12E-05	2.05E-04	5.81E-04	1.85E-03	8.31E-03	5.94E-02	6.01E-01	72	23543	0.14
LA12-w6	0.00	0.00	0.00	0.01	0.01	0.00	2.28	0.41	0.17	0.20	0.01	0.00	16	0.02	0.0015	4.06E-05	1.15E-04	2.58E-04	7.32E-04	2.07E-03	5.23E-03	1.32E-02	6.67E-02	2.67E-01	129	6593	0.31
LZ13-w2	0.01	0.01	0.02	0.04	0.05	0.05	0.43	0.37	0.38	0.28	0.16	0.09	110	0.17	0.0015	3.61E-05	8.12E-05	2.05E-04	4.61E-04	1.16E-03	2.93E-03	9.33E-03	3.74E-02	2.67E-01	81	7402	0.40
LZ14-w2	0.01	0.01	0.02	0.03	0.04	0.05	0.46	0.29	0.39	0.35	0.30	0.24	130	0.15	0.0011	2.87E-05	5.74E-05	1.15E-04	2.58E-04	5.81E-04	1.64E-03	5.23E-03	2.64E-02	2.67E-01	57	9329	0.28
LZ15-w2	0.06	0.07	0.11	0.11	0.10	0.08	0.39	0.27	0.13	-0.03	-0.17	-0.01	237	0.40	0.0017	1.02E-04	5.81E-04	2.07E-03	6.59E-03	1.87E-02	5.29E-02	1.50E-01	4.77E-01	1.91E+00	517	18679	0.79
LZ15j-w2	0.02	0.03	0.07	0.09	0.10	0.08	0.74	0.46	0.38	0.17	-0.07	-0.07	182	0.30	0.0016	6.44E-05	2.05E-04	5.81E-04	1.46E-03	3.70E-03	9.33E-03	2.35E-02	6.67E-02	3.37E-01	145	5231	0.56
LZ15j-w4	0.04	0.06	0.09	0.10	0.10	0.09	0.36	0.26	0.19	0.06	-0.04	0.04	239	0.36	0.0015	7.23E-05	3.26E-04	1.04E-03	3.29E-03	1.05E-02	3.33E-02	9.44E-02	3.37E-01	1.70E+00	461	23543	0.44
LZ15j-w5	0.04	0.06	0.08	0.09	0.09	0.08	0.38	0.26	0.18	0.03	-0.10	0.01	178	0.35	0.0020	9.12E-05	3.65E-04	1.30E-03	4.15E-03	1.18E-02	3.74E-02	1.06E-01	3.78E-01	1.70E+00	410	18679	0.50
LZ15j-w6	0.03	0.05	0.07	0.07	0.07	0.06	0.41	0.27	0.17	-0.01	-0.10	0.08	115	0.27	0.0024	8.12E-05	3.65E-04	1.30E-03	4.15E-03	1.18E-02	3.33E-02	1.06E-01	3.78E-01	1.52E+00	410	18679	0.63
LZ15j-w9	0.02	0.03	0.04	0.05	0.05	0.04	0.40	0.29	0.21	0.05	-0.06	0.05	48	0.20	0.0041	6.44E-05	2.30E-04	7.32E-04	2.33E-03	6.59E-03	1.87E-02	5.94E-02	2.12E-01	1.20E+00	290	18679	0.44
LZ16-w2	0.00	0.00	0.00	0.00	0.01	0.01	0.42	0.35	0.27	0.16	0.17	0.28	3	0.03	0.0093	2.87E-05	7.23E-05	1.83E-04	5.17E-04	1.46E-03	4.66E-03	1.66E-02	6.67E-02	4.25E-01	163	14820	0.25

Samples	**Initial frequency** (CC and GCC models)	**Final frequency** (CC and GCC models)	**Direct current resistivity** (CC model, best fitting)	**Median direct current resistivity** (CC model, Pareto set)	**Maximum direct current resistivity** (CC model, Pareto set)	**Minimum direct current resistivity** (CC model, Pareto set)	**Chargeability** (CC model, best fitting)	**Median chargeability** (CC model, Pareto set)	**Maximum chargeability** (CC model, Pareto set)	**Minimum chargeability** (CC model, Pareto set)	**Relaxation time** (CC model, best fitting)	**Median relaxation time** (CC model, Pareto set)	**Maximum relaxation time** (CC model, Pareto set)	**Minimum relaxation time** (CC model, Pareto set)	**Frequency exponent c** (CC model, best fitting)	**Median frequency exponent c** (CC model, Pareto set)	**Maximum frequency exponent c** (CC model, Pareto set)	**Minimum frequency exponent c** (CC model, Pareto set)
ID	**f_i [Hz]**	**f_f [Hz]**	**ρ_0 [Ωm]**	**ρ_0 [Ωm]**	**ρ_0 [Ωm]**	**ρ_0 [Ωm]**	**m [-]**	**m [-]**	**m [-]**	**m [-]**	**τ [s]**	**τ [s]**	**τ [s]**	**τ [s]**	**c [-]**	**c [-]**	**c [-]**	**c [-]**
O1-w2	0.013	3.16	223	223	224	223	0.08	0.08	0.09	0.07	3.98E-01	3.98E-01	5.01E-01	3.98E-01	0.32	0.32	0.38	0.28
O1-w4	0.032	1.26	147	147	148	147	0.06	0.06	0.09	0.04	3.98E-01	3.98E-01	6.31E-01	5.01E-02	0.30	0.30	0.46	0.20
O1-w5	0.032	2.00	97	97	98	97	0.06	0.06	0.07	0.05	3.98E-01	3.98E-01	1.00E+00	3.98E-01	0.30	0.30	0.36	0.28
O1-w6	0.126	3.16	65	65	66	63	0.08	0.08	0.14	0.06	6.31E+00	6.31E+00	2.00E+02	2.00E-04	0.16	0.16	0.20	0.08
O2-w2	0.013	0.79	164	164	165	161	0.07	0.07	0.08	0.04	1.00E+01	1.00E+01	2.51E+01	5.01E+00	0.26	0.26	0.48	0.24
O3-w2	0.013	79.44	117	116	118	116	0.08	0.07	0.09	0.07	1.26E-01	1.00E-01	3.16E-01	7.94E-02	0.24	0.28	0.28	0.22
O4-w2	0.013	0.79	130	130	130	128	0.05	0.05	0.06	0.03	3.16E+01	3.16E+01	5.01E+01	1.00E+01	0.28	0.28	0.38	0.20
O4-w4	0.050	2.00	107	107	110	106	0.05	0.05	0.14	0.03	3.98E-01	3.98E-01	1.58E+00	1.00E-04	0.22	0.22	0.38	0.08
O4-w5	0.050	1.59	88	88	89	87	0.06	0.06	0.08	0.04	2.00E+00	2.00E+00	6.31E+00	7.94E-01	0.20	0.20	0.32	0.14
O4-w6	0.032	0.50	57	57	57	57	0.05	0.05	0.06	0.04	1.00E+00	1.00E+00	7.94E+00	1.26E-01	0.18	0.18	0.24	0.16
O5-w2	0.013	50.12	184	184	184	182	0.16	0.16	0.16	0.15	1.58E-01	1.58E-01	1.58E-01	1.26E-01	0.32	0.32	0.34	0.32
O6j-w2	0.001	0.20	151				0.16				3.16E-04				0.18			
O6j-w5	0.001	0.13	97				0.15				2.00E-04				0.16			
O6j-w7	0.001	0.13	31				0.09				1.58E-04				0.16			
O6j-w9	0.001	0.13	5				0.01				6.31E-02				0.30			
Ob18j-w2	0.001	1.00	203				0.05				2.00E+00				0.28			
Ob18j-w4	0.001	0.08	181	181	181	181	0.04	0.04	0.04	0.04	3.98E+00	3.98E+00	5.01E+00	3.98E+00	0.32	0.32	0.32	0.32
Ob18j-w5	0.001	0.05	115	115	117	115	0.04	0.03	0,10	0.03	3.98E+00	7.94E+00	7.94E+00	6.31E-03	0.26	0.34	0.34	0.12
Ob18j-w6	0.001	0.03	75	75	75	75	0.04	0.04	0.04	0.04	1.58E+00	1.26E+00	1.58E+00	1.26E+00	0.22	0.22	0.22	0.22
Ob18j-w8	0.001	0.13	11	11	11	11	0.02	0.02	0.03	0.02	1.58E-03	1.58E-03	3.16E-02	1.00E-04	0.16	0.16	0.16	0.08
Ob19j-w2	0.001	0.20	281				0.06				1.26E+00				0.44			
Ob19j-w4	0.001	1.58	177				0.10				2.00E-01				0.30			
Ob19j-w5	0.001	0.05	103				0.03				2.51E+00				0.52			
Ob19j-w7	0.001	0.13	26				0.02				6.31E-01				0.40			
S7-w2	0.013	125.90	111	111	111	111	0.13	0.13	0.13	0.13	6.31E-02	6.31E-02	6.31E-02	6.31E-02	0.38	0.38	0.38	0.38
S7-w4	0.013	100.00	97	97	97	97	0.14	0.14	0.14	0.14	7.94E-02	7.94E-02	7.94E-02	7.94E-02	0.38	0.38	0.38	0.38
S7-w5	0.032	501.30	69	69	69	69	0.13	0.13	0.14	0.13	1.58E-02	1.58E-02	1.58E-02	1.26E-02	0.36	0.36	0.36	0.34
S7-w6	0.050	398.20	47	47	47	47	0.11	0.11	0.12	0.11	1.58E-02	1.58E-02	1.58E-02	1.58E-02	0.36	0.36	0.36	0.34
Sb7-w4	0.013	63.10	112	112	112	111	0.20	0.20	0.21	0,20	2.51E-01	3.16E-01	3.16E-01	2.51E-01	0.32	0.32	0.34	0.30
Sb7j-w2	0.001	0.79	137				0.10				2.51E-01				0.40			
Sb7j-w4	0.001	0.50	83				0.09				2.51E-01				0.38			
Sb7j-w5	0.001	0.32	64				0.05				2.51E-01				0.42			
Sb7j-w7	0.001	0.32	21				0.03				3.98E-01				0.42			
Sb8j-w2	0.001	0.32	136				0.03				3.16E-02				0.32			
Sb8j-w4	0.001	0.32	108	108	108	108	0.05	0.05	0.06	0.05	2.51E-02	2.51E-02	2.51E-02	1.00E-02	0.32	0.32	0.32	0.30
Sb8j-w5	0.001	0.32	86	86	86	86	0.03	0.05	0.09	0.02	2.51E-02	2.51E-03	1.58E-01	1.00E-04	0.34	0.30	0.42	0.26
Sb8j-w8	0.001	0.20	7				0.03				1.00E+03				0.02			
S9-w2	0.032	5.01	186	186	187	185	0.06	0.06	0.07	0.06	7.94E-01	7.94E-01	3.16E+00	1.26E-01	0.22	0.22	0.22	0.18
Sb9j-w2	0.001	1.26	214				0.04				1.00E+00				0.40			
Sb9j-w4	0.001	1.00	147				0.03				1.00E+00				0.50			
Sb9j-w5	0.001	0.79	92				0.02				1.26E+00				0.52			
Sb9j-w6	0.001	1.26	50				0.02				6.31E-01				0.42			
Sb9j-w8	0.001	0.08	7				0.01				1.00E-02				0.38			
S10-w2	0.032	1.59	156	156	156	148	0.09	0.09	0.09	0.03	3.98E+02	3.98E+02	7.94E+02	3.16E+00	0.20	0.20	0.42	0.18
Sb10j-w2	0.001	0.32	232				0.04				7.94E+00				0.40			
Sb10j-w4	0.001	0.32	177				0.04				6.31E+00				0.40			
Sb10j-w5	0.001	0.32	81				0.03				5.01E+00				0.32			
Sb10j-w6	0.001	0.32	55	55	55	55	0.02	0.02	0.02	0.02	5.01E+00	5.01E+00	5.01E+00	5.01E+00	0.38	0.38	0.38	0.38
S11-w2	0.050	25.12	242	242	242	238	0.09	0.09	0.1	0.07	5.01E-01	5.01E-01	6.31E-01	2.00E-01	0.28	0.28	0.34	0.22
S11-w4	0.013	12.59	147	147	151	145	0.08	0.08	0.15	0.06	5.01E-01	5.01E-01	1.58E+00	2.51E-03	0.22	0.22	0.28	0.12
S11-w5	0.050	2.00	95	95	99	95	0.05	0.05	0.15	0.05	2.00E-01	2.00E-01	3.16E+00	2.00E-04	0.28	0.28	0.28	0.12
S11-w6	0.050	3.98	56	56	56	55	0.06	0.06	0.1	0.03	1.00E+00	1.00E+00	1.00E+01	2.00E-04	0.16	0.16	0.26	0.10
Sb17j-w2	0.001	0.32	201				0.04				5.01E-01				0.40			
Sb17j-w4	0.001	0.32	133				0.03				5.01E-01				0.44			
Sb17j-w5	0.001	0.50	87				0.02				6.31E-01				0.48			
Sb17j-w7	0.001	0.32	21	21	21	21	0.01	0.01	0.01	0.01	1.58E-01	1.58E-01	1.58E-01	1.26E-01	0.40	0.40	0.42	0.40
LA12-w6	0.079	1.59	16	16	16	16	0.01	0.01	0.07	0.01	1.58E-01	1.58E-01	1.58E-01	1.00E-04	0.64	0.64	0.64	0.24
LZ13-w2	0.013	0.79	106	106	106	106	0.24	0.24	0.25	0.09	2.51E-04	2.51E-04	6.31E-02	1.58E-04	0.26	0.26	0.30	0.24
LZ14-w2	0.013	1.00	127	127	127	127	0.19	0.19	0.19	0.09	1.00E-04	1.00E-04	1.26E-02	1.00E-04	0.20	0.20	0.30	0.18
LZ15-w2	0.013	501.30	234				0.45				1.26E-02				0.32			
LZ15j-w2	0.001	125.89	233				0.45				2.00E-02				0.28			
LZ15j-w4	0.001	125.89	172				0.44				1.58E-02				0.30			
LZ15j-w5	0.001	125.89	109				0.33				2.00E-02				0.32			
LZ15j-w6	0.001	125.89	48				0.24				7.94E-03				0.30			
LZ15j-w9	0.001	79.43	3				0.04				3.98E-04				0.24			
LZ16-w2	0.013	794.50	162				0.41				2.51E-03				0.34			

Samples	Direct current resistivity (GCC model, best fitting)	Median direct current resistivity (GCC model, Pareto set)	Minimum direct current resistivity (GCC model, Pareto set)	Maximum direct current resistivity (GCC model, Pareto set)	Chargeability (GCC model, best fitting)	Median chargeability (GCC model, Pareto set)	Minimum chargeability (GCC model, Pareto set)	Maximum chargeability (GCC model, Pareto set)	Relaxation time (GCC model, best fitting)	Median relaxation time (GCC model, Pareto set)	Minimum relaxation time (GCC model, Pareto set)	Maximum relaxation time (GCC model, Pareto set)	Frequency exponent c (GCC model, best fitting)	Median frequency exponent c (GCC model, Pareto set)	Minimum frequency exponent c (GCC model, Pareto set)	Maximum frequency exponent c (GCC model, Pareto set)	Frequency exponent k (GCC model, best fitting)	Median frequency exponent k (GCC model, Pareto set)	Minimum frequency exponent k (GCC model, Pareto set)	Maximum frequency exponent k (GCC model, Pareto set)
ID	**ρ_0 [Ωm]**	**ρ_0 [Ωm]**	**ρ_0 [Ωm]**	**ρ_0 [Ωm]**	**m [-]**	**m [-]**	**m [-]**	**m [-]**	**τ [s]**	**τ [s]**	**τ [s]**	**τ [s]**	**c [-]**	**c [-]**	**c [-]**	**c [-]**	**k [-]**	**k [-]**	**k [-]**	**k [-]**
O1-w2	223	223	226	223	0.08	0.08	0.14	0.08	6.31E-01	6.31E-01	3.16E+01	6.31E-01	0.34	0.34	0.42	0.26	0.90	0.90	0.90	0.18
O1-w4	147	147	148	147	0.06	0.06	0.11	0.04	6.31E-01	3.98E-01	1.00E+01	3.98E-02	0.32	0.30	0.48	0.20	0.86	1.00	1.00	0.24
O1-w5	97	97	98	97	0.06	0.06	0.10	0.05	5.01E-01	5.01E-01	2.51E+00	3.98E-01	0.30	0.30	0.44	0.24	0.94	0.94	1.00	0.52
O1-w6	63	63	66	63	0.05	0.05	0.15	0.05	1.26E+01	1.26E+01	1.00E+03	1.00E-04	0.46	0.46	0.90	0.08	0.26	0.26	1.00	0.04
O2-w2	163	163	164	161	0.09	0.09	0.09	0.05	1.00E+03	1.00E+03	1.00E+03	1.26E+01	0.82	0.82	1.00	0.42	0.10	0.10	0.82	0.08
O3-w2	116	116	118	116	0.08	0.08	0.15	0.08	1.58E+00	1.58E+00	1.00E+02	1.58E+00	0.34	0.34	0.72	0.28	0.44	0.44	0.46	0.06
O4-w2	128	128	130	128	0.06	0.06	0.06	0.03	3.98E+02	3.98E+02	1.00E+03	1.26E+01	0.96	0.96	1.00	0.30	0.08	0.08	0.96	0.08
O4-w4	106	106	110	106	0.04	0.04	0.15	0.04	2.00E+00	2.00E+00	2.00E+02	1.00E-04	0.36	0.36	0.62	0.08	0.52	0.52	0.98	0.08
O4-w5	87	87	89	87	0.05	0.05	0.08	0.04	7.94E+00	7.94E+00	6.31E+02	1.26E+00	0.30	0.30	0.90	0.20	0.52	0.52	1.00	0.12
O4-w6	57	57	57	56	0.06	0.06	0.13	0.02	6.31E+00	6.31E+00	3.98E+02	6.31E+00	0.18	0.18	0.98	0.18	0.62	0.62	0.62	0.02
O5-w2	182	182	182	180	0.16	0.16	0.17	0.15	5.01E-01	5.01E-01	1.26E+00	1.58E-01	0.38	0.38	0.42	0.34	0.64	0.64	0.96	0.44
O6j-w2	151				0.25				1.00E-04				0.16				0.68			
O6j-w5	97	97	97	97	0.22	0.21	0.25	0.16	3.16E-04	7.94E-04	2.51E-03	1.26E-04	0.16	0.16	0.16	0.16	0.60	0.56	0.98	0.40
O6j-w7	31				0.13				1.00E-03				0.16				0.52			
O6j-w9	5				0.08				3.16E+01				0.46				0.02			
Ob18j-w2	203	203	203	203	0.15	0.15	0.15	0.09	3.16E+02	3.16E+02	3.16E+02	2.51E+02	0.68	0.68	0.68	0.42	0.04	0.04	0.14	0.04
Ob18j-w4	181	181	181	181	0.05	0.05	0.09	0.04	6.31E+01	3.98E+01	2.51E+02	5.01E+00	0.40	0.36	0.50	0.30	0.34	0.42	0.98	0.10
Ob18j-w5	115	115	116	115	0.10	0.10	0.14	0.04	6.31E+02	6.31E+02	6.31E+02	3.16E+00	0.54	0.54	0.60	0.20	0.06	0.06	0.82	0.04
Ob18j-w6	75	75	75	75	0.03	0.03	0.12	0.03	1.26E+01	6.31E+00	5.01E+01	5.01E-02	0.32	0.30	0.30	0.18	0.72	0.88	0.88	0.20
Ob18j-w8	11	11	11	11	0.15	0.15	0.15	0.03	1.58E-04	1.58E-04	1.00E+01	1.00E-04	0.12	0.12	0.22	0.08	0.14	0.14	0.86	0.06
Ob19j-w2	273				0.14				1.58E+01				0.56				0.14			
Ob19j-w4	179				0.22				1.26E+01				0.48				0.10			
Ob19j-w5	103	103	103	103	0.08	0.06	0.11	0.03	2.51E+01	2.00E+01	2.51E+01	3.98E+00	0.72	0.68	0.68	0.56	0.10	0.16	0.78	0.08
Ob19j-w7	26				0.08				3.16E+01				0.72				0.04			
S7-w2	111	111	111	111	0.14	0.14	0.14	0.14	3.16E-01	3.16E-01	3.98E-01	2.51E-01	0.44	0.44	0.48	0.42	0.56	0.56	0.62	0.48
S7-w4	96	96	97	96	0.15	0.15	0.16	0.15	5.01E-01	5.01E-01	7.94E-01	5.01E-01	0.48	0.48	0.54	0.48	0.44	0.44	0.44	0.32
S7-w5	69	69	69	69	0.14	0.14	0.14	0.14	3.98E-02	3.98E-02	3.98E-02	2.51E-02	0.38	0.38	0.38	0.36	0.70	0.72	0.82	0.70
S7-w6	47	47	47	47	0.14	0.14	0.15	0.12	2.51E-01	2.51E-01	3.98E-01	1.58E-02	0.46	0.46	0.54	0.34	0.32	0.32	0.90	0.22
Sb7-w4	111	111	112	111	0.21	0.21	0.22	0.20	1.26E+00	1.58E+00	3.16E+00	5.01E-01	0.38	0.40	0.40	0.32	0.60	0.54	0.86	0.44
Sb7j-w2	141				0.22				7.94E+00				0.60				0.10			
Sb7j-w4	82	82	82	82	0.20	0.21	0.21	0.21	7.94E+00	7.94E+00	7.94E+00	7.94E+00	0.60	0.58	0.58	0.58	0.10	0.10	0.10	0.10
Sb7j-w5	63				0.18				5.01E+00				0.54				0.08			
Sb7j-w7	21				0.09				1.00E+01				0.60				0.08			
Sb8j-w2	136				0.04				2.00E-01				0.34				0.44			
Sb8j-w4	108	108	108	108	0.09	0.12	0.15	0.04	7.94E-01	1.00E+00	1.00E+00	1.00E-02	0.38	0.38	0.38	0.30	0.20	0.14	1.00	0.14
Sb8j-w5	86	86	86	86	0.11	0.05	0.15	0.03	6.31E-01	1.58E-01	3.16E-01	1.00E-04	0.38	0.36	0.38	0.26	0.10	0.34	1.00	0.14
Sb8j-w8	7				0.03				1.00E+03				0.02				1.00			
S9-w2	187	187	187	185	0.07	0.07	0.14	0.07	1.26E+01	1.26E+01	7.94E+02	5.01E+00	0.22	0.22	0.90	0.20	0.64	0.64	0.84	0.04
Sb9j-w2	214				0.05				1.26E+01				0.72				0.18			
Sb9j-w4	147				0.05				1.26E+01				0.74				0.16			
Sb9j-w5	92	92	92	92	0.04	0.04	0.04	0.03	1.58E+01	1.58E+01	1.58E+01	7.94E+00	0.78	0.80	0.80	0.64	0.12	0.12	0.26	0.12
Sb9j-w6	50	50	50	50	0.03	0.03	0.05	0.03	1.26E+01	1.26E+01	2.00E+01	1.26E+01	0.76	0.76	0.86	0.68	0.14	0.14	0.16	0.06
Sb9j-w8	7				0.02				2.00E+01				0.96				0.02			
S10-w2	156	156	156	148	0.09	0.09	0.09	0.04	3.98E+02	3.98E+02	1.00E+03	5.01E+01	0.20	0.20	1.00	0.20	0.98	0.98	0.98	0.10
Sb10j-w2	228	228	228	228	0.05	0.05	0.05	0.05	7.94E+01	7.94E+01	7.94E+01	7.94E+01	0.66	0.66	0.66	0.66	0.22	0.22	0.22	0.22
Sb10j-w4	176	176	176	176	0.04	0.05	0.05	0.04	3.16E+01	7.94E+01	7.94E+01	2.51E+01	0.56	0.70	0.70	0.54	0.44	0.20	0.48	0.20
Sb10j-w5	81	81	81	81	0.03	0.03	0.03	0.03	6.31E+01	6.31E+01	6.31E+01	5.01E+01	0.58	0.62	0.62	0.52	0.28	0.26	0.34	0.26
Sb10j-w6	54	55	55	55	0.03	0.02	0.03	0.02	1.00E+02	2.00E+01	1.26E+02	7.94E+00	0.80	0.48	0.78	0.40	0.12	0.56	0.90	0.12
S11-w2	242	242	242	240	0.10	0.10	0.15	0.10	3.98E+00	3.98E+00	7.94E+01	5.01E-01	0.30	0.30	0.56	0.24	0.58	0.58	0.88	0.10
S11-w4	145	145	149	145	0.10	0.10	0.13	0.06	3.98E+01	3.98E+01	5.01E+01	1.00E-01	0.54	0.54	0.56	0.14	0.12	0.12	0.96	0.10
S11-w5	95	95	99	95	0.07	0.07	0.13	0.05	1.58E+00	1.58E+00	7.94E+02	3.98E-01	0.28	0.28	0.96	0.18	0.44	0.44	0.88	0.06
S11-w6	55	55	56	55	0.08	0.08	0.15	0.06	7.94E+01	7.94E+01	1.00E+03	1.58E+01	0.94	0.94	1.00	0.14	0.04	0.04	0.70	0.02
Sb17j-w2	201				0.13				1.58E+01				0.66				0.06			
Sb17j-w4	133	133	133	133	0.10	0.08	0.08	0.05	1.26E+01	1.00E+01	1.00E+01	6.31E+00	0.70	0.60	0.60	0.58	0.06	0.10	0.20	0.10
Sb17j-w5	87				0.04				6.31E+00				0.58				0.18			
Sb17j-w7	21	21	21	21	0.08	0.03	0.07	0.01	1.26E+01	1.00E+01	1.58E+01	3.98E+00	0.66	0.64	0.94	0.60	0.02	0.06	0.28	0.02
LA12-w6	16	16	16	16	0.02	0.02	0.15	0.01	1.00E+00	1.00E+00	1.26E+00	1.00E-04	1.00	1.00	1.00	0.24	0.12	0.12	1.00	0.02
LZ13-w2	106	106	106	106	0.23	0.23	0.25	0.11	3.98E-04	3.98E-04	7.94E-01	1.58E-04	0.26	0.26	0.30	0.24	0.94	0.94	1.00	0.18
LZ14-w2	127	127	127	127	0.25	0.24	0.25	0.10	1.26E-04	2.00E-04	1.00E-01	1.00E-04	0.20	0.20	0.30	0.18	0.70	0.68	1.00	0.22
LZ15-w2	238				0.45				7.94E-02				0.40				0.52			
LZ15j-w2	233				0.45				2.00E-02				0.28				1.00			
LZ15j-w4	176				0.45				7.94E-02				0.32				0.66			
LZ15j-w5	109				0.35				1.00E-01				0.34				0.62			
LZ15j-w6	48				0.24				1.00E-02				0.30				0.94			
LZ15j-w9	3				0.05				6.31E-03				0.28				0.42			
LZ16-w2	162	162	162	162	0.44	0.45	0.45	0.45	1.00E-02	2.00E-02	2.00E-02	2.00E-02	0.38	0.42	0.42	0.42	0.60	0.46	0.46	0.46

Samples	**Root-mean-square error** (CC model, best fitting)	**Root-mean-square error on the amplitude** (CC model, best fitting)	**Root-mean-square error on the phase** (CC model, best fitting)	**Root-mean-square error** (CC model, Pareto set)	**Root-mean-square error on the amplitude** (CC model, Pareto set)	**Root-mean-square error on the phase** (CC model, Pareto set)	**Root-mean-square error** (GCC model, best fitting)	**Root-mean-square error on the amplitude** (GCC model, best fitting)	**Root-mean-square error on the phase** (GCC model, best fitting)	**Root-mean-square error** (GCC model, Pareto set)	**Root-mean-square error on the amplitude** (GCC model, Pareto set)	**Root-mean-square error on the phase** (GCC model, Pareto set)	**Root-mean-square error** (DD model)	**Root-mean-square error on the amplitude** (DD model)	**Root-mean-square error on the phase** (DD model)
ID	**RMSE [-]**	**RMSEam [-]**	**RMSEph [-]**	**RMSE [-]**	**RMSEam [-]**	**RMSEph [-]**	**RMSE [-]**	**RMSEam [-]**	**RMSEph [-]**	**RMSE [-]**	**RMSEam [-]**	**RMSEph [-]**	**RMSE [-]**	**RMSEam [-]**	**RMSEph [-]**
O1-w2	0.31	0.07	0.28	0.31	0.07	0.28	0.13	0.09	0.08	0.13	0.09	0.08	1.35	0.45	1.11
O1-w4	0.36	0.03	0.33	0.36	0.03	0.33	0.36	0.12	0.31	0.36	0.03	0.33	0.35	0.19	0.27
O1-w5	0.21	0.06	0.18	0.21	0.06	0.18	0.19	0.07	0.16	0.19	0.07	0.16	0.61	0.30	0.49
O1-w6	0.08	0.05	0.05	0.08	0.05	0.05	0.07	0.06	0.03	0.07	0.06	0.03	0.41	0.32	0.25
O2-w2	0.38	0.07	0.34	0.38	0.07	0.34	0.14	0.08	0.10	0.14	0.08	0.10	0.55	0.34	0.37
O3-w2	0.32	0.15	0.27	0.32	0.16	0.26	0.21	0.10	0.18	0.21	0.10	0.18	0.70	0.45	0.50
O4-w2	0.28	0.09	0.26	0.28	0.09	0.26	0.08	0.06	0.05	0.08	0.06	0.05	0.79	0.33	0.67
O4-w4	0.15	0.08	0.12	0.15	0.08	0.12	0.09	0.08	0.04	0.09	0.08	0.04	0.35	0.26	0.23
O4-w5	0.14	0.05	0.13	0.14	0.05	0.13	0.07	0.05	0.04	0.07	0.05	0.04	0.42	0.29	0.28
O4-w6	0.05	0.03	0.04	0.05	0.03	0.04	0.04	0.03	0.02	0.04	0.03	0.02	0.35	0.11	0.32
O5-w2	0.64	0.35	0.42	0.64	0.35	0.42	0.43	0.16	0.32	0.43	0.16	0.32	1.26	0.75	0.83
O6j-w2	4.39	0.54	2.26				4.14	0.77	1.96				85.10	0.02	0.56
O6j-w5	2.11	0.19	1.02				1.86	0.12	1.01	2.01	0.15	0.96	0.36	0.01	0.13
O6j-w7	1.81	1.23	0.95				1.77	1.24	1.04				675.02	0.02	1.18
O6j-w9	5.16	5.13	0.56				5.15	5.11	0.58				0.42	0.02	0.37
Ob18j-w2	4.08	0.23	1.84				1.35	0.36	0.61	1.35	0.36	0.61	2.44	0.03	0.28
Ob18j-w4	1.25	0.19	0.60	1.25	0.19	0.60	0.63	0.30	0.25	0.66	0.22	0.31	1.27	0.03	0.24
Ob18j-w5	0.91	0.57	0.61	0.91	0.28	0.57	0.42	0.18	0.22	0.42	0.18	0.22	8.02	0.02	1.23
Ob18j-w6	0.81	0.04	0.58	0.83	0.06	0.57	0.41	0.38	0.09	0.42	0.34	0.08	2.87	0.01	0.10
Ob18j-w8	0.45	0.41	0.17	0.45	0.41	0.17	0.39	0.32	0.21	0.39	0.32	0.21	0.46	0.02	0.40
Ob19j-w2	11.27	3.15	4.14				5.28	0.43	1.13				3.97	0.03	0.30
Ob19j-w4	15.88	0.74	8.21				7.86	1.22	3.64				9.09	0.03	0.72
Ob19j-w5	2.42	0.27	1.66				1.28	0.43	0.79	1.40	0.40	0.44	4.79	0.01	0.27
Ob19j-w7	1.98	1.26	1.32				1.49	1.39	0.57				1.32	0.02	0.83
S7-w2	0.71	0.09	0.58	0.71	0.09	0.58	0.37	0.12	0.32	0.37	0.12	0.32	0.54	0.35	0.35
S7-w4	0.72	0.07	0.60	0.72	0.07	0.60	0.40	0.20	0.27	0.40	0.20	0.27	1.02	0.47	0.75
S7-w5	0.60	0.16	0.50	0.60	0.16	0.50	0.42	0.20	0.31	0.44	0.09	0.36	0.76	0.35	0.57
S7-w6	0.88	0.14	0.77	0.88	0.14	0.77	0.64	0.28	0.52	0.64	0.28	0.52	1.93	0.92	1.51
Sb7-w4	1.02	0.55	0.74	1.04	0.30	0.73	0.50	0.42	0.27	0.51	0.41	0.24	5.01	2.51	3.41
Sb7j-w2	12.43	0.17	5.28				7.16	3.29	5.95				3.01	0.02	0.45
Sb7j-w4	12.35	1.56	5.40				4.66	0.91	1.34	9.69	0.84	0.84	3.61	0.01	0.31
Sb7j-w5	5.37	1.65	2.87				2.65	0.20	1.30				16.46	0.01	0.28
Sb7j-w7	2.71	1.84	1.70				2.12	1.97	0.99				59.92	0.02	0.51
Sb8j-w2	1.54	1.50	0.45				1.54	1.52	0.43				0.96	0.02	0.18
Sb8j-w4	1.10	0.64	0.73	1.10	0.64	0.73	0.82	0.71	0.42	0.88	0.70	0.27	5.56	0.02	0.51
Sb8j-w5	0.99	0.84	0.54	1.08	0.80	0.53	0.88	0.86	0.19	0.89	0.85	0.18	1.63	0.01	0.52
Sb8j-w8	1.19	0.36	1.10				1.19	0.36	1.10				0.64	0.04	0.60
S9-w2	0.16	0.11	0.12	0.16	0.11	0.12	0.08	0.05	0.06	0.08	0.05	0.06	1.18	0.57	0.97
Sb9j-w2	7.43	1.02	4.97				1.87	1.51	1.13				5.04	0.02	0.21
Sb9j-w4	5.07	0.95	2.65				1.65	1.09	0.59				2.41	0.03	0.38
Sb9j-w5	3.32	0.87	2.14				1.25	0.98	0.78	1.38	0.97	0.45	1.81	0.02	0.47
Sb9j-w6	2.26	0.50	1.80				0.68	0.34	0.46	0.68	0.34	0.46	0.45	0.01	0.29
Sb9j-w8	3.24	3.21	0.44				3.19	3.19	0.21				0.76	0.75	0.10
S10-w2	0.15	0.13	0.06	0.15	0.13	0.06	0.14	0.13	0.04	0.14	0.13	0.04	1.23	1.20	0.26
Sb10j-w2	4.57	1.57	2.46				2.47	0.27	0.99	2.47	0.27	0.99	1.63	0.03	0.19
Sb10j-w4	4.07	0.67	1.99				2.05	0.43	1.00	2.12	0.53	0.76	3.29	0.02	0.22
Sb10j-w5	3.18	0.33	2.13				1.06	0.72	0.66	1.26	0.74	0.43	0.17	0.01	0.08
Sb10j-w6	1.49	0.70	1.00	1.49	0.70	1.00	1.14	0.90	0.68	1.20	0.79	0.63	2.05	0.03	1.43
S11-w2	0.32	0.09	0.28	0.32	0.09	0.28	0.16	0.08	0.13	0.16	0.08	0.13	1.00	0.42	0.84
S11-w4	0.22	0.14	0.15	0.22	0.14	0.15	0.15	0.10	0.10	0.15	0.10	0.10	0.56	0.44	0.31
S11-w5	0.09	0.05	0.07	0.09	0.05	0.07	0.06	0.05	0.03	0.06	0.05	0.03	0.24	0.21	0.11
S11-w6	0.18	0.07	0.16	0.18	0.07	0.16	0.14	0.06	0.12	0.14	0.06	0.12	0.44	0.25	0.35
Sb17j-w2	4.38	1.01	3.30				1.96	1.29	1.04				37.96	0.02	0.22
Sb17j-w4	2.60	0.89	1.92				1.50	1.06	0.96	1.67	0.98	0.84	20.92	0.03	0.91
Sb17j-w5	2.12	1.33	1.35				1.49	1.36	0.47				1.45	0.01	0.11
Sb17j-w7	0.89	0.58	0.64	0.89	0.58	0.64	0.56	0.54	0.16	0.56	0.54	0.13	0.96	0.02	0.83
LA12-w6	0.28	0.11	0.25	0.28	0.11	0.25	0.25	0.17	0.17	0.25	0.17	0.17	2.70	0.42	2.71
LZ13-w2	0.28	0.25	0.11	0.28	0.25	0.11	0.27	0.23	0.12	0.27	0.23	0.12	2.32	0.85	1.71
LZ14-w2	0.50	0.28	0.39	0.50	0.28	0.39	0.49	0.33	0.34	0.49	0.30	0.37	0.74	0.25	0.57
LZ15-w2	33.78	4.23	7.71				25.38	8.30	11.21				216.29	0.72	1.40
LZ15j-w2	3.72	0.87	33.21				3.72	0.87	33.21				0.37	0.03	1.04
LZ15j-w4	6.11	1.11	21.12				4.58	1.33	24.43				0.30	0.02	0.71
LZ15j-w5	6.47	0.29	16.69				5.19	0.10	16.86				0.13	0.02	0.28
LZ15j-w6	5.97	0.83	8.32				4.73	0.87	6.11				8.02	0.01	0.53
LZ15j-w9	3.04	2.80	1.24				2.93	2.90	0.69				0.43	0.06	0.25
LZ16-w2	5.40	0.86	1.77				2.91	0.12	1.10	6.01	0.44	0.96	5.90	0.60	1.62

Appendix D

Frequency series for SIP measurements with system ZEL-SIP04-V02 and corresponding selected frequencies from the spectra acquired with system ST.sip13.

#	**f [Hz]** ZEL-SIP04-V02	**f [Hz]** ST.sip13
1	0.0010	-
2	0.0025	-
3	0.0063	-
4	0.0126	0.0126
5	0.0200	0.0200
6	0.0316	0.0316
7	0.0501	0.0501
8	0.0794	0.0794
9	0.1259	0.1259
10	0.1995	0.1995
11	0.3162	0.3162
12	0.5012	0.5012
13	0.7943	0.7943
14	1.0000	1.0003
15	1.2589	1.2592
16	1.5849	1.5853
17	1.9953	1.9957
18	2.5119	2.5124
19	3.1623	3.1629
20	3.9811	3.9818
21	5.0119	5.0128
22	6.3096	6.3106
23	7.9433	7.9446
24	10.0000	10.0015
25	12.5893	12.5910
26	15.8489	15.8510
27	19.9526	19.9550
28	25.1189	25.1216
29	31.6228	31.6259
30	39.8107	39.8143
31	50.1187	50.1227
32	63.0957	63.1001
33	79.4328	79.4376
34	100.0000	100.0049
35	125.8925	125.8975
36	158.4893	158.4940
37	199.5262	199.5301
38	251.1886	251.1909
39	316.2278	316.3076
40	398.1072	398.2036
41	501.1872	501.3036
42	630.9573	631.0974
43	794.3282	794.4966
44	1.0000e3	1.0002e3
45	1.2589e3	1.2592e3
46	1.5849e3	1.5852e3
47	1.9953e3	1.9956e3
48	2.5119e3	2.5123e3
49	3.1623e3	3.1628e3
50	3.9811e3	3.9816e3
51	5.0119e3	5.0125e3
52	6.3096e3	6.3103e3
53	7.9433e3	7.9442e3
54	1.0000e4	1.0001e4
55	1.2589e4	-
56	1.5849e4	-
57	1.9953e4	-
58	2.5119e4	-
59	3.1623e4	-
60	3.9811e4	-
61	4.5000e4	-

Appendix E

MATLAB® codes for processing and inversion of SIP data acquired with ST.sip13 system.

1) DATA PROCESSING

```
function [f_ax,rho] = SIP_proc (L,folder,file_i,Temp);
%SIP_proc processes measured voltage-time series data in order to obtain a vector
%of complex resistivity as a function of frequency. Input files are three txt
%files named with progressive numbers. They correspond to the acquisitions with
%the three chirp input signals, ordered from high frequency to low frequency.
%
%Input variables:
%   L=distance between potential electrodes [m]
%   'folder'=name of the folder that contains txt files
%   file_i=name of the first file (numerical)
%   Temp=sample temperature [°C]
%Output variables:
%   f_ax=frequency axis vector
%   rho=complex resistivity vector

%% acquisition parameters
n=2000001;                  %number of samples in an acquisition
ni=2097152;                 %number of samples as a power-2 number
fmin=[100 1 0.01];          %minimum frequency for chirp signals [Hz]
fmax=[100000 100 1];        %maximum frequency for chirp signals [Hz]
T=[5 50 500];               %chirp duration [s]
dt=[2.5e-6 2.5e-5 2.5e-4];  %sampling rate [s]
S=0.00580880;               %cross sectional area of the sample [m2]
Rs=1000;                    %shunt resistor [Ω]

%% electrical impedance calculation
file_i=file_i-1;
tax=zeros(n,3);
tax_i=zeros(ni,3);
fax_i=zeros(ni,3);
df=zeros(1,3);
Zx=zeros(ni,3);
for k=1:3
    tax(:,k)=0:dt(k):(n-1)*dt(k);                      %time axis
    tax_i(:,k)=linspace(tax(1,k),tax(end,k),ni);       %interpolated time axis
    fax_i(:,k)=0:1/T(k):(ni-1)*1/T(k);                 %interp. frequency axis
    df(k)=fax_i(2,k)-fax_i(1,k);                       %frequency step [Hz]

    Zv=(5e11./(1+(1i*2*pi*fax_i(:,k)*5e11*20e-12))); %amplifier impedance

    %txt file reading (voltage at electrodes M, N, and B)
    [~,M,N,B]=textread(sprintf('%d.bin.txt',k+file_i),'%f %f %f %f',-
     1,'commentstyle', 'c');

    %truncation at 4th decimal position to account for voltage resolution
    M=(round(M*10.^(4)))/10.^(4);
    N=(round(N*10.^(4)))/10.^(4);
    B=(round(B*10.^(4)))/10.^(4);

    %interpolation on ni points to fasten Fourier transform calculation
    Mi=(interp1(tax(:,k),M,tax_i(:,k)));
    Ni=(interp1(tax(:,k),N,tax_i(:,k)));
    Bi=(interp1(tax(:,k),B,tax_i(:,k)));

    %Fourier transform calculation, after trend removal
    U2i=fft(Mi-mean(Mi));
```

```
    U3i=fft(Ni-mean(Ni));
    U4i=fft(Bi-mean(Bi));

    Uxi=U2i-U3i;                              %voltage difference [V]
    Ixi=U4i.*(1/Rs+1./Zv)+U3i./Zv;            %corrected current [A]
    Zx(:,k)=Uxi./Ixi*(1+0.025*(Temp-20));     %electrical impedance, after
                                              temperature correction [Ω]
end

%% filtering anomalous values,
%based on graphical observations of phase difference
Z_un=[];
for k=1:3
    Zsp=Zx(round(fmin(k)/df(k))+1:round(fmax(k)/df(k))+1,k);
    ang=angle(Zsp);
    obj=zeros(size(Zsp));
    for l=1:length(Zsp)-1
        obj(l)=ang(l)-ang(l+1);  %phase difference between adjacent points
    end
    obj2=obj-mean(obj);                     %trend removal
    figure;subplot(3,1,k);plot(obj2,'b-')   %graphical representation
    in=input('Insert threshold value to cut anomalous data points: ');
    x=find(obj2>=in);
    y=find(obj2<=-in);
    if length(x)>=1 && x(1)==1
        x=x(2:end);
    elseif length(y)>=1 && y(1)==1
        y=y(2:end);
    end

    %removal of anomalous points
    for l=1:length(Zsp)
        if ismember(l,x)==1
           Zsp(l)=NaN+1i*NaN;
        elseif ismember(l,y)==1
           Zsp(l)=NaN+1i*NaN;
        end
    end

    %substitution of anomalous points with mean values of adjacent points
    for l=2:length(Zsp)+1
        if isnan(Zsp(l-1))==1
           Zsp(l-1)=nanmean([(Zsp(find((isnan(Zsp(1:l-1))==0),1,'last'))),
                 ...(Zsp(find((isnan(Zsp(l-1:end))==0),1,'first')+l-2))]);
        end
    end

    Z_un=[Zsp;Z_un(2:end)];
end

%% complex resistivity calculation
%construction of a single frequency vector from the three series
fax_tot=[fax_i(round(fmin(3)/df(3))+1:round(fmax(3)/df(3))+1,3);
           ...fax_i(round(fmin(2)/df(2))+2:round(fmax(2)/df(2))+1,2);
           ...fax_i(round(fmin(1)/df(1))+2:round(fmax(1)/df(1))+1,1)];

% interpolation on a new common sampling interval
f_ax=logspace(log10(fax_tot(2)),5,(ni+2*(ni-1))/100);
Z_tot_i=(interp1(fax_tot,Z_un,f_ax));

%smoothing and complex resistivity calculation
b=ones(1,500)/500;
Z_tot_flt=filtfilt(b,1,(Z_tot_i));
rho=Z_tot_flt.*S/L;

%graphical representation
figure;
subplot(2,1,1);semilogx(f_ax,abs(rho),'r')
```

```
ylabel('|\rho| [\Omegam]')
xlabel('frequency [Hz]')
subplot(2,1,2);semilogx(f_ax,angle(rho),'r')
ylabel('\phi [rad]')
xlabel('frequency [Hz]')

%% data saving with the name of the sample in a specified directory
cd '...'

%if data refer to the first test of the sample, a new matrix is created with
frequency in the first column and complex resistivity in the second
if exist(sprintf('%s.mat',folder),'file')==0
    rho_cpx=[f_ax',conj(rho)'];
    newName=sprintf('%s',folder);
    S.(newName)=rho_cpx;
    save(sprintf('%s.mat',folder),'-struct', 'S');
%otherwise only complex resistivity is added as the last column in the matrix
else
    rho_cpx=load(sprintf('%s.mat',folder),sprintf('%s',folder));
    rho_cpx=rho_cpx.(sprintf('%s',folder));
    [~,columns]=size(rho_cpx);
    rho_cpx(:,columns+1)=rho;
    newName=sprintf('%s',folder);
    S.(newName)=rho_cpx;
    save(sprintf('%s.mat',folder),'-struct', 'S');
end

end    %function end
```

2) DATA INVERSION

```
function [results] = DDCC_inv (dati,samp);
%DDCC_inv models complex resistivity data by different methods: Debye
%decomposition (in a continuous and in a discontinuous domain) and Cole-type
%electrical analogue circuits (Cole-Cole and Generalized Cole-Cole)in the lowest
%frequency range that shows the presence of an arc.
%
%Input variables:
%   dati=matrix with frequency-resistivity data (column 1 frequency [Hz],
%        column 2+ resistivity [Ohm*m])
%   'samp'=reference sample name in the excel file
%Output variables:
%   results=vector containing the list of model parameters (best fitting and
            Pareto set statistics) for each adopted model

%% 1.initial data analysis on the equilibrium resistivity series
close all
clear all

figure;
subplot(2,1,1);semilogx(dati(:,1),angle(dati(:,end)));
subplot(2,1,2);semilogx(dati(:,1),angle(dati(:,end)));
%graphical determination of the lowest frequency free from anomalies
df=input('Insert starting correct frequency: ');
st=find(dati(:,1)>=df,1);
datig=[dati(st:end,1),dati(st:end,end)];

%selected points extraction from the spectral data
load('freqfile.mat')                                  %(see Appendix E)
index=zeros(size(tabfreqJ_v4));
    for k=1:length(tabfreqJ_v4)
        index(k)=find(datig(:,1)>=tabfreqJ_v4(k),1);
    end
index=unique(index);
datig=[datig(index,1),datig(index,end)];
```

```
%smoothing
b=ones(1,5)/5;
datig(:,2)=filtfilt(b,1,datig(:,2));

% substitution of low frequency lacking points with nearest available values
flack=length(tabfreqJ_v4)-length(index);
datit=[tabfreqJ_v4(1:flack),ones(flack,1).*datig(1,2);datig];

phase=angle(datig(:,2));
ampl=abs(datig(:,2));
Re=real(datig(:,2));
Im=imag(datig(:,2));

%characteristic spectra values at fixed frequencies
ff=[0.01,0.1,1,10,100,1000,10000];
punto=zeros(1,5);
    for k=1:5
    punto(k)=find(datig(:,1)>=ff(k),1);
    end

sigma=10000./datig(punto,2);     %electrical conductivity [µS/cm]
wr0=[real(sigma)',imag(sigma)'];

%data error determination
rhoa=max(abs(datig(:,2)));                    %rho_DC grafically estimated
e_a=0.01*rhoa;                                %amplitude data-error
e_p=0.001;                                    %phase data error
eps_r=cos(fase).*e_a-ampl.*sin(fase).*e_p;    %data error on real part
eps_i=sin(fase).*e_a+ampl.*cos(fase).*e_p;    %data error on imaginary part

%% 2.Debye Decomposition model (DD) - nnlsq method and tikhonov method
% eventual frequency weight on real and imaginary part
FFre=ones(size(tabfreqJ_v4));
FFim=ones(size(tabfreqJ_v4));

%normalization
rho_norm=(rhoa-datit(:,2))/rhoa;
re=FFre.*real(rho_norm);
im=FFim.*imag(rho_norm);

%construction of the two systems of linear equations C
ntau=1000;                                 %number of predetermined tau values
t_min_f=1./(2.*pi.*max(tabfreqJ_v4));
t_max_f=1./(2.*pi.*min(tabfreqJ_v4));
tmin1=-6;
tmax1=4;
tau=logspace(tmin1,tmax1,ntau);         %predetermined τ values
omega=2*pi.*datit(:,1);                 %angular frequency vector

C1=zeros(length(tabfreqJ_v4),length(tau));
C2=zeros(length(tabfreqJ_v4),length(tau));

    for n=1:length(tabfreqJ_v4)
        for k=1:length(tau)
            C1(n,k)=FFre(n)*(omega(n)*tau(k))^2/(1+(omega(n)*tau(k))^2);
            C2(n,k)=FFim(n)*(omega(n)*tau(k))/(1+(omega(n)*tau(k))^2);
        end
    end

% solution algorithm
[x1,~,~,exitflag1]=lsqnonneg(C1,re);
[x2,~,~,exitflag2]=lsqnonneg(C2,im);

% estimation of correct direct current resistivity and re-normalization
rho0=rhoa*(1+sum(x2)-sum(x1));

rho_norm=(rho0-datit(:,2))/rho0;
re=real(rho_norm);
```

```
im=imag(rho_norm);

% determination of the real/imaginary weighting factor
h=0.6;
IF=h*(sum(re))/(sum(im));
d=[FFre.*re(:,1);IF*FFim.*im(:,1)];

%solution of the inverse problem (only Tikhonov method is reported)
N=100;                    %number of relaxation times
wf=[ones(1,length(datit(:,1)));IF*ones(1,length(datit(:,1)))];

    if flack>0
    wf(:,1:flack)=0;      %for the lacking frequencies the weight is zero
    end

rp=[0.1:0.1:0.9,1:15];
    for k=1:length(rp)
      algo_options=[1,3,1000,1,rp(k)];
      [tau_SF,x_SF,~,exitflag]=decomp_NNtikh2(10.^tmin1,10.^tmax1,N,
                             datit(:,1),datit(:,2),rho0,wf,algo_options);
       if exitflag==0
           warning('Decomposition failed')
       end

      m_t_SF=sum(x_SF(tau_SF>=t_min_f & tau_SF<=t_max_f));        %tot. chargeab.

      %modelled data
      sommatoria_SF=0;
      for l=1:length(tau_SF)
             sommatoria_SF=sommatoria_SF+x_SF(l)*(1-(1./(1+1i*omega*tau_SF(l))));
      end
      ft_SF=rho0*(1-sommatoria_SF);

      %model error estimation
      RMSEamp_SF=sqrt(1/length(index(flack+1:end)))*
                norm((ampl-abs(ft_SF(flack+1:end)))./e_a);
      RMSEpha_SF=sqrt(1/length(index(flack+1:end)))*
                norm((phase-angle(ft_SF(flack+1:end)))./e_p);
      RMSEtot_SF=sqrt(sum(((Re-real(ft_SF(flack+1:end)))./eps_r).^2+
                ((Im-imag(ft_SF(flack+1:end)))./eps_i).^2)
                /length(index(flack+1:end)));

      %relaxation time distribution function
      g_DD_SF=x_SF(tau_SF>=t_min_f & tau_SF<=t_max_f)./m_t_SF;
      g_DD_SF=g_DD_SF./sum(g_DD_SF);

      goonornot=questdlg('Do you want to increase the regularization
                        parameter lambda?','Yes','No');
      switch goonornot
             case 'No'
             break
      end

    end

%estimation of the integrating parameters
m_n_SF=m_t_SF/rho0;                             %normalized chargeability
tau_freqrange=tau_SF((tau_SF>=t_min_f & tau_SF<=t_max_f));
tau_m_SF=exp(sum(x_SF(tau_SF>=t_min_f &
         tau_SF<=t_max_f).*log(tau_freqrange'))/m_t_SF); %mean relaxation time
tau10_SF=tau_freqrange(find(cumsum(x_SF(tau_SF>=t_min_f &
         tau_SF<=t_max_f))>=0.1*m_t_SF,1));
tau20_SF=tau_freqrange(find(cumsum(x_SF(tau_SF>=t_min_f &
         tau_SF<=t_max_f))>=0.2*m_t_SF,1));
tau30_SF=tau_freqrange(find(cumsum(x_SF(tau_SF>=t_min_f &
         tau_SF<=t_max_f))>=0.3*m_t_SF,1));
tau40_SF=tau_freqrange(find(cumsum(x_SF(tau_SF>=t_min_f &
         tau_SF<=t_max_f))>=0.4*m_t_SF,1));
```

```
tau50_SF=tau_freqrange(find(cumsum(x_SF(tau_SF>=t_min_f &
         tau_SF<=t_max_f))>=0.5*m_t_SF,1));
tau60_SF=tau_freqrange(find(cumsum(x_SF(tau_SF>=t_min_f &
         tau_SF<=t_max_f))>=0.6*m_t_SF,1));
tau70_SF=tau_freqrange(find(cumsum(x_SF(tau_SF>=t_min_f &
         tau_SF<=t_max_f))>=0.7*m_t_SF,1));
tau80_SF=tau_freqrange(find(cumsum(x_SF(tau_SF>=t_min_f &
         tau_SF<=t_max_f))>=0.8*m_t_SF,1));
tau90_SF=tau_freqrange(find(cumsum(x_SF(tau_SF>=t_min_f &
         tau_SF<=t_max_f))>=0.9*m_t_SF,1));
U60_SF=tau60_SF/tau10_SF;                        %non-uniformity coefficients
U90_SF=tau90_SF/tau10_SF;
n_SF=nnz(x_SF(tau_SF>=t_min_f & tau_SF<=t_max_f));        %n° debye processes

%vector of model parameters
wrDD_SF=[rp(k),m_t_SF,m_n_SF,tau_m_SF,tau10_SF,tau20_SF,tau30_SF,tau40_SF,
         tau50_SF,tau60_SF,tau70_SF,tau80_SF,tau90_SF,U60_SF,U90_SF,n_SF,
         RMSEamp_SF,RMSEpha_SF,RMSEtot_SF];

%% 3. Cole-type model (Cole-Cole CC, Generalized Cole-Cole GCC)
%identification portion with negative curvature on Argand plot
arco_start=input('Insert number of point corresponding to arc start
                    (9999 if no arc exists):');
arco_end=input('Insert number of point corresponding to arc end:');

startfreq=datig(arco_start,1);
stopfreq=datig(arco_end,1);

%if no arc is recognized this elaboration step is skipped
if arco_start~=9999

%data reduction to the first arc
datig=datig(arco_start:arco_end,:);

R=arco_end-arco_start+1;

phase=phase(arco_start:arco_end);
ampl=ampl(arco_start:arco_end);
Re=Re(arco_start:arco_end);
Im=Im(arco_start:arco_end);

eps_r=eps_r(arco_start:arco_end);
eps_i=eps_i(arco_start:arco_end);

% determination of input parameters range
    if rho0>rhoa+0.02*rhoa
    rho_vett=floor(rhoa+0.02*rhoa):ceil(rho0);
    else
    rho_vett=floor(rho0):ceil(rhoa+0.02*rhoa);
    end

    while length(rho_vett)>5
          rho_vett=rho_vett(1:2:end);
    end

m_vett=linspace(0,ceil(m_t*10)/10+0.05,ceil(m_t*10)*10+6);
c_vett=linspace(0,1,51);
k_vett=linspace(0,1,51);

tmin=-4;
tmax=3;
n=10*(floor(abs(tmin))+ceil(abs(tmax)));
tau_vett=logspace(tmin,tmax,n+1);

%data modelling with grid search method
Nax=1:(length(rho_vett)*length(m_vett)*length(tau_vett)*length(c_vett));
                                                            %iterations axis
NaxGCC=1:(length(rho_vett)*length(m_vett)*length(tau_vett)*length(c_vett)*
```

```
        length(k_vett));
iter=0;
iterGCC=0;

ma=zeros(length(Nax),4);       % sequence of parameters association tested
maGCC=zeros(length(NaxGCC),5);
Ea_CC=zeros(length(Nax),1);
Ea_GCC=zeros(length(NaxGCC),1);
Ea_amp_CC=zeros(length(Nax),1);
Ea_ang_CC=zeros(length(Nax),1);
Ea_amp_GCC=zeros(length(NaxGCC),1);
Ea_ang_GCC=zeros(length(NaxGCC),1);

    for k=1:length(rho_vett)
        for t=1:length(m_vett)
            for w=1:length(tau_vett)
                for r=1:length(c_vett)

                    iter=iter+1; %CC and CD
                    ma(iter,:)=[rho_vett(k),m_vett(t),tau_vett(w),c_vett(r)];

                    da_CC=rho_vett(k)*(1-m_vett(t)*
                       (1-1./((1+(1i*2*pi*datig(:,1).*tau_vett(w)).^c_vett(r)))));
                    Ea_CC(iter)=sqrt(sum(((Re-real(da_CC))./eps_r).^2+
                        ((Im-imag(da_CC))./eps_i).^2)/R);
                    Ea_amp_CC(iter)=sqrt(1/R)*norm((ampl-abs(da_CC))./e_a);
                    Ea_ang_CC(iter)=sqrt(1/R)*norm((phase-angle(da_CC))./e_p);

                    for q=1:length(k_vett)

                        iterGCC=iterGCC+1;    %GCC
                        maGCC(iterGCC,:)=[rho_vett(k),m_vett(t),tau_vett(w),
                                          c_vett(r),k_vett(q)];

                        da_GCC=rho_vett(k)*(1-m_vett(t)*
                               (1-1./((1+(1i*2*pi*datig(:,1).*tau_vett(w))
                               .^c_vett(r)).^k_vett(q))));
                        Ea_GCC(iterGCC)=sqrt(sum(((Re-real(da_GCC))./eps_r).^2+
                               ((Im-imag(da_GCC))./eps_i).^2)/R);
                        Ea_amp_GCC(iterGCC)=sqrt(1/R)*
                               norm((ampl-abs(da_GCC))./e_a);
                        Ea_ang_GCC(iterGCC)=sqrt(1/R)*
                               norm((phase-angle(da_GCC))./e_p);

                    end
                end
            end
        end
    end

[ii,~]=find(Ea_CC==(min(Ea_CC)),1);
mg_CC=ma(ii,:);
Eg_CC=Ea_CC(ii);
Ea_amp_bf_CC=Ea_amp_CC(ii);
Ea_ang_bf_CC=Ea_ang_CC(ii);
dmod_CC=mg_CC(1,1)*(1-mg_CC(1,2)*(1-
1./((1+(1i*2*pi*datig(:,1).*mg_CC(1,3)).^mg_CC(1,4)))));

[ii,~]=find(Ea_GCC==(min(Ea_GCC(:))),1);
mg_GCC=maGCC(ii,:);
Eg_GCC=Ea_GCC(ii);
Ea_amp_bf_GCC=Ea_amp_GCC(ii);
Ea_ang_bf_GCC=Ea_ang_GCC(ii);
dmod_GCC=mg_GCC(1,1)*(1-mg_GCC(1,2)*(1-1./((1+(1i*2*pi*datig(:,1).*mg_GCC(1,3))
          .^mg_GCC(1,4)).^mg_GCC(1,5))));

wr1_CC=[mg_CC,Eg_CC,Ea_amp_bf_CC,Ea_ang_bf_CC];
wr1_GCC=[mg_GCC,Eg_GCC,Ea_amp_bf_GCC,Ea_ang_bf_GCC];
```

```
ttt=logspace(log10(t_min_f),log10(t_max_f),100);

%Pareto set analysis (only the GCC case is reported)
a=find(Ea_ang_GCC<=min(Ea_ang_GCC(Ea_amp_GCC==min(Ea_amp_GCC))));
b=find(Ea_amp_GCC<=min(Ea_amp_GCC(Ea_ang_GCC==min(Ea_ang_GCC))));
b2=find(Ea_amp_GCC<=1);
b3=find(Ea_ang_GCC<=1);

c=intersect(a,b);
c=intersect(c,b2);
c=intersect(c,b3);

if isempty(c)==0   %Pareto analysis is done only if Pareto set is not empty

    for s=1:size(c)
        ang=find(Ea_ang_GCC(c(s))>Ea_ang_GCC(c));
        amp=find(Ea_amp_GCC(c(s))>Ea_amp_GCC(c));
        if isempty(intersect(ang,amp))==1;
           prt(s)=c(s);
        end
    end

    pf=prt(prt~=0);

    coord=[Ea_amp_GCC(pf),Ea_ang_GCC(pf)];
    dist=sqrt(sum(coord.^2, 2));      %distance from origin of each Pareto solution
    cp=find(dist==min(dist));           %corner point in the Pareto set

    %solution of the corner point of the Pareto set
    dmed_GCC=(maGCC(pf(cp),1))*(1-(maGCC(pf(cp),2))*(1-1./((1+(1i*2*pi*datig(:,1)
          .*(maGCC(pf(cp),3))).^(maGCC(pf(cp),4))).^(maGCC(pf(cp),5)))));

    %relaxation time distribution
    teta=(pi/2)-atan(((ttt./maGCC(pf(cp),3)).^maGCC(pf(cp),4)
           +cos(pi*maGCC(pf(cp),4)))./(sin(pi*maGCC(pf(cp),4))));
    g_GCC=sin(maGCC(pf(cp),5).*teta)./(pi*((ttt./maGCC(pf(cp),3))
           .^(-2*maGCC(pf(cp),4))+2*(ttt./maGCC(pf(cp),3))
           .^-maGCC(pf(cp),4).*cos(pi*maGCC(pf(cp),4))+1).^(maGCC(pf(cp),5)/2));
    g_GCC=g_GCC./sum(g_GCC);

    %vector of model parameters (best fitting and Pareto set, with statistics)
    wr2_GCC=[maGCC(pf(cp),:),Ea_GCC(pf(cp)),Ea_amp_GCC(pf(cp)),
           Ea_ang_GCC(pf(cp)),...]

else   %if Pareto set is empty RTD is calculated with best-fitting parameters
    wr2_GCC=zeros(1,93);

    teta=(pi/2)-atan(((ttt./mg_GCC(3)).^mg_GCC(4)+cos(pi*mg_GCC(4)))
          ./(sin(pi*mg_GCC(4))));
    g_GCC=sin(mg_GCC(5).*teta)./(pi*((ttt./mg_GCC(3)).^(-2*mg_GCC(4))+
          2*(ttt./mg_GCC(3)).^-mg_GCC(4).*cos(pi*mg_GCC(4))+1).^(mg_GCC(5)/2));
    g_GCC=g_CC./sum(g_GCC);

end

%vector of the results
result=[wr0,wrDD_SF,startfreq,stopfreq,wr1_CC,wr1_GCC,wr2_GCC,...]

end    %function end
```

Appendix F

MATLAB® code for multivariate statistical analysis

```
function [...] = PCA_CA (D)
%CA_PCA applies a principal component analysis and a cluster analysis on a
%input data matrix D (samples in rows and variables in columns).

[a,b]=size(D);

%% 1.Principal Components Analysis
%data standardization
Zref=(D-repmat(nanmean(D,1),a,1))./repmat(nanstd(D,0,1),a,1);

%calculation of covariance matrix for computation of principal components
Cref=cov(Zref);
[PCref,Vref]=eig(Cref);                     %eigenvectors and eigenvalues
latentref=flipud(diag(Vref));
explainedref=latentref/sum(latentref)*100;  %explained variance [%]

coefforthref=fliplr(PCref);
cpnref=Zref*coefforthref;                   %new coordinate system

lambdasref=repmat(latentref,1,b)';
rpnref=sqrt(lambdasref).*coefforthref;      %Pearson corr. coefficient

%% 2.Clustering
clust=input('Insert number of clusters: ');

Yref=pdist(Zref);                       %original distance among objects
method={'ward'}
Clref=linkage(Yref,method(k));  %distance among objects after clustering
Tref=cluster(Clref,'maxclust',clust);       %cluster assignment
cop=cophenet(Clref,Yref);                   %cophenetic coefficient

leafOrder=optimalleaforder(Clref,Yref);
tresh=Clref(end-clust+2,3)-eps;%threshold distance for a fixed n° clusters

figure;
dendrogram(Clref,0,'colorthreshold',tresh,'reorder',leafOrder);

figure;
silhouette(cpnref,Tref);

%representation of the clusters in the coordinate system of PCA
figure;
hold on;subplot(1,2,2);gscatter(cpnref(:,1),cpnref(:,2),Tref)
xlabel(sprintf('PC%g (%5.2f)',1,explainedref(1)))
ylabel(sprintf('PC%g (%5.2f)',2,explainedref(2)))
hold on;subplot(1,2,2);gscatter(cpnref(:,1),cpnref(:,3),Tref)
xlabel(sprintf('PC%g (%5.2f)',1,explainedref(1)))
ylabel(sprintf('PC%g (%5.2f)',3,explainedref(3)))

end     %function end
```

Appendix G

Typical values of electrical parameters for each cluster, according to the classifications into two, five, eight, and eleven total clusters. Values are reported in the form: 25th (50th) 75th percentiles.

	2 clusters	
parameter	**1 - blue**	**2 - red**
$\Delta\Phi_0$	0.25 (0.26) 0.30	-0.03 (0.07) 0.23
$\Delta\Phi_2$	-0.32 (-0.09) 0.04	0.09 (0.15) 0.20
$\log\tau_{10}$	-4.1 (-4.0) -3.9	-4.5 (-4.4) -4.4
$\Delta\Phi_3$	-0.22 (-0.16) -0.08	0.15 (0.21) 0.30
$\Delta\Phi_1$	-0.06 (0.15) 0.20	-0.06 (0.11) 0.23
$\log\tau_{90}$	0.03 (0.2) 0.3	-0.1 (0.3) 0.5
$\log\tau_{50}$	-2.0 (-1.9) -1.4	-2.8 (-2.5) -2.0
M_t	0.13 (0.18) 0.32	0.04 (0.05) 0.08
$\Delta\Phi_{-1}$	0.37 (0.40) 0.54	0.03 (0.26) 0.37
$\Delta\Phi_4$	0.005 (0.04) 0.09	0.23 (0.29) 0.36
$\log U_{\tau c}$	-0.3 (-0.1) 0.1	-1.0 (-0.7) -0.6
ρ_0 [Ωm]	83 (113) 184	57 (107) 154

	5 clusters				
parameter	**1 - blue**	**2 - red**	**3 - green**	**4 - cyan**	**5 - purple**
$\Delta\Phi_0$	0.12 (0.20) 0.25	0.26 (0.28) 0.34	-0.18 (-0.08) -0.03	0.05 (0.08) 0.14	0.29 (0.31) 0.35
$\Delta\Phi_2$	-0.41 (-0.39) -0.32	-0.09 (0.01) 0.05	0.02 (0.09) 0.14	0.10 (0.16) 0.19	0.18 (0.22) 0.35
$\log\tau_{10}$	-3.9 (-3.9) -3.8	-4.2 (-4.1) -4.0	-4.5 (-4.4) -4.3	-4.5 (4.4) -4.3	-4.5 (-4.5) -4.4
$\Delta\Phi_3$	-0.22 (-0.21) -0.17	-0.20 (-0.10) -0.06	0.22 (0.26) 0.30	0.12 (0.15) 0.24	0.15 (0.16) 0.31
$\Delta\Phi_1$	-0.18 (-0.11) -0.06	0.15 (0.18) 0.21	-0.15 (-0.11) -0.05	0.08 (0.12) 0.17	0.25 (0.31) 0.38
$\log\tau_{90}$	0.3 (0.4) 0.4	-0.1 (0.1) 0.2	0.5 (0.5) 0.6	0.2 (0.2) 0.4	-0.6 (-0.4) -0.3
$\log\tau_{50}$	-1.4 (-1.4) -1.2	-2.1 (-1.9) -1.9	-2.2 (-1.9) -1.8	-2.6 (-2.5) -2.2	-3.2 (-2.8) -2.8
M_t	0.13 (0.13) 0.15	0.16 (0.28) 0.36	0.04 (0.05) 0.06	0.04 (0.05) 0.07	0.02 (0.08) 0.11
$\Delta\Phi_{-1}$	0.33 (0.45) 0.57	0.38 (0.40) 0.47	-0.11 (0.00) 0.26	0.05 (0.25) 0.37	0.27 (0.41) 0.44
$\Delta\Phi_4$	0.08 (0.14) 0.19	-0.005 (0.01) 0.04	0.29 (0.34) 0.40	0.22 (0.28) 0.36	0.17 (0.21) 0.29
$\log U_{\tau c}$	0.1 (0.2) 0.2	-0.3 (-0.2) -0.1	-1.2 (-1.0) -1.0	-0.8 (-0.7) -0.6	-0.6 (-0.5) -0.4
ρ_0 [Ωm]	104 (111) 149	59 (146) 209	81 (150) 186	75 (107) 146	11 (75) 111

parameter	**8 clusters**							
	1 - blue	**2 - red**	**3 - green**	**4 - cyan**	**5 - purple**[10]	**6 - grey**	**7 - pink**	**8 - orange**
$\Delta\Phi_0$	0.02 (0.07) 0.12	0.07 (0.09) 0.15	0.29 (0.31) 0.35	0.27 (0.31) 0.34	0.41	0.12 (0.20) 0.25	0.26 (0.28) 0.34	-0.18 (-0.08) -0.03
$\Delta\Phi_2$	0.02 (0.11) 0.17	0.12 (0.18) 0.22	0.34 (0.38) 0.42	0.16 (0.19) 0.22	0.20	-0.41 (-0.39) -0.32	-0.09 (0.01) 0.05	0.02 (0.09) 0.14
$\log\tau_{10}$	-4.4 (-4.3) -4.3	-4.5 (-4.4) -4.4	-4.6 (-4.6) -4.5	-4.5 (-4.4) -4.4	-4.4	-3.9 (-3.9) -3.8	-4.2 (-4.1) -4.0	-4.5 (-4.4) -4.3
$\Delta\Phi_3$	0.05 (0.10) 0.14	0.14 (0.19) 0.30	0.31 (0.36) 0.41	0.14 (0.15) 0.16	0.01	-0.22 (-0.21) -0.17	-0.20 (-0.10) -0.06	0.22 (0.26) 0.30
$\Delta\Phi_1$	0.06 (0.10) 0.13	0.08 (0.15) 0.19	0.36 (0.39) 0.39	0.25 (0.28) 0.32	0.17	-0.18 (-0.11) -0.06	0.15 (0.18) 0.21	-0.15 (-0.11) -0.05
$\log\tau_{90}$	0.3 (0.4) 0.5	0.1 (0.2) 0.3	-1.1 (-0.9) -0.5	-0.4 (-0.3) -0.1	-0.6	0.3 (0.4) 0.4	-0.1 (0.1) 0.2	0.5 (0.5) 0.6
$\log\tau_{50}$	-2.3 (-2.2) -2.0	-2.7 (-2.6) -2.5	-3.6 (-3.5) -3.2	-2.8 (-2.8) -2.7	-2.7	-1.4 (-1.4) -1.2	-2.1 (-1.9) -1.9	-2.2 (-1.9) -1.8
M_t	0.05 (0.08) 0.12	0.04 (0.05) 0.06	0.06 (0.08) 0.10	0.02 (0.08) 0.11	0.02	0.13 (0.13) 0.15	0.16 (0.28) 0.36	0.04 (0.05) 0.06
$\Delta\Phi_{-1}$	0.01 (0.28) 0.39	0.08 (0.24) 0.36	0.40 (0.44) 0.47	0.26 (0.29) 0.42	2.28	0.33 (0.45) 0.57	0.38 (0.40) 0.47	-0.11 (0.00) 0.26
$\Delta\Phi_4$	0.20 (0.35) 0.39	0.22 (0.28) 0.32	0.28 (0.32) 0.37	0.16 (0.18) 0.23	-	0.08 (0.14) 0.19	-0.005 (0.01) 0.04	0.29 (0.34) 0.40
$\log U_{\tau c}$	-0.7 (-0.6) -0.5	-0.9 (-0.7) -0.6	-0.6 (-0.4) -0.4	-0.6 (-0.5) -0.5	-0.1	0.1 (0.2) 0.2	-0.3 (-0.2) -0.1	-1.2 (-1.0) -1.0
ρ_0 [Ωm]	122 (163) 204	26 (88) 109	67 (111) 132	8 (47) 104	16	104 (111) 149	59 (146) 209	81 (150) 186

---

[10] This cluster is composed by only one sample.

parameter	11 clusters				
	1 - blue[11]	2 - red	3 - green	4 - cyan	5 - purple
$\Delta\Phi_0$	0.13 0.16	0.05 (0.08) 0.12	-0.18 (-0.08) -0.05	-0.20 (-0.07) -0.01	0.28 (0.30) 0.34
$\Delta\Phi_2$	0.22 0.28	0.11 (0.16) 0.20	0.13 (0.13) 0.16	0.005 (0.03) 0.10	-0.16 (-0.08) 0.02
$\log\tau_{10}$	-4.6 -4.6	-4.5 (-4.4) -4.4	-4.5 (-4.4) -4.4	-4.5 (-4.4) -4.3	-4.2 (-4.1) -4.1
$\Delta\Phi_3$	0.35 0.40	0.13 (0.17) 0.30	0.22 (0.23) 0.34	0.23 (0.27) 0.29	-0.26 (-0.17) -0.08
$\Delta\Phi_1$	0.16 0.22	0.07 (0.13) 0.18	-0.05 (-0.04) 0.00	-0.19 (-0.13) -0.11	0.15 (0.19) 0.21
$\log\tau_{90}$	-0.2 0.03	0.2 (0.2) 0.3	0.5 (0.5) 0.6	0.5 (0.6) 0.6	-0.1 (0.03) 0.1
$\log\tau_{50}$	-3.3 -3.2	-2.6 (-2.6) -2.4	-2.4 (-2.3) -2.2	-2.0 (-1.8) -1.7	-2.1 (-2.0) -1.9
M_t	0.01 0.02	0.04 (0.05) 0.06	0.03 (0.04) 0.04	0.05 (0.05) 0.06	0.11 (0.16) 0.23
$\Delta\Phi_{-1}$	0.32 0.39	0.06 (0.17) 0.35	-0.11 (-0.07) 0.28	-0.13 (0.08) 0.26	0.40 (0.41) 0.47
$\Delta\Phi_4$	0.32 0.44	0.22 (0.26) 0.29	0.26 (0.28) 0.34	0.33 (0.38) 0.46	0.01 (0.03) 0.06
$\log U_{\tau c}$	-1.1 -0.8	-0.9 (-0.7) -0.6	-1.3 (-1.1) -1.0	-1.2 (-1.1) -1.0	-0.3 (-0.1) -0.02
ρ_0 [Ωm]	7 21	66 (94) 112	54 (60) 81	150 (170) 223	47 (59) 92

parameter	6 - grey	7 - pink	8 - orange	9 - black[10]	10 - military g.	11 - petrol b.
$\Delta\Phi_0$	0.26 (0.26) 0.36	0.02 (0.07) 0.12	0.29 (0.31) 0.35	0.41	0.27 (0.31) 0.34	0.12 (0.20) 0.25
$\Delta\Phi_2$	0.00 (0.04) 0.11	0.02 (0.11) 0.17	0.34 (0.38) 0.42	0.20	0.16 (0.19) 0.22	-0.41 (-0.39) -0.32
$\log\tau_{10}$	-4.2 (-4.1) -4.0	-4.4 (-4.3) -4.3	-4.6 (-4.6) -4.5	-4.4	-4.5 (-4.4) -4.4	-3.9 (-3.9) -3.8
$\Delta\Phi_3$	-0.13 (-0.08) -0.05	0.05 (0.10) 0.14	0.31 (0.36) 0.41	0.01	0.14 (0.15) 0.16	-0.22 (-0.21) -0.17
$\Delta\Phi_1$	0.15 (0.18) 0.28	0.06 (0.10) 0.13	0.36 (0.39) 0.39	0.17	0.25 (0.28) 0.32	-0.18 (-0.11) -0.06
$\log\tau_{90}$	-0.1 (0.2) 0.2	0.3 (0.4) 0.5	-1.1 (-0.9) -0.5	-0.6	-0.4 (-0.3) -0.1	0.3 (0.4) 0.4
$\log\tau_{50}$	-2.2 (-1.9) -1.8	-2.3 (-2.2) -2.0	-3.6 (-3.5) -3.2	-2.7	-2.8 (-2.8) -2.7	-1.4 (-1.4) -1.2
M_t	0.32 (0.35) 0.38	0.05 (0.08) 0.12	0.06 (0.08) 0.10	0.02	0.02 (0.08) 0.11	0.13 (0.13) 0.15
$\Delta\Phi_{-1}$	0.37 (0.38) 0.56	0.01 (0.28) 0.39	0.40 (0.44) 0.47	2.28	0.26 (0.29) 0.42	0.33 (0.45) 0.57
$\Delta\Phi_4$	-0.04 (0.00) 0.02	0.20 (0.35) 0.39	0.28 (0.32) 0.37	-	0.16 (0.18) 0.23	0.08 (0.14) 0.19
$\log U_{\tau c}$	-0.3 (-0.3) -0.2	-0.7 (-0.6) -0.5	-0.6 (-0.4) -0.4	-0.1	-0.6 (-0.5) -0.5	0.1 (0.2) 0.2
ρ_0 [Ωm]	180 (209) 238	122 (163) 204	67 (111) 132	16	8 (47) 104	104 (111) 149

---

[11] This cluster is composed by only two samples.

Typical values of textural and fluid properties for each cluster, according to the classifications into two, five, eight, and eleven total clusters. Values are reported in the form: 25th (50th) 75th percentiles.

	2 clusters	
parameter	**1 - blue**	**2 - red**
M [%]	18 (33) 47	3 (4) 12
S [%]	46 (64) 82	87 (92) 96
G [%]	0 (0) 7	0 (0) 5
vfS [%]	4 (10) 11	2 (4) 8
fS [%]	10 (15) 20	9 (21) 40
mS [%]	9 (22) 49	14 (38) 53
cS [%]	6 (9) 10	0 (7) 23
vcS [%]	0 (0) 6	0 (1) 3
$\log \Gamma_{0.063}$	0.0 (0.4) 0.7	0.9 (1.4) 1.5
$\log \Gamma_{0.125}$	-0.1 (0.2) 0.5	0.6 (1.0) 1.2
$\log \Gamma_{0.250}$	-0.3 (-0.3) 0.1	-0.3 (0.1) 0.7
d_{10} **[phi]**	10.0 (10.0) 10.5	2.5 (3.0) 4.6
d_{20} **[phi]**	3.4 (5.4) 7.4	1.9 (2.5) 3.0
d_{30} **[phi]**	2.5 (4.4) 6.1	1.5 (2.3) 2.7
d_{50} **[phi]**	1.9 (3.0) 3.8	1.3 (2.0) 2.3
d_{60} **[phi]**	1.7 (2.5) 2.9	1.1 (1.8) 2.1
d_{90} **[phi]**	-0.4 (1.1) 1.1	0.4 (1.1) 1.6
$\log U_{60}$	2.0 (2.1) 2.6	0.4 (0.4) 0.8
$\log U_{90}$	2.8 (2.8) 3.1	0.5 (0.6) 1.0
$\log U_{c}$	0.2 (0.2) 2.2	0.0 (0.1) 0.3
θ **[**m^3m^{-3}**]**	0.40 (0.43) 0.52	0.37 (0.39) 0.41
OM [%]	0.1 (0.1) 0.3	0.0 (0.1) 0.4
$\rho_{w(f)}$ **[Ωm]**	35 (57) 87	15 (30) 43

	5 clusters				
parameter	**1 - blue**	**2 - red**	**3 - green**	**4 - cyan**	**5 - purple**
M [%]	10 (15) 18	33 (47) 47	3 (4) 4	3 (4) 10	13 (26) 46
S [%]	82 (85) 90	46 (46) 64	96 (96) 96	88 (90) 96	54 (54) 59
G [%]	0 (0) 0	0 (7) 7	0 (0) 0	0 (1) 3	0 (10) 33
vfS [%]	4 (6) 8	8 (11) 11	2 (4) 8	2 (3) 7	3 (7) 25
fS [%]	20 (31) 44	10 (10) 15	9 (35) 40	10 (21) 43	5 (9) 25
mS [%]	35 (43) 49	9 (9) 29	45 (52) 53	31 (38) 54	4 (14) 14
cS [%]	3 (6) 9	9 (10) 10	0 (8) 31	0 (6) 23	0 (12) 17
vcS [%]	0 (0) 0	0 (6) 6	0 (1) 1	0 (0) 3	0 (8) 15
log $\Gamma_{0.063}$	0.7 (0.8) 1.0	0.0 (0.0) 0.4	1.4 (1.4) 1.4	0.9 (1.3) 1.5	0.1 (0.4) 0.8
log $\Gamma_{0.125}$	0.5 (0.6) 0.7	-0.1 (-0.1) 0.2	1.0 (1.1) 1.2	0.6 (1.1) 1.2	-0.4 (0.3) 0.7
log $\Gamma_{0.250}$	-0.2 (0.0) 0.1	-0.3 (-0.3) -0.1	0.0 (0.1) 0.8	-0.2 (0.4) 0.7	-1.3 (0.0) 0.6
d_{10} **[phi]**	4.2 (7.6) 10.5	10.0 (10.0) 10.5	2.5 (2.9) 3.0	2.4 (2.8) 4.4	6.2 (7.3) 9.2
d_{20} **[phi]**	2.9 (3.2) 3.4	5.4 (7.4) 7.4	1.8 (2.5) 2.7	1.9 (2.3) 3.0	2.2 (5.5) 5.6
d_{30} **[phi]**	2.5 (2.6) 2.7	4.3 (6.1) 6.1	1.5 (2.3) 2.4	1.6 (1.9) 2.7	1.4 (3.0) 5.2
d_{50} **[phi]**	1.9 (2.0) 2.2	2.8 (3.8) 3.8	1.3 (2.0) 2.0	1.3 (1.6) 2.3	0.2 (1.8) 4.1
d_{60} **[phi]**	1.7 (1.9) 2.0	2.3 (2.9) 2.9	1.1 (.8) 1.9	1.1 (1.5) 2.0	-0.6 (1.4) 3.6
d_{90} **[phi]**	1.1 (1.1) 1.4	-0.4 (-0.4) 1.1	0.6 (1.1) 1.6	0.4 (1.0) 1.5	-2.5 (-0.8) 2.3
log U_{60}	0.6 (1.7) 2.6	2.1 (2.1) 2.3	0.3 (0.4) 0.4	0.4 (0.4) 0.6	0.8 (1.5) 2.4
log U_{90}	0.8 (1.9) 2.8	2.8 (3.1) 3.1	0.4 (0.6) 0.6	0.5 (0.8) 1.0	1.2 (2.1) 2.9
log U_c	0.2 (1.3) 2.2	0.2 (0.2) 1.2	0.0 (0.0) 0.2	0.0 (0.1) 0.3	0.2 (1.1) 1.2
θ **[**m^3m^{-3}**]**	0.39 (0.40) 0.41	0.42 (0.48) 0.54	0.37 (0.38) 0.40	0.37 (0.40) 0.41	0.36 (0.38) 0.42
OM [%]	0.1 (0.1) 0.1	0.1 (0.3) 0.3	0.0 (0.1) 0.2	0.0 (0.1) 0.4	0.1 (0.2) 0.3
$\rho_{w(f)}$ **[**Ω**m]**	48 (62) 78	23 (52) 91	19 (36) 47	17 (29) 38	2 (28) 37

	8 clusters					
parameter	**1 - blue**	**2 - red**	**3 - green**	**4 - cyan**	**5 - purple**[10]	**6 - grey**
M [%]	2 (3) 8	3 (5) 10	41 (46) 46	12 (13) 20	81	10 (15) 18
S [%]	87 (88) 94	90 (91) 96	54 (54) 55	54 (54) 73	14	82 (85) 90
G [%]	0 (2) 13	0 (0) 3	0 (0) 4	10 (24) 33	5	0 (0) 0
vfS [%]	2 (3) 5	2 (4) 18	20 (25) 25	3 (3) 7	6	4 (6) 8
fS [%]	7 (15) 32	10 (31) 59	20 (25) 25	5 (6) 10	2	20 (31) 44
mS [%]	34 (38) 60	12 (38) 54	4 (4) 6	14 (14) 24	2	35 (43) 49
cS [%]	5 (15) 26	0 (5) 23	0 (0) 5	12 (17) 17	2	3 (6) 9
vcS [%]	0 (2) 11	0 (0) 3	0 (0) 4	8 (14) 15	2	0 (0) 0
$\log \Gamma_{0.063}$	1.1 (1.5) 1.9	0.9 (1.3) 1.5	0.1 (0.1) 0.2	0.6 (0.8) 0.8	-0.6	0.7 (0.8) 1.0
$\log \Gamma_{0.125}$	0.9 (1.2) 1.5	0.4 (1.1) 1.2	-0.4 (-0.4) -0.2	0.5 (0.7) 0.7	-0.8	0.5 (0.6) 0.7
$\log \Gamma_{0.250}$	0.1 (0.6) 1.0	-0.9 (0.2) 0.7	-1.3 (-1.3) -1.0	0.0 (0.6) 0.6	-0.9	-0.2 (0.0) 0.1
d_{10} **[phi]**	2.0 (2.6) 3.7	2.4 (2.8) 4.4	6.2 (6.2) 7.2	5.9 (7.3) 8.2	13.9	4.2 (7.6) 10.5
d_{20} **[phi]**	1.7 (2.1) 2.7	1.9 (2.4) 3.6	5.6 (5.6) 6.0	2.2 (2.2) 4.1	8.4	2.9 (3.2) 3.4
d_{30} **[phi]**	1.5 (1.8) 2.3	1.6 (2.1) 3.0	3.0 (3.4) 5.2	1.4 (1.4) 3.1	7.1	2.5 (2.6) 2.7
d_{50} **[phi]**	0.9 (1.5) 1.9	1.3 (1.8) 2.7	3.4 (4.1) 4.1	0.2 (0.5) 1.8	5.2	1.9 (2.0) 2.2
d_{60} **[phi]**	0.7 (1.3) 1.7	1.2 (1.7) 2.5	2.8 (3.6) 3.6	-0.6 (0.0) 1.4	4.6	1.7 (1.9) 2.0
d_{90} **[phi]**	-1.3 (0.7) 1.1	0.4 (1.1) 1.9	1.3 (2.3) 2.3	-2.5 (-1.9) -0.8	1.6	1.1 (1.1) 1.4
$\log U_{60}$	0.4 (0.4) 0.7	0.4 (0.4) 0.6	0.8 (0.8) 1.3	1.5 (2.4) 2.4	0.9	0.6 (1.7) 2.6
$\log U_{90}$	0.6 (1.0) 1.0	0.5 (0.7) 0.8	1.2 (1.2) 1.8	2.0 (2.9) 3.0	1.1	0.8 (1.9) 2.8
$\log U_c$	-0.1 (0.1) 0.2	0.0 (0.1) 0.3	-0.2 (1.1) 1.1	0.3 (1.1) 1.2	1.3	0.2 (1.3) 2.2
θ **[m^3m^{-3}]**	0.34 (0.38) 0.41	0.38 (0.40) 0.41	0.36 (0.39) 0.41	0.36 (0.37) 0.40	0.53	0.39 (0.40) 0.41
OM [%]	0.0 (0.1) 0.1	0.0 (0.2) 0.4	0.1 (0.1) 0.1	0.2 (0.3) 0.3	-	0.1 (0.1) 0.1
$\rho_{w(f)}$ **[Ωm]**	30 (41) 70	7 (23) 31	24 (35) 64	1 (16) 34	10	48 (62) 78

parameter	8 clusters - part II	
	7 - pink	**8 - orange**
M [%]	33 (47) 47	3 (4) 4
S [%]	46 (46) 64	96 (96) 96
G [%]	0 (7) 7	0 (0) 0
vfS [%]	8 (11) 11	2 (4) 8
fS [%]	10 (10) 15	9 (35) 40
mS [%]	9 (9) 29	45 (52) 53
cS [%]	9 (10) 10	0 (8) 31
vcS [%]	0 (6) 6	0 (1) 1
$\log \Gamma_{0.063}$	0.0 (0.0) 0.4	1.4 (1.4) 1.4
$\log \Gamma_{0.125}$	-0.1 (-0.1) 0.2	1.0 (1.1) 1.2
$\log \Gamma_{0.250}$	-0.3 (-0.3) -0.1	0.0 (0.1) 0.8
d_{10} [phi]	10.0 (10.0) 10.5	2.5 (2.9) 3.0
d_{20} [phi]	5.4 (7.4) 7.4	1.8 (2.5) 2.7
d_{30} [phi]	4.3 (6.1) 6.1	1.5 (2.3) 2.4
d_{50} [phi]	2.8 (3.8) 3.8	1.3 (2.0) 2.0
d_{60} [phi]	2.3 (2.9) 2.9	1.1 (.8) 1.9
d_{90} [phi]	-0.4 (-0.4) 1.1	0.6 (1.1) 1.6
$\log U_{60}$	2.1 (2.1) 2.3	0.3 (0.4) 0.4
$\log U_{90}$	2.8 (3.1) 3.1	0.4 (0.6) 0.6
$\log U_c$	0.2 (0.2) 1.2	0.0 (0.0) 0.2
θ [m^3m^{-3}]	0.42 (0.48) 0.54	0.37 (0.38) 0.40
OM [%]	0.1 (0.3) 0.3	0.0 (0.1) 0.2
$\rho_{w(f)}$ [Ωm]	23 (52) 91	19 (36) 47

parameter	**11 clusters**					
	1 - blue[11]	**2 - red**	**3 - green**	**4 - cyan**	**5 - purple**	**6 - grey**
M [%]	4 10	2 (5) 10	3 (4) 4	3 (4) 4	18 (33) 47	47 (47) 57
S [%]	90 96	89 (91) 94	96 (96) 96	96 (96) 96	46 (64) 82	39 (46) 46
G [%]	0 0	0 (1) 3	0 (0) 0	0 (0) 0	0 (3) 7	4 (7) 7
vfS [%]	4 18	2 (3) 13	2 (4) 8	2 (4) 8	4 88) 11	11 (11) 12
fS [%]	40 59	10 (21) 59	9 (38) 40	9 (35) 40	10 (15) 20	10 (10) 10
mS [%]	12 52	22 (38) 54	45 (52) 53	45 (52) 53	9 (29) 49	8 (9) 9
cS [%]	0 0	0 (6) 23	0 (4) 31	0 (8) 26	9 (9) 10	6 (10) 10
vcS [%]	0 0	0 (0) 3	0 (0) 1	0 (1) 1	0 (3) 6	3 (6) 6
log $\Gamma_{0.063}$	0.9 1.4	0.9 (1.3) 1.6	1.4 (1.4) 1.4	1.4 (1.4) 1.4	0.0 (0.4) 0.7	-0.1 (0.0) 0.0
log $\Gamma_{0.125}$	0.4 1.1	0.5 (1.1) 1.2	1.0 (1.1) 1.2	0.9 (1.1) 1.2	-0.1 (0.2) 0.5	-0.4 (-0.1) -0.1
log $\Gamma_{0.250}$	-0.9 0.0	-0.6 (0.4) 0.7	0.0 (0.0) 0.8	0.0 (0.1) 0.7	-0.3 (-0.1) 0.1	-0.7 (-0.3) -0.3
d_{10} [phi]	2.9 4.4	2.4 (2.8) 4.4	2.5 (2.9) 3.0	2.5 (2.9) 3.1	10.0 (10.2) 10.5	10.0 (10.0) 10.8
d_{20} [phi]	2.5 3.6	1.9 (2.4) 3.3	1.8 (2.5) 2.7	1.9 (2.5) 2.7	3.4 (5.4) 7.4	7.4 (7.4) 8.8
d_{30} [phi]	2.3 3.0	1.6 (1.9) 2.9	1.5 (2.3) 2.4	1.6 (2.3) 2.4	2.5 (4.3) 6.1	6.1 (6.1) 7.5
d_{50} [phi]	2.0 2.7	1.3 (1.6) 2.5	1.3 (2.0) 2.0	1.3 (2.0) 2.0	1.9 (2.8) 3.8	3.8 (3.8) 5.2
d_{60} [phi]	1.9 2.5	1.2 (1.5) 2.3	1.1 (1.8) 1.9	1.2 (1.8) 1.9	1.7 (2.3) 2.9	2.9 (2.9) 4.1
d_{90} [phi]	1.6 1.9	0.4 (1.0) 1.7	0.6 (1.3) 1.6	0.6 (1.1) 1.5	-0.4 (0.3) 1.1	-0.4 (-0.4) 0.8
log U_{60}	0.3 0.6	0.4 (0.4) 0.6	0.3 (0.4) 0.4	0.3 (0.4) 0.4	2.1 (2.3) 2.6	2.0 (2.1) 2.1
log U_{90}	0.4 0.8	0.6 (0.7) 0.9	0.4 (0.5) 0.6	0.4 (0.6) 0.6	2.8 (2.9) 3.1	3.0 (3.1) 3.1
log U_c	0.0 0.3	0.1 (0.1) 0.3	0.0 (0.0) 0.2	0.0 (0.0) 0.1	0.2 (1.2) 2.2	0.0 (0.2) 0.2
θ [m^3m^{-3}]	0.40 0.43	0.37 (0.40) 0.41	0.37 (0.38) 0.39	0.37 (0.38) 0.40	0.39 (0.42) 0.49	0.48 (0.52) 0.58
OM [%]	0.0 0.4	0.0 (0.2) 0.4	0.0 (0.0) 0.2	0.0 (0.1) 0.2	0.1 (0.2) 0.3	0.2 (0.3) 0.3
$\rho_{w(f)}$ [Ωm]	2 7	15 (27) 32	15 (16) 22	36 (43) 50	19 (23) 35	75 (91) 106

parameter	**11 clusters - part II**				
	7 - pink	**8 - orange**	**9 - black**[10]	**10 - military g.**	**11 - petrol b.**
M [%]	2 (3) 8	41 (46) 46	81	12 (13) 20	10 (15) 18
S [%]	87 (88) 94	54 (54) 55	14	54 (54) 73	82 (85) 90
G [%]	0 (2) 13	0 (0) 4	5	10 (24) 33	0 (0) 0
vfS [%]	2 (3) 5	20 (25) 25	6	3 (3) 7	4 (6) 8
fS [%]	7 (15) 32	20 (25) 25	2	5 (6) 10	20 (31) 44
mS [%]	34 (38) 60	4 (4) 6	2	14 (14) 24	35 (43) 49
cS [%]	5 (15) 26	0 (0) 5	2	12 (17) 17	3 (6) 9
vcS [%]	0 (2) 11	0 (0) 4	2	8 (14) 15	0 (0) 0
log $\Gamma_{0.063}$	1.1 (1.5) 1.9	0.1 (0.1) 0.2	-0.6	0.6 (0.8) 0.8	0.7 (0.8) 1.0
log $\Gamma_{0.125}$	0.9 (1.2) 1.5	-0.4 (-0.4) -0.2	-0.8	0.5 (0.7) 0.7	0.5 (0.6) 0.7
log $\Gamma_{0.250}$	0.1 (0.6) 1.0	-1.3 (-1.3) -1.0	-0.9	0.0 (0.6) 0.6	-0.2 (0.0) 0.1
d_{10} [phi]	2.0 (2.6) 3.7	6.2 (6.2) 7.2	13.9	5.9 (7.3) 8.2	4.2 (7.6) 10.5
d_{20} [phi]	1.7 (2.1) 2.7	5.6 (5.6) 6.0	8.4	2.2 (2.2) 4.1	2.9 (3.2) 3.4
d_{30} [phi]	1.5 (1.8) 2.3	3.0 (3.4) 5.2	7.1	1.4 (1.4) 3.1	2.5 (2.6) 2.7
d_{50} [phi]	0.9 (1.5) 1.9	3.4 (4.1) 4.1	5.2	0.2 (0.5) 1.8	1.9 (2.0) 2.2
d_{60} [phi]	0.7 (1.3) 1.7	2.8 (3.6) 3.6	4.6	-0.6 (0.0) 1.4	1.7 (1.9) 2.0
d_{90} [phi]	-1.3 (0.7) 1.1	1.3 (2.3) 2.3	1.6	-2.5 (-1.9) -0.8	1.1 (1.1) 1.4
log U_{60}	0.4 (0.4) 0.7	0.8 (0.8) 1.3	0.9	1.5 (2.4) 2.4	0.6 (1.7) 2.6
log U_{90}	0.6 (1.0) 1.0	1.2 (1.2) 1.8	1.1	2.0 (2.9) 3.0	0.8 (1.9) 2.8
log U_c	-0.1 (0.1) 0.2	-0.2 (1.1) 1.1	1.3	0.3 (1.1) 1.2	0.2 (1.3) 2.2
θ [m^3m^{-3}]	0.34 (0.38) 0.41	0.36 (0.39) 0.41	0.53	0.36 (0.37) 0.40	0.39 (0.40) 0.41
OM [%]	0.0 (0.1) 0.1	0.1 (0.1) 0.1	-	0.2 (0.3) 0.3	0.1 (0.1) 0.1
$\rho_{w(f)}$ [Ωm]	30 (41) 70	24 (35) 64	10	1 (16) 34	48 (62) 78

Appendix H

For each validation samples, the upper table reports the set of input electrical parameters, ordered with decreasing importance, and the direct and indirect compatibilities with the clusters obtained from the investigated dataset, according to the classifications into two, five, eight, and eleven total clusters. The lower table reports the comparison between the measured properties related to the sediment and the saturation fluid, and the corresponding properties inferred from the selected clusters. Here, green colour highlights a good accordance (i.e., measured value included in the IQR), and red colour no accordance, whereas yellow colour indicates a measured value close to the estimated range of variability and possibly outside due to approximation. Grey values are reported in correspondence of non available data.

Sample A (Bairlein et al. 2014)

parameter	**total number of clusters**			
	2	**5**	**8**	**11**
$\Delta\Phi_0 = 0.08$	2	4	1 - 2	2 - 7
$\Delta\Phi_2 = 0.10$	2	3 - 4	1 - 8 - (2)	4 - 6 - 7 - (2, 3)
$\log\tau_{10} = -4.6$	(2)	(3, 4, 5)	3 - (2, 4, 8)	1 - 8 - (2, 3, 4, 10)
$\Delta\Phi_3 = 0.42$	(2)	(3, 5)	(2, 3, 8)	(1, 8)
$\Delta\Phi_1 = 0.03$	1 - 2	(4)	(1)	(3, 7)
$\log\tau_{90} = 0.3$	2 - (1)	4 - (1)	1 - 2 - 6	2 - 7 - 11
$\log\tau_{50} = -2.8$	2	5	4 - (2)	10 - (9)
$M_t = 0.04$	2	3 - 4 - 5	2 - 4 - 8 - (1)	2 - 3 - 10 - (4, 7)
$\Delta\Phi_{-1} = 0.38$	1	1 - 2 - 5 - (4)	1 - 4 - 6 - 7 - (2, 3)	1 - 6 - 7 - 10 - 11 - (8)
$\Delta\Phi_4 = 0.32$	2	3 - 4	1 - 2 - 3 - 8	1 - 3 - 7 - 8 - (4)
$\log U_{\tau c} = -1.4$	(2)	(3)	(8)	(3)
$\rho_0 = 128$ [Ωm]	1 - 2	1 - 2 - 3 - 4	1 - 3 - 6 - 7 - 8	7 - 8 - 11
selected cluster	**2/2**	**4/5**	**2/8**	**2/11**

measured	**estimated**			
	2/2	**4/5**	**2/8**	**2/11**
M = 3 [%]	3 (4) 12	3 (4) 10	3 (5) 10	2 (5) 10
S = 96 [%]	87 (92) 96	88 (90) 96	90 (91) 96	89 (91) 94
G = 1 [%]	0 (0) 5	0 (1) 3	0 (0) 3	0 (1) 3
vfS = 13 [%]	2 (4) 8	2 (3) 7	2 (4) 18	2 (3) 13
fS = 28 [%]	9 (21) 40	10 (21) 43	10 (31) 59	10 (21) 59
mS = 41 [%]	14 (38) 53	31 (38) 54	12 (38) 54	22 (38) 54
cS = 14 [%]	0 (7) 23	0 (6) 23	0 (5) 23	0 (6) 23
vcS = 0 [%]	0 (1) 3	0 (0) 3	0 (0) 3	0 (0) 3
$\log\Gamma_{0.063} = 1.5$	0.9 (1.4) 1.5	0.9 (1.3) 1.5	0.9 (1.3) 1.5	0.9 (1.3) 1.6
$\log\Gamma_{0.125} = 0.7$	0.6 (1.0) 1.2	0.6 (1.1) 1.2	0.4 (1.1) 1.2	0.5 (1.1) 1.2
$\log\Gamma_{0.250} = 0.1$	-0.3 (0.1) 0.7	-0.2 (0.4) 0.7	-0.9 (0.2) 0.7	-0.6 (0.4) 0.7
$d_{10} = 3.4$ [phi]	2.5 (3.0) 4.6	2.4 (2.8) 4.4	2.4 (2.8) 4.4	2.4 (2.8) 4.4
$d_{20} = 2.0$ [phi]	1.9 (2.5) 3.0	1.9 (2.3) 3.0	1.9 (2.4) 3.6	1.9 (2.4) 3.3
$d_{30} = 1.8$ [phi]	1.5 (2.3) 2.7	1.6 (1.9) 2.7	1.6 (2.1) 3.0	1.6 (1.9) 2.9
$d_{50} = 1.3$ [phi]	1.3 (2.0) 2.3	1.3 (1.6) 2.3	1.3 (1.8) 2.7	1.3 (1.6) 2.5
$d_{60} = 1.1$ [phi]	1.1 (1.8) 2.1	1.1 (1.5) 2.0	1.2 (1.7) 2.5	1.2 (1.5) 2.3
$d_{90} = 0.9$ [phi]	0.4 (1.1) 1.6	0.4 (1.0) 1.5	0.4 (1.1) 1.9	0.4 (1.0) 1.7
$\log U_{60} = 0.7$	0.4 (0.4) 0.8	0.4 (0.4) 0.6	0.4 (0.4) 0.6	0.4 (0.4) 0.6
$\log U_{90} = 0.8$	0.5 (0.6) 1.0	0.5 (0.8) 1.0	0.5 (0.7) 0.8	0.6 (0.7) 0.9
$\log U_c = 0.3$	0.0 (0.1) 0.3	0.0 (0.1) 0.3	0.0 (0.1) 0.3	0.1 (0.1) 0.3
$\theta = 0.32$	0.37 (0.39) 0.41	0.37 (0.40) 0.41	0.38 (0.40) 0.41	0.37 (0.40) 0.41
OM = n. a.	0.0 (0.1) 0.4	0.0 (0.1) 0.4	0.0 (0.2) 0.4	0.0 (0.2) 0.4
$\rho_{w(f)} \leq 33$ [Ωm]	15 (30) 43	17 (29) 38	7 (23) 31	15 (27) 32

Sample C (Bairlein et al. 2014)

parameter	**total number of clusters**			
	2	**5**	**8**	**11**
$\Delta\Phi_0 = 0.29$	1	2 - 5	3 - 4 - 7	5 - 6 - 8 - 10 - (11)
$\Delta\Phi_2 = -0.01$	1	2	7	5 - (6)
$\log\tau_{10} = -4.3$	1	3 - 4 - (2, 5)	1 - 8 - (2, 4, 5, 7)	4 - 7 - (2, 3, 5, 6, 10)
$\Delta\Phi_3 = 0.07$	-	-	1	7
$\Delta\Phi_1 = 0.04$	1 - 2	(4)	(1)	(2, 3, 7)
$\log\tau_{90} = 0.06$	1 - 2	2	7 - (2)	5 - 6
$\log\tau_{50} = -2.2$	2	3 - 4 - (2)	1 - 8 - (7)	3 - 6 - 7 - (5)
$M_t = 0.08$	2	5 - (4)	1 - 3 - 4 - (2, 8)	7 - 8 - 10
$\Delta\Phi_{-1} = 0.55$	(1)	1	6	6 - 11
$\Delta\Phi_4 = 0.07$	1	(1)	(6, 7)	(5, 11)
$\log U_{\tau c} = 1.6$	-	-	-	-
$\rho_0 = 36$ [Ωm]	-	5	2 - 4	10 - (1, 5)
selected cluster	**1/2**	**2/5**	**7/8**	**5/11**

measured	**estimated**		
	1/2	**2/5 ≡ 7/8**	**5/11**
M = 87 [%]	18 (33) 47	33 (47) 47	18 (33) 47
S = 13 [%]	46 (64) 82	46 (46) 64	46 (64) 82
G = 0 [%]	0 (0) 7	0 (7) 7	0 (3) 7
vfS = 6 [%]	4 (10) 11	8 (11) 11	4 (8) 11
fS = 4 [%]	10 (15) 20	10 (10) 15	10 (15) 20
mS = 1 [%]	9 (22) 49	9 (9) 29	9 (29) 49
cS = 0 [%]	6 (9) 10	9 (10) 10	9 (9) 10
vcS = 0 [%]	0 (0) 6	0 (6) 6	0 (3) 6
$\log\Gamma_{0.063} = -0.8$	0.0 (0.4) 0.7	0.0 (0.0) 0.4	0.0 (0.4) 0.7
$\log\Gamma_{0.125} = -1.2$	-0.1 (0.2) 0.5	-0.1 (-0.1) 0.2	-0.1 (0.2) 0.5
$\log\Gamma_{0.250} = -1.8$	-0.3 (-0.3) 0.1	-0.3 (-0.3) -0.1	-0.3 (-0.1) 0.1
d_{10} = n. a.	10.0 (10.0) 10.5	10.0 (10.0) 10.5	10.0 (10.2) 10.5
d_{20} = 7.9 [phi]	3.4 (5.4) 7.4	5.4 (7.4) 7.4	3.4 (5.4) 7.4
d_{30} = 6.9 [phi]	2.5 (4.4) 6.1	4.3 (6.1) 6.1	2.5 (4.3) 6.1
d_{50} = 6.0 [phi]	1.9 (3.0) 3.8	2.8 (3.8) 3.8	1.9 (2.8) 3.8
d_{60} = 5.6 [phi]	1.7 (2.5) 2.9	2.3 (2.9) 2.9	1.7 (2.3) 2.9
d_{90} = 3.2 [phi]	-0.4 (1.1) 1.1	-0.4 (-0.4) 1.1	-0.4 (0.3) 1.1
$\log U_{60}$ = n. a.	2.0 (2.1) 2.6	2.1 (2.1) 2.3	2.1 (2.3) 2.6
$\log U_{90}$ = n. a.	2.8 (2.8) 3.1	2.8 (3.1) 3.1	2.8 (2.9) 3.1
$\log U_c$ = n. a.	0.2 (0.2) 2.2	0.2 (0.2) 1.2	0.2 (1.2) 2.2
$\theta = 0.51$	0.40 (0.43) 0.52	0.42 (0.48) 0.54	0.39 (0.42) 0.49
OM = n. a.	0.1 (0.1) 0.3	0.1 (0.3) 0.3	0.1 (0.2) 0.3
$\rho_{w(f)} \leq 33$ [Ωm]	35 (57) 87	23 (52) 91	19 (23) 35

Sample Kr6

parameter	**total number of clusters**			
	2	**5**	**8**	**11**
$\Delta\Phi_0 = -0.14$	(2)	3	8	3 - 4
$\Delta\Phi_2 = 0.20$	2	5 - (4)	2 - 4 - (1)	2 - 9 - 10 - (1)
$\log\tau_{10} = -4.4$	2	3 - 4 - 5	1 - 2 - 4 - 5 - 8	2 - 3 - 4 - 7 - 9 - 10
$\Delta\Phi_3 = 0.12$	(2)	4	1 - (2, 4)	7 - (2, 10)
$\Delta\Phi_1 = 0.18$	1 - 2	2 - (4)	2 - 7 - (4)	1 - 2 - 5 - 6 - (9)
$\log\tau_{90} = 0.5$	2	3 - (1, 4)	1 - 8 - (6)	3 - 4 - 7 - (11)
$\log\tau_{50} = -2.4$	2	4	(1, 2)	2 - 3 - (7)
$M_t = 0.01$	(2)	(5)	(4, 5)	1 - (9, 10)
$\Delta\Phi_{-1} = 0.04$	2	3	1 - 8	7 - (2)
$\Delta\Phi_4 = 0.54$	(2)	(3)	(8)	(4)
$\log U_{\tau c} = -0.4$	(1)	5 - (2, 4)	3 - (1, 7)	8 - (5, 6, 7, 10)
$\rho_0 = 81$ [Ωm]	2 - (1)	2 - 3 - 4 - 5	2 - 3 - 4 - 7 - 8	2 - 3 - 5 - 8 - 10
selected cluster	**2/2**	**4/5**	**2/8**	**2/11**

measured	**estimated**			
	2/2	**4/5**	**2/8**	**2/11**
M = 1 [%]	3 (4) 12	3 (4) 10	3 (5) 10	2 (5) 10
S = 42 [%]	87 (92) 96	88 (90) 96	90 (91) 96	89 (91) 94
G = 57 [%]	0 (0) 5	0 (1) 3	0 (0) 3	0 (1) 3
vfS = 1 [%]	2 (4) 8	2 (3) 7	2 (4) 18	2 (3) 13
fS = 2 [%]	9 (21) 40	10 (21) 43	10 (31) 59	10 (21) 59
mS = 5 [%]	14 (38) 53	31 (38) 54	12 (38) 54	22 (38) 54
cS = 10 [%]	0 (7) 23	0 (6) 23	0 (5) 23	0 (6) 23
vcS = 24 [%]	0 (1) 3	0 (0) 3	0 (0) 3	0 (0) 3
$\log\Gamma_{0.063} = 2.0$	0.9 (1.4) 1.5	0.9 (1.3) 1.5	0.9 (1.3) 1.5	0.9 (1.3) 1.6
$\log\Gamma_{0.125} = 1.7$	0.6 (1.0) 1.2	0.6 (1.1) 1.2	0.4 (1.1) 1.2	0.5 (1.1) 1.2
$\log\Gamma_{0.250} = 1.4$	-0.3 (0.1) 0.7	-0.2 (0.4) 0.7	-0.9 (0.2) 0.7	-0.6 (0.4) 0.7
d_{10} = 0.6 [phi]	2.5 (3.0) 4.6	2.4 (2.8) 4.4	2.4 (2.8) 4.4	2.4 (2.8) 4.4
d_{20} = 0.2 [phi]	1.9 (2.5) 3.0	1.9 (2.3) 3.0	1.9 (2.4) 3.6	1.9 (2.4) 3.3
d_{30} = -0.3 [phi]	1.5 (2.3) 2.7	1.6 (1.9) 2.7	1.6 (2.1) 3.0	1.6 (1.9) 2.9
d_{50} = -1.5 [phi]	1.3 (2.0) 2.3	1.3 (1.6) 2.3	1.3 (1.8) 2.7	1.3 (1.6) 2.5
d_{60} = -1.9 [phi]	1.1 (1.8) 2.1	1.1 (1.5) 2.0	1.2 (1.7) 2.5	1.2 (1.5) 2.3
d_{90} = n. a.	0.4 (1.1) 1.6	0.4 (1.0) 1.5	0.4 (1.1) 1.9	0.4 (1.0) 1.7
$\log U_{60} = 0.8$	0.4 (0.4) 0.8	0.4 (0.4) 0.6	0.4 (0.4) 0.6	0.4 (0.4) 0.6
$\log U_{90}$ = n. a.	0.5 (0.6) 1.0	0.5 (0.8) 1.0	0.5 (0.7) 0.8	0.6 (0.7) 0.9
$\log U_c = -0.2$	0.0 (0.1) 0.3	0.0 (0.1) 0.3	0.0 (0.1) 0.3	0.1 (0.1) 0.3
$\theta = 0.29$	0.37 (0.39) 0.41	0.37 (0.40) 0.41	0.38 (0.40) 0.41	0.37 (0.40) 0.41
OM = n. a.	0.0 (0.1) 0.4	0.0 (0.1) 0.4	0.0 (0.2) 0.4	0.0 (0.2) 0.4
$\rho_{w(f)} = 16$ [Ωm]	15 (30) 43	17 (29) 38	7 (23) 31	15 (27) 32

Sample Kr7

parameter	**total number of clusters**			
	2	**5**	**8**	**11**
$\Delta\Phi_0 = 0.30$	1	2 - 5	3 - 4 - 7	5 - 6 - 8 - 10
$\Delta\Phi_2 = 0.41$	(2)	(5)	3	8
$\log \tau_{10} = -4.6$	(2)	(3, 4, 5)	3 - (2, 8)	1 - 8 - (2, 3, 4, 10)
$\Delta\Phi_3 = 0.24$	2	3 - 4 - 5	2 - 8	2 - 3 - 4
$\Delta\Phi_1 = 0.45$	(2)	(5)	(3)	(8)
$\log \tau_{90} = -0.8$	(2)	(5)	3	8
$\log \tau_{50} = -3.3$	(2)	(5)	3	1 - 8
$M_t = 0.04$	2	3 - 4 - 5	2 - 4 - 8 - (1)	2 - 3 - 10 - (7)
$\Delta\Phi_{-1} = 0.40$	1 - (2)	1 - 2 - 5 - (4)	3 - 4 - 6 - 7 - (1)	5 - 6 - 8 - 10 - 11 - (1)
$\Delta\Phi_4 = 0.24$	2	3 - 4 - 5 - (1)	1 - 2 - (4)	2 - 7 - (10)
$\log U_{\tau c} = -0.4$	2 - (1)	5 - (2)	3 - (1, 4, 7)	8
$\rho_0 = 80$ [Ωm]	2 - (1)	2 - 4 - 5 - (3)	2 - 3 - 4 - 7 - (8)	2 - 3 - 5 - 8 - 10
selected cluster	**2**	**5**	**3**	**8**

measured	**estimated**		
	2/2	**5/5**	**3/8 ≡ 8/11**
M = 8 [%]	3 (4) 12	13 (26) 46	41 (46) 46
S = 69 [%]	87 (92) 96	54 (54) 59	54 (54) 55
G = 23 [%]	0 (0) 5	0 (10) 33	0 (0) 4
vfS = 5 [%]	2 (4) 8	3 (7) 25	20 (25) 25
fS = 10 [%]	9 (21) 40	5 (9) 25	20 (25) 25
mS = 20 [%]	14 (38) 53	4 (14) 14	4 (4) 6
cS = 17 [%]	0 (7) 23	0 (12) 17	0 (0) 5
vcS = 16 [%]	0 (1) 3	0 (8) 15	0 (0) 4
$\log \Gamma_{0.063} = 1.1$	0.9 (1.4) 1.5	0.1 (0.4) 0.8	0.1 (0.1) 0.2
$\log \Gamma_{0.125} = 0.6$	0.6 (1.0) 1.2	-0.4 (0.3) 0.7	-0.4 (-0.4) -0.2
$\log \Gamma_{0.250} = 0.4$	-0.3 (0.1) 0.7	-1.3 (0.0) 0.6	-1.3 (-1.3) -1.0
$d_{10} = 3.4$ [phi]	2.5 (3.0) 4.6	6.2 (7.3) 9.2	6.2 (6.2) 7.2
$d_{20} = 2.2$ [phi]	1.9 (2.5) 3.0	2.2 (5.5) 5.6	5.6 (5.6) 6.0
$d_{30} = 1.7$ [phi]	1.5 (2.3) 2.7	1.4 (3.0) 5.2	3.0 (3.4) 5.2
$d_{50} = 0.5$ [phi]	1.3 (2.0) 2.3	0.2 (1.8) 4.1	3.4 (4.1) 4.1
$d_{60} = -0.2$ [phi]	1.1 (1.8) 2.1	-0.6 (1.4) 3.6	2.8 (3.6) 3.6
$d_{90} = -2.2$ [phi]	0.4 (1.1) 1.6	-2.5 (-0.8) 2.3	1.3 (2.3) 2.3
$\log U_{60} = 1.1$	0.4 (0.4) 0.8	0.8 (1.5) 2.4	0.8 (0.8) 1.3
$\log U_{90} = 1.7$	0.5 (0.6) 1.0	1.2 (2.1) 2.9	1.2 (1.2) 1.8
$\log U_c = -0.1$	0.0 (0.1) 0.3	0.2 (1.1) 1.2	-0.2 (1.1) 1.1
$\theta = 0.30$	0.37 (0.39) 0.41	0.36 (0.38) 0.42	0.36 (0.39) 0.41
OM = n. a.	0.0 (0.1) 0.4	0.1 (0.2) 0.3	0.1 (0.1) 0.1
$\rho_{w(f)} = 18$ [Ωm]	15 (30) 43	2 (28) 37	24 (35) 64

All'inizio mi dissero che mi attendevano anni di "puro divertimento scientifico", e così è stato.

Ringrazio tutte le persone che in questi tre anni hanno contribuito alla parte scientifica di questo lavoro a alla parte di divertimento,

a Milano e a Jülich,

rendendo questi anni formativi e stimolanti, ricchi di esperienze, conoscenze e domande, e facendomi realizzare il sogno di essere una ricercatrice.

Desidero ringraziare ciascuna persona che ha avuto tempo per ascoltare una domanda o la curiosità per ascoltare una risposta,

Alberto Grisoni, Alberto Pullia, Alessandro Comunian, Antonio Tartaglia, Aryadeep Chakraborty, Bianca Ortuani, Chiara Compostella, Chiara Zuffetti, Curzio Malinverno, il DAAD, Egon Zimmermann, Elena Ferrari, Elena Pettinelli, Elena Rondolini, Elisabetta Erba, Franco Uggeri, Franz Hubert-Hägel, Fulvia Baratelli, GianPaolo Bertolotti, Giovanna De Filippis, Giuliano Vannaroni, Laura Cattaneo, Lucia Pagliari, Luciana Pedrazzini, Luisa De Capitani, Mariangelo Baio, Matthias Kelter, Mauro Mele, Michele Zucali, Monica Dapiaggi, Nicole Asante, Nicoletta Fusi, Odilia Esser, Patrizia Mussini, Riccardo Bersezio, Sameh Othman, Sander Huisman, Shirin Moradi, Stefania Stevenazzi e i colleghi dottorandi, Stefano Poli, Tiziana Apuani, Tiziano Sanvito, Zhan Gao, la mia famiglia, Massimo, tutte le persone di cui ho dimenticato l'aiuto,

e naturalmente Mauro Giudici.

Silvia